

CUTTER-WORKPIECE ENGAGEMENT IDENTIFICATION  
IN MULTI-AXIS MILLING

by

EYYUP ARAS

A THESIS SUBMITTED IN PARTIAL FULFILLEMENT OF  
THE REQUIREMENTS FOR THE DEGREE OF

DOCTOR OF PHILOSOPHY

in

THE FACULTY OF GRADUATE STUDIES  
(Mechanical Engineering)

THE UNIVERSITY OF BRITISH COLUMBIA  
(Vancouver)

July 2008

© Eyyup Aras, 2008

## Abstract

This thesis presents cutter swept volume generation, in-process workpiece modeling and Cutter Workpiece Engagement (*CWE*) algorithms for finding the instantaneous intersections between cutter and workpiece in milling. One of the steps in simulating machining operations is the accurate extraction of the intersection geometry between cutter and workpiece. This geometry is a key input to force calculations and feed rate scheduling in milling. Given that industrial machined components can have highly complex geometries, extracting intersections accurately and efficiently is challenging. Three main steps are needed to obtain the intersection geometry between cutter and workpiece. These are the Swept volume generation, in-process workpiece modeling and *CWE* extraction respectively.

In this thesis an analytical methodology for determining the shapes of the cutter swept envelopes is developed. In this methodology, cutter surfaces performing 5-axis tool motions are decomposed into a set of characteristic circles. For obtaining these circles a concept of *two-parameter-family of spheres* is introduced. Considering relationships among the circles the swept envelopes are defined analytically. The implementation of methodology is simple, especially when the cutter geometries are represented by pipe surfaces.

During the machining simulation the workpiece update is required to keep track of the material removal process. Several choices for workpiece updates exist. These are the solid, faceted and vector model based methodologies. For updating the workpiece surfaces represented by the solid or faceted models third party software can be used. In this thesis multi-axis milling update methodologies are developed for workpieces defined by discrete vectors with different orientations. For simplifying the intersection calculations between discrete vectors and the tool envelope the properties of canal surfaces are utilized.

A typical NC cutter has different surfaces with varying geometries and during the material removal process restricted regions of these surfaces are eligible to contact the in-process workpiece. In this thesis these regions are analyzed with respect to different tool motions. Later using the results from these analyses the solid, polyhedral and vector based *CWE* methodologies are developed for a range of different types of cutters and multi-axis tool motions. The workpiece surfaces cover a wide range of surface geometries including sculptured surfaces.

## Table of Contents

<b>Abstract .....</b>	<b>ii</b>
<b>Table of Contents .....</b>	<b>iii</b>
<b>List of Tables.....</b>	<b>vii</b>
<b>List of Figures.....</b>	<b>viii</b>
<b>List of Algorithms.....</b>	<b>xiv</b>
<b>Acknowledgements.....</b>	<b>xv</b>
<b>Chapter 1 Introduction.....</b>	<b>1</b>
1.1 Virtual Machining .....	1
1.2 Geometric Modeling .....	3
1.2.1 Swept Volume Generation.....	4
1.2.2 In-process Workpiece Modeling .....	5
1.2.3 Cutter Workpiece Engagement Extraction.....	10
1.3 Process Modeling .....	15
1.4 Scope of this Research .....	15
1.5 Organization of Thesis .....	16
<b>Chapter 2 Literature Review .....</b>	<b>18</b>
2.1 Swept Volume Generation .....	18
2.1.1 Sweep Differential Equation Approach .....	19
2.1.2 Jacobian Rank Deficiency Approach .....	20
2.1.3 Swept profile based Approaches .....	20
2.1.4 Discussion .....	21
2.2 In-process Workpiece Modeling .....	22

2.2.1 Solid Modeler Based Methodologies .....	22
2.2.2 Approximate Modeler Based Methodologies .....	24
2.2.3 Discussion .....	28
2.3 Cutter Workpiece Engagement Extraction.....	29
2.3.1 Solid model Based Methods.....	30
2.3.2 Polyhedral Model Based Methods .....	32
2.3.3 Discrete Vector Based Methods.....	33
2.3.4 Other Existing Methods .....	34
2.3.5 Discussion .....	35
2.4 Summary .....	37
<b>Chapter 3 Cutter Swept Volume Generation .....</b>	<b>38</b>
3.1 Canal Surfaces.....	38
3.1.1 Explicit Representation of Canal Surfaces.....	39
3.1.2 Cutting Tool Geometries as Canal Surfaces .....	41
3.2 Two-Parameter-Family of Spheres in Multi-Axis Milling .....	42
3.2.1 Applying the Methodology on the Cylinder Surface .....	46
3.2.2 Applying the Methodology on the Frustum of a Cone Surface .....	48
3.2.3 Applying the Methodology on the Toroidal Surface .....	50
3.3 Closed Form Swept Profile Equations .....	52
3.4 Examples .....	58
3.5 Discussion .....	59
<b>Chapter 4 In-process Workpiece Modeling.....</b>	<b>61</b>
4.1 Modeling the In-process Workpiece in Solid and Facetted Representation.....	62
4.2 Modeling the In-process Workpiece in Vector Based Representation .....	64
4.2.1 Milling Cutter Geometries in Parametric Form .....	64
4.2.1.1 Cylinder Surface.....	66
4.2.1.2 Frustum of a Cone Surface.....	66
4.2.1.3 Torus Surface .....	67

4.2.2 Workpiece Model and Localization .....	68
4.2.3 Updating In-process Workpiece in Multi-Axis Milling.....	74
4.2.3.1 Updating with Flat-End mill .....	78
4.2.3.2 Updating with Tapered-Flat-End Mill.....	84
4.2.3.3 Updating with Fillet-End mill .....	87
4.2.4 Implementation.....	94
4.3 Discussion .....	97
<b>Chapter 5 Feasible Contact Surfaces .....</b>	<b>98</b>
5.1 Tool Motions in Milling.....	99
5.2 Milling Cutter Geometries .....	102
5.3 Calculating the Feasible Contact Surfaces .....	105
5.3.1 Envelope Boundary of the Upper-Cone .....	108
5.3.2 Envelope Boundary of the Corner-Torus .....	111
5.3.3 Envelope Boundary of the Lower-Cone.....	113
5.4 Analyzing the Distribution of Feasible Contact Surfaces .....	114
5.5 Discussion .....	124
<b>Chapter 6 Cutter Workpiece Engagements.....</b>	<b>125</b>
6.1 Cutter Workpiece Engagements in Solid Models .....	127
6.1.1 Engagement Extraction Methodology in 3-Axis Milling.....	128
6.1.2 Implementation.....	136
6.1.3 Engagement Extraction Methodology in 5 Axis Milling.....	138
6.2 Cutter Workpiece Engagements in Polyhedral Models .....	143
6.2.1 Engagement Extraction Methodology in 3-Axis Milling.....	146
6.2.1.1 Mapping $M$ for Linear Toolpath.....	149
6.2.1.2 Mapping $M$ for Circular Toolpath.....	157
6.2.1.3 Mapping $M$ for Helical Toolpath .....	160
6.2.1.4 Implementation.....	163
6.2.2 Engagement extraction Methodology in 5-axis Milling .....	171
6.3 The Cutter Workpiece Engagements in Vector Based Model .....	173

6.3.1 Intersecting Segment Against Plane.....	173
6.3.2 Intersecting Segment Against Sphere .....	174
6.3.3 Intersecting Segment Against Cylinder.....	175
6.3.4 Intersecting Segment Against a Cone .....	177
6.3.5 Obtaining the Cutter Workpiece Engagements.....	179
6.4 Discussion .....	179
<b>Chapter 7 Conclusions.....</b>	<b>183</b>
7.1 Contributions and Limitations .....	183
7.2 Future Work .....	187
<b>Bibliography .....</b>	<b>188</b>
<b>Appendix A .....</b>	<b>193</b>
<b>Appendix B .....</b>	<b>196</b>

## List of Tables

<b>Table 1.1:</b> Comparisons between <i>CWE</i> extraction methods .....	14
<b>Table 5.1:</b> The angular ranges of the feed angle .....	116
<b>Table 5.2:</b> $CWE_K$ point sets of the generic cutter under different tool motions .....	123
<b>Table 6.1:</b> Constituent surfaces of cutter geometries after geometric decomposition in 3-axis milling.....	131
<b>Table 6.2:</b> Feasible engagement points for cutter surfaces with respect to the tool motions.....	132

## List of Figures

<b>Figure 1.1:</b> Virtual Machining .....	2
<b>Figure 1.2:</b> Steps in the geometric modeling for extracting <i>CWEs</i> .....	3
<b>Figure 1.3:</b> Swept volumes from 2 ½ -Axis milling .....	4
<b>Figure 1.4:</b> Sweeping the profile curve along tool path (3-Axis helical milling) .....	5
<b>Figure 1.5:</b> A CSG tree.....	6
<b>Figure 1.6:</b> ACIS representational hierarchy .....	7
<b>Figure 1.7:</b> Generation of in-process workpiece and the removal volume .....	8
<b>Figure 1.8:</b> (a) STL file structure, and (b) A tessellated mechanical part.....	9
<b>Figure 1.9:</b> Updating the workpiece surfaces represented by z-vectors.....	9
<b>Figure 1.10:</b> Cutter Workpiece Engagement parameters .....	10
<b>Figure 1.11:</b> (a) <i>CWE</i> boundaries during a rectangular block, and (b) A sculptured surface machining .....	11
<b>Figure 1.12:</b> Final machined surfaces with cusps .....	12
<b>Figure 1.13:</b> Possible cutter/facet intersections.....	13
<b>Figure 1.14:</b> The chordal error in cutter facet intersections .....	13
<b>Figure 1.15:</b> Z-map calculation errors when the grid size is large .....	14
<b>Figure 1.16:</b> <i>CWE</i> area for the force prediction .....	15
<b>Figure 1.17:</b> <i>CWE</i> area decompositions for sculptured surfaces.....	15
<b>Figure 2.1:</b> Decomposing object boundary .....	19
<b>Figure 2.2:</b> (a) The pseudo-inserts of the toroidal End mill, and (b) the position of a pseudo-insert at two tool positions.....	21
<b>Figure 2.3:</b> Updating in-process workpiece .....	23
<b>Figure 2.4:</b> 3-axis cutter swept volume with the boundary faces.....	24
<b>Figure 2.5:</b> Simulation of the NC milling by projecting pixels of a computer graphics image onto the part surface.....	24
<b>Figure 2.6:</b> Updating the workpiece surfaces represented by parallel z-vectors.....	26
<b>Figure 2.7:</b> (a) A 3-axis approximation of 5-axis swept volume, and (b) the extended z-buffer model of workpiece .....	26

<b>Figure 2.8:</b> <i>DNV</i> and <i>DVV</i> representation of the workpiece surfaces .....	27
<b>Figure 2.9:</b> Regular mesh decimation for 3-axis NC milling simulation.....	28
<b>Figure 2.10:</b> Extracting <i>CWEs</i> by advancing semi circle approach for 2 ½ -axis milling.....	31
<b>Figure 2.11:</b> Extracting <i>CWEs</i> by advancing semi cylinder approach for 2 ½ -Axis milling.....	31
<b>Figure 2.12:</b> 3-axis <i>CWE</i> extraction with Ball-End mill.....	32
<b>Figure 2.13:</b> Procedure for extracting in-cut segments of the cutting edges.....	32
<b>Figure 2.14 :</b> Cutter engagement portion .....	33
<b>Figure 2.15:</b> (a) Chordal error in the cutter facet intersection, and (b) the radius enlargement of the cutter.....	33
<b>Figure 2.16:</b> The Entry/exit angle calculation for each disc .....	34
<b>Figure 2.17:</b> The pixel based engagement extraction.....	34
<b>Figure 2.18:</b> A linear tool path and region expressed as a Boolean expression of half spaces.....	35
<b>Figure 3.1:</b> Geometric description of a canal surface .....	40
<b>Figure 3.2:</b> Some typical milling cutter geometries.....	42
<b>Figure 3.3:</b> Generating cutter geometries with a moving sphere .....	42
<b>Figure 3.4:</b> (a) The characteristic <i>K</i> , and (b) the great <i>S</i> circles.....	44
<b>Figure 3.5:</b> Intersecting the characteristic ( <i>K</i> ) and the great ( <i>S</i> ) circles .....	45
<b>Figure 3.6:</b> Intersection cases between <i>K</i> and <i>S</i> .....	45
<b>Figure 3.7:</b> The moving sphere of a cylinder surface in 5-axis motion .....	46
<b>Figure 3.8:</b> The moving sphere of a cone surface in 5-axis motion.....	48
<b>Figure 3.9:</b> The moving sphere of a toroidal surface in 5-axis motion.....	50
<b>Figure 3.10:</b> The characteristic circle <i>K</i> of the torus in the Frenet Frame .....	53
<b>Figure 3.11:</b> The characteristic circle <i>K</i> in <i>TCS</i> .....	54
<b>Figure 3.12:</b> Limits of the grazing points in the general .....	56
<b>Figure 3.13:</b> The characteristic circle <i>K</i> becomes a great circle in (a) torus, and in (b) cylinder surfaces .....	57
<b>Figure 3.14:</b> Envelopes surfaces of (a) Flat-End, (b) Ball-End, and (c) Fillet-End cutters.....	58

<b>Figure 3.15:</b> Envelopes surfaces of a Taper-Ball-End mill from different point of views in 5-axis milling.....	59
<b>Figure 3.16:</b> Different cutter geometries generated by a moving sphere.....	60
<b>Figure 4.1:</b> A B-rep Solid Modeler based in-process workpiece update .....	63
<b>Figure 4.2:</b> A Polyhedral Modeler based in-process workpiece update.....	63
<b>Figure 4.3:</b> Cutter geometries as canal surfaces: (a) cylinder, (b) frustum of a cone, and (c) torus.....	65
<b>Figure 4.4:</b> Representing the workpiece surfaces by (a) surface normal vectors and (b) vertical vectors.....	69
<b>Figure 4.5:</b> Representing the feature shapes in Discrete Normal vector and discrete vertical vector approaches.....	70
<b>Figure 4.6:</b> (a) 3-Axis machining, and (b) (3+2) - Axis machining .....	70
<b>Figure 4.7:</b> Representing initial workpiece with discrete vectors located in XY, XZ and YZ planes).....	71
<b>Figure 4.8:</b> AABB of a tool movement in Oxy coordinate system.....	73
<b>Figure 4.9:</b> Decomposing the swept surface into three regions).....	76
<b>Figure 4.10:</b> Envelope surfaces generated by the cylindrical part of a Flat-End mill.....	79
<b>Figure 4.11:</b> Possible intersections between a vector and envelope plane: (a) no intersection, (b) one intersection and (c) vector lies in the plane .....	80
<b>Figure 4.12:</b> Parameter sets for updating the discrete vector .....	81
<b>Figure 4.13:</b> Intersecting the Bottom-Flat surface with a discrete vector .....	82
<b>Figure 4.14:</b> Intersection cases between the Bottom-Flat surface and a discrete vector.....	84
<b>Figure 4.15:</b> Envelope surfaces generated by the frustum of a cone part .....	86
<b>Figure 4.16:</b> Motion types with respect to the feed vector $\mathbf{f}$ : (a) descending, (b) horizontal and (c) ascending motion .....	87
<b>Figure 4.17:</b> The envelope parameters of a toroidal surface under the plunging motion ....	88
<b>Figure 4.18:</b> Envelope /vector intersection cases: two points (1), one point (2) and no intersection (3).....	91
<b>Figure 4.19:</b> The roots of the nonlinear equation $f(t)$ when the vector intersects (a) in one point or in (b) two points .....	92
<b>Figure 4.20:</b> NC milling simulation of a Door mold.....	95

<b>Figure 4.21:</b> NC milling simulation of an Auto hood .....	95
<b>Figure 4.22:</b> NC milling simulation results for a Gearbox cover with (a) A Flat-End mill and (b,c) Ball-End mills .....	96
<b>Figure 4.23:</b> NC milling simulation for 5-axis impeller machining.....	96
<b>Figure 5.1:</b> Cutter motions in milling: (a) 2 ½-axis, (b) 3-axis, (c) 5-axis .....	99
<b>Figure 5.2:</b> The local and reference frames of a cutter .....	100
<b>Figure 5.3:</b> Geometric definition of the generic cutter.....	103
<b>Figure 5.4:</b> Boundary partition of the generic cutter.....	106
<b>Figure 5.5:</b> Point sets used in defining engagements .....	107
<b>Figure 5.6:</b> Boundaries of the $CWE_K$ in the Fillet-End mill.....	108
<b>Figure 5.7:</b> Arbitrary points $I_U$ , $I_T$ and $I_L$ on the upper-cone, corner-torus and lower-cone surfaces respectively.....	109
<b>Figure 5.8:</b> Instantaneous cutter contact surfaces in (a,b) 5-axis, and in (c,d) 3-axis plunge motions .....	115
<b>Figure 5.9:</b> Feed angle ranges .....	116
<b>Figure 5.10:</b> The corner-torus with upper and lower surface boundaries .....	118
<b>Figure 5.11:</b> Envelope boundary sets on (a) the front, and (b) the back faces of the corner- torus .....	119
<b>Figure 5.12:</b> Feasible contact surfaces of the toroidal part with respect to the cutter feed angle.....	121
<b>Figure 6.1:</b> $CWE$ Extraction Steps .....	125
<b>Figure 6.2:</b> $CWE$ area for the force prediction .....	126
<b>Figure 6.3:</b> A B-rep Solid Modeler based $CWE$ extraction.....	128
<b>Figure 6.4:</b> Point sets used in defining Engagements .....	129
<b>Figure 6.5:</b> $CWE$ parameters of an arbitrary point $\mathbf{P}$ .....	130
<b>Figure 6.6:</b> Defining $CWE$ parameters $u$ and $v$ on (a) torus, (b) sphere, (c) frustum of a cone, (d) cylinder, and (e) flat bottom surfaces of common milling cutters .....	130
<b>Figure 6.7:</b> Geometric decomposition of the cutter surfaces .....	131
<b>Figure 6.8:</b> Decomposing the point set $CWE_K$ of the torus into three parts .....	132
<b>Figure 6.9:</b> Swept volumes generated by the kinematically feasible	

engagement point sets .....	133
<b>Figure 6.10:</b> Procedure for obtaining the <i>CWEs</i> .....	134
<b>Figure 6.11:</b> <i>CWEs</i> for the Flat End mill performing a linear 3-axis descending motion..	136
<b>Figure 6.12:</b> <i>CWEs</i> for the Taper-End mill performing a linear 3-axis ascending motion.....	137
<b>Figure 6.13:</b> Helical Tool Motions with a Flat-End Mill and <i>CWEs</i> .....	138
<b>Figure 6.14:</b> Envelope boundary in (a) 5-axis milling, and in (b) 3-axis milling respectively .....	139
<b>Figure 6.15:</b> Offsetting the feasible contact surface.....	140
<b>Figure 6.16:</b> <i>CWE</i> steps in 5-axis milling methodology .....	141
<b>Figure 6.17:</b> 5-axis <i>CWEs</i> during the first pass of the impeller machining .....	142
<b>Figure 6.18:</b> 5-axis <i>CWEs</i> during the second pass of the impeller machining.....	142
<b>Figure 6.19:</b> In-process workpieces after the third and fourth passes respectively .....	143
<b>Figure 6.20:</b> Typical intersections between a facet and a cutting tool.....	143
<b>Figure 6.21:</b> The edges of facets deviate from the real surface .....	144
<b>Figure 6.22:</b> (a) Constituent surfaces of milling cutters and (b) some typical milling cutter surfaces .....	145
<b>Figure 6.23:</b> <i>CWE</i> parameters .....	146
<b>Figure 6.24:</b> Point sets $CWE_K(t)$ , $CWE(t)$ and $bCWE(t)$ used in defining engagements....	148
<b>Figure 6.25:</b> <i>CWE</i> calculations in the parametric domain $P(\varphi, d, L)$ .....	148
<b>Figure 6.26:</b> Description of a point on a cutter moving along a Tool Path.....	149
<b>Figure 6.27:</b> 3-axis Linear Tool Motions with a BNEM.....	150
<b>Figure 6.28:</b> Engagement regions of the front (a) and back (b) contact faces .....	151
<b>Figure 6.29:</b> Procedure for performing Mapping $M_G: E^3 \rightarrow P(\varphi, d, L)$ .....	151
<b>Figure 6.30:</b> Different cutter locations for $\mathbf{I} \in CWE_K(t)$ .....	154
<b>Figure 6.31:</b> Cylindrical contact face $CWE_{K,C}(t)$ of BNEM.....	157
<b>Figure 6.32:</b> Moving coordinate frame for circular tool path .....	158
<b>Figure 6.33:</b> Parameter values of the cutter tool tip.....	159
<b>Figure 6.34:</b> Sweeps for Helical Milling.....	160
<b>Figure 6.35:</b> Removal volumes of (a) side face and (b) bottom face.....	161
<b>Figure 6.36:</b> Parameters describing a helical tool motion for the Flat-End mill.....	162

<b>Figure 6.37:</b> Different cutter locations for an engagement point $\mathbf{I} \in CWE_K(t)$ .....	163
<b>Figure 6.38:</b> Implementation of <i>CWE</i> extraction methodology .....	164
<b>Figure 6.39:</b> <i>CWEs</i> for Ball-End mill performing a linear 3-axis move .....	166
<b>Figure 6.40:</b> <i>CWEs</i> for Flat End mill performing a linear 3-axis move .....	166
<b>Figure 6.41:</b> <i>CWEs</i> for Tapered-Flat-End mill performing a linear 3-axis move .....	167
<b>Figure 6.42:</b> Helical Tool Motions with a Flat-End mill and <i>CWEs</i> .....	168
<b>Figure 6.43:</b> <i>CWEs</i> for Flat-End mill performing a circular move .....	169
<b>Figure 6.44:</b> <i>CWEs</i> for Ball-End mill performing a linear 3-axis move .....	170
<b>Figure 6.45:</b> Helical tool path application with removal volumes for each half turn .....	170
<b>Figure 6.46:</b> <i>CWEs</i> of the Helical Tool Motions.....	171
<b>Figure 6.47:</b> <i>CWE</i> extraction steps for 5-axis milling.....	172
<b>Figure 6.48:</b> Intersecting a segment against a plane .....	174
<b>Figure 6.49:</b> Different cases in segment/sphere intersections: (a) Two intersection points, (b) intersecting tangentially, (c) no intersection, (d) segment starts inside sphere, and (e) segment starts outside sphere .....	175
<b>Figure 6.50:</b> A segment is intersected against the cylinder given by points $B$ and $Q$ and the radius $r$ .....	176
<b>Figure 6.51:</b> A cone with defining parameters.....	178
<b>Figure 6.52:</b> Decomposing cutter surfaces into grids.....	179
<b>Figure 6.53:</b> Removal Volumes and <i>CWEs</i> for different resolutions.....	181
<b>Figure 6.54:</b> The effect of the facet resolutions .....	182
<b>Figure B.1:</b> (a) Cylindrical $CWE_{K,c1}(t)$ and (b) bottom $CWE_{K,c2}(t)$ , faces of the Flat End Mill.....	196
<b>Figure B.2:</b> (a) Front $CWE_{K,co1}(t)$ and (b) back $CWE_{K,co2}(t)$ conical faces of Tapered Flat End Mill.....	198
<b>Figure B.3:</b> (a) Front $CWE_{K,t1}(t)$ and (b) back $CWE_{K,t2}(t)$ contact faces of Toroidal End Mill .....	200
<b>Figure B.4:</b> Cutter interferences with a point in space.....	201

## List of Algorithms

<b>Algorithm 4.1:</b> Obtaining the roots of $f(t)$ .....	94
<b>Algorithm 6.1:</b> Obtaining the closed boundaries of the <i>CWEs</i> .....	135

## **Acknowledgments**

I would like to express my sincere thanks and gratitude to my research co-supervisors Dr. Derek Yip-Hoi and Dr. Hsi-Yung (Steve) Feng for their invaluable guidance throughout the study. Also I would like to express my deepest gratitude and thanks to Dr. Yusuf Altintas for his continuous moral and financial support throughout the course of this research. I would like to extend my sincere gratitude and appreciation to my colleagues and staff at the Mechanical Engineering Department for their encouragement and help at various occasions. My friend (dear brother) Dr. Dimitri Ostafiev deserves special thanks for his various supportive roles. I would like to thank my family for their unwavering encouragement. I dedicate this thesis to my son Ibrahim T. Aras.

# Chapter 1

## Introduction

Manufacturing is an integral and indispensable part of the economy. As a result of global competition, manufacturers are facing challenges for both reducing the production costs and improving the product quality at the same time. They are trying to reduce the lead time before the implementation of a new product and also to minimize the cycle of the product development. Manufacturing contains different areas such as forging, casting, machining etc. Machining or cutting of metal is a key activity in most manufacturing environments. Today modern machine tools are CNC (Computer Numeric Control) milling machines and lathes. A microprocessor in each machine reads the NC-Code program that the user creates and performs the programmed operations. Traditionally, the NC program is verified and corrected by a costly time consuming process of machining plastic or wooden models. For solving this problem a new approach *Virtual Machining (VM)* has been introduced.

### 1.1 Virtual Machining

One of the techniques for advancing the productivity and quality of machining processes is to design, test and produce the parts in a virtual environment. *VM* is used for simulation of the machining process prior to actual machining, thereby avoiding costly test trials on the shop floor. Virtual machining can be considered *manufacturing in the computer*. Figure 1.1 shows three major components of the *VM*: Computer Aided Process Planning (CAPP), Geometric modeling and Process modeling.

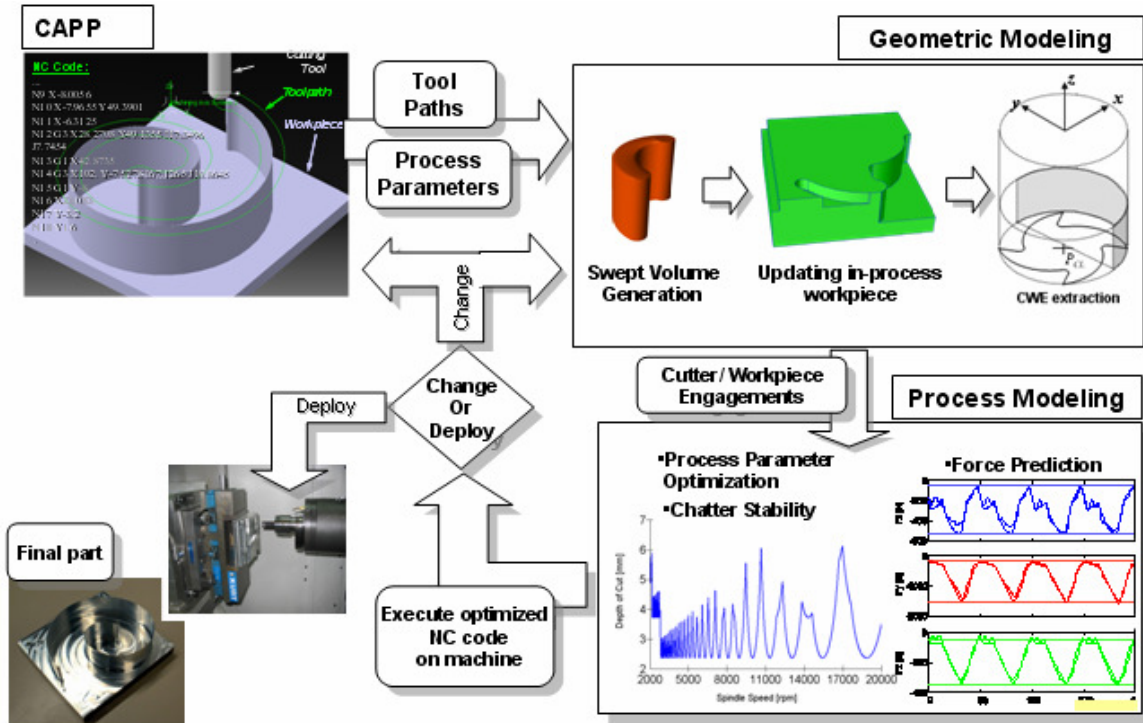


Figure 1.1: Virtual Machining

A CAD model is taken as an input into CAPP. In CAPP, machining operations which include tool paths and process parameters such as spindle speed and feed rate are generated. The generated tool paths and the process parameters are input to geometric modeling. In geometric modeling NC toolpaths are verified to eliminate un-cut material and gouges on the final part surfaces, to prevent cutter and workpiece collisions during machining. Cutting forces are a key input to simulating the vibration of machine tools (chatter) prior to implementing the real machining process. This simulation can be used to optimize instantaneous process parameters to avoid chatter and improve machining quality. Instantaneous cutting forces are determined by the feed rate, spindle speed, and *Cutter Workpiece Engagements (CWEs)*. *CWEs* are extracted in geometric modeling for supporting cutting force prediction in process modeling. In process modeling, cutting forces, power and torque are predicted by utilizing the laws of the metal cutting process and *CWEs* obtained from geometric modeling. Also process parameters can be optimized to obtain better machined part quality. The optimized process parameters and the tool paths are sent to a CNC machine for producing the final workpiece. In the following sections geometric modeling and process modeling are introduced.

## 1.2 Geometric Modeling

In geometric modeling *CWEs* are extracted according to the input requirements from process modeling. Figure 1.2 illustrates the steps involved in geometric modeling for extracting *CWEs*. Inputs from a CAD/CAM system include the geometric representation of the initial workpiece, the tool path and the geometric description of the cutting tool.

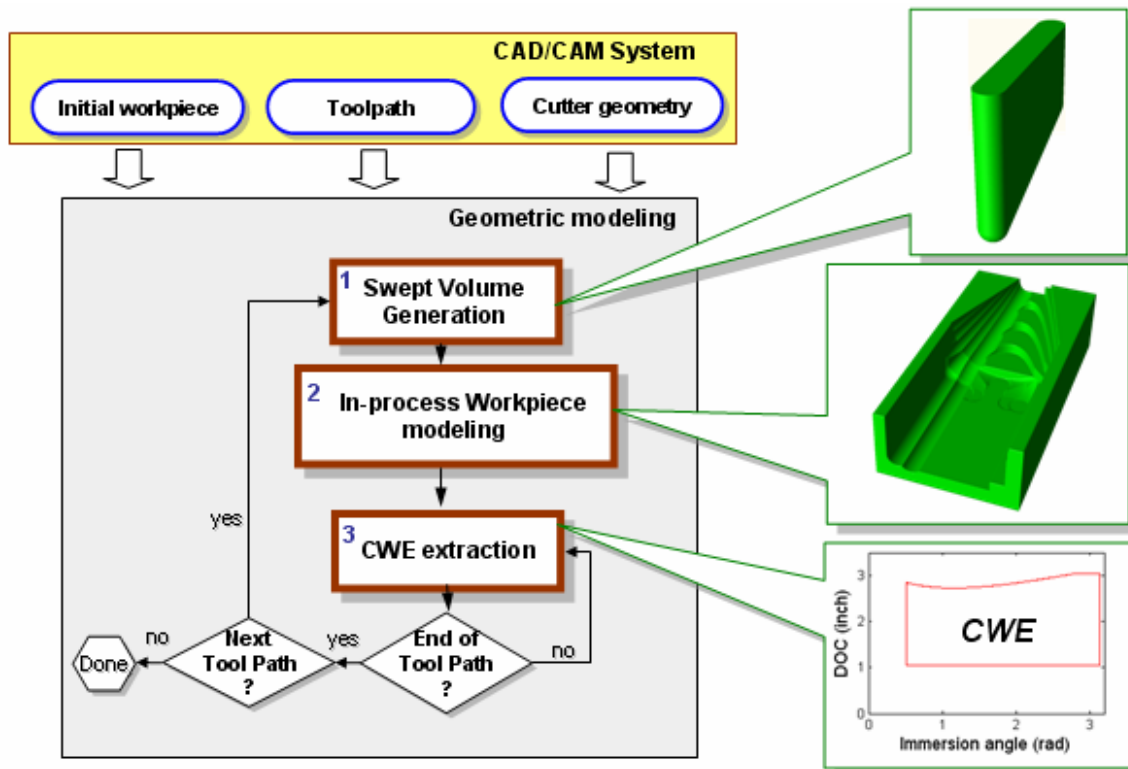


Figure 1.2: Steps in the geometric modeling for extracting *CWEs*

In the first step, swept volumes are generated for the cutting tool following a tool path. Then in the second step these swept volumes are subtracted from the initial workpiece sequentially to obtain the updated workpiece (*in-process workpiece*). The in-process workpiece in geometric modeling is important for both NC toolpath verification and *CWE* extraction. In step 3 the in-process workpiece geometry is used to find the *CWEs* for each tool path. The output from *CWE* extraction is passed on to process modeling where cutting forces are predicted and used to analyze and optimize the process.

Three main steps are therefore needed to obtain *CWEs* in geometric modeling

- Swept Volume Generation

- In-process Workpiece Modeling
- *CWE* Extraction

In the next subsections each step is introduced.

### 1.2.1 Swept Volume Generation

One of the subtasks in identifying the *CWE* geometry involves updating the in-process workpiece geometry after each non-self intersecting tool path (or tool path segment). An accurate model of the in-process workpiece is therefore important to ensure that correct *CWE* geometry is calculated as the simulation progresses and the cutting tool reenters regions previously milled. Creating the in-process workpiece requires modeling and subtracting the swept volume generated by each cutter movement along successive tool paths from the model of the stock, finally yielding the machined surfaces of the final part model. *Mathematically, the swept volume is the set of all points in space encompassed within the object envelop during its motion.* The moving object which is called the generator can be a curve, a surface or a solid and in this thesis the generator is a rigid milling cutter. The motion of the generator is called the sweep motion. The simplest sweep motions are the translational sweep (Figure 1.3(a)) and rotational sweep about a fixed axis (Figure 1.3(b)).

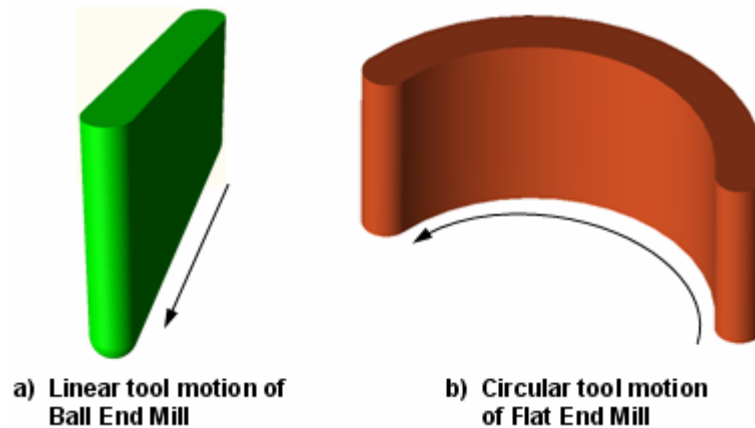


Figure 1.3: Swept volumes from 2 ½ -Axis milling

In 2 ½ Axis and 3 Axis milling, the swept volumes of the cutters can be generated by sweeping the profile curve along the tool path. Figure 1.4 illustrates the swept volume generated by a helical tool motion. If a cutter takes a complex tool motion such as translational plus rotational (non fixed rotational axis), the corresponding sweep operation is

called a general sweep. This kind of tool motions appears in 5-Axis milling. There is a great challenge in swept volume generation for 5-Axis tool motions where cutters with different surface geometries move along 3- dimensional spatial curves with changing tool axis orientations. Although important research has been done on swept volumes, today's CAD systems do not include swept volume generation as a component.

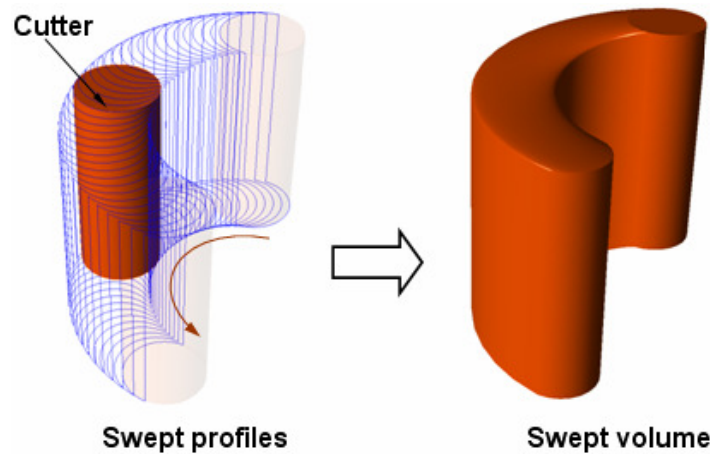


Figure 1.4: Sweeping the profile curve along tool path  
(3-Axis helical milling)

For swept volume generation some methods have been developed. Unfortunately in these methods swept volume computations have been done with complex differential equations that require numerical solutions. These limit their practicality and therefore, few methods have been proposed to determine efficiently the swept profile in NC machining. But these methodologies are either cutter geometry specific or they provide approximate solutions. The efficiency of these methodologies still needs to be improved.

### 1.2.2 In-process Workpiece Modeling

For NC verification and *CWE* extraction an accurate in-process workpiece representation is needed. The modeling of the in-process workpiece and the calculation of *CWE* geometry involves trade-offs between computational efficiency and the accuracy of the result. Determining the correct combination of these two factors is an open question that involves developing and understanding of the requirements for milling process modeling for which the *CWE* geometry is an input. Several choices for modeling the in-process work piece exist. The two most common are mathematically accurate solid modeling that are used in CAD systems

and approximate modeling such as those used in computer graphics: faceted and z-Map models. Solid modeling offers the best choice for highly accurate modeling of the geometric conditions. However challenges exist to making this approach both efficient and generally robust to handle degenerate geometric conditions that can occur when large numbers of tool paths need to be simulated. Further, the presence of accurate geometric and topological (connectivity between geometry) information can potentially be exploited to develop “intelligent” approaches for *CWE* geometry extraction. These would search for patterns (features) in the removal volumes where the engagement geometry is constant or changing in a predictable way. This is not possible when using approximate models where accurate geometry and relationships are not maintained in the data structure. The use of solid models therefore has unstudied potential. The approaches to In-process Workpiece Modeling are discussed in the following subsections.

- **Solid Modeling**

Solid modeling technique also called volumetric modeling is used in many applications such as geometric design, NC code generation and visualization. The use of solid models for manufacturing is becoming more widespread with developing computer technology. The most popular solid modeling representation schemes are the constructive solid geometry (CSG) and boundary representation (B-rep) schemes.

In the CSG approach a complex surface is created from simpler solids called primitives by using Boolean operators: Intersection ( $\cap$ ), Union ( $\cup$ ) and Difference ( $-$ ). The primitives are parameterized solids that are either regular geometric shapes such as spheres, cones and cubes or complex application specific features such as drill/counter-bored holes. The hierarchical representation of features and the Boolean operations is captured in a binary tree called the CSG tree where leaves represent primitives and nodes represent Boolean operations (Figure 1.5).

Figure 1.5 has been removed due to copyright restrictions. The information removed is the hierarchical representation of features and the Boolean operations in a binary tree for describing the CSG tree [35].

In solid modeling, boundary representation (B-rep) is a methodology for representing shapes using their limits. If it is compared with the CSG representation which uses only Boolean operations and primitive objects, the B-rep has a much richer set of operations and because of this for CAD systems it is more appropriate. B-rep models contain two parts: geometry and topology. The geometry information in the B-rep model is composed of curve/surface equations and point coordinates. The topology information is the connectivity between geometric entities FACE, EDGE and VERTEX.

- The shape of a FACE is defined by a surface which has a boundary represented by connected EDGES.
- The shape of an EDGE is defined by a curve which has a boundary represented by two VERTEXs.
- A point represents the location of the VERTEX.

Other elements in the B-rep representation are the SHELL (a set of connected FACES), the LUMP (collection of SHELLs) and the LOOP (a circuit or list of EDGES bounding a FACE). There are several ways of viewing this data structure. For example it can be considered as a tree or a hierarchy with BODY as a root. A BODY can have LUMPs which are comprised of SHELLs formed from a group of FACES.

In this thesis both for updating the in-process workpiece and for extracting the *CWEs*, under the solid modeler section, a B-rep methodology is used. For this reason a commercial geometric modeler ACIS [4] is utilized. ACIS is an object oriented geometric modeling toolkit designed for use as a geometric engine. Figure 1.6 shows the data structure used in ACIS.

Figure 1.6 has been removed due to copyright restrictions. The information removed is the ACIS representational hierarchy [4].

In the B-rep based approach, the in-process workpiece can be generated by subtracting a swept volume of the cutter from the workpiece. Figure (1.7) illustrates the generation of the in-process workpiece in the  $i^{\text{th}}$  tool motion.  $S_{G_i}$  Represents the swept volume in the  $i^{\text{th}}$  tool motion and  $W_{i-1}$  is the in-process workpiece before the  $i^{\text{th}}$  tool motion. Subtracting  $S_{G_i}$  from

$W_{i-1}$  i.e.  $(W_{i-1} -^* S_{G_i} = W_i)$  updates the in-process workpiece for the next tool motion and also intersecting  $S_{G_i}$  with  $W_{i-1}$  generates the removal volume  $RV_i$ .

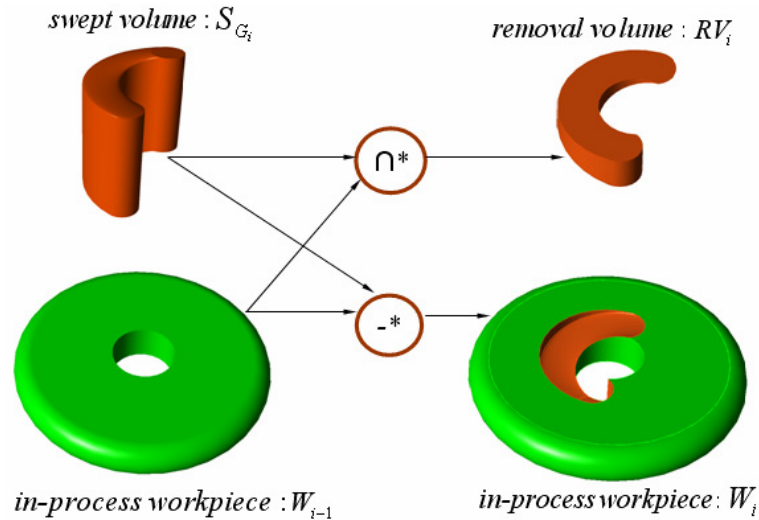


Figure 1.7: Generation of in-process workpiece and the removal volume

- **Facetted Models**

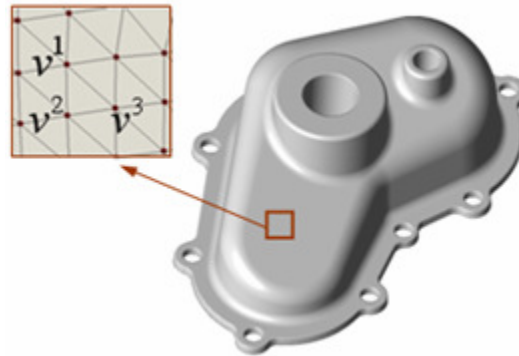
Another alternative for modeling the in-process geometry that is starting to receive more attention are Polyhedral Models. These may offer a good compromise between manageable computational speed, robustness and accuracy. These models have become pervasive in supporting engineering applications. They are found in all CAD applications as facetted models for visualization and are used extensively in simulation, CAE and rapid prototyping. In this modeling approach workpiece surfaces are represented by a finite set of polygonal planes called *facets*. The most commonly used shapes are the triangles and because of this the term facet is usually understood to mean triangular facet. Converting the mathematically precise models to the triangulated model is called *tessellation*. For *tessellation* the original surfaces of the model are sampled for sets of points and then these points are connected for constructing triangles. The STL (Stereolithography Tessellation Language) format for rapid prototyping is the most well-known file format for the triangulated models. In the STL model each facet is described by three vertices and a normal direction of the triangle as shown in Figure 1.8. The normal vector is directed outward from the surface and the vertices

are ordered with respect to the right hand rule. For the non-planar surfaces using a greater number of facets gives a better approximation of the tessellation to the original surface.

```

facet normal  $n_x$   $n_y$   $n_z$ 
  outer loop
    vertex  $v_x^1$   $v_y^1$   $v_z^1$ 
    vertex  $v_x^2$   $v_y^2$   $v_z^2$ 
    vertex  $v_x^3$   $v_y^3$   $v_z^3$ 
  endloop
endfacet

```



(a)

(b)

Figure 1.8: (a) STL file structure, and (b) a tessellated mechanical part.

### ▪ Z-Map Models

In these modeling techniques the workpiece geometry is broken into a set of evenly distributed discrete vectors which are called z-direction vectors or ZDVs (Figure 1.9). The length of the each vector represents the depth of the workpiece. The spacing of the ZDVs is adjusted according to a desired level of accuracy. The z-Map approach has three sub-tasks: Discretization of workpiece, Localization and intersection. In the discretization, the design surface is transformed into a sufficiently dense distribution of surface rays. The localization process finds the possible subset of rays for each tool motion. Finally in the intersection task the cut values between z-direction vectors and the tool swept envelope are found for updating the workpiece surfaces. In this methodology the toolpath envelope is modeled as a set of geometric primitives such as cylinder and plane. Thus the computational cost for calculating the intersections between the cutter and the workpiece is reduced by doing simple line/primitive intersection for multi-Axis machining.

Figure 1.9 has been removed due to copyright restrictions. The information removed is the updating the workpiece surfaces represented by z-vectors [7].

### 1.2.3 Cutter Workpiece Engagement Extraction

One of the steps in simulating machining operations (Virtual Machining) is the accurate extraction of the intersection geometry between the cutting tool and the workpiece during machining. Given that industrial machined components can have a highly complex workpiece and cutting tool geometries, extracting Cutter/Workpiece Engagement (*CWE*) geometry accurately and efficiently is challenging. *CWE* geometry is a key input to force calculations and feed rate scheduling in milling operations. This geometry defines the instantaneous intersection boundary between the cutting tool and the in-process workpiece at each location along a tool path. From the *CWE*, the cutter flute entry/ exit angles ( $\varphi_{Entry}$  and  $\varphi_{Exit}$ ) and depth of cut  $d$  are found (Figure 1.10) and are in turn used to calculate the instantaneous cutting forces in the radial, tangential and feed directions. The primary task in finding the *CWE* geometry is finding the boundary of the engagement region. This may also be multiple regions. The representation of this boundary will depend on the mathematical representation of the workpiece's surfaces.

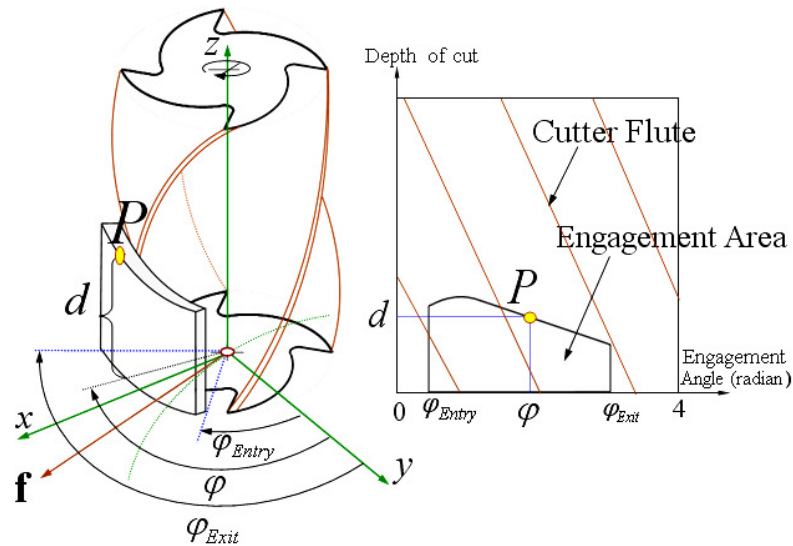


Figure 1.10: Cutter Workpiece Engagement parameters.

In *CWE* extraction the task is relatively simple when cylindrical end mills and simple workpieces are used (Figure 1.11(a)). However in practice this is often not the case. The force prediction and feedrate scheduling are largely affected by accuracy of the predicted area. The most complicated *CWE* calculations occur during the machining of *sculptured*

*surfaces* (Figure 1.11(b)). Forces in sculptured surface machining are difficult to determine because of the continuously changing *CWE* geometry that can occur at each feed step. This makes feedrate scheduling for the complex part quite difficult. For this reason when machining complex parts the feedrate is typically set to a constant value over a number of cutter tool paths based on the worst case engagement geometry that the cutter encounters. Furthermore if the cutting tool geometry is also complex and the machining process involves rotational axes i.e. 4 or 5 axis machining then finding the engagement geometry becomes an even more challenging task.

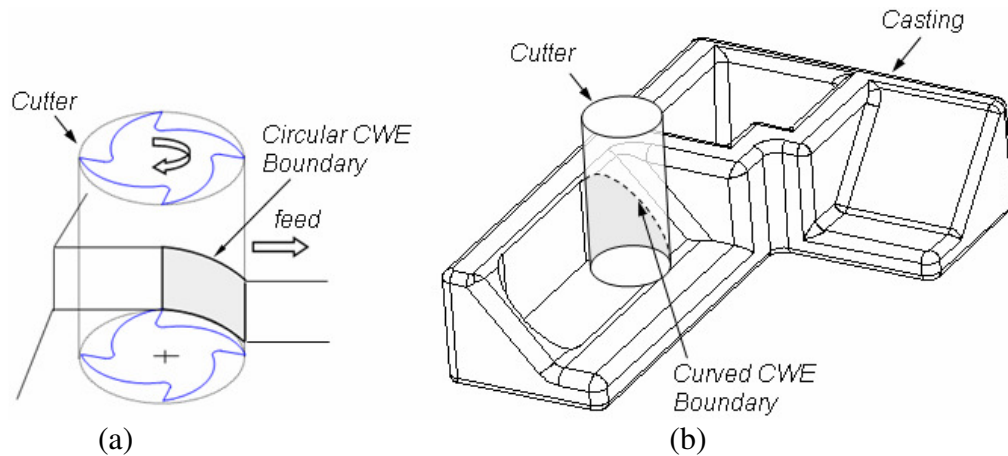


Figure 1.11: (a) *CWE* boundaries during a rectangular block, and (b) a sculptured surface machining

The approaches for finding the *CWE* geometry can be classified into two major categories based on the mathematical representation of the workpiece geometry. These are *Solid modeling approaches*, and *Discrete modeling approaches*. These approaches to *CWE* extraction are discussed in the following subsections.

- **Solid Modeling Approach to *CWE* Extraction**

For solid models these take the form of simple dual form algebraic/parametric surfaces (planes, spheres, cylinders, cones, tori) or pure parametric surfaces (Bezier, B-spline, NURBS). When the workpiece and cutting tool are represented by parametric surfaces then the solid modeling approach applies numerical parametric surface intersection algorithms which are based on *subdivision*, and *curve tracing (marching) methods* [10,11,59,65]. On the other hand if the workpiece and cutting tool are represented by the natural quadric surfaces then *analytical methods* that are either *geometric* or *algebraic* may be applied

[33,48,55,56,63]. While solid modelers have been recognized as one approach to finding *CWE* geometry, for limited applications, computational complexity and robustness remain issues that need to be addressed if the approach is to be viable from a practical perspective. Other limitations come for the size of the data structure that is necessary in particular for capturing relationships between topology. These relationships are preserved when using a solid modeler for small surface artifacts such as *cusps* that are generated during machining (Figure 1.12). This results in a data structure that is large and that grows as the simulation progresses particularly when ball and bull nose cutters are being used.

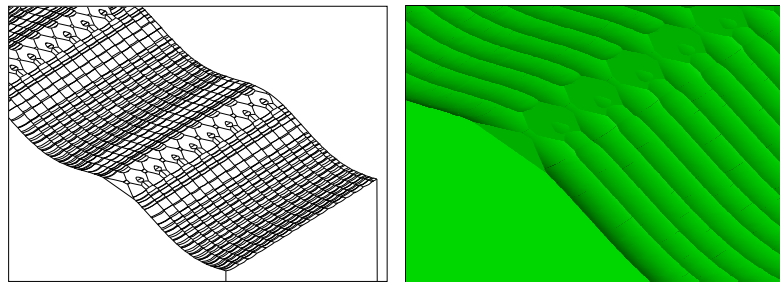


Figure 1.12: Final machined surfaces with cusps

- **Discrete Modeling Approaches to *CWE* Extraction**

Discrete modeling approaches have been used in verifying the correctness of NC tool paths. Some of these have been extended to extracting *CWEs* in support of physical simulation of the process that starts with the calculation of the cutting forces. A number of approaches in this area can be classified into two groups: *CWE* extraction in *polyhedral* and in *z-Map and vector based models*.

*CWE* extraction in polyhedral models

Polyhedral models use facets (in this thesis triangular facets) and they are supported by many CAD softwares. Since each facet in the model is planar with linear boundaries, the intersection algorithms that need to be applied are simpler than those used in the solid modeling approach. A cutting tool intersects with a facet in a different ways (Figure 1.13). For obtaining the *CWE* area, facets of the removal volume which contain linear boundaries are intersected with the surface of the cutter and then the intersection points are connected to

each other. The use of the removal volume as the basis for *CWE* extraction greatly reduces the size of the data structure that must be manipulated.

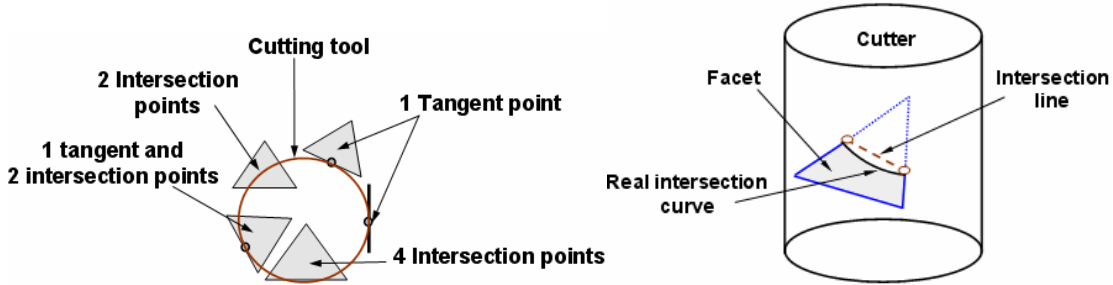


Figure 1.13: Possible cutter/facet intersections

The faceting algorithm that generates this model approximates surfaces to a specified chordal error. As can be seen from the 2D view (Figure 1.14) this results in facets that lie outside the tool envelop at a given location even though the cutting tool is in contact with the actual removal volume surface. This facet should be considered in finding the *CWE* boundary but would be difficult to detect since it does not intersect with the tool geometry. These errors can be reduced by increasing both the resolution of the polyhedral mesh and the radius of the cutter.

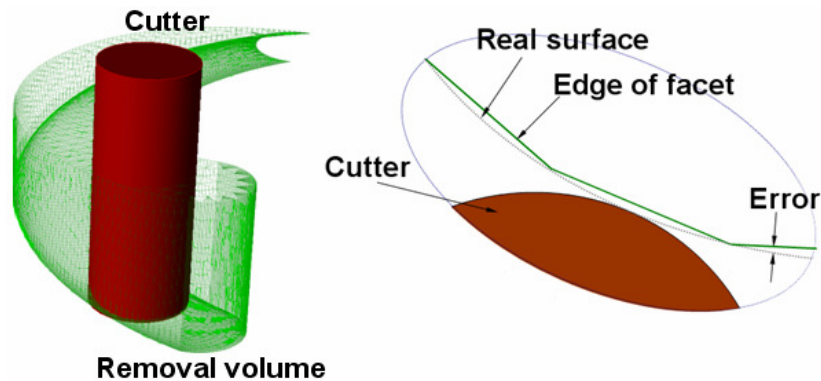


Figure 1.14: The chordal error in cutter facet intersections

*CWE extraction in Z-Map and vector based models*

The z-Map and vector based models represent the workpiece using directional vectors emanating from a grid on a workpiece surface. These are updated as the cutting tool sweeps

through different regions of the grid to capture the new heights of the workpiece i.e. the in-process workpiece boundary. The engagements are determined by finding intersections between the cutting tool geometry and vectors along the normals at discrete points on the surface. These intersections are calculated by a vector/surface intersection instead of surface/surface intersection in solid modeling. Although this approach results in a shorter computation time than a solid modeler based approach for example, the accuracy of this approach greatly depends on the resolution of workpiece. In geometric simulation, the dominant approaches are the vector based solutions. Though mathematically more tractable than the solid modeler approach, as shown in Figure 1.15 these techniques suffer from inaccuracies due to the rasterization effect common to many discretized problems [91].

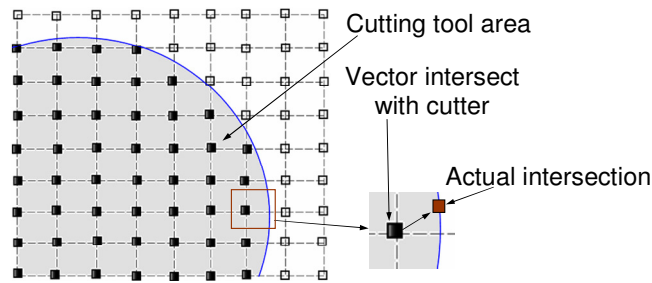


Figure 1.15: Z-map calculation errors when the grid size is large

Though accuracy is improved by increasing the resolution of the underlying grid, this comes with the expense of larger memory and computational requirements.

There is always a tradeoff between computational efficiency and accuracy in these approaches. Table 1.1 shows the comparison of the solid modeler and the discrete modeler approaches for the *CWE* extractions.

	<b>Workpiece representation</b>	<b>CWE calculations</b>	<b>Computational complexity</b>	<b>CWE results</b>	<b>Robustness</b>	<b>Size of the model during simulation</b>
<b>Solid Modeler</b>	Boundary representation	Surface/surface	High	Exact	Low	grows
<b>Polyhedral Modeler</b>	Triangular mesh	Surface/plane	Low	Approximate	High	Slightly grows
<b>Z-Map</b>	Vectors along z direction	Surface/line	Low	Approximate	High	constant

Table 1.1: Comparisons between *CWE* extraction methods

### 1.3 Process Modeling

Physical simulation needs *CWEs* as inputs to predict cutting forces. In process modeling, the cutting forces are predicted by utilizing *CWEs* obtained from geometric modeling. In order to properly define the input format from *CWE* for force prediction, a force model must be identified. Numerous models have been proposed in the literature e.g. Refs. [5,18,30,70]. In this thesis we calculate the *CWEs* for supporting the force prediction model described in [5]. This model finds the Cartesian force components by analytically integrating the differential cutting forces along the in-cut portion of each cutter flute. In this model the *CWE* area with a fixed axial depth of cut is defined by mapping the engagement region on the cutter surface onto the  $\phi - z$  plane which represents the engagement angle ( $\phi$ ) versus the depth ( $z$ ) of cut respectively (Figure 1.16).

Figure 1.16 has been removed due to copyright restrictions. The information removed is the *CWE* area for the force prediction [5].

As shown in Figure 1.16, the inputs from *CWEs* to this force model are the entry ( $\phi_{st}$ ) and the exit ( $\phi_{ex}$ ) angles of the cutter with respect to the feed vector and the axial location ( $d_{min}, d_{max}$ ) of the cutter engagement area. This force model is limited to a *CWE* area with a boundary defined by four connected lines. For general engagement conditions, the *CWE* area can be discretized into smaller engagement zones (Figure 1.17) and the overall result is obtained by integrating the forces obtained from these zones.

Figure 1.17 has been removed due to copyright restrictions. The information removed is the *CWE* area decompositions for sculptured surfaces [89].

### 1.4 Scope of This Research

From the above it can be seen that to support the development of Virtual Machining a number of challenges exist in performing Cutter Workpiece Engagement (*CWE*) calculations and making these more efficient and robust. These are: Swept volume generation, In-process

work piece modeling and *CWE* extractions. Considering these challenges together, the objectives of this thesis are:

- To develop a computationally efficient and generic swept volume methodology for multi-axis milling operations. A toolpath may contain hundreds or thousands of tool motions which make the computational cost for characterizing the geometry of each tool swept volume prohibitively expensive. This limitation motivates research in this thesis into methodologies that provide computationally simple analytical solutions to the swept volume generation problem.
- To develop an efficient and robust in-process workpiece update methodology. During machining simulation for each tool movement the modification of the workpiece geometry is required to keep track of the material removal process. Because NC verification and Cutter Workpiece Engagement (*CWE*) extraction directly depend on material removal an accurate in-process workpiece update is needed.
- To develop a methodology for identifying regions of the cutter surfaces that have the potential to engage with the workpiece during machining. A typical NC cutter has different surfaces with varying geometries and during the material removal process restricted regions of these cutter surfaces are eligible to contact the in-process workpiece. Identifying these regions is critical to simplifying the *CWE* extraction calculations for a wide range of cutters performing multi-axes machining.
- To develop solid (B-rep), polyhedral and vector based multi-axes *CWE* extraction methodologies to support the calculation of cutting forces in milling. These methodologies should be developed using a range of different types of cutters and tool paths defined by 3, 5-axes tool motions. The workpiece surfaces should cover a wide range of surface geometries such as the sculptured surfaces.

### **1.5 Organization of Thesis**

Henceforth the thesis is organized as follows: A review of related literature is presented in Chapter 2, followed by a new generic swept volume methodology for multi-axes milling in Chapter 3. In Chapter 4 efficient in-process update methodologies are presented. Feasible engagement regions of the cutter surfaces during the machining are analyzed in Chapter 5,

followed by the *CWE* extraction methodologies for solid, polyhedral and vector based representations in Chapter 6. The conclusions and possible future research directions are discussed in Chapter 7. Appendices clarifying some of the computational details are provided following the Bibliography.

## **Chapter 2**

### **Literature Review**

As is shown in Chapter 1, Virtual Machining has two main parts: the geometric modeling and the process modeling. The process modeling requires Cutter Workpiece Engagement (*CWE*) calculations from the geometric modeling to predict the cutting forces in milling. This becomes a challenging task when the geometry of the cutter and the workpiece are complex in multi-axis machining. An extensive amount of research has focused on geometric and physical simulations of the machining process. The important contributions from these research works are integrated in the virtual machining environment. In this chapter some of the important research contributions in this field will be reviewed. Specifically research into swept volume generation, in-process workpiece modeling and *CWE* extraction methodologies is reviewed.

#### **2.1 Swept Volume Generation**

Mathematically, the swept volume is the set of all points in space encompassed within the object envelop during its motion. A swept surface is the boundary of the swept volume. The swept surfaces and volumes are frequently used in graphical modeling, computer aided design, NC machining verification and robot analysis etc. As mentioned in chapter (1), swept volume generation is considered one of the important steps in virtual machining, since removal volume generation and the in-process work piece update require swept volumes.

The mathematical formulation of the swept volume problem has been investigated using jacobian rank deficiency method [1,2], sweep differential equation (SDE) [15], envelope theory [53,61,82], implicit modeling [75] and Minkowski sums [25]. Abdel Malek *et al.* [3] presented a comprehensive survey and review on the methodologies for the swept volume generation. Although in the past decades the problem of the swept volume generation has been studied widely, the problem is still not considered to be sufficiently well solved.

The basic idea in NC verification and simulation is to remove the cutter swept volume from the workpiece stock and thus to obtain the final machined surfaces. For NC machining

some swept volume generation methods have been developed. Wang *et al.* [83] computed the boundary points for the swept volume of APT-type cutter using the sweep envelope differential equations method (SEDE) [15]. Abdel-Malek *et al.* [1] and Blackmore *et al.* [15] solved systems of the implicit equations numerically for obtaining the swept envelopes. Wang *et al.* [82] derived the tangency condition in which the velocity of a point on the envelope surface must be tangent to the envelope surface.

Unfortunately in these methods swept volume computations have been done with complex differential equations that require numerical solutions and these limit their practicality. Therefore, few methods have been proposed to determine the swept profile in NC machining efficiently. In the following sub-sections some of the dominant techniques will be discussed.

### 2.1.1 Sweep Differential Equation Approach

The Sweep Differential Equation (SDE) method and its variants [13,14,15,16,83] were developed for representing and analyzing swept volumes. The key element of this approach is the sweep differential equation (SDE). In this method the boundary of the swept volume of an object can be represented to be the subset of the union of a) the grazing points on the boundary of the object during the entire sweep at which the vector field of the SDE neither points into or out of the object interior b) the ingress points at the beginning of the sweep and c) the egress points on the object boundary (Figure 2.1). The SDE method has been implemented for 3D swept volume representations generated by a Flat-End and a Ball-End mill. But the computational cost increased in 3D problems seriously and this affected the speed of the implementation. In order to overcome this computational difficulty, Blackmore *et al.* [15] developed an extension of the SDE method that they called the sweep envelope differential equation (SEDE) approach. The SEDE algorithm is used to calculate the swept volume generated by a general 7-parameter APT tool in 5-axis NC milling process.

Figure 2.1 has been removed due to copyright restrictions. The information removed is the decomposing object boundary [15].

### 2.1.2 Jacobian Rank Deficiency Approach

The Jacobian Rank Deficiency (JRD) method was presented by Abdel Malek *et al.* [1]. This approach is based on the singularity theory in differential geometry. A Jacobian rank deficiency condition is implemented in order to determine all entities that appear internal and external to the swept volume. A perturbation method is then introduced in order to select those entities that are boundary to the swept volume. They showed that the implicit surface is defined when all the 3x3 sub-Jacobians are simultaneously zero. With this approach the exact boundary envelope of a swept volume in a closed form can be generated. Although the presented formulation is valid for any number of parameters in an entity, it becomes more difficult to implement because the non-linear equations resulting from the determinants of the sub-jacobians also increases and system becomes more difficult to solve.

### 2.1.3 Swept Profile Based Approaches

Chung *et al.* [21] developed a methodology for representing the cutter swept surface of a generalized cutter in a single valued form. They obtained analytical expressions of the generating curve for different cutter geometries. However this methodology is limited to 3-axis milling with linear tool motions. Sheltami *et al.* [67] proposed a method that is based on identifying generating curves along the toolpath and connecting them into a solid model of the swept volume. It has been shown that at each instance in time there exists a curve on the cutter surface that describes the contribution of the tool position to the final bottom swept surface. This curve represents the imprint of the tool on the machined surface. However this technique has not yet been extended to include turns or twist of the general 5-axis tool motions. Also it is assumed that this curve could be approximated by a circle. However this assumption loses its validity in 5-axis tool motions. Roth *et al.* [75] presented a geometric method for generating swept volume of a toroidal end mill performing 5-axis tool motions. This technique, called imprint or cross product method, uses vector algebra for obtaining the points on the swept envelope and thus eliminates the use of the complicated SEDE equations. The method is based on discretizing the tool into pseudo-inserts (Figure 2.2) and identifying imprint points using a modified principle of silhouettes. For obtaining the imprint curve the imprint points of each pseudo-insert are connected by a piecewise linear curve. Later the collection of imprint curves is joined to approximate the swept surface.

Figure 2.2 has been removed due to copyright restrictions. The information removed is the (a) The pseudo-inserts of the toroidal End mill, and (b) the position of a pseudo-insert at two tool positions [75].

Pottman and Peternell [61] described an explicit geometric method for computing the characteristic points of a moving surface of revolution. In this method the plane, normal to the velocity vector is intersected with a circle chosen from the surface of revolution. The valid intersections generate the characteristic points on the envelope surface. Later Mann *et al.* [52] extended the imprint method to simulate the milling operations with different cutter geometries. They described that the imprint method can be used with cylinder and torus cutter geometries for obtaining the swept profiles. Chiou *et al.* [20] developed a swept profile methodology for a generalized cutter in 5-axis NC machining by analyzing the machine tool motions based on the machine configurations. In this work the swept envelope of a cutter is constructed by integrating the intermediate swept profiles. Later Du *et al.* [86] introduced a new B-Rep based approach which is partly derived from Wang's method [82]. In this work instantaneous profiles of the Fillet-End cutter are calculated by introducing the basis of the moving frame. This approach approximates the swept profile of a Fillet-End mill in the parametric form by interpolating a set of points on the cutter surface.

#### 2.1.4 Discussion

From the above discussion it can be seen that sweep differential equation and jacobian rank deficiency approaches generate the most precise boundaries of a swept volume in the parametric or implicit form. But because they contain numerical calculations their application to NC machining is limited. On the other hand, the nature of the swept profile based approaches promises an approximation to the swept volume. Though accuracy is improved by decreasing the distance between consecutive tool locations and by using more grazing points for the swept profile, this comes at the expense of longer simulation runs. A toolpath may contain hundreds or thousands of tool motions which make the computational cost for characterizing the geometry of each tool swept volume prohibitively expensive. This limitation motivates research in this thesis into methodologies that provide computationally

simple analytical solutions to the swept volume generation. Also in the literature the swept profile based approaches have concentrated mainly on the simpler milling cutter geometries. A comprehensive analytical solution in 5-axis milling has not yet been described for the general surface of revolution which covers the broadest range of cutter geometries.

In this thesis an analytical methodology for determining the shape of the swept envelopes generated by a general surface of revolution is developed. In this methodology, cutter surfaces performing 5-axis tool motions are decomposed into a set of characteristic circles. For obtaining these circles a new concept *two-parameter-family of spheres* is introduced. In this concept the center of a moving sphere is a function of two parameters representing the cutter surface and the tool motion. For a given 5-axis tool motion a member from this family of spheres generates two circles: a characteristic and a great circle. Considering the relationship between these circles an analytical formula which describes the swept envelope is developed. The implementation of the methodology is simple, especially with cutter geometries represented by pipe surfaces such as the torus and circular cylinder with fewer calculations being used.

## 2.2 In-process Workpiece Modeling

For NC simulation and *CWE* extraction an accurate in-process workpiece representation is needed. NC simulation usually implies cutting simulation and verification. The cutting simulation is for visualization of the cutting process and the verification is for comparison of the machined surface with the design surface. The modeling of the in-process workpiece geometry involves trade-offs between computational efficiency and the accuracy of the result. Several choices for modeling the in-process work piece exist. The two most common are mathematically accurate *Solid modeler based methodologies* that are used in CAD systems and *approximate modeler based methodologies* such as those used in computer graphics. In the following sub-sections these approaches will be discussed.

### 2.2.1 Solid Modeler Based Methodologies

Solid modeling theory was developed in the late 1960s and early 1970s. Currently the most popular schemes used in solid modelers are the Boundary representation (B-rep) and Constructive Solid Geometry (CSG). In the B-rep methodology an object is represented by

both its boundaries defined by Faces, Edges, Vertices and the connectivity information. In the CSG representation the Boolean operations and the simple primitives are saved in a binary tree data structure. Solid modeling methodologies offer the possibility of doing both simulation and verification. For simulation the swept volumes of the tool movements are subtracted from the in-process workpiece model. Verification is performed by Boolean differences between the processed workpiece and the design part. Researchers have in the past investigated the potential of solid modelers for supporting the machining process [68-71,73,76,80]. The computational complexity due to the Boolean operations was identified as one of the difficulties in applying this methodology. Developments in computer processor speeds and new computational technologies such as parallel computing now make this a more viable prospect [72].

Voelcker and Hunt [80] did an exploratory study of the feasibility of using CSG modeling system for NC simulation. It has been reported that the cost of simulation in the CSG approach is proportional to the fourth power of the number of tool movements. A typical NC program can contain more than 10000 tool movements. Spence and Altintas [70] developed a 2 ½-axis instantaneous cutter/workpiece immersion simulation method based on a CSG model. This work was later transferred to the B-rep modeler [9,64]. Later Spence *et al.* [71] presented integrated solid modeler based solutions for machining. In this work, geometric and milling process simulation combined with online monitoring and control is illustrated for 2 ½-axis pocket milling application (Figure 2.3). For this purpose the ACIS solid modeler kernel is utilized.

Figure 2.3 has been removed due to copyright restrictions. The information removed is the updating in-process workpiece [71].

Elbestawi *et al.* [37] developed an improved process simulation system for Ball-End milling of sculptured surfaces. The workpiece, cutter and *CWE* geometries are modeled using a geometric simulation system which uses the commercial solid modeler (ACIS) as a geometric engine. Later Imani *et al.* [38] presented a method for geometrically simulating a 3-axis Ball-End milling operation. They developed an advanced sweeping/skinning technique for generating a precise B-rep model of the Ball-End mill swept volume (Figure 2.4). In this

work semi finishing operations are simulated by performing consecutive Boolean operations between the in-process workpiece and the cutter swept volumes. The critical geometric information such as the instantaneous chip geometry and the scallop heights are extracted from the in-process workpiece.

Figure 2.4 has been removed due to copyright restrictions. The information removed is the 3-axis cutter swept volume with the boundary faces [38].

### **2.2.2 Approximate Modeler Based Methodologies**

For increasing efficiency and robustness in the process of the workpiece update a number of approximate approaches have been developed. The approaches can be classified into three major categories: *Image space (or view based) methods*, *Object based methods* and *polyhedral model based method*.

#### **▪ Image space (or view based) methods**

Chappel [19] developed a method called the “point vector technique”. The design surface is approximated by a set of points and the vectors originating from these points extend until they reach the boundary of the original stock. For simulating the machining, each vector on the workpiece surface is intersected with the cutter swept volumes and the vector length is shortened if it intersects the swept volume. Oliver and Goodman [58,74] presented an approach similar to Chappel’s. In this approach the workpiece is discretized into arrays containing the surface coordinates and the corresponding normal vectors. The discretization of the workpiece surfaces are done according to the computer graphics image of the workpiece surfaces. Each pixel on the screen is projected onto workpiece surface and these pixel points on the surface become the approximation of the workpiece (Figure 2.5). In this work the vector - cutter swept volume intersections are performed with a similar approach to Chappel’s.

Figure 2.5 has been removed due to copyright restrictions. The information removed is the simulation of the NC milling by projecting pixels of a computer graphics image onto the part surface [58].

Later Wang [81,82] developed an image space approach. For each pixel on the screen a vector is generated and using a scan-line algorithm the intersections between vectors and the toolpath envelope are calculated. The z-buffer of the workpiece is modified by applying Boolean difference operations with the z-buffer of the tool swept volumes. Also Van Hook [78] developed an approach called the “extended z-buffer”. The pixel images of the cutter are pre-computed and then the cutter is subtracted from the workpiece as it moves along a toolpath. This method is applied to 3-axis milling in which the orientation of the cutter is fixed. Later Atherton [6] extended Van Hook’s method to handle 5-axis milling.

The main limitations with the image space methodologies are: Because they are view dependant, errors not visible in the chosen viewing direction are undetected. For detecting the errors in another view of the part, the entire simulation must be started again. Also small machining errors i.e. less than 0.1mm are unlikely to be detected by a visual inspection of the computer graphics image. Despite their limitations the view based approaches are the best approximation methodologies for determining how much material is being removed for a given tool movement. Each pixel can represent a volume of material and, material removal can be approximated with accuracy dependent on the size of the object and the number of the pixels [41].

- **Object based methods**

The Object based in-process workpiece update methodologies are developed in [23, 24,32,39,40]. In these methodologies a set of points are chosen on the workpiece surfaces and using these points actual surfaces are approximated. These methodologies use similar calculation techniques from Chappel’s [19] and Oliver’s [58] approaches. Using the tool movements the vectors on the surface of the workpiece are updated. Some of the advantageous of these approaches are [41]: a) Material removal simulation is efficiently accomplished by intersecting the surface normals with the tool swept volumes. b) The machining verification is easily done by the updated vector length. Also using the color contour map of the workpiece surface, out of tolerance areas can be seen. c) The user can specify the accuracy of the simulation.

Jerard et al. [40] described a 3-axis machining methodology for simulating the geometric aspects of numerically controlled machining. The methodology is based on a discrete approximation of the object into a set of surface points. Vectors passed through these points are intersected with the tool movements (Figure 2.6). For increasing the efficiency the localization methodology described in [41] is used.

Figure 2.6 has been removed due to copyright restrictions. The information removed is the updating the workpiece surfaces represented by parallel z-vectors [40].

Fussell and Jerard in their recent research [32] used an extended z-Buffer model and a discrete axial slice model for representing the workpiece and the cutting tool (Ball-End mill) respectively. In this work a 3-axis approximation of the 5-axis tool movement is used to simplify the calculations while maintaining a desired level of accuracy (Figure 2.7-a). Since the tool swept volume is modeled as a set of geometric primitives such as natural quadric surfaces and planes, the intersection calculations are simplified to a set of line/surface intersections. It is assumed that all primitives are linear and the curvatures in the toolpath and the tool orientations are neglected. For this reason 5-axis tool paths are subdivided into many 3-axis toolpaths. Although approximating the 5-axis tool moves with 3-axis linear tool moves is a primary drawback in this work, the comparisons by Quinn [62] to the exact 5-axis tool moves with the 3-axis approximation method show that the 3-axis method is faster and robust. Another drawback in this work is that all discrete vectors of the workpiece model lie in one direction regardless of surface normal directions, where the directions are along the vertical z-axis of a Cartesian coordinate system (Figure 2.7-b).

Figure 2.7 has been removed due to copyright restrictions. The information removed is the (a) A 3-axis approximation of 5-axis swept volume, and (b) the extended z-buffer model of workpiece [32].

Baek *et al.* presented a z-Map update method for linearly [7] and circularly [8] moving APT-type tools in 3-axis milling. Machining process is simulated through numerically calculating the intersection points between the z-Map vectors and the tool swept envelope.

The intersection points are expressed as the solution of a system of *nonlinear* equations. This system of equations is transformed into a single-variable function whose zero is a solution of the system. Also in this work they show how to calculate the candidate interval in which the unique zero exists. In this methodology both the tool rotation axis and the z-Map vectors are restricted to lie along the vertical z-axis of a Cartesian coordinate system.

Park et. al. [43] developed a hybrid cutting simulation methodology via the Discrete Normal Vector (*DNV*) and the Discrete Vertical Vector (*DVV*) models. In the *DNV* approach a workpiece consists of discrete vectors whose direction vectors are surface normal vectors, where all directions are not necessarily identical. Also spacing may vary depending upon the surface local properties. On the other hand, in the *DVV* approach all discrete vectors of the workpiece model lie in only one direction regardless of surface normal directions, where the directions are along the vertical z-axis of a Cartesian coordinate system. The *DNV* approach generates better surface quality especially when the workpiece model has vertical walls, sharp edges, and overhang (Figure 2.8). But on the other hand in the *DNV* representation the localization of the cutter swept envelope is difficult and this decreases the computational efficiency. The main idea in this work is to take full advantage of each type's strengths in terms of speed. But on the other hand, in this hybrid methodology the cutter swept volumes are generated by a *solid modeler*. A typical toolpath may contain thousands of tool motions. In this case using the solid modeler for the cutter swept volume generation increases the computational cost during the simulation.

Figure 2.8 has been removed due to copyright restrictions. The information removed is the *DNV* and *DVV* representation of the workpiece surfaces [43].

- **Polyhedral model based method**

Another alternative for updating the in-process workpiece in NC machining is a polyhedral model based method. In the polyhedral model the workpiece surfaces are represented by a finite set of polygonal planes called facets. The most commonly used shapes are triangles and converting the mathematically precise models to the triangulated models is called *tessellation*. In this approach in order to achieve real time NC simulation the number of polygons has to be reduced. But this results in poor image quality. Ong et. al. [49]

developed an approach to reduce the number of polygons without much loss in image quality (Figure 2.9). They proposed an adaptive regular mesh decimation algorithm which uses a quadtree to represent the milling surface. This algorithm can automatically adjust the polygon density to approximate the milling surface during the simulation in real time.

Figure 2.9 has been removed due to copyright restrictions. The information removed is the regular mesh decimation for 3-axis NC milling simulation [49].

### 2.2.3 Discussion

During the machining simulation for each tool movement the modification of the workpiece geometry is required to keep track of the material removal process. Because the NC verification and Cutter Workpiece Engagement (*CWE*) extraction directly dependent on the material removal an accurate in-process workpiece modeling is needed.

From the literature review it can be seen that several choices for modeling the in-process work piece exist. The two most common are mathematically accurate solid modeling that are used in CAD systems and approximate modeling such as those used in computer graphics: faceted and discrete vector models. Each methodology has its own strengths and weaknesses in terms of computational complexity, representation accuracy and the robustness. It can be seen from the literature that for updating the workpiece surfaces represented by the solid or faceted models third party softwares can be used. For example the ACIS solid modeling kernel is one of these softwares.

But on the other hand for the workpiece geometries represented by discrete vectors accurate and computationally efficient in-process workpiece update methodologies are needed. In the literature the discrete vectors have orientations along the z-axis of the standard bases of  $\mathbb{R}^3$ . But when the in-process workpiece has some features like vertical walls and sharp edges, representing the workpiece with one directional vectors generates less accurate results in visualization of the final product and *CWE* extractions. Also in recent works [7,8] the tool axis has a fixed orientation along the z-axis of the standard bases of  $\mathbb{R}^3$  and the workpiece updates are performed numerically for the common milling cutters. Still needed are in-process workpiece update methodologies in which the workpiece geometries are represented by discrete vectors having different orientations and the tool rotation axes have

arbitrary inclinations in space. Also in these methodologies for the given cutter geometry the calculations, if it is possible, must be analytic for computational efficiency.

In this thesis the discrete vectors with their orientations in the directions of x,y,z-axes of the standard bases of  $\mathbb{R}^3$  are used. Therefore in this representation more vectors in different directions are used and thus the quality in the visualization of the final product has been increased. A typical milling tool path contains thousands of tool movements and during the machining simulation for calculating the intersections only a small percentage of all the discrete vectors is needed. For this purpose for localizing the tool envelope during simulation the Axis Aligned Bounding Box (AABB) is used. For simplifying the intersection calculations the properties of canal surfaces are utilized. In the developed methodologies the tool motions in (3+2)-axis milling in which the cutter can have an arbitrary fixed orientation in space are considered. The 5-axis tool motions can be approximated by (3+2)-axis tool motions and an example is given for illustrating this situation. The calculations for the major cutter geometries such as the sphere, cylinder, frustum of a cone and flat-bottom surfaces are made analytically. Because of the complexity of the torus shape the calculations are made by using the numerical root finding methods. For this purpose a root finding analysis is developed for guaranteeing the root(s) in the given interval.

### **2.3 Cutter Workpiece Engagement Extraction**

The goal in *CWE* extraction is to obtain engagement conditions between milling cutter and the in-process workpiece for supporting process modeling. From the *CWEs* instantaneous in-cut segments or engaged portions of the cutting edges are obtained. For extracting the in-cut segments *CWE* boundaries are intersected with the cutter edges either in 2D or in 3D Euclidian space. In both approaches edge/edge intersection is performed. In the 2D-space approach, first the cutter contact face is intersected with the in-process workpiece and *CWE* boundary is obtained in 3D Euclidian space. Then this *CWE* boundary and the cutter edges are mapped into two dimensional space. Finally for obtaining the in-cut segments, each cutting edge is intersected with the *CWE* boundary in this space [70,89]. In the 3D-space approach intersections between *CWE* boundary and cutter edges are performed in 3D Euclidian space [26,37]. In this thesis for extracting in-cut segments the 2D-space approach is utilized.

In the literature, based on the mathematical representation of the workpiece geometry, the *CWE* extraction methodologies can be classified into three major categories: *Solid model based*, *polyhedral model based* and *discrete vector based* methods. Also some other existing *CWE* extraction methods are discussed in section (2.3.4).

### 2.3.1 Solid model based methods

Some research on Solid model based *CWE* extraction methodologies for supporting process modeling has been reported [26,,37,47,70,89]. In these *CWE* extraction methodologies the initial workpiece geometry is represented by using the B-rep model. Geometric and topological algorithms of this model are utilized for both updating the in-process workpiece and extracting the *CWE* geometry. For updating the in-process workpiece geometry first the swept volume of the cutter is generated for a given toolpath segment and then this volume is subtracted from the current workpiece state using regularized Boolean subtraction. Cutter workpiece engagement calculations are performed using this new workpiece state until the start of the following tool path segment. If the toolpath has self intersections then for obtaining the correct *CWEs* it may be necessary to decompose the given toolpath into non-intersecting smaller segments. From the literature the *CWE* extractions using a solid modeler can be classified into two groups: 2 ½-axis and 3-axis methods.

#### ▪ 2 ½-Axis methods

For calculating *CWEs* in 2 ½-axis milling with a Flat-End mill, a B-rep based approach has been presented by Spence *et al.* [70]. Figure 2.10(a) illustrates that a Flat-End mill engages with the in-process workpiece  $W_i$  at a constant depth of cut  $d$  along the entire toolpath. It is shown in Figure 2.10(b) that engagements are determined by performing the intersections between an advancing semi circle  $C_i$  moving in the tangential direction of the toolpath and the boundaries of  $W_i$  on an engagement plane  $PL_{Z-Top}$ . The engagement geometry is calculated as entry ( $\phi_{st}$ ) and exit ( $\phi_{ex}$ ) angles for each step of the Flat-End mill (Figure 2.10(c)). The step taken between each *CWE* calculation is the feed per revolution of the cutter. Although this methodology is an important step in applying solid modeling technology to the *CWE* extraction problem, it only generates the constant depth of cut.

Figure 2.10 has been removed due to copyright restrictions. The information removed is the extracting *CWEs* by advancing semi circle approach for 2 ½ -axis milling [70].

Later Yip-Hoi *et al.* [89] presented another B-rep based approach for extracting *CWEs* in 2 ½ - axis milling. He extended Spence's methodology by performing the regularized Boolean intersection operation between a semi cylindrical cutter surface and the in-process workpiece (Figure 2.11). In this work for imprinting the engagement region boundaries on the cutter surface, the solid modeler's (ACIS) surface/surface intersection algorithms are used. Then the engagement boundaries are mapped from 3D Euclidian space into 2D space defined by the engagement angle and the depth of cut respectively. Later these engagement regions are decomposed into smaller rectangular regions for fulfilling the requirement of the force model described in [5]. The advantage of this methodology is that it can be applied to a wider range of workpiece geometries i.e. the initial workpiece geometry is not rectangular prismatic. On the other hand it is still a 2 ½ -axis methodology with a Flat-End mill and the engagement boundaries are limited to straight lines and circular arcs.

Figure 2.11 has been removed due to copyright restrictions. The information removed is the extracting *CWEs* by advancing semi cylinder approach for 2 ½ -Axis milling [89].

### ▪ 3-Axis methods

Elbestawi *et al.* [37] developed a Ball-End milling process simulation system. In this work the Ball End mill performs 2-axis or an ascending (with different up-hill angles) 3-axis motion. The geometries of the workpiece, the cutter and *CWEs* are modeled using (ACIS) as a geometric engine. The engaged portion of the cutting edge (the instantaneous in-cut segment) is computed in two steps: In the first step the boundary of the contact face between the spherical portion of the Ball-End mill and the in-process workpiece is obtained. This boundary consists of one circular edge and two B-spline edges (Figure 2.12). In the second step the intersection points between interpolated cutting edge and boundary curves of the contact face are found. This is performed by using edge/edge intersections with a prescribed tolerance. Finally the cutting edge is decomposed into in-cut and out-cut segments.

Figure 2.12 has been removed due to copyright restrictions. The information removed is the 3-axis *CWE* extraction with Ball-End mill [37].

Also El-Mounayri *et al.* [26] presented a geometric approach for 3-axis machining process simulation using a Ball-End mill. In this work solid models are used for representing the in-process workpiece and the removal volume. The cutting edges are represented by Bezier curves in 3D Euclidian space. For obtaining the in-cut segments of the cutting edges, the Bezier curves are intersected with the removal volume (Figure 2.13). Later these segments are used for evaluating the instantaneous cutting forces.

Figure 2.13 has been removed due to copyright restrictions. The information removed is the procedure for extracting in-cut segments of the cutting edges [26].

### 2.3.2 Polyhedral Model Based Methods

Although they are approximate, polyhedral models provide the advantage of simplifying the workpiece surface geometry to planes which consist of linear boundaries. Thus the intersection calculations reduce to line / surface intersections. These can be performed analytically for the geometry found on cutting tools. Some research [88,90] on polyhedral based *CWE* extraction methodologies for supporting the process modeling has been reported.

Yao [88] presented geometric algorithms for *estimating* cutter engagement values for 3-axis Ball-End milling processes of tessellated free-form surfaces. In this work 3D surface geometry is represented by an STL (“Stereo lithography”) model in which surfaces are tessellated or broken down into a series of small triangles. It is assumed that the toolpath is a linear segment and only the frontier of the Ball-End mill has engagement with the workpiece (Figure 2.14). The engaged portion of the cutter is estimated in three steps: First finding triangles that intersect the cutter, then intersecting those triangles with the cutter for obtaining the intersection curve segments and finally using those curve segments to form the closed engagement region.

Figure 2.14 has been removed due to copyright restrictions. The information removed is the cutter engagement portion [88].

Later Yip-Hoi *et al.* [90] presented a polyhedral model based *CWE* calculation methodology in 2 ½-axis and 3-axis millings. For reducing the amount of data and calculations this methodology works on removal volumes instead of the in-process workpiece. To further reduce the number of intersections an  $R^*$ -tree based localization technique is applied for localizing the facets that have potential intersections with the cutting tool. The methodology first calculates the intersection points between facet edges and the cutter, and then using a mark circle method it creates intersection segments between these intersection points. Finally an undirected graph is used for connecting those intersection segments to form the boundary of the *CWE* area. As explained in section (1.2.3) there is a chordal error in the polyhedral model representations. In this case the cutter does not intersect the facets on the side-wall surfaces of the removal volume. In this work for solving this problem the cutter radius is enlarged slightly (Figure 2.15). Therefore the entry angles are slightly larger while the exit angles are less than what they should be.

Figure 2.15 has been removed due to copyright restrictions. The information removed is the (a) Chordal error in the cutter facet intersection, and (b) the radius enlargement of the cutter [90].

### 2.3.3 Discrete Vector Based Methods

Some research on discrete vector based *CWE* extraction for supporting process modeling has been reported [18,31,32,42,91]. In these approaches the workpiece is broken into a set of evenly distributed parallel lines which have directions along the vertical  $z$  axis of the Cartesian coordinate system. Multiple  $z$  values are stored in one vector, allowing extensions to multi-axis milling with multiple tool passes. The spacing between vectors can be determined based on the desired accuracy, local surface curvature of the workpiece and the tool size. *CWEs* are extracted according to requirements of the mechanistic force model. The mechanistic force model divides the cutting tool into a set of axial disc elements.

There are two primary concerns for each disc element. First concern is whether or not the disc element is in contact with the in-process workpiece and the second concern for a disc engaged with the in-process workpiece is to define the limits of the engagement in terms of entry/exit angles. The entry and exit angles are calculated by solving for the normal direction component of each intersection, and storing the maximum and minimum normal positions found during a given tool move (Figure 2.16).

Figure 2.16 has been removed due to copyright restrictions. The information removed is the Entry/exit angle calculation for each disc [31].

### 2.3.4 Other Existing Methods

So far it is shown that there are mainly three major approaches for extracting *CWEs*. Also there are some other existing methodologies which are not classified under major approaches. For example Stori *et al.* [84] presented a metric based approach for toolpath optimization in high speed machining. For obtaining cutter engagements a pixel based simulation procedure is used (Figure 2.17). In this work a Flat-End mill follows a 2D linear toolpath. Both the local in-process geometry and the cutter is discretized. Any un-machined area is represented by a 0, and the machined area is represented by a 1. The instantaneous engagements are estimated by checking the status of the in-process workpiece geometry for the pixels that overlap the circumference of the cutting tool in the given cutter location point.

Figure 2.17 has been removed due to copyright restrictions. The information removed is the pixel based engagement extraction [84].

Also Gupta *et al.* [34] developed an analytical method for computing cutter engagement functions in 2.5D machining. In this work the analytical approaches are described for determining the cutter engagements utilizing the engagement functions for individual half spaces that comprise the workpiece geometry (Figure 2.18). The edges of the workpiece are represented as half spaces. The formulae are obtained for determining the cutter engagement functions in the cases: circular cut and linear half space, and circular cut and circular half space.

Figure 2.18 has been removed due to copyright restrictions. The information removed is the “A linear tool path and region expressed as a Boolean expression of half spaces” [34].

### 2.3.5 Discussion

The purpose of Cutter Workpiece Engagement (*CWE*) extraction is to identify engagement conditions between the cutter and the in-process workpiece during the milling operation for predicting the cutting forces. From the above discussion it can be seen that Research work on *CWE* extraction can be classified into three main approaches: Solid modeler based, polyhedral modeler based and vector based methodologies. There is always a tradeoff between computational efficiency and accuracy in these approaches. For example the polyhedral and vector based approaches generate approximated *CWE* results and because of this they require a shorter computational time than does the solid modeler based approach. But on the other hand in the solid modeler based approach the most accurate *CWEs* are obtained with the cost of higher computational time. These three main approaches to *CWE* extraction are discussed in the following parts.

- In the literature solid modeling approaches are concentrated on simple workpiece surfaces such as cylinders and planes. But the most complicated *CWE* calculations occur during the machining of *sculptured surfaces*. Because of continuously changing surface geometry, modeling *CWEs* in sculptured surface machining is not so easy. In the given approaches the cutters perform either 2 ½ -axis machining or 3-axis machining with ascending motion in which only the front part of the cutter removes material. But sometimes with respect to the motion type the back side or the bottom-flat part of a cutter may have contact with the in-process workpiece. For example in a plunging motion of a Flat-End mill the bottom flat surface removes material. Therefore *CWE* extraction with different surfaces of a cutter must be addressed. Also there is a needed for a 5-axis *CWE* extraction methodology in which cutter has changing orientations.
- From the literature, it can be seen that for the polyhedral model based *CWE* extractions so far little work has been conducted. Also there is a robustness issue in *CWE* extractions because of the chordal error.

- In the literature, the proposed discrete vector based methodologies represent the in-process workpiece by using discrete vectors which lie in only one direction regardless of the surface normal direction. But when the orientation of the cutter axis is parallel to these vectors, for some cutter geometries, extracting *CWEs* becomes difficult i.e. 3-axis machining with a Flat-End mill.

From the above discussion it can be seen that comprehensive methods for extracting *CWEs* using solid, polyhedral and discrete vector approaches are yet to be fully developed. In this thesis solid, polyhedral and vector based *CWE* methodologies are developed using a range of different types of cutters and tool paths defined by 3, 5-axes tool motions. The workpiece surfaces cover a wide range of surface geometries such as the sculptured surfaces. In 3-axis solid and polyhedral model approaches to reduce the size of the data structure that needs to be manipulated the removal volume is used instead of the in-process workpiece. For 5-axis machining it is the workpiece itself.

In the 3-axis solid modeler methodology the cutter surfaces are decomposed into sub-constituent surfaces with respect to the feed vector direction. Then these surfaces are intersected with their removal volumes for obtaining the boundary curves of the closed *CWE* area. Decomposing the cutter surfaces allows *CWEs* for different parts of a given cutter geometry, i.e. bottom flat or back side of a cutter to be more easily extracted. During the material removal process only certain parts of the cutter surfaces are eligible to contact the in-process workpiece. In this thesis for representing these regions of the cutter boundary a terminology *feasible contact surfaces (FCS)* is introduced. The word feasible is used because although these surfaces are eligible to contact the in-process workpiece, they may or may not remove material depending on the cutter position relative to the workpiece. Because in a solid model the envelope boundary for 5-axis tool motions are approximated by spline curves, applying the same methodology described for the 3-axis milling generates non robust results. Because of this in the 5-axis methodology an offset body obtained from the feasible contact surface is intersected with the in-process workpiece at a given cutter location point. Then face/face intersections are performed for obtaining the boundaries of the *CWEs*.

For addressing the chordal error problem in polyhedral models a 3-axis mapping technique is developed that transforms a polyhedral model of the removal volume from

Euclidean space to a parametric space defined by location along the tool path, engagement angle and the depth-of-cut. As a result, intersection operations are reduced to first order plane-plane intersections. This approach reduces the complexity of the cutter/workpiece intersections and also eliminates robustness problems found in standard polyhedral modeling. Because in 5-axis tool motions the direction of the tool axis vector continuously changes applying the mapping described for the 3-axis milling increases the distortions of the facets. Therefore an approach similar to that of the 5-axis solid modeler is developed. In this approach the only difference is the application of the face-face intersections.

In the discrete vector approach the cutter surfaces are sliced along the tool rotation axis and then the surface of each slice is decomposed into buckets. The sizes of the buckets are adjusted with respect to the resolution of discrete vectors. Later during the simulation discrete vectors are intersected with the cutter surfaces for representing the material removal and the buckets which contain the intersection points are plotted

## 2.4 Summary

In this chapter, a review of the literature in swept volume generation, in-process workpiece modeling and *CWE* extraction are presented. It has been shown that because a toolpath contains thousands of tool motions the swept volume generation becomes costly in terms of large memory and computational requirements. For this reason for NC machining the swept volume construction must be easy and the geometric information for defining the volume must require less memory. The accuracy of the in-process workpiece modeling effects the quality of the *CWEs*. Especially in the object based in-process workpiece update methods using discrete vectors lying only in one direction generates problems in both workpiece surface quality and *CWE* representations. For the *CWE* extractions there is a need to develop 3 to 5-axis machining approaches for different types of cutter and workpiece surfaces in solid, polyhedral and vector based models.

## Chapter 3

### Cutter Swept Volume Generation

This chapter presents an analytical methodology to calculate cutter profiles for modeling the swept volumes of general surfaces of revolution with respect to 5-axis tool motions. In this methodology the geometry of a cutter is considered as a *canal surface*. Briefly a canal surface is an envelope of a moving sphere with varying radius. In this methodology, cutter surfaces performing 5-axis tool motions are decomposed into a set of characteristic circles. For obtaining these circles a new concept *two-parameter-family of spheres* is introduced. In this concept the center of a moving sphere is a function of two parameters representing the cutter surface and the tool motion. On the other hand the radius of the moving sphere is only a function of one parameter. For a given 5-axis tool motion a member from this family of spheres generates two circles: a characteristic and a great circle. Considering the relationship between these circles an analytical formula which describes the swept envelope is developed. Also applying this methodology, the implicit envelope equations of the common cutter geometries performing 5-Axis tool motions are derived.

The parametric representations of canal surfaces in one-parameter family of spheres are presented in section (3.1). The concept of the two-parameter-family of spheres is introduced in section (3.2), followed by the closed form swept profile equations in section (3.3). Examples from the implementation of the methodology are shown in section (3.4), and finally the chapter ends with the discussion in section (3.5).

### 3.1 Canal Surfaces

A canal surface  $\Phi$  is the envelope of a moving sphere with varying radius, defined by a trajectory of its center (spine curve)  $\mathbf{m}(t)$  and a radius function  $r(t)$ , where  $t \in \mathbb{R}$ . When the radius function  $r(t)$  has a constant value, the canal surface is also called as a pipe surface. Canal surfaces have wide applications in different areas such as shape reconstruction, construction of blending surfaces, transition surfaces between pipes and robotic path planning [28,66,83]. Some examples of the canal surfaces are pipe surfaces, tori, natural

quadrics and dupin cyclides [50,60]. For simulation and computer graphics, a model which contains canal surfaces has some advantageous such as the model construction is easy, the geometric information for defining the model requires less space and efficiency is high for rendering the model [45,57,87]. Defining equations of a canal surface are expressed as [60]

$$\Sigma(t) : (P - \mathbf{m}(t))^2 - r(t)^2 = 0 \quad (3.1)$$

$$\Sigma'(t) : (P - \mathbf{m}(t)) \cdot \mathbf{m}'(t) + r(t)r'(t) = 0 \quad (3.2)$$

where  $\Sigma(t)$  represents one-parameter family of spheres and  $P = (x,y,z)$  is a point on the sphere surface (see Figure 3.1). A canal surface can contain a one parameter set of so called *characteristic circles*  $K(t)$ . The characteristic circles are obtained by the following intersection

$$K(t) = \Sigma(t) \cap \Sigma'(t) \quad (3.3)$$

where the plane  $\Sigma'$  is perpendicular to the vector of  $\mathbf{m}'$ . The reality of a canal surface in general depends on  $r'(t)$  and the length of  $\mathbf{m}'$ . If the envelope is real then the following condition holds

$$\|\mathbf{m}'(t)\|^2 - r'(t)^2 \geq 0 \quad (3.4)$$

### 3.1.1 Explicit Representation of Canal Surfaces

Fig. 3.1 illustrates a canal surface with defining parameters. In this figure for a given parameter value  $t$ , a moving sphere touches the canal surface  $\Phi$  at a characteristic circle  $K(t)$ . A canal surface can be parameterized by using  $K(t)$ . For parameterization the center  $\mathbf{C}(t)$  and the radius  $R(t)$  of the characteristic circle are used. The center can be expressed as

$$\mathbf{C}(t) = \mathbf{m}(t) + r(t) \cos \varphi(t) \frac{\mathbf{m}'(t)}{\|\mathbf{m}'(t)\|} \quad (3.5)$$

where  $\varphi(t)$  is an angle (Fig. 3.1) between two vectors  $\mathbf{m}'(t)$  and  $P - \mathbf{m}(t)$ , and it satisfies the following dot product equation

$$(P - \mathbf{m}(t)) \cdot \mathbf{m}'(t) = \|P - \mathbf{m}(t)\| \|\mathbf{m}'(t)\| \cos \varphi(t) \quad (3.6)$$

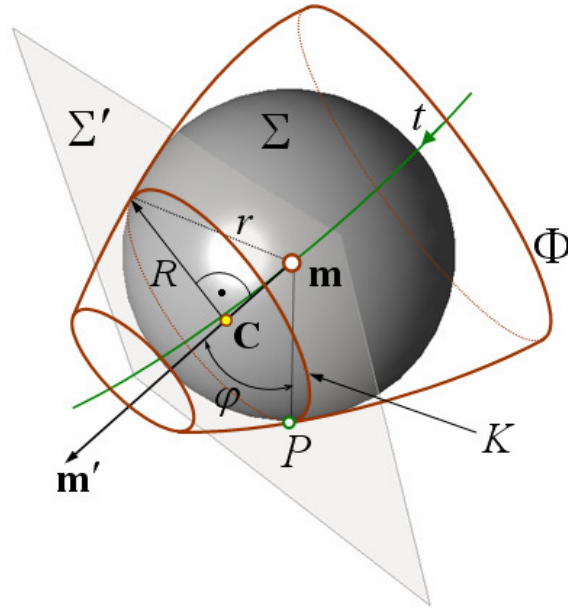


Figure 3.1: Geometric description of a canal surface

Using Eqs.(3.1), (3.2) and (3.6) the following trigonometric equation is derived

$$\cos \varphi(t) = \frac{(P - \mathbf{m}(t)) \cdot \mathbf{m}'(t)}{\|P - \mathbf{m}(t)\| \|\mathbf{m}'(t)\|} = -\frac{r'(t)}{\|\mathbf{m}'(t)\|} \quad (3.7)$$

By substituting the equivalent of  $\cos \varphi(t)$  into Eq.(3.5) the center of the characteristic circle is expanded as follows

$$\mathbf{C}(t) = \mathbf{m}(t) - r(t) r'(t) \frac{\mathbf{m}'(t)}{\|\mathbf{m}'(t)\|^2} \quad (3.8)$$

Also the radius  $R(t)$  of the characteristic circle is obtained by

$$R(t) = r(t) \sin \varphi(t) = r(t) \frac{\sqrt{\|\mathbf{m}'(t)\|^2 - r'(t)^2}}{\|\mathbf{m}'(t)\|} \quad (3.9)$$

where the equivalent of  $\sin \varphi(t)$  is derived from Eq.(3.7). A canal surface  $\Phi$  can be considered as a set of characteristic circles, and thus by using Eqs. (3.8) and (3.9)  $\Phi$  can be expressed as

$$K(t, \theta) = \mathbf{C}(t) + R(t)(\cos \theta \mathbf{M}(t) + \sin \theta \mathbf{B}(t)) \quad (3.10)$$

where  $\theta$  is an angle of the characteristic circle and it changes in the ranges of 0 to  $2\pi$ . Also in Eq.(3.10),  $\mathbf{M}(t)$  and  $\mathbf{B}(t)$  are the unit normal and binormal vectors of the Frenet trihedron and they are on the plane  $\Sigma'(t)$  which contains the characteristic circle. For the canal surface the frenet trihedron is formed with the following components

$$\mathbf{T}(t) = \frac{\mathbf{m}'(t)}{\|\mathbf{m}'(t)\|}, \quad \mathbf{M}(t) = \frac{\mathbf{m}'(t) \times \mathbf{m}''(t)}{\|\mathbf{m}'(t) \times \mathbf{m}''(t)\|}, \quad \mathbf{B}(t) = \mathbf{T}(t) \times \mathbf{M}(t) \quad (3.11)$$

where  $\mathbf{T}(t)$  is the unit tangent vector in the direction of  $\mathbf{m}'$ . It is assumed in Eq. (3.11) that the spine curve  $\mathbf{m}$  is biregular, in other words along  $\mathbf{m}$  the following condition is fulfilled

$$\mathbf{m}'(t) \times \mathbf{m}''(t) \neq 0 \quad (3.12)$$

### 3.1.2 Cutting Tool Geometries as Canal Surfaces

According to the Automatically Programmed Tool (APT) definition [46] milling cutters can be defined. The cutter geometries are represented by natural quadrics and torus. Natural quadrics consist of the sphere, circular cylinders and the cone. Together with the plane (a degenerate quadric) and torus these constitute the surface geometries found on the majority of cutters used in milling. For example a ball nose end mill is defined by two natural quadric surfaces – spherical and cylindrical. Other examples are shown in Fig 3.2.

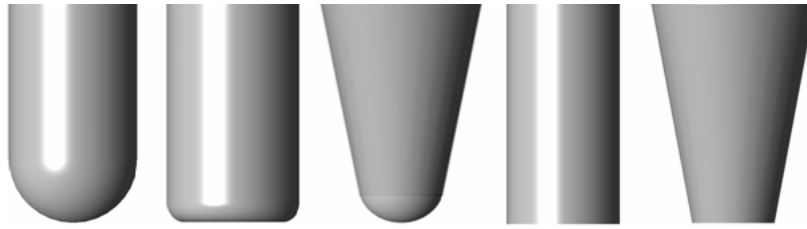


Figure 3.2: Some typical milling cutter geometries

Also the cutters shown in Fig. 3.2 can be considered as canal surfaces. For example, if a sphere moves along a straight line and the radius of the sphere increases linearly, a canal surface so called a frustum of a cone is generated (Fig. 3.3(a)). On the other hand if a sphere with a constant radius follows a spine curve trajectory, it envelopes a special canal surface called a pipe surface. Two common pipe surfaces cylinder and torus are built when the sphere moves along linear path and a circular path respectively (Fig. 3.3(b)-(c))

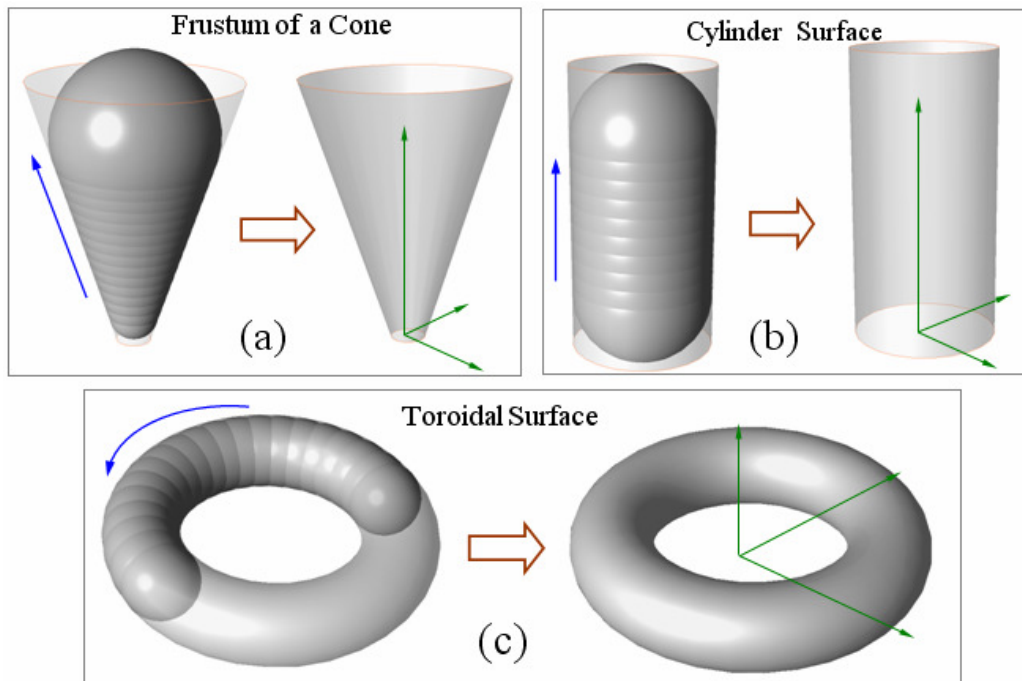


Figure 3.3: Generating cutter geometries with a moving sphere

### 3.2 Two-Parameter-Family of Spheres in Multi-Axis Milling

It is shown in section (3.1) that a moving sphere  $\Sigma(t)$  follows a spine curve trajectory and it envelopes a canal surface  $\Phi$ , where  $t$  is a spine curve parameter. But when a cutter

performs a milling simulation, a moving sphere of the cutter geometry follows two different trajectories: the first one is the spine curve and the second one is the toolpath trajectory represented by the parameter  $u \in \mathbb{R}$ . In this case the center of the moving sphere can be represented by two parameters. The two-parameter-family of spheres can be defined by

$$\Sigma(t,u) : \Sigma(P - \mathbf{m}(t,u))^2 - r(t)^2 = 0 \quad (3.13)$$

where  $\Sigma(t,u)$  represents two-parameter family of spheres and  $P$  is a point on the sphere surface. Note that in Eq. (3.13), although the center of the sphere  $\mathbf{m}$  is a function of two parameters  $t$  and  $u$ , the radius  $r$  is only a function of the parameter  $t$ . This is because the cutter radius only changes along the spine curve for a given cutter location. Let  $\Sigma_t$  and  $\Sigma_u$  be the partial derivatives of  $\Sigma(t,u)$  with respect to  $t$  and  $u$ . These partial derivatives can be expressed as

$$\Sigma_t(t,u) : \Sigma(P - \mathbf{m}(t,u)) \cdot \mathbf{m}_t + r r_t = 0 \quad (3.14)$$

$$\Sigma_u(t,u) : \Sigma(P - \mathbf{m}(t,u)) \cdot \mathbf{m}_u = 0 \quad (3.15)$$

where  $\mathbf{m}_t$  and  $\mathbf{m}_u$  are the partial derivatives of  $\mathbf{m}(t,u)$  with respect to corresponding parameters. Note that when the cutter geometry is pipe surface  $r_t$  becomes zero. Eqs. (3.14) and (3.15) represent two planes with the surface normals  $\mathbf{m}_t$  and  $\mathbf{m}_u$  respectively. In this section it will be shown that under a tool motion the two-parameter-family of spheres generates so called grazing points on the cutter envelope surface. Grazing points are the discrete points that the surface of the cutter will leave behind as it moves in the space. The following remarks and the property motivate finding grazing points.

**Remark 3.1:** A characteristic circle  $K$  embedded in  $\Sigma(t,u)$  is a solution of the system of Eqs. (3.13) and (3.14)

$$K(t,u) = \Sigma(t,u) \cap \Sigma_t(t,u)$$

This is an intersection of a sphere  $\Sigma$  with a plane  $\Sigma_t$  which has a normal vector in the direction of  $\mathbf{m}_t$ .

**Remark 3.2:** By definition a *great circle* is a section of a sphere that contains a diameter of the sphere [44]. A great circle  $S$  is a solution of the system of Eqs. (3.13) and (3.15)

$$S(t, u) = \Sigma(t, u) \cap \Sigma_u(t, u)$$

Also this is an intersection of a sphere  $\Sigma$  with a plane  $\Sigma_u$  which has a normal vector in the direction of  $\mathbf{m}_u$ . It can be concluded from remarks (3.1) and (3.2) that the characteristic and the great circles lie on the planes  $\Sigma_t$  and  $\Sigma_u$  respectively. These circles are illustrated in Fig. 3.4 for a given parameter set  $t$  and  $u$ .

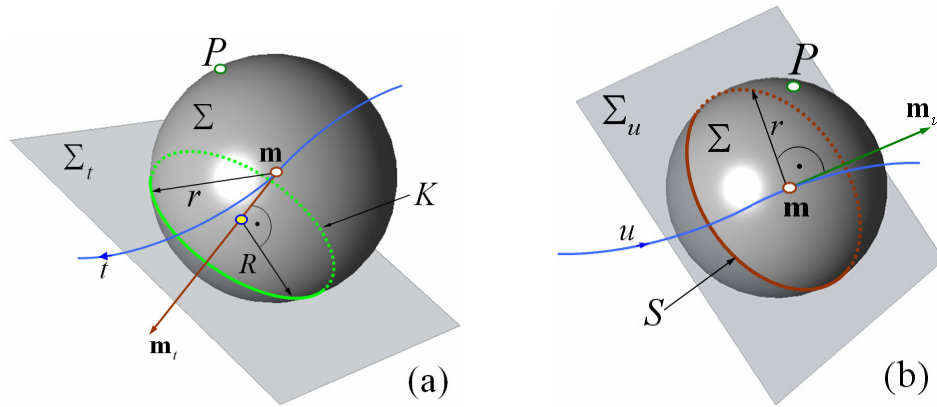


Figure 3.4: (a) The characteristic  $K$ , and (b) the great  $S$  circles

**Property 3.1:**

(i) Intersecting characteristic and great circles generates points on the cutter envelope surface (see Fig. 3.5) and also these points are the solution of the system of Eqs. (3.13-3.15)

(ii) Alternatively if a point  $P = (x, y, z)$  is one of these intersection points then it satisfies the following system of envelope equations [82]

$$f(x, y, z, u) = 0 \tag{3.16}$$

$$\frac{\partial f(x, y, z, u)}{\partial u} = 0 \tag{3.17}$$

where  $f(x, y, z, u)$  implicitly represents the family of cutter surfaces with respect to the toolpath parameter  $u$ .

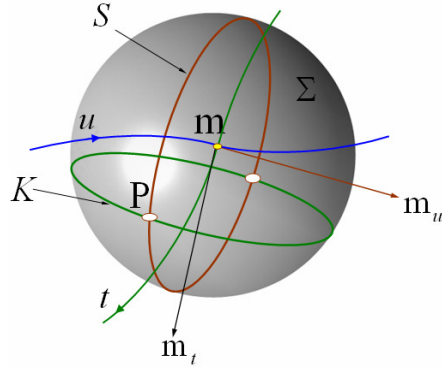


Figure 3.5: Intersecting the characteristic ( $K$ ) and the great ( $S$ ) circles

According to property (3.1) if a point  $P$  lies on the cutter envelope surface then  $P$  satisfies both circle equations i.e.  $P \in K \cap S$ . The relative positions of two circles  $K$  and  $S$  may be classified into three cases: (i) they intersect at two different points, (ii) they intersect at one point tangentially and (iii) they don't intersect (Fig. 3.6).

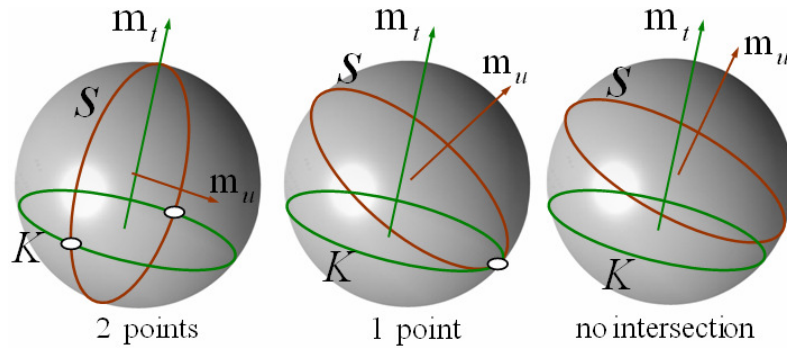


Figure 3.6: Intersection cases between  $K$  and  $S$ .

The common cutter geometries are defined by cylinder, frustum of a cone and torus surfaces. In the following subsections using those geometries which perform 5-axis motion the validity of property (3.1) will be analyzed. Also for these geometries the implicit envelope equations will be derived. Later in section (3.3) the methodology will be generalized for a surface of revolution. 5-axis tool motions are represented by the trajectory of the tool center point  $\mathbf{F}(u)$ , and the instantaneous orientation of the tool axis  $\mathbf{A}(u)$  which is always coincident with the

tool rotation axis. Using  $\mathbf{F}(u)$  and  $\mathbf{A}(u)$ , a Tool Coordinate System (*TCS*) on the tool can be defined by a set of mutually orthogonal unit vectors  $\mathbf{n}$ ,  $\mathbf{d}$ , and  $\mathbf{e}$  as

$$\mathbf{n} = \mathbf{A}, \quad \text{if } \left| \frac{\partial \mathbf{A}}{\partial u} \right| \neq 0 \text{ then } \mathbf{d} = \frac{\partial \mathbf{A} / \partial u}{|\partial \mathbf{A} / \partial u|} \text{ and } \mathbf{e} = \mathbf{d} \times \mathbf{n}$$

or

$$\text{if } \left| \frac{\partial \mathbf{A}}{\partial u} \right| = 0 \text{ and } \mathbf{A} \times \frac{\partial \mathbf{F}}{\partial u} \neq 0 \text{ then } \mathbf{e} = \frac{\mathbf{A} \times \frac{\partial \mathbf{F}}{\partial u}}{|\mathbf{A} \times \frac{\partial \mathbf{F}}{\partial u}|} \text{ and } \mathbf{d} = \mathbf{e} \times \mathbf{n}$$

(3.18)

According to Eq. (3.18) the position and the orientation of the cutter must be piecewise differentiable. And also plunging motion along the cutter rotational axis is not allowed.

### 3.2.1 Applying the Methodology on the Cylinder Surface

Fig. 3.7 illustrates a cylinder surface with a member of two-parameter-family of spheres which is also called *moving sphere*. In this figure  $\mathbf{F}$  and  $\mathbf{F}_u$  represent the tool center point which is defined at the tool bottom surface and the velocity vector at this point respectively.

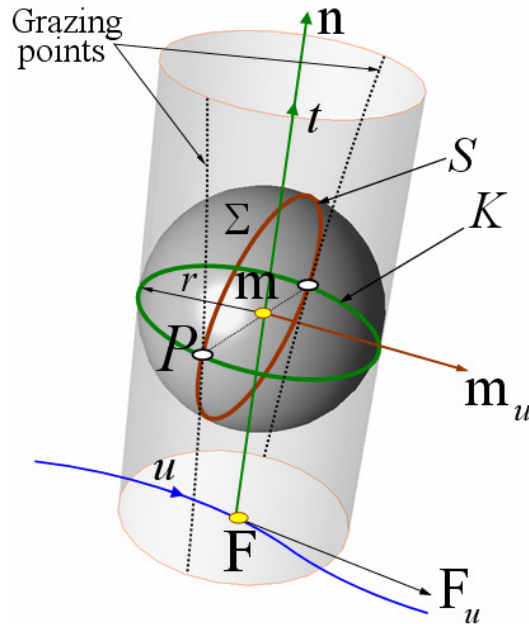


Figure 3.7: The moving sphere of a cylinder surface in 5-axis motion

The center of the moving sphere can be expressed by

$$\mathbf{m}(t, u) = \mathbf{F}(u) + t \mathbf{n}(u) \quad (3.19)$$

where  $\mathbf{n}$  is a function of the parameter  $u$ . After taking partial derivatives of  $\mathbf{m}$  with respect to parameters  $t$  and  $u$ , the following equations are obtained.

$$\mathbf{m}_t(t, u) = \mathbf{n}(u) \quad (3.20)$$

$$\mathbf{m}_u(t, u) = \mathbf{F}_u(u) + t \mathbf{n}_u(u) \quad (3.21)$$

where subscripts represent the corresponding derivatives. Because the cylinder surface is a pipe surface, the radius of the moving sphere is constant i.e.  $r(t) = r$  and thus  $r_t = 0$ . When  $\mathbf{m}$ ,  $\mathbf{m}_t$ ,  $\mathbf{m}_u$ ,  $r$  and  $r_t$  are substituted into Eqs. (3.13-3.15), they yields the following expanded versions respectively.

$$(P - \mathbf{F}(u)) \cdot (P - \mathbf{F}(u)) - 2t\{(P - \mathbf{F}(u)) \cdot \mathbf{n}(u)\} + t^2 - r^2 = 0 \quad (3.22)$$

$$(P - \mathbf{F}(t) - t \mathbf{n}(u)) \cdot \mathbf{n}(u) = 0 \quad (3.23)$$

$$(P - \mathbf{F}(u) - t \mathbf{n}(u)) \cdot (\mathbf{F}_u(u) + t \mathbf{n}_u(u)) = 0 \quad (3.24)$$

According to property (3.1) if a point  $P$  satisfies the system of Eqs. (3.22 – 3.24) then it lies at the intersection of the characteristic and the great circles. The characteristic circles ( $K$ ) are the solution of system of Eqs.(3.22) and (3.23), and the great circles ( $S$ ) are the solution of system of Eqs.(3.22) and (3.24). For solving this system of equations the parameter  $t$  from Eq.(3.23) is extracted as

$$t = (P - \mathbf{F}(u)) \cdot \mathbf{n}(u) \quad (3.25)$$

and then it is plugged into Eq.(3.22). This yields the following implicit representation of the cylinder surface in 3D Euclidian space

$$(P - \mathbf{F}(u)) \cdot (P - \mathbf{F}(u)) - \{(P - \mathbf{F}(u)) \cdot \mathbf{n}(u)\}^2 - r^2 = 0 \quad (3.26)$$



The tip of the cone can be expressed by (see Fig. 3.8)

$$\mathbf{V}(u) = \mathbf{F}(u) - \frac{r_b}{\tan \alpha} \mathbf{n}(u) \quad (3.29)$$

where  $r_b$  is the radius of lower base. Also from this figure, the center of the moving sphere can be obtained by

$$\mathbf{m}(t, u) = \mathbf{V}(u) + t \mathbf{n}(u) \quad (3.30)$$

The partial derivatives of  $\mathbf{m}$  with respect to  $t$  and  $u$  are derived as

$$\mathbf{m}_t(t, u) = \mathbf{n}(u) \quad (3.31)$$

$$\mathbf{m}_u(t, u) = \mathbf{V}_u(u) + t \mathbf{n}_u(u) \quad (3.32)$$

For the frustum of a cone surface the radius of the moving sphere linearly increases. This radius and its derivative can be expressed by  $r(t) = t \sin \alpha$  and  $r_t(t) = \sin \alpha$  respectively. By substitutions of  $\mathbf{m}$ ,  $\mathbf{m}_t$ ,  $\mathbf{m}_u$ ,  $r$  and  $r_t$ , the system of Eqs. (3.13-3.15) is expanded respectively as

$$(P - \mathbf{V}(u)) \cdot (P - \mathbf{V}(u)) - 2t\{(P - \mathbf{V}(u)) \cdot \mathbf{n}(u)\} + t^2 \cos^2 \alpha = 0 \quad (3.33)$$

$$(P - \mathbf{V}(u) - t \mathbf{n}(u)) \cdot \mathbf{n}(u) + t \sin^2 \alpha = 0 \quad (3.34)$$

$$(P - \mathbf{V}(u)) \cdot \mathbf{V}_u(u) - t \{\mathbf{V}_u(u) \cdot \mathbf{n}(u) - (P - \mathbf{V}(u)) \cdot \mathbf{n}_u(u)\} = 0 \quad (3.35)$$

For solving the system of Eqs. (3.33-3.35), the parameter  $t$  from Eq.(3.34) is extracted as

$$t = \frac{(P - \mathbf{V}(u)) \cdot \mathbf{n}(u)}{\cos^2 \alpha} \quad (3.36)$$

Substituting Eq. (3.36) into Eq. (3.33) yields the implicit representation  $f(x, y, z, u) = 0$  of the frustum of a cone surface in 3D Euclidian space

$$(P - \mathbf{V}(u)) \cdot (P - \mathbf{V}(u)) - (1 + \tan^2 \alpha) \{(P - \mathbf{V}(u)) \cdot \mathbf{n}(u)\}^2 = 0 \quad (3.37)$$



$$\mathbf{m}_t(t, u) = -R \sin t \mathbf{d}(u) + R \cos t \mathbf{e}(u) \quad (3.40)$$

$$\mathbf{m}_u(t, u) = \mathbf{F}_u(u) + R \cos t \mathbf{d}_u(u) + R \sin t \mathbf{e}_u(u) \quad (3.41)$$

Because the torus is a pipe surface the radius of the moving sphere is constant i.e.  $r(t) = r$  and thus  $r_t = 0$ . When  $\mathbf{m}$ ,  $\mathbf{m}_t$ ,  $\mathbf{m}_u$ ,  $r$  and  $r_t$  are plugged into Eqs. (3.13-3.15), the following expanded versions are obtained respectively.

$$(P - \mathbf{F}(u)) \cdot (P - \mathbf{F}(u)) - 2R \cos t (P - \mathbf{F}(u)) \cdot \mathbf{d} - 2R \sin t (P - \mathbf{F}(u)) \cdot \mathbf{e} + R^2 - r^2 = 0 \quad (3.42)$$

$$(P - \mathbf{F}(u) - R \cos t \mathbf{d} - R \sin t \mathbf{e}) \cdot (-R \sin t \mathbf{d} + R \cos t \mathbf{e}) = 0 \quad (3.43)$$

$$(P - \mathbf{F}(u) - R \cos t \mathbf{d} - R \sin t \mathbf{e}) \cdot (\mathbf{F}_u(u) + R \cos t \mathbf{d}_u + R \sin t \mathbf{e}_u) = 0 \quad (3.44)$$

Solving Eq.(3.43) for the parameter  $t$  yields the following two expressions

$$\cos t = \frac{(P - \mathbf{F}(u)) \cdot \mathbf{d}}{\sqrt{\{(P - \mathbf{F}(u)) \cdot \mathbf{d}\}^2 + \{(P - \mathbf{F}(u)) \cdot \mathbf{e}\}^2}} \quad (3.45)$$

$$\sin t = \frac{(P - \mathbf{F}(u)) \cdot \mathbf{e}}{\sqrt{\{(P - \mathbf{F}(u)) \cdot \mathbf{d}\}^2 + \{(P - \mathbf{F}(u)) \cdot \mathbf{e}\}^2}} \quad (3.46)$$

Plugging  $\cos t$  and  $\sin t$  into Eq. (3.42) yields the following implicit representation  $f(x, y, z, u) = 0$  of the toroidal surface in 3D Euclidian space.

$$(P - \mathbf{F}(u)) \cdot (P - \mathbf{F}(u)) + R^2 - r^2 = 2R \sqrt{\{(P - \mathbf{F}(u)) \cdot \mathbf{d}\}^2 + \{(P - \mathbf{F}(u)) \cdot \mathbf{e}\}^2} \quad (3.47)$$

The above equation can be arranged by squaring the both sides and this yields

$$\{(P - \mathbf{F}(u)) \cdot (P - \mathbf{F}(u)) + R^2 - r^2\}^2 - 4R^2 (\{(P - \mathbf{F}(u)) \cdot \mathbf{d}\}^2 + \{(P - \mathbf{F}(u)) \cdot \mathbf{e}\}^2) = 0 \quad (3.48)$$

For example when  $P = (x,y,z)$ ,  $\mathbf{F} = (0,0,0)$ ,  $\mathbf{d} = [1 \ 0 \ 0]^T$  and  $\mathbf{e} = [0 \ 1 \ 0]^T$  are plugged into the Eq. (3.48), the well known formula of a torus is obtained in the origin of the Euclidian space as follows

$$(x^2 + y^2 + z^2 + R^2 - r^2)^2 - 4R^2(x^2 + y^2) = 0$$

Also plugging  $\cos t$  and  $\sin t$  into Eq. (3.44) yields the following partial derivative  $\partial f(x, y, z, u) / \partial u = 0$  of the Eq. (3.47) with respect to  $u$ .

$$(P - \mathbf{F}(u)) \cdot \mathbf{F}_u(u) + 2R \frac{\partial}{\partial u} \left( \sqrt{\{(P - \mathbf{F}(u)) \cdot \mathbf{d}\}^2 + \{(P - \mathbf{F}(u)) \cdot \mathbf{e}\}^2} \right) = 0 \quad (3.49)$$

Thus the property (3.1) holds for the toroidal surface also.

### 3.3 Closed Form Swept Profile Equations

In section (3.1) a canal surface has been described explicitly by  $K(t, \theta)$ , where the parameter  $t$  represents the spine curve or the trajectory of the moving sphere center. Later in section (3.2), a methodology based on the two-parameter-family of spheres concept has been introduced. For describing the motion of the moving sphere, a new parameter  $u$  which represents a toolpath has been introduced. In this section by utilizing the two-parameter families of spheres, the closed form swept profile equations for the general surface of revolution will be derived. In general the radius  $R(t, u)$  and the center  $\mathbf{C}(t, u)$  of the characteristic circle are defined by the following equations.

$$R(t, u) = r(t) \frac{\sqrt{\|\mathbf{m}_t(t, u)\|^2 - r_t(t)^2}}{\|\mathbf{m}_t(t, u)\|} \quad (3.50)$$

$$\mathbf{C}(t, u) = \mathbf{m}(t, u) - r(t) r_t(t) \frac{\mathbf{m}_t(t, u)}{\|\mathbf{m}_t(t, u)\|^2} \quad (3.51)$$

where the center of the moving sphere  $\mathbf{m}(t, u)$  defined by two parameters. Note that these equations are very similar to those of canal surfaces defined in section (3.1.1), where the

center of the moving sphere is the function of  $t$ . A cutter surface considered as a set of the characteristic circles can be defined by using Eqs. (3.50) and (3.51) as

$$K(t, u, \theta) = \mathbf{C}(t, u) + R(t, u)(\cos \theta \mathbf{w}_1(t, u) + \sin \theta \mathbf{w}_2(t, u)) \quad (3.52)$$

where  $\theta \in [0, 2\pi]$ . In Eq. (3.52), two orthogonal unit vectors  $\mathbf{w}_1(t, u)$  and  $\mathbf{w}_2(t, u)$  define the plane of the characteristic circle  $K$ . In general the cutter geometries have either circular or linear spine curves. For example, the toroidal surface has a circular spine curve (Figure 3.10). In this case  $\mathbf{w}_1(t, u)$  and  $\mathbf{w}_2(t, u)$  represent respectively the normal  $\mathbf{M}(t, u)$  and bi-normal  $\mathbf{B}(t, u)$  unit vectors of the Frenet frame, i.e. the frame formed by the following three vectors

$$\mathbf{T}(t, u) = \frac{\frac{\partial \mathbf{m}(t, u)}{\partial t}}{\left\| \frac{\partial \mathbf{m}(t, u)}{\partial t} \right\|}, \quad \mathbf{M}(t, u) = \frac{\frac{\partial \mathbf{m}(t, u)}{\partial t} \times \frac{\partial^2 \mathbf{m}(t, u)}{\partial^2 t}}{\left\| \frac{\partial \mathbf{m}(t, u)}{\partial t} \times \frac{\partial^2 \mathbf{m}(t, u)}{\partial^2 t} \right\|}, \quad \mathbf{B}(t, u) = \mathbf{T}(t, u) \times \mathbf{M}(t, u) \quad (3.53)$$

where  $\mathbf{T}(t, u)$  is the tangent vector along the spine curve  $\mathbf{m}(t, u)$ .

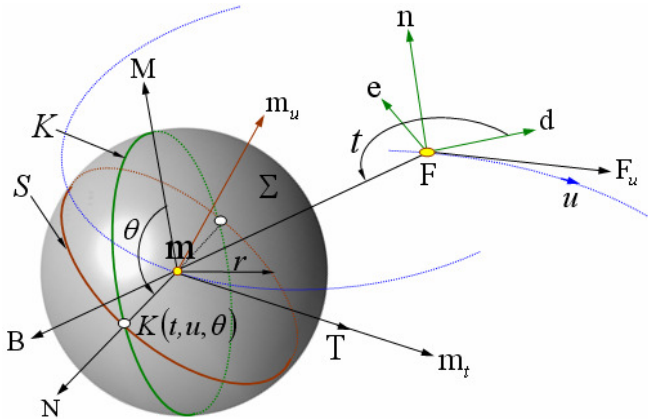


Figure 3.10: The characteristic circle  $K$  of the torus in the Frenet Frame

On the other hand, cylindrical and conical surfaces have linear spine curves (Figure 3.11). In this case the Frenet Frame components are not applicable for them because the curvature vanishes and the following condition does not hold



After replacing  $K$  with its equivalent from Eq. (3.52) and taking the dot product, Eq. (3.57) takes the following trigonometric form

$$A_2 \cos \theta + A_1 \sin \theta - A_0 = 0 \quad (3.58)$$

where

$$A_2 = R(t, u) (\mathbf{w}_1(t, u) \cdot \mathbf{m}_u(t, u))$$

$$A_1 = R(t, u) (\mathbf{w}_2(t, u) \cdot \mathbf{m}_u(t, u))$$

$$A_0 = \frac{r(t) r_t(t)}{\|\mathbf{m}_t(t, u)\|^2} (\mathbf{m}_t(t, u) \cdot \mathbf{m}_u(t, u))$$

Equation (3.58) can be written in the following form

$$\sqrt{A_1^2 + A_2^2} \sin(\theta + \beta) - A_0 = 0 \quad (3.59)$$

where  $\beta = \tan^{-1}(A_2, A_1)$ . Solving Eq. (3.59) for  $\theta$  yields

$$\begin{cases} \theta_1 = \sin^{-1}\left(\frac{A_0}{\sqrt{A_1^2 + A_2^2}}\right) - \beta \\ \theta_2 = \pi - \sin^{-1}\left(\frac{A_0}{\sqrt{A_1^2 + A_2^2}}\right) - \beta \end{cases}$$

Under the condition of  $A_1^2 + A_2^2 \geq A_0^2$ , the inverse function  $\sin^{-1}(x)$  is in the range of  $[-\pi/2, \pi/2]$ . In this case, there exist real solutions for  $\theta_{1,2}$  and the characteristic circle  $K$  contains one or two grazing points. Plugging  $\theta_{1,2}$  into Eq. (3.52) yields the closed form equation of the cutter envelope surface

$$K(t, u, \theta) = \mathbf{C}(t, u) + R(t, u)(\cos \theta_{1,2} \mathbf{w}_1(t, u) + \sin \theta_{1,2} \mathbf{w}_2(t, u)) \quad (3.60)$$

Note that, under the condition of  $A_1^2 + A_2^2 < A_0^2$ , the Eq. (3.58) does not have a real solution. When this is the case, certain cross sections of the cutter do not contain any grazing point (Figure 3.12).

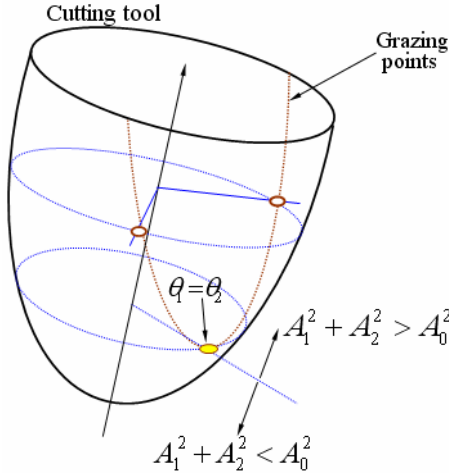


Figure 3.12: Limits of the grazing points in the general surface of revolution

As mentioned before in section (3.1.2) cylinder and torus surfaces are called *pipe surfaces*. By definition a pipe surface is an envelope of the family of spheres with a constant radius. In this surface type the centers of the characteristic circle and the moving sphere equal to each other. Eq. (3.14) which represents a plane with a normal direction vector  $\mathbf{m}_t$  contains an  $r_t$  term. For a pipe surface because the radius of the moving sphere  $r$  is constant, this term becomes equal to zero, i.e.  $r_t = 0$ . In this case the characteristic circle obtained by intersecting Eq. (3.13) and Eq.(3.14) becomes a great circle of the moving sphere, lying in the normal plane of the spine curve. Also this great circle is perpendicular to the vector  $\mathbf{m}_t$ . Thus a moving sphere of a pipe surface under a cutter motion contains two great circles: The first one which is perpendicular to vector  $\mathbf{m}_t$  represents the cutter surface geometry and the second one which is perpendicular to vector  $\mathbf{m}_u$  represents the tool motion. Both great circles share the same center  $\mathbf{m}$  along a spine curve (Figure 3.13)

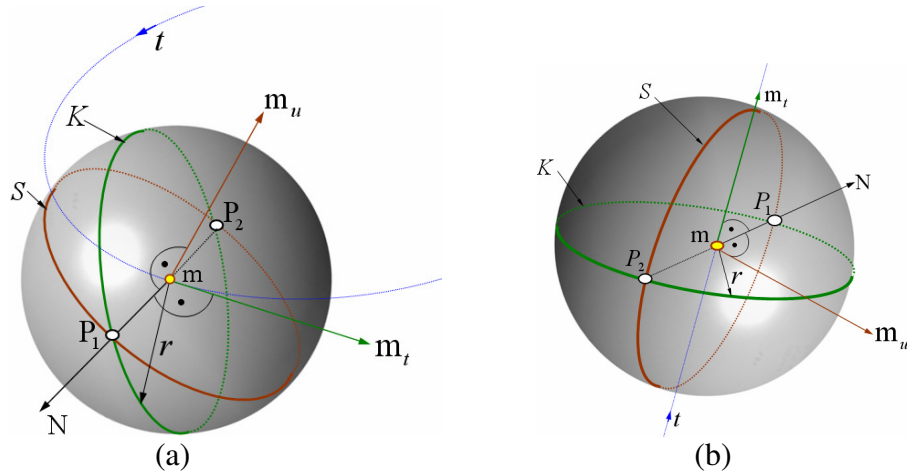


Figure 3.13: The characteristic circle  $K$  becomes a great circle in (a) torus, and in (b) cylinder surfaces

If a cutter geometry is a pipe surface, there is an alternative simpler solution for obtaining grazing points on the cutter envelope surface. The following property motivates this alternative solution for pipe surfaces.

**Property 3.2:** A surface normal vector of a moving sphere, generated by the vector product of  $\mathbf{m}_t$  and  $\mathbf{m}_u$ , passes through a grazing point on the envelope surface.

According to property (3.2), the normal vector of a moving sphere  $\mathbf{N}$  which passes through a grazing point  $P_1$  and the center of the moving sphere  $\mathbf{m}$ , is perpendicular to both  $\mathbf{m}_t$  and  $\mathbf{m}_u$  (Figure 3.13(a-b)). Thus  $\mathbf{N}$  can be expressed by the following equation.

$$\mathbf{N} = \mathbf{m}_t(t, u) \times \mathbf{m}_u(t, u) \quad (3.61)$$

Using equation (3.61), points  $P_1$  and  $P_2$  on the envelope surface can be calculated as

$$\begin{aligned} P_1 &= \mathbf{m}(t, u) + r \frac{\mathbf{N}}{\|\mathbf{N}\|}, \\ P_2 &= \mathbf{m}(t, u) - r \frac{\mathbf{N}}{\|\mathbf{N}\|} \end{aligned} \quad (3.62)$$

Note that the angle between two grazing points  $P_1$  and  $P_2$  is  $180^0$  for cutter geometries represented by pipe surfaces. A detailed proof of the property (3.2) is presented in Appendix A.1.

### 3.4 Examples

The presented methodology has been implemented using the ACIS solid modeling kernel. Figure 3.14 shows the envelope surfaces of Flat-End, Ball-End and Fillet-End cutters in 5-axis milling. For each illustration three cutter geometries are shown for the cutter locations: at the beginning, at the middle and at the end of the toolpath respectively. Also for these cutter locations their corresponding swept profiles curves colored by red are shown. In these figures cutter envelope surfaces are generated by the two-parameter-family of spheres. For the Flat-End and the Ball-End mills a member of this family is shown by a red sphere. On the other hand for the Fillet-End mill two spheres are shown, green sphere is for the torus part and the red sphere is for the cylinder part respectively. For these examples a single toolpath segment is used. In another example a Taper-Ball-End mill is performing 5-axis tool motions (Figure 3.15). The cutter envelope surfaces are shown from different point of views. In this case the toolpath contains a number of segments.

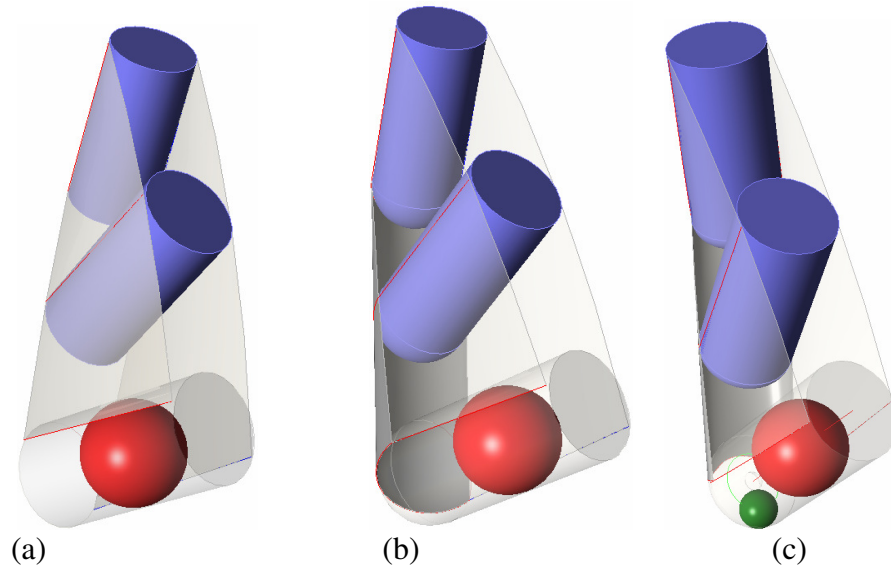


Figure 3.14: Envelopes surfaces of (a) Flat-End, (b) Ball-End, and (c) Fillet-End cutters.

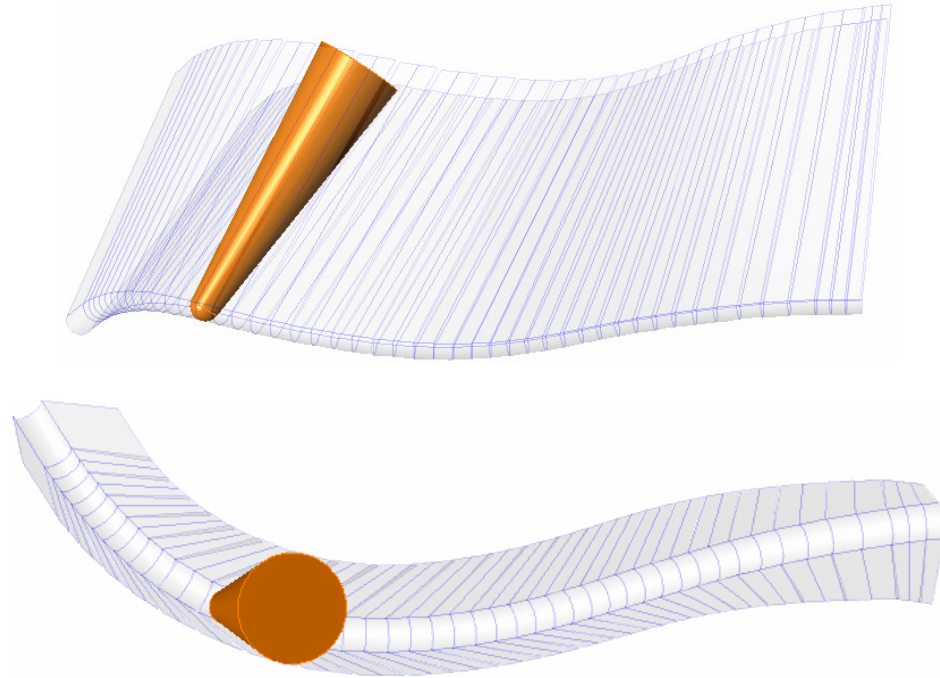


Figure 3.15: Envelope surfaces of a Taper-Ball-End mill from different points of view in 5-axis milling

### 3.5 Discussion

A typical NC toolpath may contain thousands of tool motions which make the computational cost for characterizing the geometry of each tool swept volume prohibitively expensive. In this chapter an analytical approach for determining the shape of the swept envelopes generated by a general surface of revolution has been presented. The cutter geometries have been modeled as canal surfaces generated by the one-parameter family of spheres. For modeling the 5-axis tool motions a new parameter has been introduced for the center of the moving sphere. For describing the cutter envelope surfaces the *two-parameter-family of spheres* has been introduced. Analytically it has been proven for a general surface of revolution that any point on the envelope surface also belongs to a member from the two-parameter-family of spheres. In this methodology describing the radius function and the spine curve of the moving sphere different cutter surfaces can be obtained. From this sense the methodology is independent of any particular cutter geometry. The implementation of the methodology is simple, especially if the cutter geometries are pipe surfaces such as torus and circular cylinder fewer calculations are used. Although the examples from the application of

the methodology are shown for the common milling geometries described by 7-parameter APT like cutters [46], the developed methodology can be applied to rare cutter geometries also (Figure 3.16). Later in the next chapter it will be shown that using the methodology developed in this chapter brings computational efficiency to the update process of in-process workpieces represented by discrete vectors. The spherical surface has not been considered in developments because simply the swept profile of a sphere is the great circle which is passing through the center of the sphere and having a normal along the direction of the motion. Self intersections in this research have not been considered. Modifications to the methodology will need to be developed for this special case.

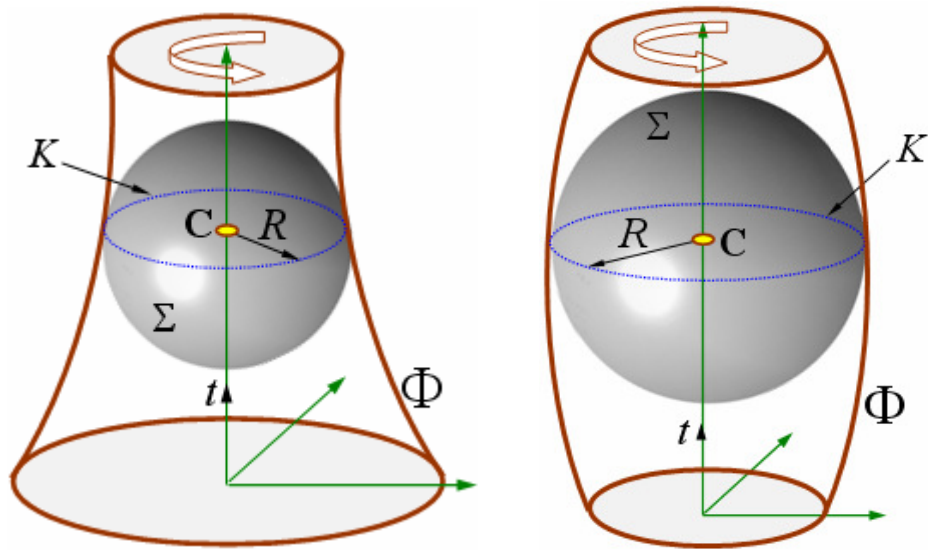


Figure 3.16: Different cutter geometries generated by a moving sphere

## Chapter 4

### In-process Workpiece Modeling

In this chapter the methodologies for modeling the in-process workpiece in milling operations are presented. During the machining simulation for each tool movement the modification of the workpiece geometry is required to keep track of the material removal process. Because the NC verification and Cutter Workpiece Engagement (*CWE*) extraction are directly dependent on the material removal an accurate in-process workpiece modeling is needed. Several choices for modeling the in-process work piece are exist. The two most common are mathematically accurate solid modeling that is used in CAD systems and approximate modeling such as those used in computer graphics: faceted and discrete vector models. In the workpiece update process first the swept volume of a given tool movement in the cutter location data file is modeled and then this volume is subtracted from the in-process workpiece. For updating the workpiece surfaces represented by the solid or faceted models third party softwares can be used. For example in the solid modeler based approach the cutter swept volumes can be generated by using the ACIS solid modeling kernel and then using the Boolean subtraction operation defined in this kernel the cutter swept volumes are subtracted from the in-process workpiece. These update methodologies are briefly introduced in this chapter. On the other hand for the workpiece geometries represented by discrete vectors efficient in-process workpiece update methodologies for different cutter geometries performing multi-axis machining are needed. In the literature [7,8,18,24,32,41,91] the discrete vectors have orientations along the z-axis of the standard bases of  $\mathbb{R}^3$ . But when the in-process workpiece has features like vertical walls and sharp edges, representing the workpiece with one directional vectors generates less accurate results in visualization of the final product [43] and *CWE* extractions. For increasing the accuracy more vectors with different orientations are needed. But in this case localizing the cutter envelope during the simulation becomes difficult and therefore the computational time increases. Therefore an efficient localization methodology is required. Also in recent works [7,8] the tool axis has a fixed orientation along the z-axis of the standard bases of  $\mathbb{R}^3$  and the workpiece updates are performed numerically for the milling cutter geometries. Therefore in this chapter the vector

based update methodologies are developed for the vectors having different orientations. These methodologies allow multi-axis milling in which the tool may have an arbitrary orientation in space. Also for the cutter geometries defined by a circular cylinder, frustum of a cone, sphere and plane the updating calculations are performed analytically. For the torus geometry numerical approaches with guaranteed root finding results are utilized.

The common milling cutter geometries are presented in section (4.2.1). In these representations cutter surfaces are defined parametrically at the origin of the standard bases of  $\mathbb{R}^3$ . In this section for derivations the properties of canal surfaces given in chapter (3) are utilized. The vector based workpiece model and the localization of the cutter envelope are presented in section (4.2.2). In the first part of this section a workpiece modeling strategy is introduced and in the second part a localization methodology for the cutter envelope surfaces is presented. The workpiece update methodologies in multi-axis milling for different cutter geometries are presented in section (4.2.3). In the introduction part of this section the general formulas for defining the cutter envelopes are derived and then in the following subsections these formulas are utilized in the intersection calculations of different cutter geometries. Examples from the implementation of the methodologies are shown in section (4.2.4), and finally the chapter ends with the discussion in section (4.3).

#### **4.1 Modeling the In-process Workpiece in Solid and Facetted representation**

A solid modeler based in-process workpiece update is illustrated in Figure (4.1). Inputs from a CAD/CAM system include the geometric representation of the initial workpiece, the tool path and the geometric description of the cutting tool. In the first step, the swept volumes of the cutting tool are generated for a given tool path. Then in the second step these swept volumes are subtracted from the initial workpiece sequentially for obtaining the updated workpiece (*in-process workpiece*). In this research for modeling the in-process workpiece and the swept volume the B-rep based geometric modeler ACIS kernel and C++ is utilized.

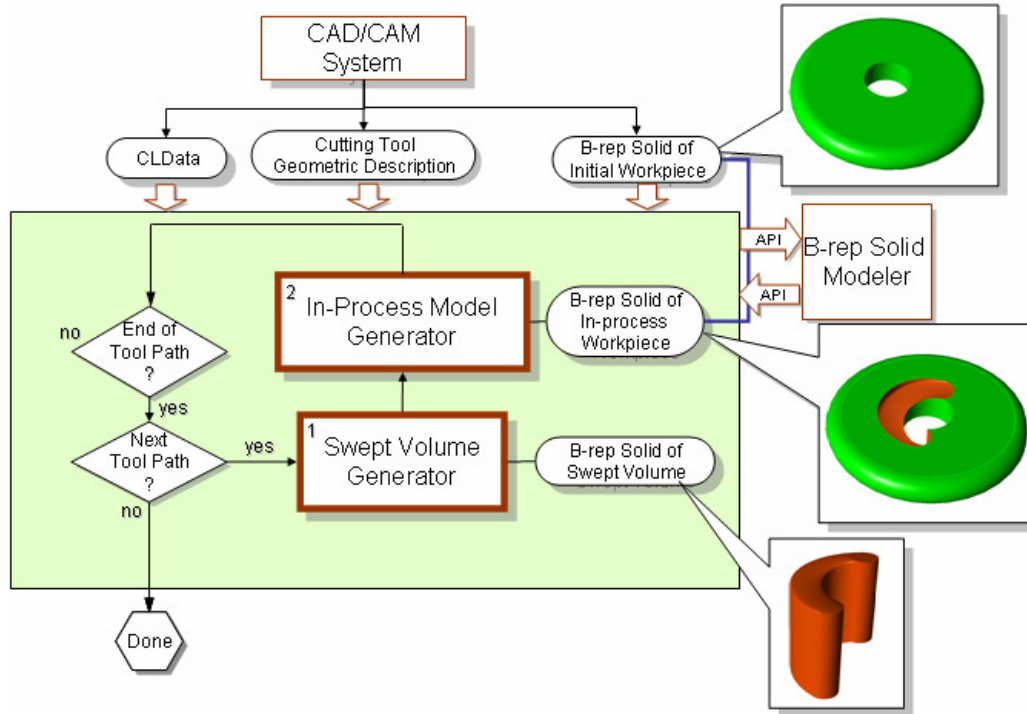


Figure 4.1: A B-rep Solid Modeler based in-process workpiece update.

In this research for updating the in-process workpiece represented by tessellated models a prototype system is assembled using existing commercial software applications and C++ implementations. This system is shown in (Figure4.2). The cutter swept volume is generated by the ACIS solid modeler and then this swept volume is exported as a STL format using ACIS functions. A Boolean intersection between this swept volume and the current in-process workpiece is performed using the polyhedral modeling Boolean operators implemented in a commercial application, Magics X [51]. This prototype system creates STL model of the in-process workpiece.

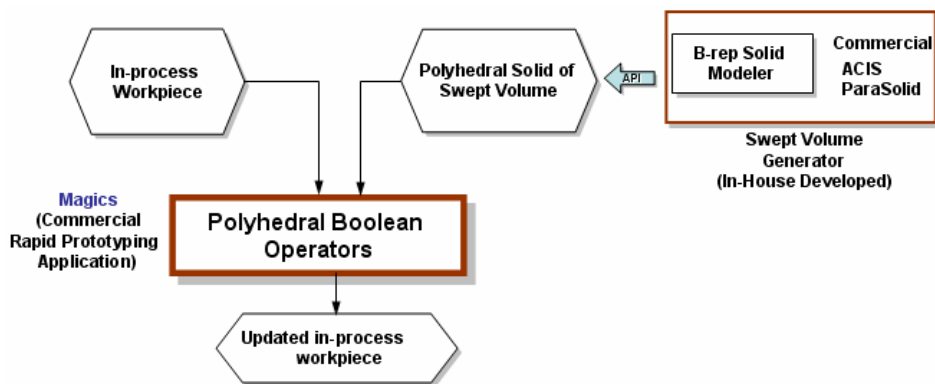


Figure 4.2: A Polyhedral Modeler based in-process workpiece update.

## 4.2 Modeling the In-process Workpiece in Vector Based Representation

In this section the multi-axis milling update methodologies are developed for workpieces defined by discrete vectors with different orientations. For simplifying the intersection calculations between discrete vectors and the tool envelope the properties of canal surfaces are utilized.

### 4.2.1 Milling Cutter Geometries in Parametric Form

The methodologies for updating the in-process workpiece represented by discrete vectors are developed for cutters with natural quadrics and toroidal surfaces. Natural quadrics consist of the sphere, circular cylinders and the cone. Together with the plane (a degenerate quadric) and torus these constitute the surface geometries found on the majority of cutters used in milling. In this chapter the major cutter geometries (circular cylinder, frustum of a cone and torus) are defined parametrically by using the properties of the canal surfaces defined in chapter (3). The parametric representation of a canal surface generated by a one-parameter families of spheres is given by the characteristic circle as

$$K(t, \theta) = \mathbf{C}(t) + R(t)(\cos \theta \mathbf{w}_1(t) + \sin \theta \mathbf{w}_2(t)) \quad (4.1)$$

where  $\theta \in [0, 2\pi]$ .  $\mathbf{C}(t)$  and  $R(t)$  represent the center and radius of the characteristic circle respectively and they are expressed as follows

$$\mathbf{C}(t) = \mathbf{m}(t) - r(t) r'(t) \frac{\mathbf{m}'(t)}{\|\mathbf{m}'(t)\|^2} \quad \text{and} \quad (4.2)$$

$$R(t) = r(t) \frac{\sqrt{\|\mathbf{m}'(t)\|^2 - r'(t)^2}}{\|\mathbf{m}'(t)\|} \quad (4.3)$$

where for  $t \in \mathbb{R}$ ,  $\mathbf{m}(t)$  and  $r(t)$  are the center of the moving sphere and the radius function respectively. The center  $\mathbf{m}(t)$  is located on the spine curve (the trajectory of the moving sphere). Also in Eq. (4.1) two orthogonal unit vectors  $\mathbf{w}_1(t)$  and  $\mathbf{w}_2(t)$  define the plane of the characteristic circle  $K(t, \theta)$ . Figure (4.3) illustrates the major cutter geometries as canal

surfaces with respect to the standard basis of  $\mathbb{R}^3$  denoted by  $(\mathbf{i}, \mathbf{j}, \mathbf{k})$  unit vectors and the origin  $\mathbf{O}$ . In this figure the cutter geometries have either circular or linear spine curves. If they have linear spine curves (See Figure 4.3,a-b)  $\mathbf{w}_1(t)$  and  $\mathbf{w}_2(t)$  represent the x and y axis of the local coordinate system respectively. On the other hand if they have a circular spine curve (see Figure 4.3 -c)  $\mathbf{w}_1(t)$  and  $\mathbf{w}_2(t)$  represent respectively the normal  $\mathbf{M}(t)$  and bi-normal  $\mathbf{B}(t)$  unit vectors of the Frenet frame, i.e. the frame formed by the following three vectors

$$\mathbf{T}(t) = \frac{\mathbf{m}'(t)}{\|\mathbf{m}'(t)\|}, \quad \mathbf{M}(t) = \frac{\mathbf{m}'(t) \times \mathbf{m}''(t)}{\|\mathbf{m}'(t) \times \mathbf{m}''(t)\|}, \quad \mathbf{B}(t) = \mathbf{T}(t) \times \mathbf{M}(t) \quad (4.4)$$

where  $\mathbf{T}(t)$  is the unit tangent vector in the direction of  $\mathbf{m}'(t)$ . It is assumed in Eq. (4.4) that the spine curve represented by  $\mathbf{m}(t)$  is biregular, in other words along  $\mathbf{m}(t)$  the following condition is fulfilled

$$\mathbf{m}'(t) \times \mathbf{m}''(t) \neq 0 \quad (4.5)$$

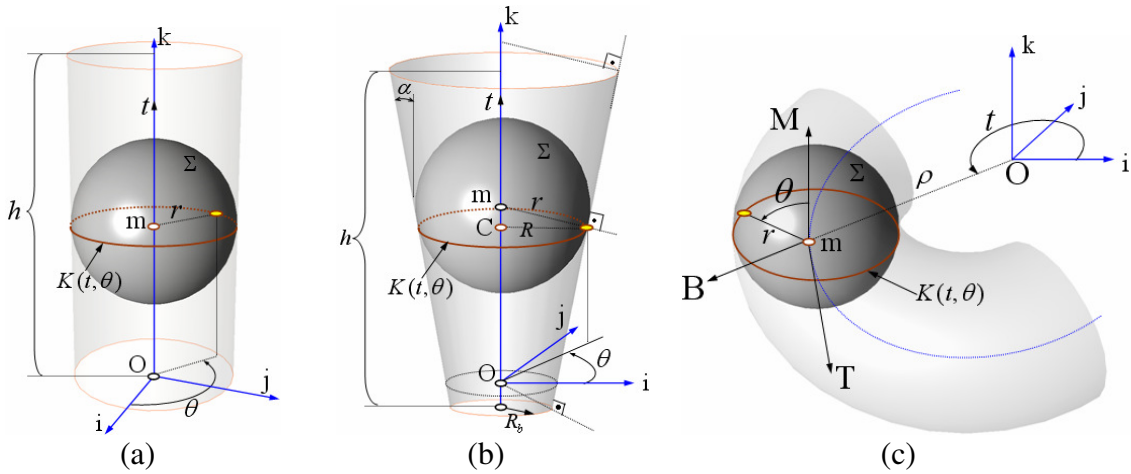


Figure 4.3: Cutter geometries as canal surfaces: (a) cylinder, (b) frustum of a cone and (c) torus).

In the following sub sections the parametric representations of the surface geometries shown in Figure (4.3) are found by using the Eqs. (4.1-4.5). Later in section (4.2.3) they will be used for updating the in-process workpiece.

#### 4.2.1.1 Cylinder Surface

The cylinder surface can be parameterized by using the characteristic circle given in Eq.(4.1). Two of the variables in this equation  $\mathbf{C}(t)$  and  $R(t)$  depend on the center and the radius function of a moving sphere. From Figure (4.3 -a), the center of a one-parameter family of spheres can be written as

$$\mathbf{m}(t) = t \mathbf{k} = \begin{bmatrix} 0 \\ 0 \\ t \end{bmatrix} \quad (4.6)$$

where the parameter  $t$  takes values between zero and the height of the cylinder, i.e.  $t \in [0, h]$ . The partial derivative of the Eq. (4.6) with respect to  $t$  equals to the unit vector  $\mathbf{k}$  and thus  $\|\mathbf{m}'(t)\| = 1$ . As explained in chapter (3), the cylinder surface is also a pipe surface with a constant radius  $r$ . Therefore the derivative of the radius function is equal to zero i.e.  $r'(t) = 0$ . Thus the center and the radius of the characteristic circle can be represented by  $\mathbf{C}(t) = t\mathbf{k}$  and  $R(t) = r$  respectively. Plugging the center and the radius into Eq. (4.1) yields the cylinder surface geometry in the following parametric form

$$K_{cylinder}(t, \theta) = t \mathbf{k} + r (\cos \theta \mathbf{i} + \sin \theta \mathbf{j}) = \begin{bmatrix} r \cos \theta \\ r \sin \theta \\ t \end{bmatrix} \quad (4.7)$$

#### 4.2.1.2 Frustum of a Cone Surface

As illustrated in Figure (4.3 -b), the origin of the standard basis  $\mathbf{O}$  is located above the cutter bottom center with distance equal to  $R_b \tan \alpha$ , where  $R_b$  and  $\alpha$  represent the radius of the cutter bottom and the cone half-angle respectively. The center of a moving sphere is obtained by  $\mathbf{m}(t) = t \mathbf{k}$ , where the limits of  $t$  from Figure (4.3-b) are defined by

$$t \in \left[ 0, \frac{h}{\cos^2 \alpha} \right] \quad (4.8)$$

where  $h$  represents the height. For the frustum of a cone surface the radius of a moving sphere  $r(t)$  is given by

$$r(t) = t \sin \alpha + \frac{R_b}{\cos \alpha} \quad (4.9)$$

When  $\mathbf{m}(t)$ ,  $r(t)$  and their derivatives with respect to  $t$  are plugged into Eqs.(4.2) and (4.3), the center and the radius of the characteristic circle is obtained as follows

$$\mathbf{C}(t) = (t \cos^2 \alpha - R_b \tan \alpha) \mathbf{k} \quad (4.10-a)$$

$$R(t) = t \sin \alpha \cos \alpha + R_b \quad (4.10-b)$$

Plugging Eqs.(4.10-a,b) into Eq. (4.1) yields the frustum of a cone surface geometry in the following parametric form

$$\begin{aligned} K_{frustum}(t, \theta) &= (t \cos^2 \alpha - R_b \tan \alpha) \mathbf{k} + (t \sin \alpha \cos \alpha + R_b) (\cos \theta \mathbf{i} + \sin \theta \mathbf{j}) \\ &= \begin{bmatrix} (t \sin \alpha \cos \alpha + R_b) \cos \theta \\ (t \sin \alpha \cos \alpha + R_b) \sin \theta \\ (t \cos^2 \alpha - R_b \tan \alpha) \end{bmatrix} \end{aligned} \quad (4.11)$$

#### 4.2.1.3 Torus Surface

In Figure (4.3-c) a torus surface is shown with the origin  $\mathbf{O}$  in the center of the torus. For a torus the spine curve is a circle and therefore the center of a moving sphere is obtained by

$$\mathbf{m}(t) = \rho \cos t \mathbf{i} + \rho \sin t \mathbf{j} = \begin{bmatrix} \rho \cos t \\ \rho \sin t \\ 0 \end{bmatrix} \quad (4.12)$$

where  $\rho$  is the major radius of the torus and  $t \in [0, 2\pi]$ . The partial derivative of Eq. (4.12) with respect to  $t$  is obtained as follows

$$\mathbf{m}'(t) = -\rho \sin t \mathbf{i} + \rho \cos t \mathbf{j} \quad (4.13)$$

As a pipe surface torus has a constant radius  $r$  and therefore  $r'(t) = 0$ . When  $\mathbf{m}(t)$ ,  $\mathbf{m}'(t)$ ,  $r(t)$  and  $r'(t)$  are plugged into Eqs.(4.2) and (4.3), the center and the radius of the characteristic circle are obtained as follows

$$\mathbf{C}(t) = \rho \cos t \mathbf{i} + \rho \sin t \mathbf{j} \quad (4.14-a)$$

$$R(t) = r \quad (4.14-b)$$

Also for describing the characteristic circle of the torus the components of the Frenet frame are needed. For this purpose the partial derivative of Eq.(4.13) with respect to  $t$  is obtained as follows

$$\mathbf{m}''(t) = -R \cos t \mathbf{i} - R \sin t \mathbf{j} \quad (4.15)$$

Plugging  $\mathbf{m}(t)$ ,  $\mathbf{m}'(t)$  and  $\mathbf{m}''(t)$  into Eq. (4.4) yields

$$\mathbf{T}(t) = -\sin t \mathbf{i} + \cos t \mathbf{j}, \quad \mathbf{M}(t) = \mathbf{k}, \quad \mathbf{B}(t) = \cos t \mathbf{i} + \sin t \mathbf{j} \quad (4.16)$$

Finally plugging Eqs. (4.14-a,b) and (4.16) into Eq. (4.1) yields torus surface geometry in the following parametric form

$$\begin{aligned} K_{torus}(t, \theta) &= \rho \cos t \mathbf{i} + \rho \sin t \mathbf{j} + r (\cos \theta \mathbf{k} + \sin \theta (\cos t \mathbf{i} + \sin t \mathbf{j})) \\ &= \begin{bmatrix} (\rho + r \sin \theta) \cos t \\ (\rho + r \sin \theta) \sin t \\ r \cos \theta \end{bmatrix} \end{aligned} \quad (4.17)$$

#### 4.2.2 Workpiece Model and Localization

There are two main approaches for representing the in-process workpiece using discrete vectors [43]: *Discrete Normal Vector* and *Discrete Vertical Vector* approaches. In the

*Discrete Normal Vector* approach (Figure 4.4 -a) a workpiece is made up of discrete vectors whose directions are the surface normals of the workpiece. In this representation all directions are not necessarily identical. Also spacing may vary depending upon the surface local properties. On the other hand, in the *Discrete Vertical Vector* approach (Figure 4.4-b) all discrete vectors of the workpiece model lie in only one direction regardless of surface normal directions, where the directions are along the vertical z-axis of the standard basis of  $\mathbb{R}^3$ .

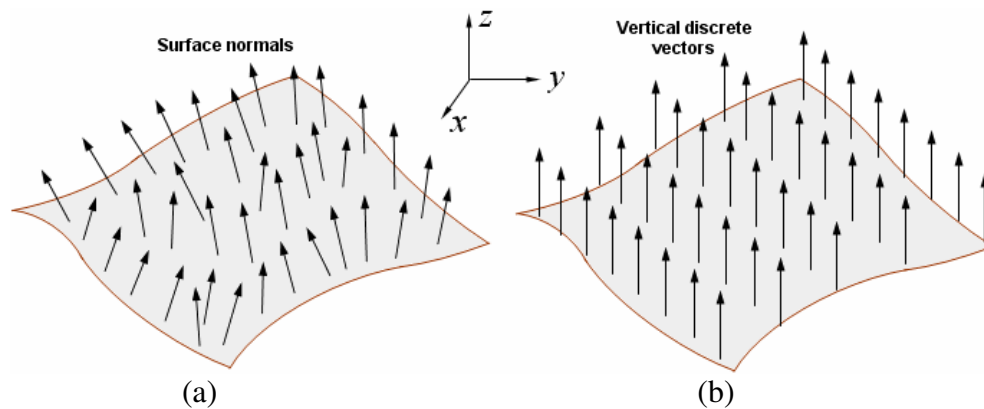


Figure 4.4: Representing the workpiece surfaces by (a) surface normal vectors and (b) vertical vectors.

The workpiece model can have vertical walls and sharp edges (Figure 4.5). The *Discrete Normal Vector* approach can represent those surface features well with respect to a given tolerance. But because in this approach the directions of discrete vectors are not identical, localizing the cutter envelope surface during the machining simulation becomes difficult and therefore the computational time increases. During the machining simulation the most time consuming process is the localization of the cutter envelope [43]. Although the *Discrete Vertical Vector* approach gives less accurate results in the representation of the vertical walls and the sharp edges, it is computationally faster and the localization of the cutter envelope is easy.

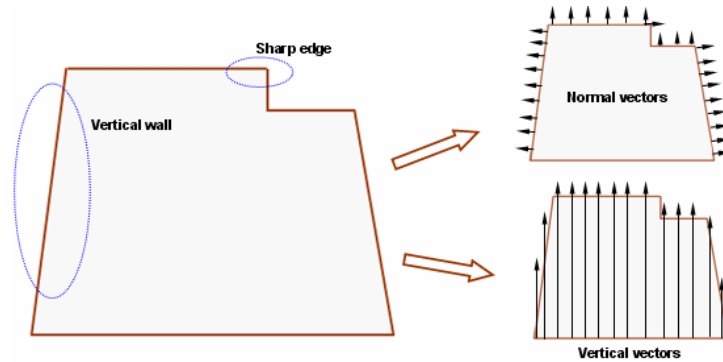


Figure 4.5: Representing the feature shapes in Discrete Normal vector and discrete vertical vector approaches.

For some workpiece geometries 3-axis machining is not suitable for updating the surfaces. For example, if the part is deep (Figure 4.6-a) a 3-axis tool path is not sufficient enough for finishing. Nor can they be used for milling hard material with long cutters without generating a bad surface finish and long machining times. For solving this problem the spindle of the cutter is tilted and a shorter cutting tool is used (Figure 4.6-b). This type of the machining is called as (3+2)-axis milling in which a cutter can have an arbitrary fixed orientation in space. In this thesis the discrete vector update methodologies are developed for (3+2)-axis milling. Also this methodology can be adapted to 5-Axis milling with some approximations.

Figure 4.6 has been removed due to copyright restrictions. The information removed is the (a) 3-Axis machining, and (b) (3+2) - Axis machining [36].

In this research the workpiece is modeled by discrete vectors having orientations in the directions of  $x, y, z$ -axes of the standard basis of  $\mathbb{R}^3$ . Therefore this representation can be seen as an enhanced version of the *Discrete Vertical Vector* approach. In this representation more vectors in different directions are used and thus, especially when the workpiece has features like vertical walls and sharp edges, the quality in the visualization of the final product and *CWE* area is increased. Also the localization advantage of the *Discrete Vertical Vector* approach is preserved. In machining simulations the initial workpiece geometry is mostly represented by a rectangular stock. The modeling this stock with discrete vectors is easy because for a given direction all discrete vectors have the same height and the same

orientation. But on the other hand if the initial workpiece surfaces have arbitrary shapes then some steps must be taken for representing the initial workpiece using discrete vectors. In this research the workpiece is initially represented by a tessellated (triangular facets) model. For transforming this tessellated model into a discrete vector model first the Axis Aligned Bounding Box (AABB) of the initial workpiece model is obtained (Figure 4.7-a). For this purpose the maximum and minimum x,y,z coordinates of the facets are used. The AABB is a rectangular six-sided box (in 3D, four sided in 2D) categorized by having its faces oriented in such a way that its face normals are at all times parallel with the axes of  $\mathbb{R}^3$ . Then from the faces represented by Oxy, Oxz and Oyz coordinate systems (see figure 4.7-b) rays are shot through the tessellated model in the directions of the z, y and x - axes of  $\mathbb{R}^3$  respectively. For finding the portions of the rays which represent the workpiece, triangle/ ray intersections are performed. If a ray is made up of several sub lines then using the linked list data structure these lines are connected to each other. Also later during the machining simulation if a line is partitioned into smaller lines again the linked list data structure is used for connecting them. Note that for localization purposes (it will be explained later) the discrete vectors are located in the buckets.

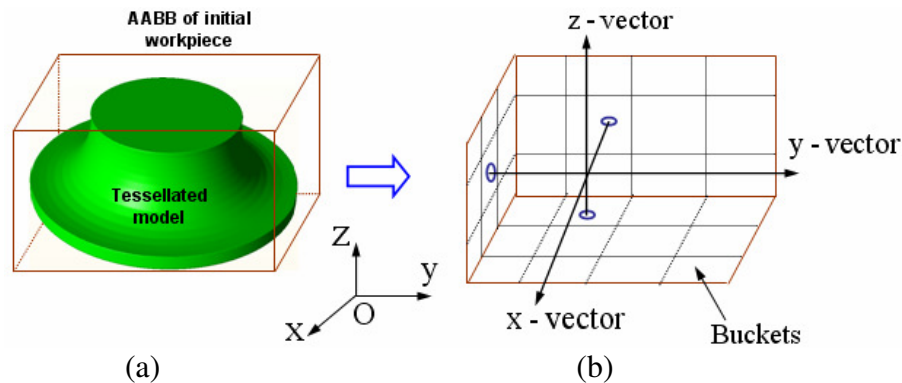


Figure 4.7: Representing initial workpiece with discrete vectors located in XY, XZ and YZ planes

For updating the in-process workpiece the discrete vectors are intersected with the tool envelope. It would be computationally expensive to calculate the intersections of all the discrete vectors for each tool movement. It is therefore desirable to localize the calculations by eliminating from consideration the vectors which have no possibility of intersecting the tool envelope for the given toolpath segment. In this research for localizing the cutter envelope during the simulation the bounding box concept is utilized. There are several types

of bounding boxes in 2D space such as a circle, Axis Aligned Bounding Box (AABB), Oriented Bounding Box (OBB), convex hull etc. There is always a tradeoff between a better bound and a faster test in these approaches. For this research the AABB approach in 2D space is utilized. The best feature of the AABB is its fast overlap check, which simply involves direct comparison of individual coordinate values. In this work for a given tool movement three AABBs which are the projections of the tool envelope on to  $Oxy$ ,  $Oxz$  and  $Oyz$  coordinate systems are generated. In the following section the steps for obtaining the AABB of the tool envelope in  $Oxy$  coordinate system are given. The AABBs in  $Oxz$  and  $Oyz$  coordinate systems can be obtained following the same steps. The localization of the tool envelope in  $Oxy$  coordinate system has four steps. For these steps please refer to Figure (4.8). In this figure a Taper-Ball-End mill is moving between the cutter locations  $P_S$  and  $P_E$ .

**Step 1: Finding the bounding cylinder in 3D:** In this step at the cutter location point  $P_S$  the bounding cylinder of the cutter having an orientation in the direction of the tool axis is found. The dimensions of the bounding cylinder are defined by the height and the largest radius of the cutter. For example for the Taper-Ball-End mill shown in (Figure 4.8) the top circle ( $c_{top}$ ) has the largest radius  $r$ . Therefore using the same radius  $r$  the bottom circle ( $c_{bottom}$ ) of the bounding cylinder can be obtained. The center of the  $c_{bottom}$  is located at the tool tip point of the cutter. There is a symmetry plane which contains the tool rotation axis and passes through the centers of the  $c_{top}$  and  $c_{bottom}$ . The normal vector of this plane ( $\mathbf{N}_{plane}$ ) can be obtained by  $\mathbf{N}_{plane} = \mathbf{n} \times [0 \ 0 \ 1]$ . Intersecting this plane with  $c_{top}$  and  $c_{bottom}$  of the bounding cylinder generates four points  $\mathbf{I}_1$ ,  $\mathbf{I}_2$ ,  $\mathbf{I}_3$ , and  $\mathbf{I}_4$  respectively in 3D space.

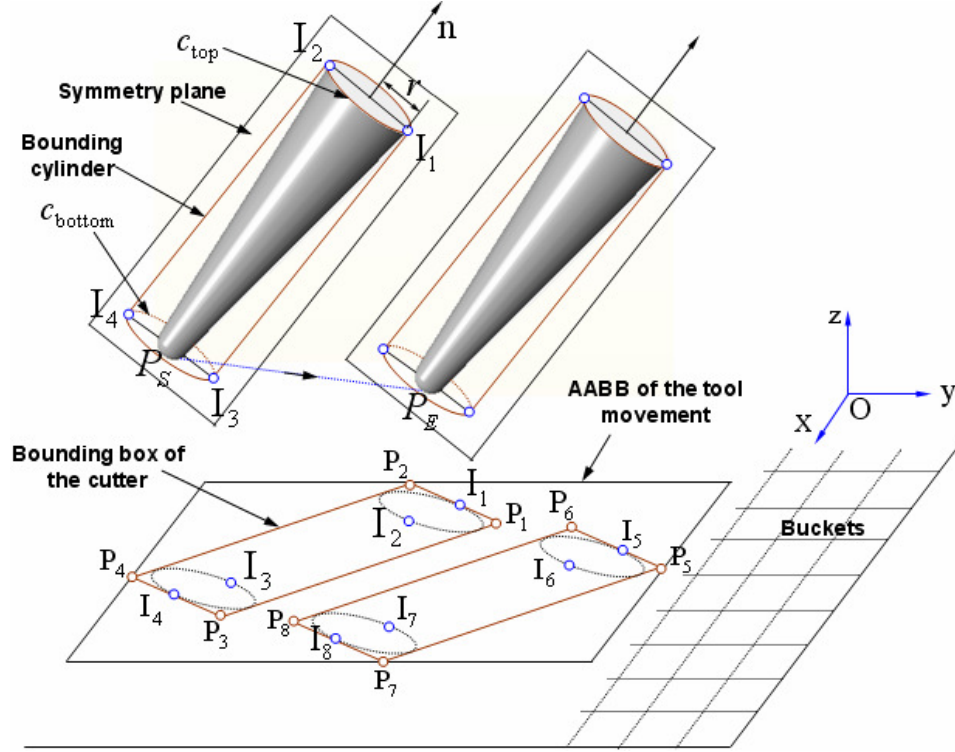


Figure 4.8: AABB of a tool movement in Oxy coordinate system.

**Step 2: Finding the bounding box of the cutter in 2D:** Assuming  $I_1$  and  $I_4$  are the outermost points, two circles  $c_{top}$  and  $c_{bottom}$  and those four intersection points are projected onto Oxy coordinate system. This projection generates the bounding box of the cutter which has the corner points  $P_1$ ,  $P_2$ ,  $P_3$ , and  $P_4$ . These corner points can be calculated by

$$\begin{aligned}
 \mathbf{P}_1 &= \mathbf{I}_1 + r \begin{bmatrix} n_y / \sqrt{n_x^2 + n_y^2} \\ -n_x / \sqrt{n_x^2 + n_y^2} \\ 0 \end{bmatrix} & \mathbf{P}_2 &= \mathbf{I}_1 - r \begin{bmatrix} n_y / \sqrt{n_x^2 + n_y^2} \\ -n_x / \sqrt{n_x^2 + n_y^2} \\ 0 \end{bmatrix} \\
 \mathbf{P}_3 &= \mathbf{I}_4 + r \begin{bmatrix} n_y / \sqrt{n_x^2 + n_y^2} \\ -n_x / \sqrt{n_x^2 + n_y^2} \\ 0 \end{bmatrix} & \mathbf{P}_4 &= \mathbf{I}_4 - r \begin{bmatrix} n_y / \sqrt{n_x^2 + n_y^2} \\ -n_x / \sqrt{n_x^2 + n_y^2} \\ 0 \end{bmatrix}
 \end{aligned} \tag{4.18}$$

where  $n_x$  and  $n_y$  are the components of the tool rotation axis vector  $\mathbf{n}$ .

**Step 3: Finding the AABB of the tool movement:** In this stage first using the same steps (1 and 2) the bounding box of the cutter for the location of  $P_E$  is found. Now there are two bounding boxes with eight corner points in Oxy coordinate system. Then using the minimum and maximum  $x$  and  $y$  coordinates of those eight corner points ( $\mathbf{P}_1$  to  $\mathbf{P}_8$ ) the AABB of the tool movement is obtained. Note that because the tool performs a motion with a constant orientation, the projections of the intermediate tool motions between  $P_S$  and  $P_E$  are also contained in the same AABB of the tool movement.

**Step 4: Finding the set of buckets:** In this step the overlap check is performed between the buckets and the AABB of the tool movement. The buckets in Oxy coordinate system can be thought as AABBs. For finding the overlapping buckets the AABB – AABB intersection is performed. The algorithm for this test can be found in [27]. If an overlap is found then the discrete vectors in the overlapping bucket are used for the intersection test for updating the in-process workpiece. Thus only a small percentage of all the discrete vectors are examined for each tool movement. The intersections will be shown in the next section for different cutter geometries.

### 4.2.3 Updating In-process Workpiece in Multi-Axis Milling

In this section the in-process workpiece surfaces are updated by using different milling cutters. Although in section (4.2.2) the discrete vectors have orientations along the  $x$ ,  $y$  and  $z$ -axes of the standard basis of  $\mathbb{R}^3$ , in this section the update formulas will be derived for the general case in which the discrete vectors have arbitrary orientations. Also for the calculations (3+2)-axis milling in which a cutter can have an arbitrary fixed orientation in space is considered.

In multi-axis milling tool motions are represented by the trajectory of the tool control point  $\mathbf{F}(u)$  and the instantaneous orientation of the tool axis  $\mathbf{A}(u)$  which is always coincident with the tool rotation axis, where  $u \in [0,1]$ . In section (4.2.1) the major cutter geometries are parametrically defined with respect to the standard basis of  $\mathbb{R}^3$  which has an origin at  $\mathbf{O}$ . In this section the control points of these geometries are defined with respect to the location which corresponds to  $\mathbf{O}$ . For example the location of the control point for the cylindrical surface is at the bottom radial center, for the frustum of a cone surface it is above the bottom radial center with distance equals to  $R_b \tan \alpha$  and for the toroidal surface it is at the center of

the torus. A complex toolpath can be considered as the combination of line segments, where each segment represents the linear distance between two consecutive cutter location points. For a linear tool path (line segment) the control point can be expressed with respect to the tool path start  $P_S(x_S, y_S, z_S)$  and end  $P_E(x_E, y_E, z_E)$  coordinates as follows

$$\mathbf{F}(u) = P_S + (P_E - P_S) u \quad (4.19)$$

where the difference of  $(P_E - P_S)$  is called as the instantaneous feed direction denoted by  $\mathbf{f}$ . Note that for the (3+2)-axis machining the instantaneous tool orientation  $\mathbf{A}(u)$  is fixed between the tool locations  $P_S$  and  $P_E$ . Two sets of coordinate systems are used in this paper. A *Work Piece Coordinate System (WCS)* which is coincident with the standard basis of  $\mathbb{R}^3$  denoted by unit vectors  $[\mathbf{i} \ \mathbf{j} \ \mathbf{k}]$ , and a local *Tool Coordinate System (TCS)* denoted by unit vectors  $[\mathbf{d} \ \mathbf{e} \ \mathbf{n}]$ . Using  $\mathbf{F}$  and  $\mathbf{A}$ , one can define *TCS* on the tool defined by a set of mutually orthogonal unit vectors  $\mathbf{n}$ ,  $\mathbf{d}$ , and  $\mathbf{e}$ . The *TCS* is defined as

$$\mathbf{n} = [n_x \ n_y \ n_z] = \mathbf{A} / |\mathbf{A}| \quad (4.20)$$

$$\text{if } \mathbf{A} \times \frac{\partial \mathbf{F}}{\partial u} \neq 0 \text{ then } \mathbf{e} = [e_x \ e_y \ e_z] = \frac{\mathbf{A} \times \frac{\partial \mathbf{F}}{\partial u}}{|\mathbf{A} \times \frac{\partial \mathbf{F}}{\partial u}|} \text{ and } \mathbf{d} = [d_x \ d_y \ d_z] = \mathbf{e} \times \mathbf{n}$$

According to above definitions it is not allowed for the cutter to plunge along its rotational axis  $\mathbf{A}(u)$ . Also it is assumed that the  $\mathbf{d}$  axis of the *TCS* is aligned with the instantaneous feed direction. In this work the discrete vectors which represent the workpiece are defined by

$$I(v) = I_a + (I_b - I_a) v \quad (4.21)$$

where  $v \in [0, 1]$  and also  $I_a(x_a, y_a, z_a)$  and  $I_b(x_b, y_b, z_b)$  are the start and end points of a vector respectively. If the cutter surfaces parameterized in section (4.2.1) move with respect to *TCS* a point on the cutter surface can be described in *WCS* as follows

$$G_M(t, \theta, u) = \mathbf{F}(u) + [\mathbf{d} \ \mathbf{e} \ \mathbf{n}] K_M(t, \theta) \quad (4.22)$$

where the subscript  $M$  represents the cutter surface type i.e. *cylinder*, *frustum* and *torus*. When a cutter moves along a toolpath three types of surfaces are generated: The ingress surface  $G_M^-(t, \theta, u)$  at  $u = 0$ , the intermediate portion (also called as the envelope surface)  $G_M^0(t, \theta, u)$  at  $0 < u < 1$  and the egress surface  $G_M^+(t, \theta, u)$  at  $u = 1$  (see Figure 4.9). Updating the in-process workpiece at the start and end of the toolpath segment is easy, for this purpose the discrete vectors are intersected with the tool geometry at  $P_S$  and  $P_E$  respectively. In the following sub sections the formulas will be developed for updating the in-process workpiece in the intermediate portion  $G_M^0(t, \theta, 0 < u < 1)$ .

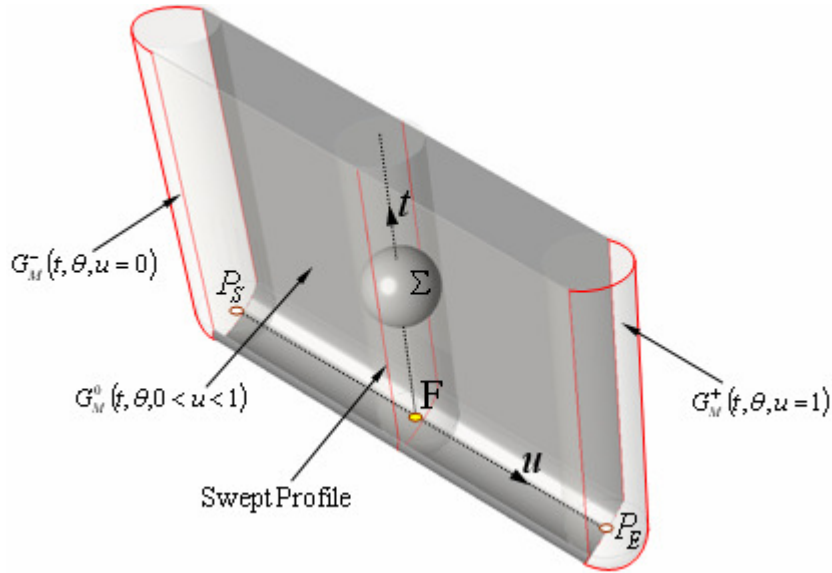


Figure 4.9: Decomposing the swept surface into three regions

Cutter surface geometries given in section (4.2.1) are canal surfaces and therefore their surface normal  $\mathbf{N}$  can be represented in the  $WCS$  as follows

$$\mathbf{N}(t, \theta, u) = G_M(t, \theta, u) - \mathbf{m}(t, u) \quad (4.23)$$

where  $\mathbf{m}(t, u)$  is the center of a moving sphere which is defined in the  $WCS$  as follows

$$\mathbf{m}(t, u) = \mathbf{F}(u) + [\mathbf{d} \ \mathbf{e} \ \mathbf{n}] \mathbf{m}(t) \quad (4.24)$$

A point on the envelope surface is embedded in  $G_M(t, \theta, u)$  and also the surface normal ( $\mathbf{N}$ ) passing through it is perpendicular to the velocity vector at the center of the moving sphere. In (3+2)-axis milling with linear toolpath the velocity vector is equal to the feed direction vector ( $\mathbf{f}$ ). Therefore for an arbitrary point on the envelope surface the following dot product equation holds

$$G_M^0(t, \theta, u) = \mathbf{N}(t, \theta, u) \cdot \mathbf{f} = 0 \quad (4.25)$$

Plugging Eq. (4.23) into the above equation yields

$$(G_M(t, \theta, u) - \mathbf{m}(t, u)) \cdot \mathbf{f} = 0 \quad (4.26)$$

The above equation is solved for  $\theta$  with respect to the given values of parameters  $u$  and  $t$ . There are three possible solutions for  $\theta$ : two distinct real solutions  $\theta_{1,2}$ , two equal real solutions  $\theta_1 = \theta_2$ , and no real solution. Plugging the values of  $\theta$  into Eq. (4.22) yields the locations of the points on the envelope surface

$$G_M(t, \theta_{1,2}, u) = P_{1,2} = \mathbf{F}(u) + [\mathbf{d} \ \mathbf{e} \ \mathbf{n}] K_M(t, \theta_{1,2}) \quad (4.27)$$

where  $P_{1,2}$  represents two points which correspond to  $\theta_{1,2}$  respectively. As explained in chapter (3), the circular cylinder and torus are pipe surfaces. By definition a *pipe surface* is described as an envelope of the family of the spheres with a constant radius. The spine curve (also called as trajectory) of a moving sphere is a line for the cylinder and a circle for the torus. It has been proven in chapter (3) that for the circular cylinder and torus surfaces there is an alternative solution in finding the location of an arbitrary point on the envelope surface. In this alternative solution the normal vector passing through a point on the envelope surface can be obtained by

$$\mathbf{N}(t, u) = \frac{\partial \mathbf{m}(t, u)}{\partial u} \times \frac{\partial \mathbf{m}(t, u)}{\partial t} \quad (4.28)$$

Then using the above equation the coordinates of an arbitrary point on the envelope surface with respect to the given values of  $u$  and  $t$  are found by

$$P_{1,2} = \mathbf{m}(t, u) \mp r \frac{\mathbf{N}(t, u)}{\|\mathbf{N}(t, u)\|} \quad (4.29)$$

where  $r$  is the radius of the moving sphere. In Eq. (4.29) the signs ( $\mp$ ) indicates that there are two opposite points on the cutter envelope surface with an angular difference equals to  $180^\circ$ . The formulas developed in this section will be used in the following sub sections for different cutter geometries.

#### 4.2.3.1 Updating with Flat-End mill

A Flat-End mill is made up of a cylindrical surface at the side and a flat surface at the bottom. Depending on the feed vector direction the cylindrical and flat surfaces engage with the workpiece within  $[0, \pi]$  and  $[0, 2\pi]$  angular ranges respectively. In the following two subsections the analytical formulas will be derived for these surfaces.

##### Cylindrical surface

As explained before the circular cylinder is a pipe surface and a location of a point on the envelope surface can be found with either Eq. (4.27) or Eq. (4.29). Because of its simplicity the Eq. (4.29) will be used in derivations. The center of the moving sphere for the cylindrical surface can be obtained by plugging Eqs. (4.6) and (4.19) into Eq. (4.24)

$$\mathbf{m}(t, u) = P_S + (P_E - P_S)u + [\mathbf{d} \ \mathbf{e} \ \mathbf{n}] \begin{bmatrix} 0 \\ 0 \\ t \end{bmatrix} \quad (4.30)$$

For finding the normal vector defined in Eq. (4.28) the partial derivatives of Eq. (4.30) with respect to  $u$  and  $t$  are taken as follows

$$\frac{\partial \mathbf{m}(t,u)}{\partial u} = (P_E - P_S) = \mathbf{f}, \quad \frac{\partial \mathbf{m}(t,u)}{\partial t} = \mathbf{n} \quad (4.31)$$

Plugging Eqs. (4.30) and (4.31) into Eq.(4.29) yields the coordinates of points on the cylinder envelope surface as follows

$$P_{1,2} = (P_S \mp r \mathbf{e}) + u \mathbf{f} + t \mathbf{n} \quad (4.32)$$

When the values of  $t \in [0, h]$  and  $u \in [0, 1]$  are substituted into Eq. (4.32) two planar envelope surfaces denoted by  $G_{cylinder}^0$  are generated (see Figure 4.10). These surfaces spanned by two linearly independent vectors  $\mathbf{f}$  and  $\mathbf{n}$  have their origins at the locations  $P_S + r \mathbf{e}$  and  $P_S - r \mathbf{e}$ . The feed ( $\mathbf{f}$ ) and tool axis ( $\mathbf{n}$ ) vectors are linearly independent because according to *TCS* definition given in Eq. (4.20) the cutter does not have a plunging motion along its rotational axis. Therefore the directions of these two vectors are not opposite.

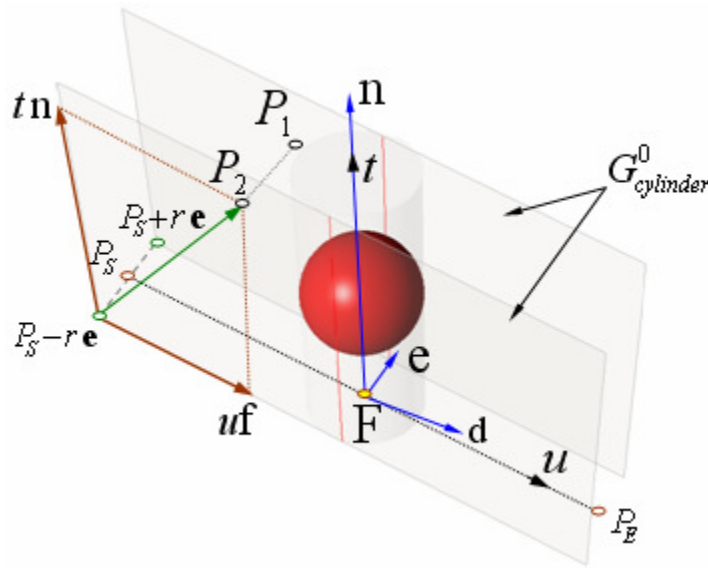


Figure 4.10: Envelope surfaces generated by the cylindrical part of a Flat-End mill

A point at which a vector intersects the envelopes ( $G_{cylinder}^0$ ) is described by setting the vector line  $I(v)$  given in Eq. (4.21) equals to  $P_{1,2}$  given in Eq. (4.32). Thus this yields a linear system of three equations in three variables  $t, u$  and  $v$  as follows

$$I_a + (I_b - I_a) v = (P_S \mp r e) + u f + t n \quad (4.33)$$

The Eq. (4.33) can be written in a matrix forms as

$$\begin{bmatrix} u \\ v \\ t \end{bmatrix} = B^{-1} A \quad (4.34)$$

where

$$A = \begin{bmatrix} x_a - x_S \mp r e_x \\ y_a - y_S \mp r e_y \\ z_a - z_S \mp r e_z \end{bmatrix}_{3 \times 1}, \quad B = \begin{bmatrix} x_E - x_S & n_x & x_a - x_b \\ y_E - y_S & n_y & y_a - y_b \\ z_E - z_S & n_z & z_a - z_b \end{bmatrix}_{3 \times 3}$$

There are three possible intersection cases between an envelope plane and a vector: no intersection, vector intersects in one point and vector lies in the plane. All these cases are illustrated in Figure (4.11 -a,b,c).

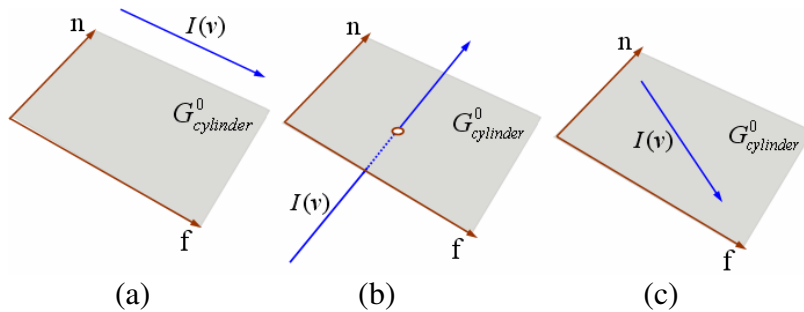


Figure 4.11: Possible intersections between a vector and envelope plane: (a) no intersection, (b) one intersection, and (c) vector lies in the plane.

If the vector is parallel to the envelope plane or if it lies in the envelope plane then the columns of the matrix  $B$  will be linearly dependant. In this case because the matrix  $B$

becomes singular there will be no real solution for Eq. (4.34). If the vector intersects the envelope planes (see Figure 4.12), the real parameter values  $u_{1,2}$ ,  $v_{1,2}$  and  $t_{1,2}$  are obtained from Eq. (4.34). If these parameter values satisfy the ranges defined by  $t \in [0, h]$ ,  $u \in [0, 1]$  and  $v \in [0, 1]$  then the vector is updated.

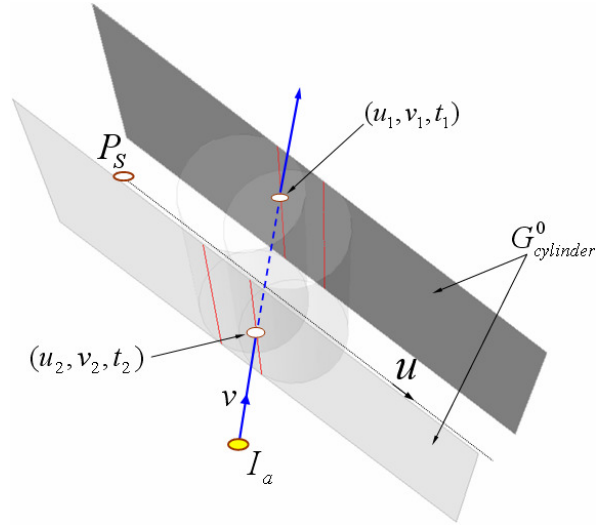


Figure 4.12: Parameter sets for updating the discrete vector

### **Bottom-Flat surface**

Figure (4.13) illustrates the Bottom-Flat surface of a Flat-End mill. This surface (also it can be thought as a disc) is enclosed by a circle defined in *WCS*. Because a disc is not a canal surface, in this section a different approach is used for the derivations. The parametric representation for a circle of radius  $R$  centered at  $\mathbf{F}(u)$  is given by

$$P(u, t) = \mathbf{F}(u) + R \cos t \mathbf{d} + R \sin t \mathbf{e} \quad (4.35)$$

where  $t \in [0, 2\pi]$ ,  $\mathbf{d} = [d_x \ d_y \ d_z]$  and  $\mathbf{e} = [e_x \ e_y \ e_z]$  are two orthogonal unit vectors of the *TCS* which define the plane of the circle.

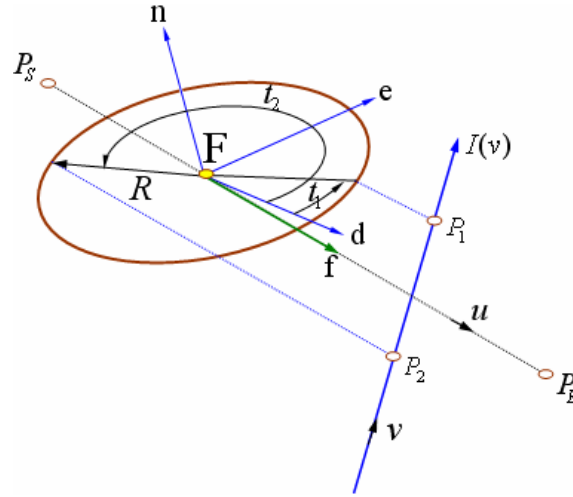


Figure 4.13: Intersecting the Bottom-Flat surface with a discrete vector.

A point at which a vector intersects the Bottom-Flat surface is described by setting the line  $I(v)$  from Eq.(4.21) equals to  $P(u,t)$  given in Eq. (4.35). Thus this yields a nonlinear system of three equations in three variables  $u$ ,  $t$  and  $v$  as follows

$$x_a + (x_b - x_a) v = x_s + (x_E - x_s) u + R \cos t d_x + R \sin t e_x \quad (4.36-a)$$

$$y_a + (y_b - y_a) v = y_s + (y_E - y_s) u + R \cos t d_y + R \sin t e_y \quad (4.36-b)$$

$$z_a + (z_b - z_a) v = z_s + (z_E - z_s) u + R \cos t d_z + R \sin t e_z \quad (4.36-c)$$

For the general solution of this system, first the equivalent of the variable  $v$  from Eq. (4.36-b) is substituted into Eqs.(4.36-a) and (4.36-c) respectively. Thus two nonlinear equations with variables  $u$  and  $t$  are obtained. Then the equivalent of  $u$  from one of these two equations is plugged into another for eliminating  $u$ . Therefore the final nonlinear equation only depends on the variable  $t$  and it can be solved *analytically*. But as explained in section (4.2.2), because of the localization approach adopted the workpiece is represented by discrete vectors having orientations in the directions of  $x,y,z$ -axes of the standard basis of  $\mathbb{R}^3$ . In this section the formulas are derived for the discrete vectors having orientations in the direction of the  $z$ -axis of  $\mathbb{R}^3$ . For the  $x$  and  $y$  directions similar steps can be applied. Having orientations along the  $z$ -axis of  $\mathbb{R}^3$  eliminates  $v$  from Eqs. (4.36-a) and (4.36-b). Further for eliminating  $u$  the

equivalent of  $u$  from Eq. (4.36-a) is plugged into Eq. (4.36-b) and this yields the following equation with variable  $t$

$$A \cos t + B \sin t - C = 0 \quad (4.37)$$

where the constant coefficients are given by

$$A = R \left( (y_E - y_S) d_x - (x_E - x_S) d_y \right)$$

$$B = R \left( (y_E - y_S) e_x - (x_E - x_S) e_y \right)$$

$$C = (x_E - x_S) (y_S - y_a) + (y_E - y_S) (x_a - x_S)$$

Eq. (4.37) can be written in the following form

$$\sqrt{A^2 + B^2} \sin(t + \beta) - C = 0 \quad (4.38)$$

where  $\beta = \tan^{-1}(A, B)$ . Solving Eq. (4.38) for  $t$  yields

$$\left\{ \begin{array}{l} t_1 = \sin^{-1} \left( \frac{C}{\sqrt{A^2 + B^2}} \right) - \beta \\ t_2 = \pi - \sin^{-1} \left( \frac{C}{\sqrt{A^2 + B^2}} \right) - \beta \end{array} \right. \quad (4.39)$$

If in Eq. (4.39)  $A^2 + B^2 \geq C^2$  then the inverse function  $\sin^{-1}(\cdot)$  is in the range of  $[-\pi/2, \pi/2]$ . In this case, there exist real solutions  $t_{1,2}$ . For updating the discrete vector the values of  $u$  and  $v$  must be checked also. Therefore  $t_{1,2}$  are plugged into Eq. (4.36-a) for obtaining  $u$  values. Later the values of  $t$  and  $u$  are plugged into Eq. (4.36-c) and this yields the values of  $v$ . If the parameter values are in the ranges defined by  $u \in [0,1]$  and  $v \in [0,1]$ , then the vector is updated. Also note that when the Bottom-Flat surface moves along a linear tool path, an elliptical cylinder is generated (plunging or horizontal motions are excluded). In Figure (4.14) three possible intersection cases between this cylinder and a vector are illustrated for a given tool path defined between  $P_S$  and  $P_E$ .

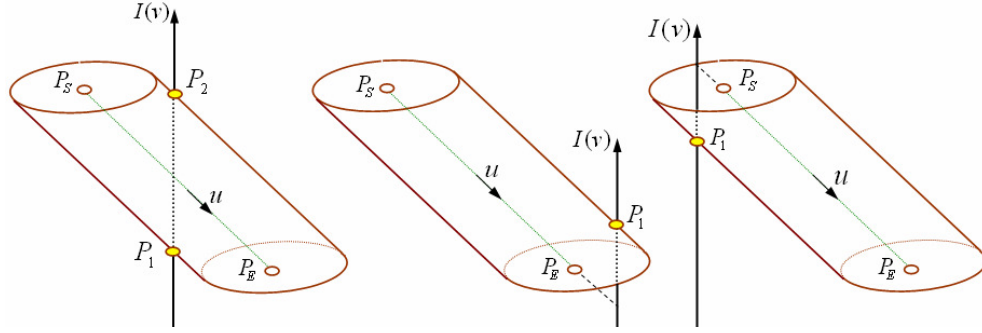


Figure 4.14: Intersection cases between the Bottom-Flat surface and a discrete vector

#### 4.2.3.2 Updating with Tapered-Flat-End Mill

A Tapered-Flat-End mill is made up of a frustum of a cone surface at the side and a flat surface at the bottom. With respect to the feed vector both surfaces engage with the workpiece within  $[0, 2\pi]$  angular ranges. In this section the analytical formulas for updating the in-process workpiece are derived for the frustum of a cone surface. The formulas for the bottom flat part can be used from section (4.2.3.1). When Eq. (4.11) is plugged into Eq. (4.22) the frustum of a cone surface in *WCS* is obtained as follows

$$G_{frustum}(t, \theta, u) = \mathbf{F}(u) + [\mathbf{d} \ \mathbf{e} \ \mathbf{n}] \begin{bmatrix} (t \sin \alpha \cos \alpha + R_b) \cos \theta \\ (t \sin \alpha \cos \alpha + R_b) \sin \theta \\ (t \cos^2 \alpha - R_b \tan \alpha) \end{bmatrix} \quad (4.40)$$

For finding the center of a moving sphere in *WCS*,  $\mathbf{m}(t) = t \mathbf{k}$  from section (4.2.1.2) is plugged into Eq. (4.24) and this yields

$$\mathbf{m}(t, u) = \mathbf{F}(u) + [\mathbf{d} \ \mathbf{e} \ \mathbf{n}] \begin{bmatrix} 0 \\ 0 \\ t \end{bmatrix} \quad (4.41)$$

The locations of arbitrary points on the envelope surfaces generated by the frustum of a cone are obtained by Eq. (4.27). For this purpose it is needed to calculate  $\theta_{1,2}$  for the given parameter values of  $u$  and  $t$ . Eqs (4.40) and (4.41) are plugged into Eq. (4.26) and this yields

$$(t \sin \alpha \cos \alpha + R_b) \cos \theta (\mathbf{d} \cdot \mathbf{f}) - (t \sin^2 \alpha + R_b \tan \alpha) (\mathbf{n} \cdot \mathbf{f}) = 0 \quad (4.42)$$

Notice that  $\mathbf{e} \cdot \mathbf{f} = 0$ . When the Eq.(4.42) is solved for  $\theta$  the following equation is obtained

$$\theta_{1,2} = \mp \cos^{-1} \left( \tan \alpha \left( \frac{\mathbf{n} \cdot \mathbf{f}}{\mathbf{d} \cdot \mathbf{f}} \right) \right) \quad (4.43)$$

Plugging Eqs.(4.43), (4.11) and (4.19) into Eq.(4.27) yields the following envelope surface equation for the frustum of a cone

$$\begin{aligned} G_{frustum}(t, \theta_{1,2}, u) = & P_S + (P_E - P_S) u + (t \sin \alpha \cos \alpha + R_b) \cos \theta_{1,2} \mathbf{d} \\ & + (t \sin \alpha \cos \alpha + R_b) \sin \theta_{1,2} \mathbf{e} + (t \cos^2 \alpha - R_b \tan \alpha) \mathbf{n} \end{aligned} \quad (4.44)$$

The above equation can be rearranged as follows

$$G_{frustum}(t, \theta_{1,2}, u) = \mathbf{O}_{1,2} + u \mathbf{f} + k \mathbf{S}_{1,2} \quad (4.45)$$

where

$$\mathbf{O}_{1,2} = P_S + R_b \cos \theta_{1,2} \mathbf{d} + R_b \sin \theta_{1,2} \mathbf{e} - R_b \tan \alpha \mathbf{n}$$

$$\mathbf{S}_{1,2} = \sin \alpha \cos \theta_{1,2} \mathbf{d} + \sin \alpha \sin \theta_{1,2} \mathbf{e} + \cos \alpha \mathbf{n}$$

$$k = t \cos \alpha$$

When the values of  $t \in [0, h / \cos^2 \alpha]$  and  $u \in [0, 1]$  are substituted into Eq. (4.45) two planar envelope surfaces are generated (see Figure 4.15). These envelope surfaces spanned by linearly independent vectors  $\mathbf{f}$  and  $\mathbf{S}_{1,2}$  have origins at  $\mathbf{O}_{1,2}$ .

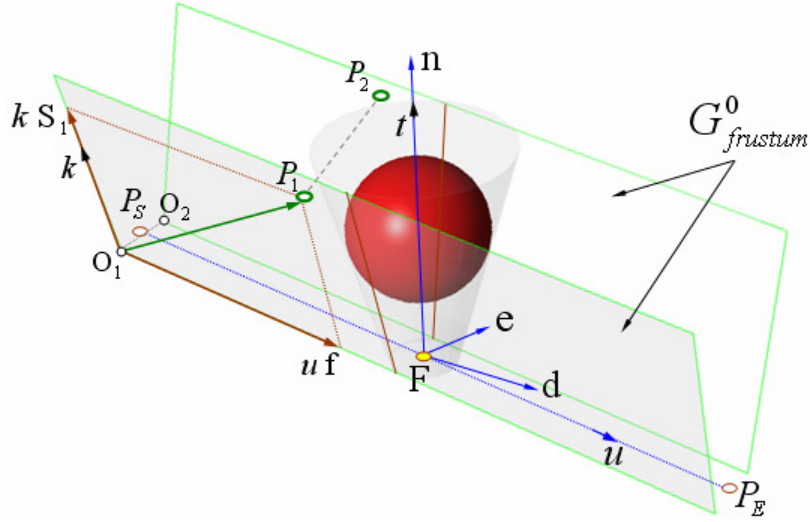


Figure 4.15: Envelope surfaces generated by the frustum of a cone part.

By setting a vector line  $I(v)$  from Eq.(4.21) equal to  $G_{frustum}(t, \theta_{1,2}, u)$ , a linear system of three equations in three variables are obtained as follows

$$I_a + (I_b - I_a)v = \mathbf{O}_{1,2} + u \mathbf{f} + k \mathbf{S}_{1,2} \quad (4.46)$$

The Eq. (4.46) can be written in a matrix forms as

$$\begin{bmatrix} u \\ v \\ t \end{bmatrix} = B^{-1} A \quad (4.47)$$

where

$$A = [I_a - \mathbf{O}_{1,2}]_{3 \times 1}, \quad B = [\mathbf{f} \quad \mathbf{S}_{1,2} \quad (I_a - I_b)]_{3 \times 3} \quad (4.48)$$

If the columns of the matrix  $B$  are linearly independent then Eq. (4.47) generates the real parameter values  $u_{1,2}$ ,  $v_{1,2}$  and  $t_{1,2}$ . If these parameter values satisfy the ranges defined by  $t \in [0, h / \cos^2 \alpha]$ ,  $u \in [0, 1]$  and  $v \in [0, 1]$  then the vector is updated.

### 4.2.3.3 Updating with Fillet-End mill

A Fillet-End mill is made up of a toroidal surface at the lower side, a flat surface at the bottom and a cylindrical surface at the upper side. Depending on the feed vector direction each one of these surfaces updates the in-process workpiece. For example in Figure (4.16) three possible motion types are illustrated with respect to the feed vector  $\mathbf{f}$ : descending (plunging), horizontal and ascending motion respectively. In these figures redlines on the cylindrical surfaces and red curves on the toroidal surfaces represent the grazing points at which the discrete vectors may intersect the envelope surface  $G_{torus}^0$ . In this section for calculations the descending motion shown in Figure (4.16 -a) will be used and solutions of the other motion types can be obtained by using the same steps. In this section the workpiece update formulas will be derived for the toroidal surface of the Fillet-End mill. The formulas for the cylindrical and bottom flat parts can be used from section (4.2.3.1).

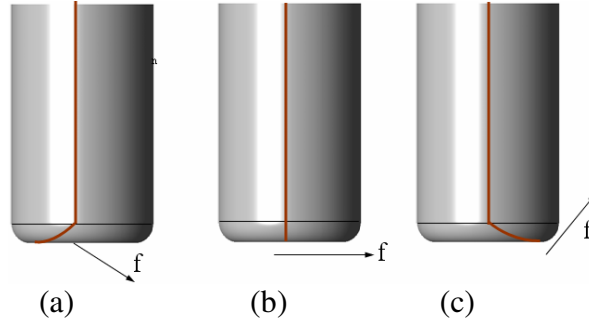


Figure 4.16: Motion types with respect to the feed vector  $\mathbf{f}$ : (a) descending, (b) horizontal, and (c) ascending motion.

For a toroidal surface the center of a moving sphere in *WCS* is obtained by plugging Eqs. (4.12) and (4.19) into Eq. (4.24) and this yields

$$\mathbf{m}(t,u) = P_S + (P_E - P_S)u + [\mathbf{d} \ \mathbf{e} \ \mathbf{n}] \begin{bmatrix} \rho \cos t \\ \rho \sin t \\ 0 \end{bmatrix} \quad (4.49)$$

The partial derivatives of Eq.(4.49) with respect to  $u$  and  $t$  are obtained as follows

$$\frac{\partial \mathbf{m}(t,u)}{\partial u} = (P_E - P_S) = \mathbf{f}, \quad \frac{\partial \mathbf{m}(t,u)}{\partial t} = -\rho \sin t \mathbf{d} + \rho \cos t \mathbf{e} \quad (4.50)$$



For simplifying the calculations the cross products in Eq. (4.52) will be denoted by  $\mathbf{k} = [k_x \ k_y \ k_z] = \mathbf{f} \times \mathbf{d}$  and  $\mathbf{q} = [q_x \ q_y \ q_z] = \mathbf{f} \times \mathbf{e}$ . A point at which a vector intersects the cutter envelope is described by setting the vector line  $I(v)$  described in Eq.(4.21) equals to  $P_1$  given in Eq. (4.51). Thus this yields a nonlinear system of three equations in three variables  $t$ ,  $u$  and  $v$  as follows

$$x_a + (x_b - x_a) v = x_s + (x_E - x_s) u + \rho \cos t d_x + \rho \sin t e_x + r \frac{-\sin t k_x + \cos t q_x}{\|-\sin t \mathbf{k} + \cos t \mathbf{q}\|} \quad (4.53-a)$$

$$y_a + (y_b - y_a) v = y_s + (y_E - y_s) u + \rho \cos t d_y + \rho \sin t e_y + r \frac{-\sin t k_y + \cos t q_y}{\|-\sin t \mathbf{k} + \cos t \mathbf{q}\|} \quad (4.53-b)$$

$$z_a + (z_b - z_a) v = z_s + (z_E - z_s) u + \rho \cos t d_z + \rho \sin t e_z + r \frac{-\sin t k_z + \cos t q_z}{\|-\sin t \mathbf{k} + \cos t \mathbf{q}\|} \quad (4.53-c)$$

For solving the above system of equations, first the equivalent of the variable  $v$  from Eq. (4.53-b) is plugged into Eqs.(4.53-a) and (4.53-c) respectively. Thus with this process two nonlinear equations with variables  $u$  and  $t$  are obtained. Later the equivalent of  $u$  from one of these equations is plugged into another for eliminating  $u$ . Therefore the final nonlinear equation depends on the variable  $t$  only. But in this research, as explained in section (4.2.2), for representing the in-process workpiece the directions of discrete vector lines are taken along the x, y and z axes of the standard basis of  $\mathbb{R}^3$ . Therefore in the following parts the nonlinear system given by Eqs. (4.53-a,b,c) will be solved for discrete vectors having orientations along the z-axis of  $\mathbb{R}^3$  and the similar steps can be used for the discrete vectors pointing in the direction of x and y axes of  $\mathbb{R}^3$ .

When the discrete vectors are oriented in the z-axis direction of  $\mathbb{R}^3$ , the variable  $v$  from Eqs. (4.53-a) and (4.53-b) are eliminated and thus these two equations are only dependent on  $u$  and  $t$ . Further for eliminating  $u$  the equivalent of  $u$  from Eq. (4.53-a) is plugged into Eq. (4.53-b) and this yields the following nonlinear function with variable  $t$

$$f(t) = A(t)\cos t + B(t)\sin t + C = 0 \quad (4.54)$$

where

$$A(t) = \rho (y_E - y_S) d_x - \rho (x_E - x_S) d_y + r \frac{q_x (y_E - y_S) - q_y (x_E - x_S)}{\|-\sin t \mathbf{k} + \cos t \mathbf{q}\|}$$

$$B(t) = \rho (y_E - y_S) e_x - \rho (x_E - x_S) e_y + r \frac{k_y (x_E - x_S) - k_x (y_E - y_S)}{\|-\sin t \mathbf{k} + \cos t \mathbf{q}\|}$$

$$C = (x_E - x_S) (y_a - y_S) + (y_E - y_S) (x_S - x_a)$$

The following property motivates finding the solution of the nonlinear function  $f(t)$

**Property 4.1:** For a given linear toolpath the swept envelope of the torus ( $G_{torus}^0$ ) has a convex shape and a discrete vector intersects this envelope at most two points.

According to property (4.1) there are three possible intersection cases between an envelope surface generated by a torus and a discrete vector: vector intersects in two points, vector intersects in one point and no intersection. All three cases are illustrated in Figure (4.18). In this figure the envelope surface  $G_{torus}^0$  has two parts, the lower envelope ( $G_{torus, Lower}^0$ , colored by green) and the upper envelope ( $G_{torus, Upper}^0$ , colored by gray) surfaces, i.e.  $G_{torus}^0 = G_{torus, Lower}^0 \cup G_{torus, Upper}^0$ . As explained before the cutter is performing a descending motion. Therefore for updating the in-process workpiece the lower envelope surface is taken into account. The upper envelope surface is not considered in the calculations because during the tool motion it is enclosed within the cylindrical part of the Fillet-End mill. Thus the intersection points shown in Figure (4.18) are located on the lower envelope surface ( $G_{torus, Lower}^0$ ).

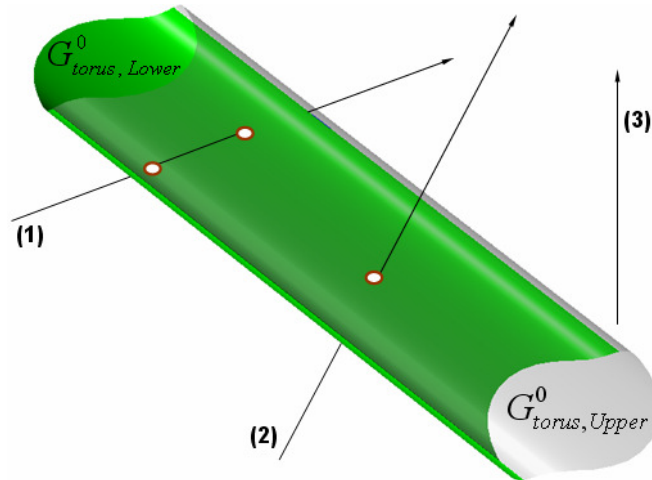


Figure 4.18: Envelope /vector intersection cases: two points (1), one point (2) and no intersection (3).

The real solutions of Eq. (4.54) correspond to the intersection points described by the property (4.1). For solving the nonlinear function  $f(t)$  given in Eq. (4.54) a parameter interval for  $t$  is required. As illustrated in Figure (4.19 -a,b), for obtaining  $G_{torus, Lower}^0$  the parameter  $t$  takes values in the range defined by  $t \in [\pi/2, 3\pi/2]$ . In these figures the envelope boundary made up of grazing points (colored by red) intersects with discrete vectors in one or two points. It can be seen from Figure (4.19 -a) that if there is one intersection point ( $\mathbf{I}_1$ ) which corresponds to  $t_1$  the function values at  $\pi/2$  and  $3\pi/2$  have opposite signs i.e.  $f(\pi/2) f(3\pi/2) < 0$ . On the other hand if there are two intersection points ( $\mathbf{I}_1$  and  $\mathbf{I}_2$ ) which correspond to  $t_1$  and  $t_2$  then the function values at  $\pi/2$  and  $3\pi/2$  have the same sign i.e.  $f(\pi/2) f(3\pi/2) > 0$ .

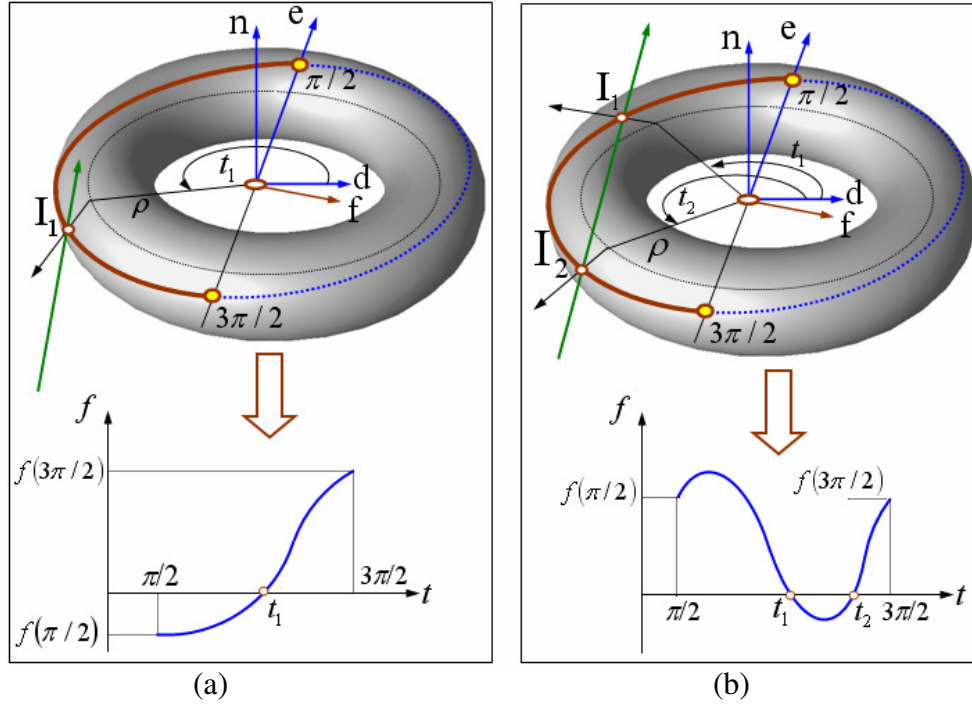


Figure 4.19: The roots of the nonlinear equation  $f(t)$  when the vector intersects in (a) one point or in (b) two points.

Thus the first step for solving the Eq. (4.54) is to check the signs of function  $f(t)$  at  $\pi/2$  and  $3\pi/2$ . If the signs are opposite then there is only one root in the interval defined by  $t \in [\pi/2, 3\pi/2]$ . Therefore one of the numerical root finding methods, i.e. Bisection, can be used to calculate the single root  $t_1$ . But on the other hand if the signs of function  $f(t)$  at  $\pi/2$  and  $3\pi/2$  are the same then the numerical methods can not be applied directly. For this case the following theorem motivates finding two roots  $t_1$  and  $t_2$ .

**Theorem 4.1:** (Rolle's Theorem) Let the function  $f$  be continuous on  $[a, b]$ , and differentiable on  $(a, b)$ , and suppose that  $f(a) = f(b)$ . Then there is some  $c$  with  $a < c < b$  such that  $f'(c) = 0$ .

The function  $f(t)$  given in Eq. (4.54) has coefficients  $A(t)$  and  $B(t)$  which are also a function of  $t$ . These coefficients have a denominator given by  $\|-\sin t \mathbf{k} + \cos t \mathbf{q}\|$ . Expanding this denominator yields

$$\|-\sin t \mathbf{k} + \cos t \mathbf{q}\| = \sqrt{\sin^2 t (k_x^2 + k_y^2 + k_z^2) + \cos^2 t (q_x^2 + q_y^2 + q_z^2)} \quad (4.55)$$

Note that for the above equation the dot product between  $\mathbf{k}$  and  $\mathbf{q}$  equals to zero i.e.

$$\mathbf{k} \cdot \mathbf{q} = (\mathbf{f} \times \mathbf{d}) \cdot (\mathbf{f} \times \mathbf{e}) = (\mathbf{f} \cdot \mathbf{f}) (\mathbf{d} \cdot \mathbf{e}) - (\mathbf{f} \cdot \mathbf{e}) (\mathbf{d} \cdot \mathbf{f}) = 0$$

It can be seen from Eq. (4.55) that the denominator can not be zero. Therefore the function  $f(t)$  given in Eq. (4.54) is continuous.

Also because  $A(t)$ ,  $\cos t$ ,  $B(t)$ ,  $\sin t$  and  $C$  are differentiable at  $(\pi/2, 3\pi/2)$ , the nonlinear function  $f(t)$  given in Eq.(4.54) is also differentiable in the open interval given by  $(\pi/2, 3\pi/2)$ . Furthermore, if the function  $f(t)$  has two roots  $t_1$  and  $t_2$  in the interval  $t \in [\pi/2, 3\pi/2]$  then  $f(t_1) = f(t_2) = 0$ . Therefore the Rolle's Theorem holds for the Eq. (4.54) and thus there is a value  $c$  between two roots  $t_1$  and  $t_2$  for which  $f'(c) = 0$ . If the  $c$  value is found, the interval given by  $t \in [\pi/2, 3\pi/2]$  is partitioned into two sub intervals defined by  $[\pi/2, c]$  and  $[c, 3\pi/2]$ . Now  $f(\pi/2) f(c) < 0$  and  $f(c) f(3\pi/2) < 0$  and thus by applying one of the numerical root finding methods, i.e. Bisection, into these two sub intervals the roots  $t_1$  and  $t_2$  can be found. In this research for finding  $c$  value, a Matlab [54] function *fminbnd* is used. *fminbnd* finds the minimum of a function of one variable within a fixed interval. The algorithm used in *fminbnd* is based on golden section search and parabolic interpolation. See [29] and [17] for details about the algorithm. Note that when the signs of  $f(t)$  at  $\pi/2$  and  $3\pi/2$  are the same i.e.  $f(\pi/2) f(3\pi/2) > 0$ , then each one of  $f(\pi/2)$  and  $f(3\pi/2)$  has a minus sign or vice versa. If each one has a minus sign then for finding the local minimum value at  $c$  using *fminbnd* the nonlinear function  $f(t)$  is multiplied by minus. This process only reflects the function  $f(t)$  with respect to  $t$ -axis in  $(t, f(t))$  graph and it does not change the locations of the roots. The whole process for finding the roots of the nonlinear equation  $f(t)$  is given in Algorithm (4.1).

<p><b>Inputs:</b> Non linear function, <math>f</math>, interval <math>[\pi/2, 3\pi/2]</math></p> <p><b>Outputs:</b> Roots of function <math>f</math></p> <hr/> <p><b>if</b> <math>f(\pi/2)f(3\pi/2) &lt; 0</math> <b>then</b>  <math>t_1 = \text{Bisection}(f, \pi/2, 3\pi/2)</math></p> <p><b>elseif</b> <math>f(\pi/2)f(3\pi/2) &gt; 0</math> <b>then</b>  <b>if</b> <math>f(\pi/2) &lt; 0</math> <b>and</b> <math>f(3\pi/2) &lt; 0</math> <b>then</b>  <math>f = -f</math></p> <p><math>c = \text{fminbnd}(f, \pi/2, 3\pi/2)</math></p> <p><b>if</b> <math>c</math> <b>exists</b> <b>then</b>  <math>t_1 = \text{Bisection}(f, \pi/2, c)</math>  <math>t_2 = \text{Bisection}(f, c, 3\pi/2)</math></p>
---

Algorithm 4.1: Obtaining the roots of  $f(t)$ .

If the function  $f(t)$  has root(s) then for updating the discrete vector the values of the parameters  $u$  and  $v$  must be checked. The root(s) obtained from Algorithm (4.1) are plugged into Eq. (4.53-a) for finding the value(s) of the toolpath parameter  $u$ . Then the root(s) and  $u$  value(s) are plugged into Eq. (4.53-c) for obtaining the vector parameter  $v$ . If the parameter values are in the ranges of  $u \in [0,1]$  and  $v \in [0,1]$ , then the vector is updated. Otherwise it can be concluded that there is no intersection between the cutter envelope and the discrete vector.

#### 4.2.4 Implementation

The presented methodologies have been implemented by using C++ software. Figure (4.20) and (4.21) show the simulation of the Door mold and Auto hood respectively. The initial workpieces are given as rectangular stocks and for the machining a Ball-End mill with 10 mm radius in Figure (4.20) and 5 mm radius in Figure (4.21) is used. In the both machining simulations one layer of toolpahts (colored by red) are used. The toolpath files for these two examples are taken from VERICUT [79]. For visualizing the final workpieces discrete vectors are tessellated by using Matlab.

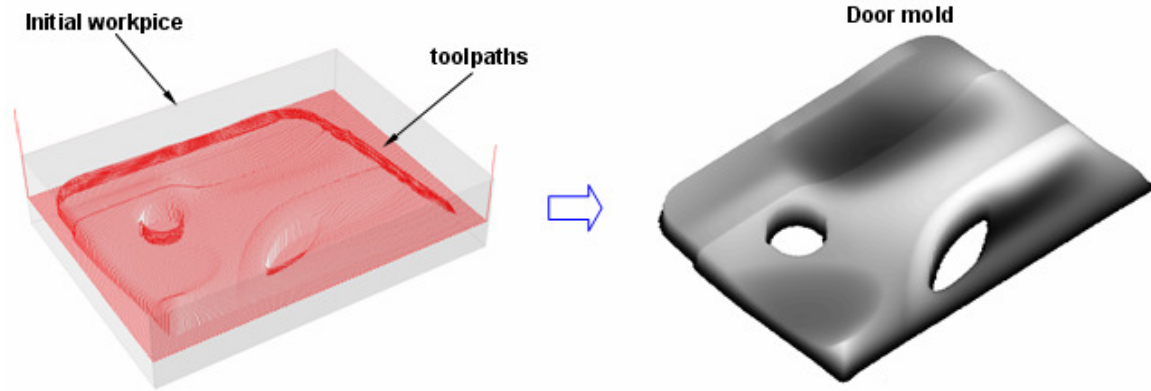


Figure 4.20: NC milling simulation of a Door mold.

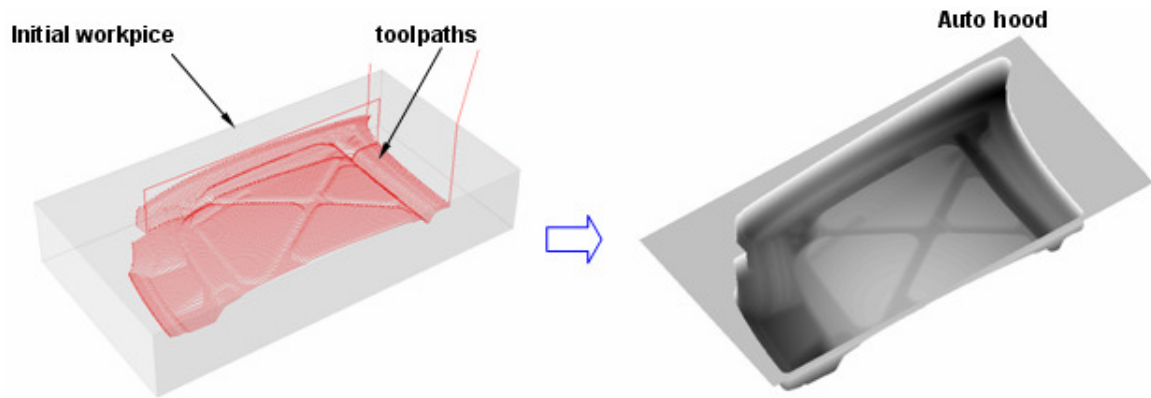


Figure 4.21: NC milling simulation of an Auto hood.

In the next example the machining simulation of the gearbox cover is illustrated (Figure 4.22). For designing the gear box cover and then generating the toolpaths UGS NX3 [77] is used. For this machining simulation there are three layers of toolpaths. In the first layer a Flat-End mill with 5mm radius updates the in-process workpiece (Figure 4.22 -a). In the second and third layers the Ball-End mills with radiuses 5mm and 2.5 mm respectively perform the simulation (Figure 4.22 -b, c). For visualizing the in-process workpiece after each processed layer Matlab is used for tessellation. The green lines in these figures represent the toolpaths.

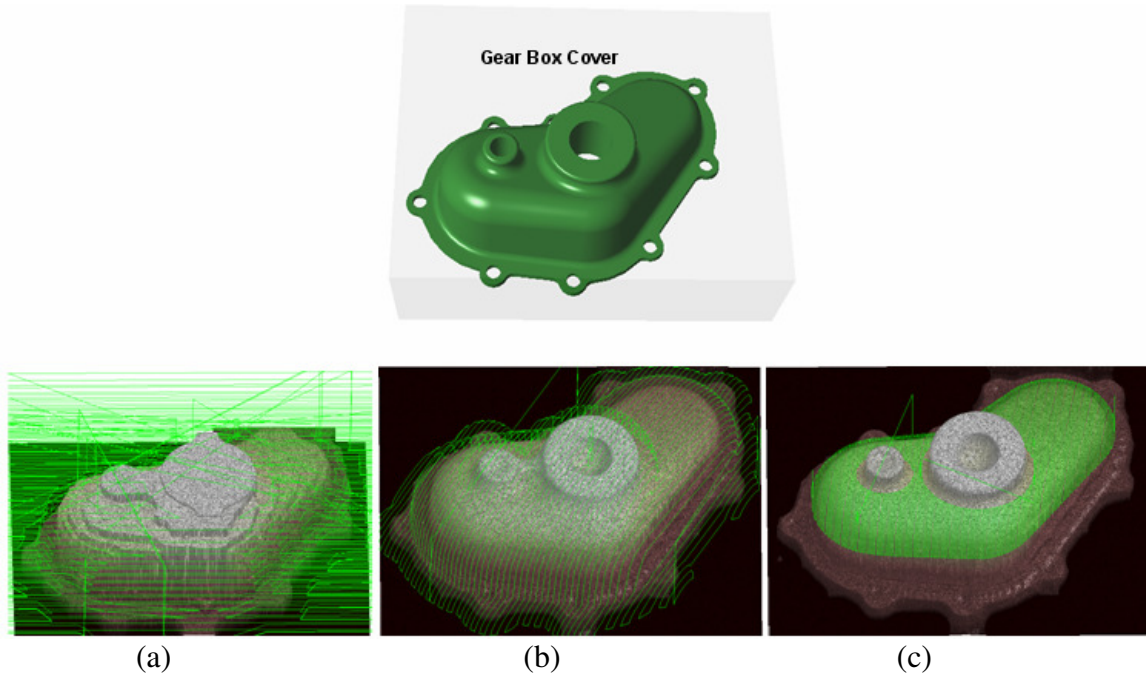


Figure 4.22: NC milling simulation results for a Gearbox cover with (a) A Flat-End mill and (b,c) Ball-End mills.

In the last example the developed methodology is applied to the 5-axis impeller machining (see Figure (4.23)). The Taper-Ball-End mill is used. In Figure (4.23 -a) the initial workpiece with toolpaths and in Figure (4.23 -b) the finished cavity of one blade are shown. In this example 5-axis tool moves are approximated by (3+2)-axis tool moves. This is achieved by subdividing each 5-axis toolpath into as many (3+2)-axis toolpaths as necessary to maintain the desired level of accuracy. For minimizing the error introduced by (3+2)-axis approximation the average of the tool orientations at the beginning and at the end of a toolpath segment is used for the fixed tool orientation on this segment.

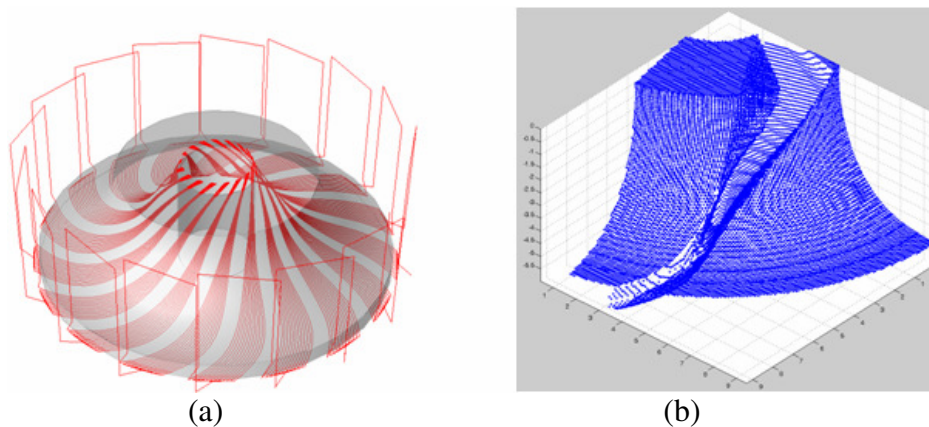


Figure 4.23: NC milling simulation for 5-axis impeller machining.

### 4.3 Discussion

In this chapter discrete vector based in-process workpiece update methodologies have been presented. The discrete vectors with their orientations in the directions of x,y,z-axes of  $R^3$  have been used. Therefore in this representation more vectors in different directions have been used and thus, especially when the workpiece has features like vertical walls and sharp edges, the quality in the visualization of the final product has been increased. Also the localization advantage of the *Discrete Vertical Vector* approach has been preserved. A typical milling tool path contains thousands of tool movements and during the machining simulation for calculating the intersections only the small percentage of all the discrete vectors is needed. For this purpose for localizing the tool envelope during the simulation the Axis Aligned Bounding Box (AABB) has been used. The best feature of the AABB is its fast overlap check, which simply involves direct comparison of individual coordinate values. As explained in this chapter for some workpiece geometries 3-axis machining is not suitable for updating the workpiece surfaces. Because of this in the developed methodologies the tool motions in (3+2)-axis milling in which the cutter can have an arbitrary fixed orientation in space have been considered. The exact 5-axis milling motions are not preferable in the workpiece update simulations because all the calculations require using the nonlinear root finding algorithms and therefore the computational time becomes high. Under this consideration 5-axis tool motions can be approximated by (3+2)-axis tool motions. An example has been given in Figure (4.23) for illustrating this situation. In this chapter for simplifying the intersection calculations the properties of canal surfaces defined in section (3) are utilized. The cutter envelope and vector intersection calculations for the cylinder, frustum of a cone and Flat-Bottom surfaces have been made analytically. Because of the complexity of the torus shape these calculations have been made by using the numerical root finding methods. For this purpose a root finding analysis has been developed for guaranteeing the root(s) in the given interval. The intersection formulas for the sphere surface have not been developed because when a sphere moves along a linear toolpath it envelopes a cylinder which has an orientation in the direction of the feed vector. Therefore the update formulas for the spherical part of a cutter are reduced to cylinder-vector intersection.

## Chapter 5

### Feasible Contact Surfaces

In this chapter the feasible contact surfaces of NC cutters under varying tool motions are presented. A typical NC cutter has different surfaces with varying geometries. For example a Flat-End mill has a cylindrical part at the side and a flat part at the bottom. During the material removal process only *certain parts* of the cutter surfaces are eligible to contact the in-process workpiece. In this chapter for representing these so-called certain parts a terminology *feasible contact surfaces (FCS)* is introduced. The word feasible is used because although these surfaces are eligible to contact the in-process workpiece, they may or may not remove material depending on the cutter position relative to the workpiece. When the *FCS* contact the in-process workpiece the Cutter Workpiece Engagements (*CWEs*) are generated. Since *CWEs* are subsets of *FCS*, formulating the *FCS* helps us to better understand the *CWE* generation process. The boundaries of the *FCS* are defined by the cutter geometry and the envelope boundary set. The envelope boundary set contains points that the cutter surface will leave behind as it moves along a toolpath. Throughout this chapter it is assumed that the cutter follows a rigid motion. Simply a rigid motion is a transformation over time that does not change the shape of the cutter, only its location and orientation. Therefore for the given tool motions the cutter geometry stays fixed but on the other hand the envelope boundary set may change.

Two factors effect the construction process of the *FCS*: the cutter geometry and the motion type. For example for a Flat-End cutter, in 2 ½-axis milling only the cylindrical part has a *FCS*, but on the other hand in 3-axis plunge milling both the cylindrical and the flat parts have a *FCS*. The general tool motions in milling are presented in section (5.1) and followed by the milling cutter geometries in section (5.2). For obtaining the *FCS* the envelope boundary sets of a generic cutter performing 5-axis tool motions are formulated in section (5.3). For this purpose a tangency function defined by the surface normal and the tool velocity is utilized. Later in section (5.4) the distribution of the feasible contact surfaces with respect to cutter velocity is analyzed. Then finally the chapter ends with the discussion in section(5.5).

### 5.1 Tool Motions in Milling

As mentioned in the introduction, tool motions are one of the inputs in the construction of feasible contact surfaces (*FCS*). Later it will be shown in section (5.4) with examples that the type of the tool motion is a key component in the decision of “whether or not cutter surfaces contain the *FCS*”. In the first part of this section the main milling motions with their typical characteristics are introduced and then in the second part the formulae which define the location and the velocity of an arbitrary point on the cutter surface are derived.

There are mainly three types of cutter motions in milling: 2 ½-axis, 3-axis and 5-axis. In 2 ½ - axis motion which is the simplest, a cutter simultaneously translates along two Cartesian axes with a fixed tool axis vector (Figure 5.1-a). On the other hand a 3-axis tool motion which has a fixed tool axis vector allows the cutter three degrees of freedom. These three degrees of freedom correspond to simultaneous translations along three Cartesian axes (Figure 5.1-b). One of these degrees allows the cutter to slide up and down. In 5-axis tool motion, a cutter has five axes of movement, three of which are translational and the other two rotational (Figure 5.1-c).

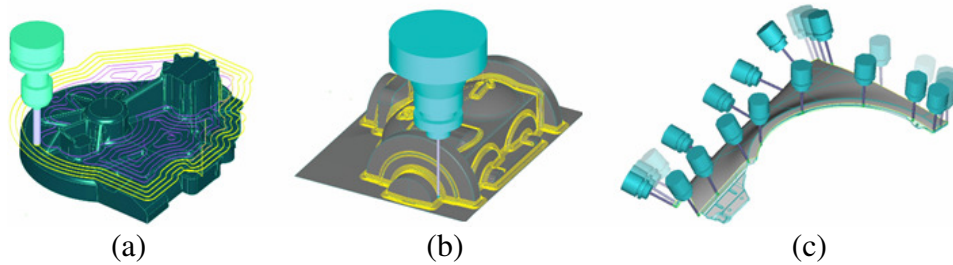


Figure 5.1: Cutter motions in milling: (a) 2 ½-axis, (b) 3-axis, (c) 5-axis.

In this work two kinds of coordinate systems are used: The local - Tool Coordinate System (*TCS*) and the reference - Machine Coordinate System (*MCS*). The three unit Cartesian coordinates of the *TCS* are denoted by  $\mathbf{x}_L$ ,  $\mathbf{y}_L$ , and  $\mathbf{z}_L$ . The *TCS* is positioned at the tool tip  $\mathbf{F}$  with  $\mathbf{z}_L$  along the rotation axis vector  $\mathbf{n}$  (Figure 5.2). On the other hand the *MCS* is represented by the basis vectors  $\mathbf{i}$ ,  $\mathbf{j}$ , and  $\mathbf{k}$  along  $\mathbf{x}_M$  -  $\mathbf{y}_M$  -  $\mathbf{z}_M$  respectively. The position and the orientation of the *TCS* are specified with respect to the *MCS*. Let the basis of the *TCS* be defined as

$$\mathbf{z}_L = \mathbf{n}, \quad \text{if } |\dot{\mathbf{n}}| \neq 0 \text{ then } \mathbf{x}_L = \frac{\dot{\mathbf{n}}}{|\dot{\mathbf{n}}|} \text{ and } \mathbf{y}_L = \mathbf{x}_L \times \mathbf{z}_L$$

$$\text{if } |\dot{\mathbf{n}}| = 0, \text{ then} \quad (5.1)$$

$$\mathbf{z}_L = \mathbf{n}, \mathbf{y}_L = \frac{\mathbf{n} \times \mathbf{V}_F}{|\mathbf{n} \times \mathbf{V}_F|} \text{ if } \mathbf{n} \times \mathbf{V}_F \neq 0 \text{ and } \mathbf{x}_L = \mathbf{y}_L \times \mathbf{z}_L$$

where  $\mathbf{V}_F$  is the velocity in the origin of  $TCS$ . According to Eq. (5.1) the position and the orientation of a cutter ( $G$ ) must be piecewise differentiable and also plunging motion along the cutter rotation axis is not allowed.

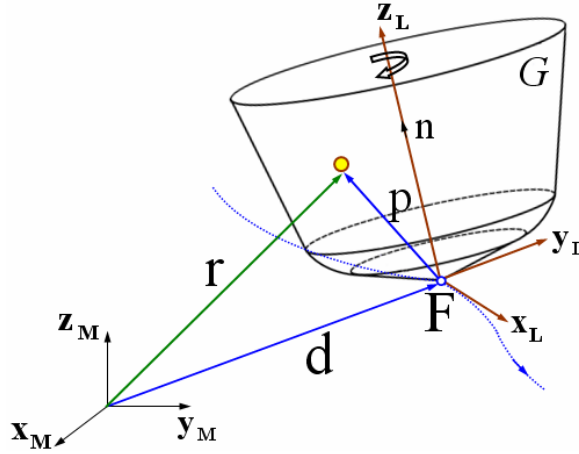


Figure 5.2: The local and reference frames of a cutter

As mentioned in the introduction, throughout this chapter it is assumed that the cutter follows a rigid motion in  $E^3$ . Thus a tool motion can be described analytically by

$$\mathbf{r} = \mathbf{d} + R \mathbf{p} \quad (5.2)$$

where  $\mathbf{p}$  and  $\mathbf{r}$  are the position vectors of an arbitrary point on  $G$  in the local and the reference coordinate system respectively.  $R$  is a rotation matrix and  $\mathbf{d}$  is a translation vector. The rotation matrix is an orthogonal matrix for a rigid body transformation. In general  $\mathbf{d}$  and  $R$  are functions of time  $t$ . Therefore Eq. (5.2) determines the location of a point in  $MCS$  at a given time. The velocity of a point on  $G$  can be obtained by differentiating Eq.(5.2) with respect to  $t$

$$\dot{\mathbf{r}} = \dot{\mathbf{d}} + \dot{R} \mathbf{p} \quad (5.3)$$

Plugging the equivalent of  $\mathbf{p}$  from Eq.(5.2) into Eq. (5.3) yields

$$\dot{\mathbf{r}} = \dot{\mathbf{d}} + \dot{R}R^{-1} (\mathbf{r} - \mathbf{d}) \quad (5.4)$$

where the multiplication of two matrices ( $\dot{R}R^{-1}$ ) is called as the angular velocity matrix denoted by  $\Omega$ .  $\Omega$  is a skew symmetric matrix. This can be proven as follows: Since  $R$  is an orthogonal matrix,  $RR^T = I$  and  $R^{-1} = R^T$ . By differentiating  $RR^T = I$ , the following equation is obtained.

$$\dot{R}R^T + R\dot{R}^T = 0 \quad (5.5)$$

The second term in Eq.(5.5) can be written as  $R\dot{R}^T = (R^{-1})^T \dot{R}^T = (\dot{R}R^{-1})^T$ . And also the first term in this equation is equal to  $\dot{R}R^{-1}$ . Thus Eq. (5.5) takes the following form

$$\dot{R}R^{-1} = -(\dot{R}R^{-1})^T \quad (5.6)$$

The above equation proves that  $\Omega$  is a skew symmetric matrix. The general form of  $\Omega$  is given by

$$\Omega = \begin{bmatrix} 0 & -\Omega_z & \Omega_y \\ \Omega_z & 0 & -\Omega_x \\ -\Omega_y & \Omega_x & 0 \end{bmatrix} \quad (5.7)$$

where  $\Omega_x$ ,  $\Omega_y$  and  $\Omega_z$  are three components of the angular velocity in MCS. The skew symmetric matrix  $\Omega$  can also be represented as a vector. For example by using the components of  $\Omega$  the angular velocity vector  $\boldsymbol{\omega}$  can be represented by

$$\boldsymbol{\omega} = \Omega_x \mathbf{i} + \Omega_y \mathbf{j} + \Omega_z \mathbf{k} \quad (5.8)$$

It can be easily verified that the multiplication of  $\Omega$  with an arbitrary vector, let say  $\mathbf{m}$ , in *MCS* is equal to the cross product between  $\omega$  and this vector, i.e.

$$\Omega \mathbf{m} = \omega \times \mathbf{m} \quad (5.9)$$

Therefore Eq. (5.4) which defines the velocity of an arbitrary point on *G* can be rewritten as

$$\dot{\mathbf{r}} = \dot{\mathbf{d}} + \Omega (\mathbf{r} - \mathbf{d}) = \dot{\mathbf{d}} + \omega \times \mathbf{p} \quad (5.10)$$

Later in section (5.3) the instantaneous velocity of the tool axis will be required. It is derived from the following equation

$$\mathbf{n} = R \mathbf{k} \quad (5.11)$$

Differentiating Eq. (5.11) yields

$$\dot{\mathbf{n}} = \dot{R} \mathbf{k} = \dot{R} R^{-1} \mathbf{n} = \Omega \mathbf{n} \quad (5.12)$$

From Eq. (5.9), the above equation takes the following form

$$\dot{\mathbf{n}} = \omega \times \mathbf{n} \quad (5.13)$$

Thus the instantaneous velocity of the tool axis can be calculated in terms of angular velocity and the rotation axis vector.

## 5.2 Milling Cutter Geometries

The construction of feasible contact surfaces requires the modeling of the tool geometry. In this section for obtaining a variety of cutter shapes a parametric model of a generic cutter is used (Figure 5.3). The geometry of the generic cutter can be described by the following parameters [46]

$R$ : Major radius,  $r_c$ : Minor radius of the corner torus.

$h_c$ : Distance between cutter tip point and the center of the corner radius.

$\alpha$ : Angle from tool rotation axis to the cutter bottom, ( $0 < \alpha \leq \pi/2$ ).

$\beta$ : Angle between upper cone side and tool rotation axis, ( $-\pi/2 < \beta < \pi/2$ ).

$r$ : Cutter radius,  $h$ : The height of the tool.

By appropriately choosing these parameters a variety of cutter shapes can be obtained.

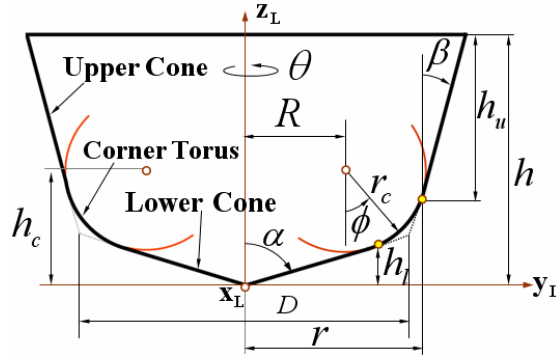


Figure 5.3: Geometric definition of the generic cutter

The generic cutter can be decomposed into Upper-Cone ( $G_U$ ), Corner-Torus ( $G_T$ ) and Lower-Cone ( $G_L$ ) parametric surfaces and the boundaries between these surfaces are  $C_1$  - continuous. The representations of these surfaces with respect to  $TCS$  are given by

$$G_U(\theta, c_u, t) = \begin{pmatrix} (r + c_u \tan \beta) \cos \theta \\ (r + c_u \tan \beta) \sin \theta \\ h_c - r_c \sin \beta + c_u \end{pmatrix} \quad (5.14-a)$$

$$G_T(\theta, \phi, t) = \begin{pmatrix} (R + r_c \sin \phi) \cos \theta \\ (R + r_c \sin \phi) \sin \theta \\ h_c - r_c \cos \phi \end{pmatrix} \quad (5.14-b)$$

$$G_L(\theta, c_l, t) = \begin{pmatrix} c_l \tan \alpha \cos \theta \\ c_l \tan \alpha \sin \theta \\ c_l \end{pmatrix} \quad (5.14-c)$$

where  $\theta \in [0, 2\pi]$ ,  $c_u \in [0, h_u]$ ,  $c_l \in [0, h_l]$ ,  $\phi \in [(\pi/2 - \alpha), (\pi/2 - \beta)]$  and also there are following relationships between the geometric parameters.

$$r = R + r_c \cos \beta, \quad h_l = (R + r_c \cos \alpha) / \tan \alpha$$

$$h_c = h_l + r_c \sin \alpha, \quad h_u = h - h_c + r_c \sin \beta$$

Also Eqs. (5.14,a-c) can be written in the *MCS* as:

$${}^M G_U(\theta, c_u, t) = \mathbf{F}(t) + (h_c - r \sin \beta + c_u) \mathbf{z}_L + (r + c_u \tan \beta) \cos \theta \mathbf{x}_L + (r + c_u \tan \beta) \sin \theta \mathbf{y}_L \quad (5.15-a)$$

$${}^M G_T(\theta, \phi, t) = \mathbf{F}(t) + (h_c - r_c \cos \phi) \mathbf{z}_L + (R + r_c \sin \phi) \cos \theta \mathbf{x}_L + (R + r_c \sin \phi) \sin \theta \mathbf{y}_L \quad (5.15-b)$$

$${}^M G_L(\theta, c_l, t) = \mathbf{F}(t) + c_l \mathbf{z}_L + c_l \tan \alpha \cos \theta \mathbf{x}_L + c_l \tan \alpha \sin \theta \mathbf{y}_L \quad (5.15-c)$$

where  $t \in R$  is a toolpath parameter and  $M$  indicates that representations are in the *MCS*. The normal of a cutter surface can be described in the *TCS* as

$$\mathbf{N} = \frac{\partial G}{\partial s} \times \frac{\partial G}{\partial q} \Big/ \left| \frac{\partial G}{\partial s} \times \frac{\partial G}{\partial q} \right| \quad (5.16)$$

where  $s$  and  $q$  are the geometric parameters. Also the normal can be written in the *MCS* for each part of the generic cutter as

$${}^M \mathbf{N}_U(Q) = -\sin \beta \mathbf{z}_L + \cos \theta \cos \beta \mathbf{x}_L + \sin \theta \cos \beta \mathbf{y}_L \quad (5.17-a)$$

$${}^M \mathbf{N}_T(Q) = -\cos \phi \mathbf{z}_L + \cos \theta \sin \phi \mathbf{x}_L + \sin \theta \sin \phi \mathbf{y}_L \quad (5.17-b)$$

$${}^M \mathbf{N}_L(Q) = -\sin \alpha \mathbf{z}_L + \cos \theta \cos \alpha \mathbf{x}_L + \sin \theta \cos \alpha \mathbf{y}_L \quad (5.17-c)$$

where  $Q$  is an arbitrary point on the cutter surface.

### 5.3 Calculating the Feasible Contact Surfaces

Two inputs for describing the Feasible Contact Surfaces (*FCS*), the tool motions and the milling tool geometries have been presented in the previous two sections. The formulae developed in these sections will be used for describing the *FCS*. A typical milling cutter contains varying geometries and during the machining each one of these geometries behaves differently and in turn this effects the construction of the *FCS*. This can be explained with a simple example. For example a Flat-End mill has a cylindrical part at the side and a flat part at the bottom. In a 2 ½-axis milling only the cylindrical part can contact in-process workpiece and also only the front of the cylinder can remove material. From this example it can be seen that bottom flat part and the back of the cylinder can not remove material. In this example the front part of the cylinder represents the feasible contact surface. The more complicated situation occurs when a cutter performs a multi-axis machining. In this work for calculating *FCS* of the generic cutter performing 5-axis tool motions a tangency function is utilized. The tangency function  $f$  is defined with respect to surface normal  ${}^M\mathbf{N}(p,t)$  and instantaneous velocity  ${}^M\mathbf{V}(p,t)$  as [82]

$$f(p,t) = {}^M\mathbf{N}(p,t) \cdot {}^M\mathbf{V}(p,t) \quad (5.18)$$

where  $p$  and  $t$  represent the cutter geometry and the toolpath parameter respectively. At any instant the surface boundary of a cutter can be partitioned into three sub boundaries with respect to tangency function: forward boundary (*egress points*), envelope boundary (*grazing points*) and backward boundary (*ingress points*). Figure (5.4) illustrates these three boundaries. Thus cutter surfaces at time  $t$  are enclosed within these three boundaries

$${}^M G(p,t) = {}^M G^-(p,t) \cup {}^M G^0(p,t) \cup {}^M G^+(p,t) \quad (5.19)$$

where

${}^M G^+(p,t)$  is the forward boundary with  $f(p,t) > 0$

${}^M G^0(p,t)$  is the envelope boundary with  $f(p,t) = 0$ , and

${}^M G^-(p,t)$  is the backward boundary with  $f(p,t) < 0$

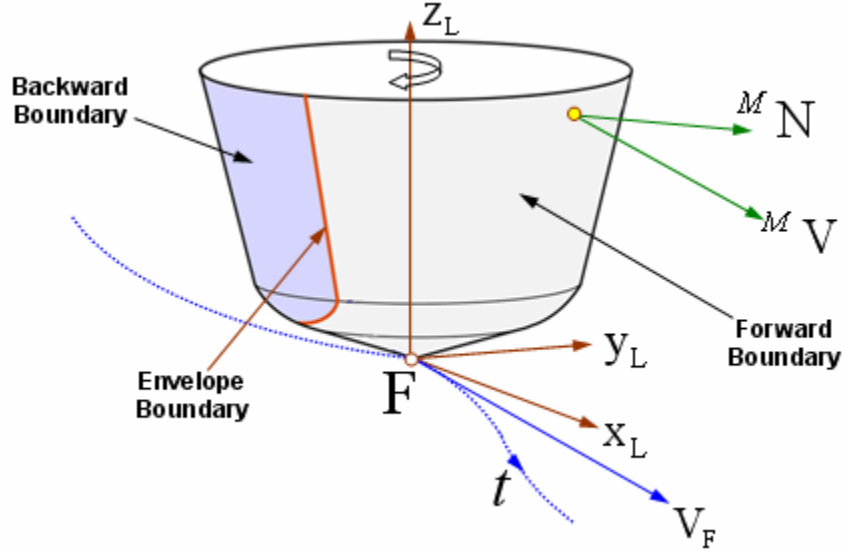


Figure 5.4: Boundary partition of the generic cutter.

The cutting tool can contact the in-process workpiece through the forward and the envelope boundaries and therefore the combination of these two boundaries defines the feasible contact surfaces of a cutter. The word feasible is used because these surfaces are eligible to contact the in-process workpiece. Although they are eligible to contact the material removal depends on the cutter position relative to the workpiece. The Cutter Workpiece Engagements (*CWEs*) are the imprints of *FCS* on the in-process workpiece and for a given instant both the in-process workpiece and the cutter surface must share a point from *FCS*. To clearly see the relationship between *FCS* and *CWEs* the following terminology is introduced.

### General Terminology

$CWE_K(p,t)$ : The set of all points on a cutter surface at location  $t$  where  $f(p,t) \geq 0$ . These are also called as *kinematically feasible engagement points*.

$CWE(p,t)$ : The set of all points on a cutter surface at location  $t$  that are engaged with the workpiece.

According to the above terminology the feasible contact surfaces can be represented by the set  $CWE_K$  where  $CWE_K(p,t) = {}^M G^+(p,t) \cup {}^M G^0(p,t)$ . Also the relationships among these sets can be written as  $(CWE \subset CWE_K \subset CWE_G)$ , where  $CWE_G$  denotes the set of all points on a cutter surface.

A typical NC cutter has different surfaces with varying geometries and during the machining the engagement characteristics of each surface become different. In this work for clearly seeing this, the  $FCS$  are distributed among actively cutting surfaces. Under this consideration the set  $CWE_K$  can be divided into constituent sub sets. For example in Figure (5.5) a Flat-End mill is moving along a helical tool path for enlarging a hole. Because of the plunging effect both the side (cylindrical) and the bottom (flat) faces have contacts with the in-process workpiece. For this case the set  $CWE_K$  can be written as

$$CWE_K = CWE_{K,Side} \cup CWE_{K,Bottom} \quad (5.20)$$

where the sets  $CWE_{K,Side}$  and  $CWE_{K,Bottom}$  represent the  $FCS$  generated by the cylindrical and the flat part respectively. Also in this figure the cutter workpiece engagements as the subsets of  $FCS$  are shown.

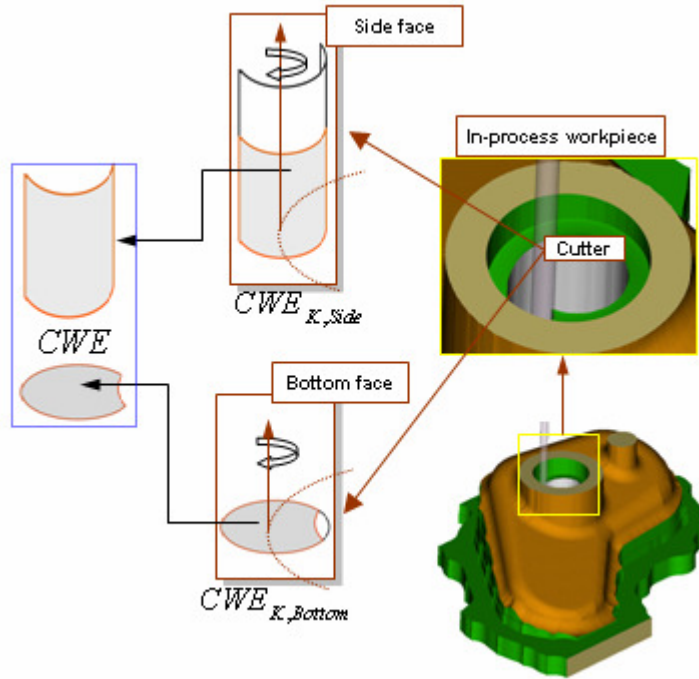


Figure 5.5: Point sets used in defining engagements

It will be shown in the next chapter that for obtaining the cutter workpiece engagements the geometric limits of the set  $CWE_K$  are required. These geometric limits are determined by the

cutter surface boundaries and the envelope boundary. Figure (5.6) illustrates these geometric limits for the toroidal part of a Fillet-End mill.

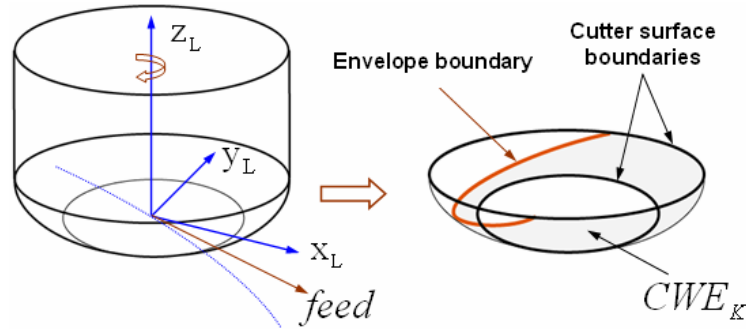


Figure 5.6: Boundaries of the  $CWE_K$  in the Fillet-End mill

Because the cutter performs a rigid motion defined in section (5.1) the cutter surface boundaries stay fixed. These boundaries can be calculated by using the formulae defined in section (5.2). But on the other hand, the content of the envelope boundary changes. Therefore for modeling the *FCS* the calculation of the envelope boundary is the primary concern in this work. In the following subsections the envelope boundary of the generic cutter performing 5-axis tool motions will be calculated. As noted before in section (5.2), the defined geometry of a generic cutter can be decomposed into three sub surfaces: upper-cone, corner-torus and lower-cone. Therefore the full envelope boundary of the cutter can be generated by combining the partial envelope boundaries which are described on the individual cutter surfaces.

### 5.3.1 Envelope Boundary of the Upper-Cone

In Figure (5.7) a general end mill performing 5-axis machining is shown with three arbitrary points on different surfaces. From this figure, the velocity of an arbitrary point  $I_U$  on the upper-cone surface can be expressed in *MCS* by

$${}^M \mathbf{V}_U(I_U) = \mathbf{V}_F + \boldsymbol{\omega} \times \vec{FI}_U \quad (5.21)$$

where the vector  $\vec{FI}_U$  is defined in *TCS*. When the Eq. (5.14-a) is plugged into the above equation, the velocity becomes as

$${}^M \mathbf{V}_U(I_U) = \mathbf{V}_F + (h_c - r_c \sin \beta + c_u) (\boldsymbol{\omega} \times \mathbf{z}_L) + (r + c_u \tan \beta) \cos \theta (\boldsymbol{\omega} \times \mathbf{x}_L) + (r + c_u \tan \beta) \sin \theta (\boldsymbol{\omega} \times \mathbf{y}_L) \quad (5.22)$$

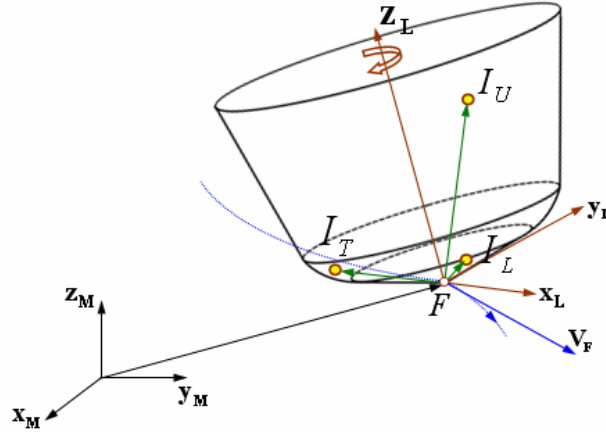


Figure 5.7: Arbitrary points  $I_U$ ,  $I_T$  and  $I_L$  on the upper-cone, corner-torus and lower-cone surfaces respectively.

For obtaining the envelope boundary of the upper-cone, Eqs. (5.22) and (5.17-a) are plugged into the following equation

$$f^U(\theta, c_u, t) = {}^M \mathbf{V}_U(I_U) \cdot {}^M \mathbf{N}_U(I_U) = 0 \quad (5.23)$$

Then by performing vector operations Eq. (5.23) takes the following form

$$f^U(\theta, c_u, t) = \cos \theta [\cos \beta (\mathbf{x}_L \cdot \mathbf{V}_F) + (r + c_u \tan \beta) \sin \beta (\boldsymbol{\omega} \cdot \mathbf{y}_L) + \cos \beta (h_c - r_c \sin \beta + c_u) (\boldsymbol{\omega} \cdot \mathbf{y}_L)] + \sin \theta [\cos \beta (\mathbf{y}_L \cdot \mathbf{V}_F)] - \sin \beta (\mathbf{z}_L \cdot \mathbf{V}_F) = 0 \quad (5.24)$$

Note that for the above expansion the scalar triple product is evaluated as

$$\mathbf{a} \cdot (\mathbf{b} \times \mathbf{c}) = \mathbf{b} \cdot (\mathbf{c} \times \mathbf{a}) = \mathbf{c} \cdot (\mathbf{a} \times \mathbf{b})$$

and also Eq. (5.13) is utilized for the following operation

$$\boldsymbol{\omega} \cdot \mathbf{x}_L = \boldsymbol{\omega} \cdot \frac{\dot{\mathbf{n}}}{|\dot{\mathbf{n}}|} = \boldsymbol{\omega} \cdot \frac{(\boldsymbol{\omega} \times \mathbf{n})}{|\dot{\mathbf{n}}|} = 0$$

Eq. (5.24) can be written in a closed form

$$f^U(\theta, c_u, t) = A_U \cos \theta + B_U \sin \theta - C_U = 0 \quad (5.25)$$

where

$$A_U = \cos \beta (\mathbf{x}_L \cdot \mathbf{V}_F) + (r + c_u \tan \beta) \sin \beta (\boldsymbol{\omega} \cdot \mathbf{y}_L) + \cos \beta (h_c - r_c \sin \beta + c_u) (\boldsymbol{\omega} \cdot \mathbf{y}_L)$$

$$B_U = \cos \beta (\mathbf{y}_L \cdot \mathbf{V}_F)$$

$$C_U = \sin \beta (\mathbf{z}_L \cdot \mathbf{V}_F)$$

In  $(a \cos x + b \sin x)$  type equations, the combination of cosine and sine functions can be written as a single sine function as

$$a \cos x + b \sin \theta = c \sin(x + \zeta) \quad (5.26)$$

where the amplitude  $c = \sqrt{a^2 + b^2}$ , the phase  $\zeta = \arctan(a/b)$  and  $b \neq 0$ . The derivation of Eq. (5.26) can be shown by utilizing the complex domain operations as

$$\begin{aligned} a \cos x + b \sin x &= a \frac{e^{ix} + e^{-ix}}{2} + b \frac{e^{ix} - e^{-ix}}{2i} = \frac{1}{2} [(a - ib)e^{ix} + (a + ib)e^{-ix}] \\ &= \frac{1}{2} \left[ \sqrt{a^2 + b^2} e^{i \arctan\left(\frac{-b}{a}\right)} e^{ix} + \sqrt{a^2 + b^2} e^{i \arctan\left(\frac{b}{a}\right)} e^{-ix} \right] \\ &= \frac{1}{2} \left[ \sqrt{a^2 + b^2} e^{i\left(x - \arctan\left(\frac{b}{a}\right)\right)} + \sqrt{a^2 + b^2} e^{-i\left(x - \arctan\left(\frac{b}{a}\right)\right)} \right] \\ &= \sqrt{a^2 + b^2} \cos\left(x - \arctan\left(\frac{b}{a}\right)\right) = \sqrt{a^2 + b^2} \sin\left(x + \arctan\left(\frac{a}{b}\right)\right) \end{aligned} \quad (5.27)$$

Note that in the last line of the above equation cosine representation is transformed into sine representation under the consideration of arctan function as

$$\arctan(y) = \begin{cases} -\frac{1}{2}\pi - \arctan\left(\frac{1}{y}\right), & \text{for } y < 0 \\ \frac{1}{2}\pi - \arctan\left(\frac{1}{y}\right), & \text{for } y > 0 \end{cases}$$

Thus the Eq. (5.25) can be written in the following form

$$\sqrt{A_U^2 + B_U^2} \sin(\theta + \kappa_U) - C_U = 0 \quad (5.28)$$

where  $\kappa_U = \arctan(A_U / B_U)$ . Solving Eq. (5.28) for  $\theta$  yields

$$\theta(c_u, t) = \begin{cases} \sin^{-1}\left(\frac{C_U}{\sqrt{A_U^2 + B_U^2}}\right) - \kappa_U \\ \pi - \sin^{-1}\left(\frac{C_U}{\sqrt{A_U^2 + B_U^2}}\right) - \kappa_U \end{cases} \quad (5.29)$$

When Eq. (5.29) is plugged into Eq. (5.15-a), for a given cutter location point the envelope boundary of the upper-cone surface is obtained.

### 5.3.2 Envelope Boundary of the Corner-Torus

The velocity of arbitrary point  $I_T$  on the toroidal surface (Figure 5.7) can be expressed in *MCS* by

$${}^M \mathbf{V}_T(I_T) = \mathbf{V}_F + \boldsymbol{\omega} \times \vec{FI}_T \quad (5.30)$$

Plugging Eq. (5.14-b) into Eq. (5.30) yields

$$\begin{aligned} {}^M \mathbf{V}_T(I_T) = \mathbf{V}_F + (h_c - r_c \cos \phi) (\boldsymbol{\omega} \times \mathbf{z}_L) + (R + r_c \sin \phi) \cos \theta (\boldsymbol{\omega} \times \mathbf{x}_L) \\ + (R + r_c \sin \phi) \sin \theta (\boldsymbol{\omega} \times \mathbf{y}_L) \end{aligned} \quad (5.31)$$

For obtaining the envelope boundary of the corner-torus, Eqs. (5.31) and (5.17-b) are plugged into the following equation

$$f^T(\phi, \theta, t) = {}^M \mathbf{V}_T(I_T) \cdot {}^M \mathbf{N}_T(I_T) = 0 \quad (5.32)$$

and considering the vector operations the above equation yields

$$f^T(\phi, \theta, t) = A_T \cos \theta + B_T \sin \theta - C_T = 0 \quad (5.33)$$

where

$$A_T = \sin \phi (\mathbf{x}_L \cdot \mathbf{V}_F) + h_c \sin \phi (\boldsymbol{\omega} \cdot \mathbf{y}_L) + \cos \phi (\boldsymbol{\omega} \cdot \mathbf{y}_L)$$

$$B_T = \sin \phi (\mathbf{y}_L \cdot \mathbf{V}_F)$$

$$C_T = \cos \phi (\mathbf{z}_L \cdot \mathbf{V}_F)$$

Eq. (5.33) can be written in the following form

$$\sqrt{A_T^2 + B_T^2} \sin(\theta + \kappa_T) - C_T = 0 \quad (5.34)$$

where  $\kappa_T = \arctan(A_T / B_T)$ . Solving Eq. (5.34) for  $\theta$  yields

$$\theta(\phi, t) = \begin{cases} \sin^{-1} \left( \frac{C_T}{\sqrt{A_T^2 + B_T^2}} \right) - \kappa_T \\ \pi - \sin^{-1} \left( \frac{C_T}{\sqrt{A_T^2 + B_T^2}} \right) - \kappa_T \end{cases} \quad (5.35)$$

When Eq. (5.35) is plugged into Eq. (5.15-b), for a given cutter location point the envelope boundary of the corner-torus surface is obtained.

### 5.3.3 Envelope Boundary of the Lower-Cone

The velocity of a point  $I_L$  on the lower-cone surface (Figure 5.7) is given by

$${}^M \mathbf{V}_L(I_L) = \mathbf{V}_F + \boldsymbol{\omega} \times \vec{FI_L} \quad (5.36)$$

The Eq. (5.36) is expanded by substitution of Eq. (5.14-c) as

$$\begin{aligned} {}^M \mathbf{V}_L(I_L) = \mathbf{V}_F + c_l (\boldsymbol{\omega} \times \mathbf{z}_L) + c_l \tan \alpha \cos \theta (\boldsymbol{\omega} \times \mathbf{x}_L) \\ + c_l \tan \alpha \sin \theta (\boldsymbol{\omega} \times \mathbf{y}_L) \end{aligned} \quad (5.37)$$

Eqs. (5.37) and (5.17-c) are plugged into the following equation

$$f^L(\theta, c_l, t) = {}^M \mathbf{V}_L(I_L) \cdot {}^M \mathbf{N}_L(I_L) = 0 \quad (5.38)$$

and after the vector operations the envelope boundary of the lower-cone is obtained in the closed form

$$f^L(\theta, c_l, t) = A_L \cos \theta + B_L \sin \theta - C_L = 0 \quad (5.39)$$

where

$$A_L = \sin \alpha c_l \tan \alpha (\boldsymbol{\omega} \cdot \mathbf{y}_L) + \cos \alpha (\mathbf{x}_L \cdot \mathbf{V}_F) + \cos \alpha c_l (\boldsymbol{\omega} \cdot \mathbf{y}_L)$$

$$B_L = \cos \alpha (\mathbf{y}_L \cdot \mathbf{V}_F)$$

$$C_L = \sin \alpha (\mathbf{z}_L \cdot \mathbf{V}_F)$$

The Eq. (5.39) is transformed into the following form

$$\sqrt{A_L^2 + B_L^2} \sin(\theta + \kappa_L) - C_L = 0 \quad (5.40)$$

where  $\kappa_L = \arctan(A_L / B_L)$ , and it is solved for  $\theta$  as

$$\theta(c_l, t) = \begin{cases} \sin^{-1} \left( \frac{C_L}{\sqrt{A_L^2 + B_L^2}} \right) - \kappa_L \\ \pi - \sin^{-1} \left( \frac{C_T}{\sqrt{A_L^2 + B_L^2}} \right) - \kappa_L \end{cases} \quad (5.41)$$

When Eq. (5.41) is plugged into Eq. (5.15-c), for a given cutter location point the envelope boundary of the lower-cone surface is obtained.

#### 5.4 Analyzing the Distribution of Feasible Contact Surfaces

In the previous section the generic cutter surfaces have been partitioned into three boundary point sets by utilizing the tangency function. Then for each surface patch the envelope boundary which defines the limits of the feasible contact surfaces (*FCS*) has been formulated by calculating the parameter  $\theta$ . For a given cutter geometry, any change in the tool tip velocity  $\mathbf{V}_F$  and the angular velocity  $\boldsymbol{\omega}$  will effect the range of  $\theta$  and in turn the location of the point set  $CWE_K$  which represent the feasible contact surfaces. Therefore the cutter motion type has direct effect in the construction process of *FCS*.

In 5-axis machining the cutter rotation axis can be tilted in any direction. In general during machining the side face of the cutter has instant contact with the in-process workpiece and the engagement angle covers the angular range of  $[0^0, 180^0]$ . For example in Figure 5.8(a-b) Taper-End and Ball-End mills are performing 5-axis motions and only the side faces of these cutters contain the point set  $CWE_K$ . But on the other hand in 3-axis milling the tool rotation axis is fixed and with respect to the tool tip velocity, more cutter surfaces may be involved in machining. This is illustrated for 3-axis plunge motion in Figures (5.8-c) for a Flat-End mill and ((5.8-d) for a Ball-End mill respectively.

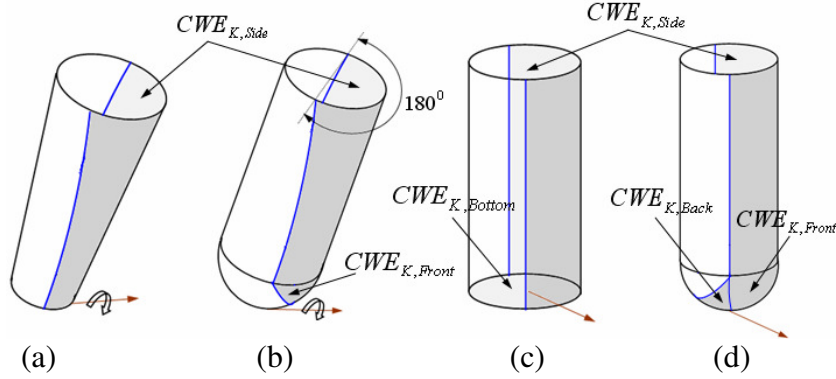


Figure 5.8: Instantaneous cutter contact surfaces in (a,b) 5-axis, and in (c,d) 3-axis plunge motions

Because 3-axis motion can cover more contact surfaces, in this section the distribution of the *FCS* on the cutter will be analyzed with respect to this motion type. For defining the limits of the *FCS* two boundaries are used: the surface boundaries and the envelope boundary. The surface boundaries are fixed for a given tool motion and they can be calculated from section (5.2). For calculating the envelope boundary, the formulae developed in section (5.3) will be utilized by considering that the angular velocity is zero. Also the tool tip velocity  $\mathbf{V}_F$  will be denoted by  $\mathbf{f}$  which is short for the feed. In Figure (5.9-a) the generic cutter profile and the feed vector  $\mathbf{f}$  are shown. Initially the feed vector is coincident with the  $\mathbf{z}_L$  axis of the *TCS*. From this figure the feed angle  $\psi$  which is measured from the  $\mathbf{z}_L$  axis in the clock wise direction can be obtained as

$$\psi = \cos^{-1} \left( \frac{\mathbf{f} \cdot \mathbf{z}_L}{|\mathbf{f}| |\mathbf{z}_L|} \right) \quad (5.42)$$

Any change in the direction of feed vector will effect the distribution of the *FCS* on the cutter. For clearly seeing this, the generic cutter is partitioned into two sections (Figure 5.9-b): Front face (F) and Back face (B). An unbounded plane which passes through  $\mathbf{y}_L$  and  $\mathbf{z}_L$  axes of *TCS* separates these two faces.

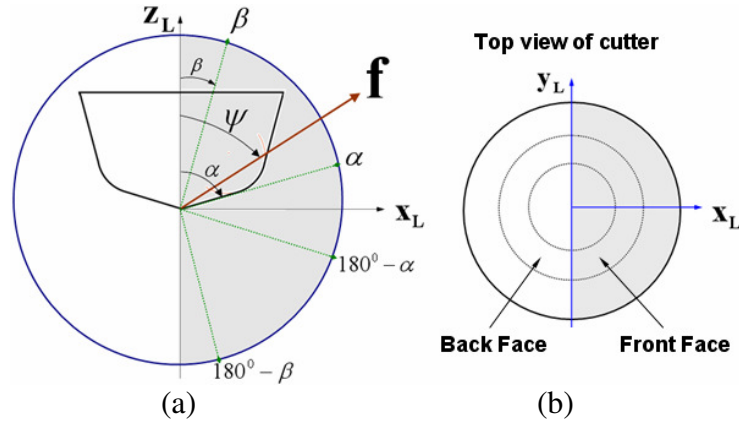


Figure 5.9: Feed angle ranges

Figure (5.9-a) illustrates that the feed angle  $\psi$  takes different values in five different regions (shaded area). The angles which separate these regions are defined by the geometric parameters  $\alpha$  and  $\beta$  of the generic cutter from section (5.2). Also the second and the fourth columns of Table (5.1) show the feed angle ranges corresponding to these five regions. In this table the first and the third columns show alpha numeric symbols i.e. F1, B2 etc. for different ranges of the feed angle. Letters F and B denote the front and the back faces of the cutter (Figure 5.9-b) respectively.

Front Face	Range	Back Face	Range
F1	$\psi = \beta$	B1	$\psi \in (90^\circ, 180^\circ - \alpha)$
F2	$\psi \in (\beta, \alpha)$	B2	$\psi = 180^\circ - \alpha$
F3	$\psi = \alpha$	B3	$\psi \in (180^\circ - \alpha, 180^\circ - \beta)$
F4	$\psi \in (\alpha, 90^\circ)$	B4	$\psi = 180^\circ - \beta$
F5	$\psi = 90^\circ$		

Table 5.1: The angular ranges of the feed angle

According to the feed angle ranges given in Table (5.1) the cutter can have three types of motion: Ascending type (F1 to F4), Horizontal type (F5) and Descending type (B1 to B4). With respect to these tool motions the following propositions can be given

**Proposition 5.1:** When the cutter has ascending and horizontal type motions which cover the range of  $\psi \in [\beta, 90^\circ]$ , the point set  $CWE_K$  is located on the front face (F) of the cutter. Therefore only the front face can contain the feasible contact surfaces during the machining

**Proposition 5.2:** When the cutter has descending motion which covers the range of  $\psi \in (90^\circ, 180^\circ - \beta]$ , the point set  $CWE_K$  is located on both the front and the back faces of the cutter. Therefore both faces can contain the feasible contact surfaces during the machining.

Note that feed angles ( $\psi < \beta$ ) and ( $\psi > 180^\circ - \beta$ ) are excluded from these propositions. because in the former one the top circle of the upper-cone touches the workpiece and in the latter one all cutter surfaces totally plunge into the workpiece. These propositions will be proven for the corner-torus surface of the generic cutter by considering the feed angle in the ranges of F1, F3, B2 and B4 from Table (5.1). The results for the other surface patches can be found in Table (5.2). The results of these propositions will be used in the next chapter during the cutter work piece engagement identifications.

**Proof:** It has been shown in section (5.2) that two of the geometric parameters for describing the corner-torus are  $\theta$  and  $\phi$ . Figures (5.10-a, b) illustrates that  $\phi$  is measured in *CCW* direction from the tool rotation axis and  $\theta$  is measured in *CCW* direction from the  $\mathbf{x}_L$  axis of *TCS*. It can be seen from these figures that the  $\phi$  angle of an arbitrary point  $P$  must lie within the range of  $[90^\circ - \alpha, 90^\circ - \beta]$  i.e.

$$(90^\circ - \alpha) \leq \phi(P \mid P \in G_T) \leq (90^\circ - \beta) \quad (5.43)$$

When the lower  $\phi^L = (90^\circ - \alpha)$  and the upper  $\phi^U = (90^\circ - \beta)$  limits of  $\phi$  from Eq. (5.43) are plugged into Eq. (5.35), the following expressions are obtained:

$$\theta_{1,2}^L = \mp \cos^{-1} \left( \frac{(\mathbf{f} \cdot \mathbf{z}_L) \tan \alpha}{(\mathbf{f} \cdot \mathbf{x}_L)} \right) \quad (5.44-a)$$

$$\theta_{1,2}^U = \mp \cos^{-1} \left( \frac{(\mathbf{f} \cdot \mathbf{z}_L) \tan \beta}{(\mathbf{f} \cdot \mathbf{x}_L)} \right) \quad (5.44-b)$$

where superscripts L and U represent the lower and the upper limit respectively. Note that the angular velocity in Eq. (5.35) becomes zero in 3-axis machining.

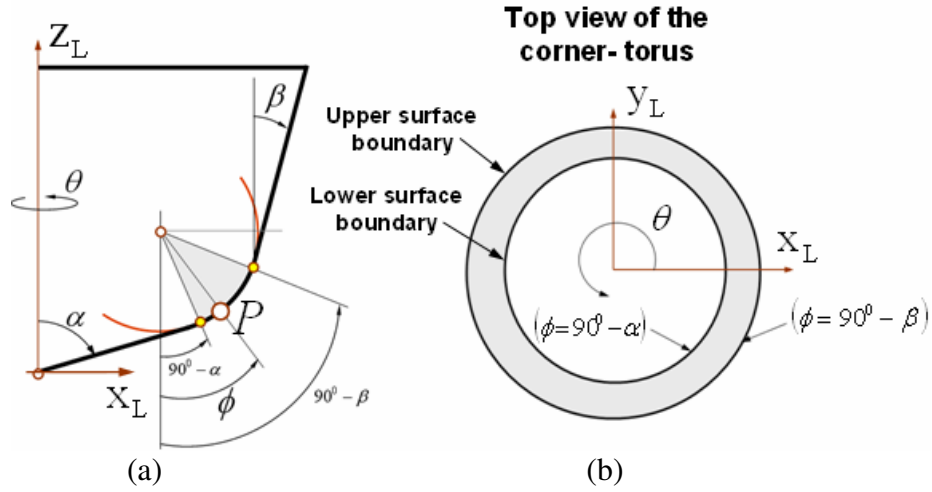


Figure 5.10: The corner-torus with upper and lower surface boundaries.

- **Cutter has a feed angle ( $\psi = \beta$ )**

In this case the angle between the feed vector  $\mathbf{f}$  and  $\mathbf{z}_L$  axis equals to  $\beta$  and the cutter has an ascending motion. For this feed angle the dot products in Eqs. (5.44,a-b) are evaluated as follows

$$\mathbf{f} \cdot \mathbf{z}_L = |\mathbf{f}| |\mathbf{z}_L| \cos \beta \quad \mathbf{f} \cdot \mathbf{x}_L = |\mathbf{f}| |\mathbf{x}_L| \cos(90^\circ - \beta)$$

Plugging the above equations back into Eqs. (5.44-a, b) yields

$$\theta_{1,2}^L = \mp \cos^{-1} \left( \frac{\tan \alpha}{\tan \beta} \right) \quad (5.45-a)$$

$$\theta_{1,2}^U = 0^\circ \quad (5.45-b)$$

Note that when the lower and the upper limits of  $\phi$  are equal to each other i.e.  $(90^\circ - \alpha) = (90^\circ - \beta)$ , the corner-torus disappears from the generic cutter. For the corner-torus geometry to be present, the inequality  $(\beta < \alpha)$  must hold and thus under this consideration  $(\tan \beta < \tan \alpha)$ . In calculations these inequalities will be used frequently. The ratio inside the parenthesis of Eq. (5.45-a) is greater than one and thus the inverse cosine function does not have a real solution. In Eq. (5.45-b)  $\theta$  has repeated roots of zeros.

From the above results it can be concluded that when the generic cutter moves with the feed angle equal to  $\beta$ , the envelope boundary of the corner-torus contains only *one point* which corresponds to angles  $\phi^U = (90^\circ - \beta)$  and  $\theta_{1,2}^U = 0^\circ$ . In Figure (5.11-a), F1 represents this point which is located on the front face of the corner-torus. Thus this proves the proposition (5.1) for this motion type.

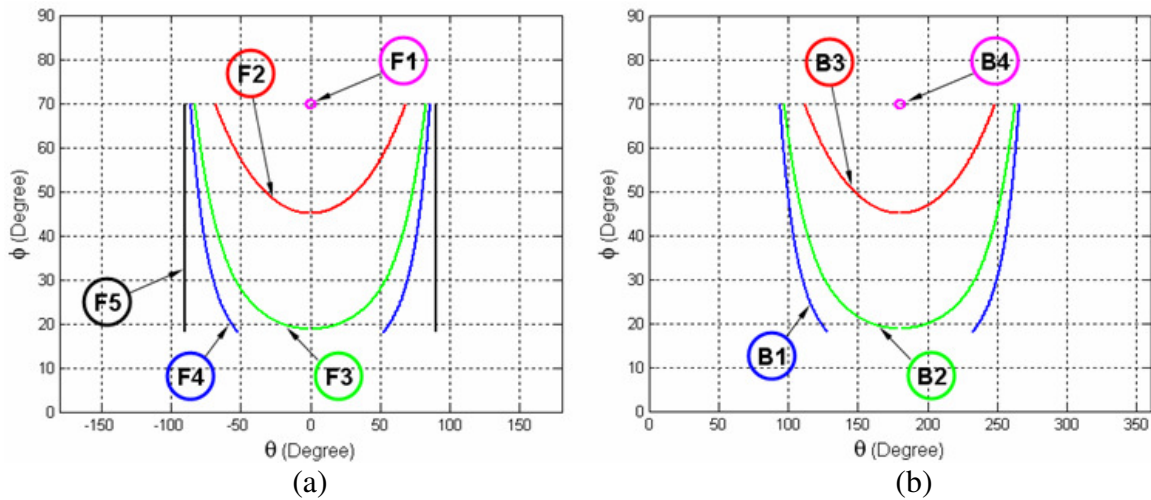


Figure 5.11: Envelope boundary sets on the (a) front, and the (b) back faces of the corner-torus.

▪ **Cutter has a feed angle ( $\psi = \alpha$ )**

In this case the cutter is performing an ascending motion with a feed angle equals to  $\alpha$ . After evaluating Eqs. (5.44-a, b) with  $\alpha$ , the following equations are obtained

$$\theta_{1,2}^L = 0^\circ \tag{5.46-a}$$

$$\theta_{1,2}^U = \mp \cos^{-1} \left( \frac{\tan \beta}{\tan \alpha} \right) \tag{5.46-b}$$

The ratio inside the parenthesis of Eq. (5.46-b) is positive and less than one. Therefore for a given parameter set  $\phi^U = (90^\circ - \beta)$  and  $\theta_{1,2}^U$  the upper surface boundary of the corner-torus contains two points which are members of the envelope boundary. These are two symmetric points with respect to the feed vector and they are located on the front face of the corner-torus. The repeated roots in Eq. (5.46-a) and the lower limit of  $\phi$ ,  $\phi^L = (90^\circ - \alpha)$  generate a point on the lower surface boundary of the corner-torus. This single point which is also a member of the envelope boundary is located on the front face. From these results it can be seen that the upper and the lower surface boundaries of the corner-torus contain envelope boundary points on the front face. Therefore it can be concluded that changing  $\phi$  between  $\phi^L = (90^\circ - \alpha)$  and  $\phi^U = (90^\circ - \beta)$  generates new envelope boundary points on the front face. F3 in Figure (5.11-a) shows an example of the envelope boundary for this motion.

Thus for this motion type the envelope boundary on the front face and the portion of the upper surface boundary on the front face draw the limits of the point set  $CWE_K$ . Thus this proves the proposition (5.1) for this motion type. F3 in Figure (5.12) illustrates the point set  $CWE_K$  with shaded area.

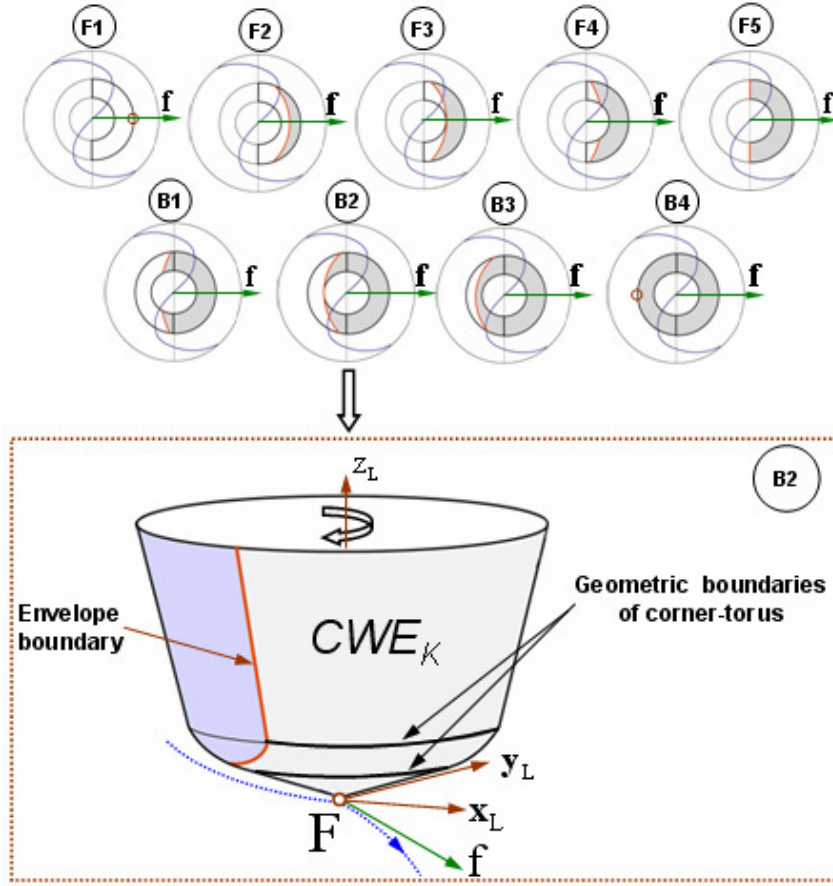


Figure 5.12: Feasible contact surfaces of the toroidal part with respect to the cutter feed angle.

- **Cutter has a feed angle ( $\psi = 180^\circ - \alpha$ )**

In this and the following case the cutter has a plunging motion with respect to feed vector. When the feed angle  $\psi = 180^\circ - \alpha$  is plugged into Eqs. (5.44-a, b), the following results are obtained

$$\theta_{1,2}^L = \mp 180^\circ \quad (5.47-a)$$

$$\theta_{1,2}^U = \mp \cos^{-1} \left( \frac{\tan \beta}{-\tan \alpha} \right) \quad (5.47-b)$$

In Eq.(5.47-a), the lower limit of  $\theta$  has two real solutions  $\mp 180^\circ$ . These two solutions and the lower limit of  $\phi$ ,  $\phi^L = (90^\circ - \alpha)$  generate only one point on the lower surface boundary of the

corner-torus. This point which also belongs to the envelope boundary is located on the back face. The ratio inside the parenthesis of Eq. (5.47-b) is greater than -1 and therefore there are two distinct real solutions for the upper limit of  $\theta$ . These solutions and the upper limit of  $\phi$ ,  $\phi^u = (90^\circ - \beta)$  produce two distinct points on the upper surface boundary of the corner-torus. These points which are members of the envelope boundary are located on the back face. Therefore by changing  $\phi$  between its limits other envelope boundary points are generated on the back face. In Figure (5.11-b), B2 represents the envelope boundary for this motion type. The limits of the point set  $CWE_K$  are defined by the envelope boundary on the back face and the portion of the upper surface boundary on the front face. Thus this proves the proposition (5.2). B2 in Figure (5.12) illustrates the point set  $CWE_K$  with shaded area.

▪ **Cutter has a feed angle ( $\psi = 180^\circ - \beta$ )**

With this feed angle Eqs. (5.44, a-b) take the following form

$$\theta_{1,2}^L = \mp \cos^{-1} \left( \frac{\tan \alpha}{-\tan \beta} \right) \quad (5.48-a)$$

$$\theta_{1,2}^U = \mp 180^\circ \quad (5.48-b)$$

Because the ratio in Eq.(5.48-a) is less than -1, there is no real solution for the lower limit of  $\theta$ . The upper limit has two solutions in Eq. (5.48-b). These solutions and the upper limit of  $\phi$ ,  $\phi^u = (90^\circ - \beta)$  produce only one point on the upper surface boundary of the corner-torus. B4 in Figure (5.11-b) shows this point on the back face. For this motion it can be said that even there is only one envelope boundary point, the whole surface of the corner-torus contains points from the set  $CWE_K$ . B4 in Figure (5.12) illustrates the point set  $CWE_K$  with shaded area. For clearly seeing this situation the tangency function in Eq. (5.18) is utilized for the corner torus. Under the 3-axis machining the tangency function of the corner-torus takes the following form

$$f(\theta, \phi, t) = -\cos \phi (\mathbf{f} \cdot \mathbf{z}_L) + \cos \theta \sin \phi (\mathbf{f} \cdot \mathbf{x}_L) + \sin \theta \sin \phi (\mathbf{f} \cdot \mathbf{y}_L) \quad (5.49)$$

When the Eq. (5.49) is evaluated for the feed angle  $\psi = 180^\circ - \beta$ , it yields

$$f(\theta, \phi, t) = |\mathbf{f}| (\cos \phi \cos \beta + \sin \phi \sin \beta \cos \theta) \quad (5.50)$$

where  $\theta \in [0, 2\pi]$  and thus  $\cos \theta \in [-1, 1]$ . Note that because the feed vector  $\mathbf{f}$  and  $\mathbf{y}_L$  axis of *TCS* are orthogonal, their dot product is equal to zero. According to Eq. (5.43) it can be said that  $\cos \phi \geq \sin \beta$  and  $\cos \beta \geq \sin \phi$ . When these inequalities are evaluated in Eq. (5.50) the tangency function becomes  $f(\theta, \phi, t) \geq 0$ , where  $\phi \in [90^\circ - \alpha, 90^\circ - \beta]$ . Therefore the whole surface of the corner-torus contains the point set  $CWE_K$ . Thus this proves the proposition (5.2). B4 in Figure (5.12) illustrates the point set  $CWE_K$  with shaded area.

Also the upper and the lower cone surface patches of the generic cutter may have feasible contact surfaces (*FCS*). The distribution of *FCS* on these surfaces can be analyzed using the same steps taken for the corner-torus. Table (5.2) shows the distribution of *FCS* on each surface patch of the generic cutter with respect to the motion types defined in Table (5.1).  $CWE_{K,U}$ ,  $CWE_{K,T}$  and  $CWE_{K,L}$  represent the feasible engagement point sets of the upper-cone, the corner-torus and the lower-cone surface respectively. If for a given feed angle, the surface patch does not contain any point from the *FCS*, the symbol  $\{ \}$  is used for representing this situation. For example, in Table (5.2) for the feed angle in F2 only the upper-cone and the corner-torus surfaces have *FCS* and thus during the material removal only these surfaces can contact the in-process workpiece.

Range	Upper-Cone	Corner-Torus	Lower-Cone
F1	{}	{}	{}
F2	$CWE_{K,U}$	$CWE_{K,T}$	{}
F3	$CWE_{K,U}$	$CWE_{K,T}$	{}
F4	$CWE_{K,U}$	$CWE_{K,T}$	$CWE_{K,L}$
F5	$CWE_{K,U}$	$CWE_{K,T}$	$CWE_{K,L}$
B1	$CWE_{K,U}$	$CWE_{K,T}$	$CWE_{K,L}$
B2	$CWE_{K,U}$	$CWE_{K,T}$	$CWE_{K,L}$
B3	$CWE_{K,U}$	$CWE_{K,T}$	$CWE_{K,L}$
B4	$CWE_{K,U}$	$CWE_{K,T}$	$CWE_{K,L}$

Table 5.2:  $CWE_K$  point sets of the generic cutter under different tool motions.

## 5.5 Discussion

In this chapter the engagement behaviors of NC cutter surfaces under varying tool motions have been presented by introducing *the feasible contact surfaces (FCS)* terminology. The description of the *FCS* has been made by utilizing the kinematically feasible engagement points contained in the set  $CWE_K$ . In a typical NC cutter the constituent surface geometries show differences and because of this during the machining the engagement characteristics for these surfaces become different. Under this consideration the set  $CWE_K$  has been partitioned among the constituent surfaces of a cutter. As mentioned in this chapter, the Cutter Workpiece Engagements (*CWEs*) are the subsets of the *FCS* and for calculating *CWEs* the boundaries of the *FCS* must be identified. In this work these boundaries which are limits of the set  $CWE_K$  have been defined by the cutter surface boundaries and the envelope boundaries. Under the rigid tool motions the cutter surface boundaries stay fixed. But on the other hand the envelope boundaries may change. For modeling the envelope boundaries a tangency function defined by the surface normal and the tool velocity has been utilized. Later by changing the tool velocity direction the distributions of the *FCS* on the cutter have been analyzed. Also it has been shown with examples that only the certain parts of the cutter surfaces have contacts with the in-process workpiece. The results from this chapter will be used in the *CWEs* generation.

## Chapter 6

### Cutter Workpiece Engagements

In this chapter the methodologies for obtaining Cutter Workpiece Engagements (*CWEs*) in milling are presented. Cutting forces are a key input to simulating the vibration of machine tools (chatter) prior to implementing the real machining process. These forces are determined by the feed rate, spindle speed, and *CWEs* (captures the depth of cut). Of these finding the *CWE* is most challenging due to the complex geometry of the in-process workpiece and varying tool motions. The *CWE* geometry defines the instantaneous intersection boundary between the cutting tool and the in-process workpiece at each location along a tool path. Figure (6.1) summarizes the steps involved in *CWE* extraction. Inputs from CAD/CAM include the tool paths in the form of a CL Data (cutter location data) file, geometric description of the cutting tool and a geometric representation (B-rep, polyhedral, vector based model) of the initial workpiece. The key steps which are the swept volume generation and the in-process workpiece update have been presented in the previous chapters.

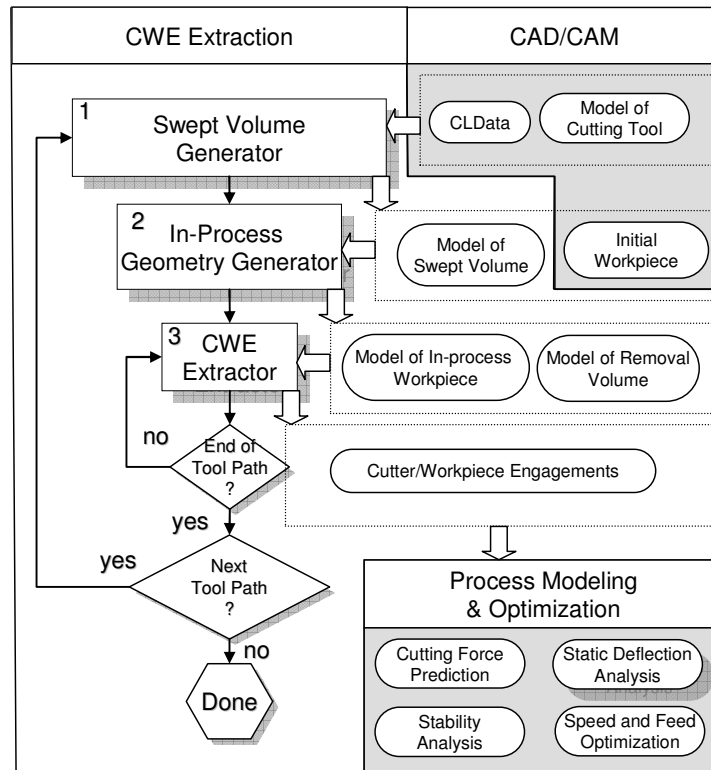


Figure 6.1: *CWE* Extraction Steps

In this chapter the *CWEs* are calculated for supporting the force prediction model described in [5]. This model finds the Cartesian force components by analytically integrating the differential cutting forces along the in-cut portion of each cutter flute. In this model *CWE* area with a fixed axial depth of cut is defined by mapping the engagement region on the cutter surface onto X - Y plane which represents the engagement angle versus the depth of cut respectively (Figure 6.2).

Figure 6.2 has been removed due to copyright restrictions. The information removed is *CWE* area for the force prediction, [5].

In this chapter the methodologies for finding the *CWEs* are developed based on the mathematical representation of the workpiece geometry. The workpiece geometries are defined by a solid, a polyhedral and a vector based modeler respectively. Although polyhedral and vector based approaches require a shorter computational time than does the solid modeler based approach, the accuracy of these approaches depends greatly on the resolution of the workpiece. There is always a tradeoff between computational efficiency and accuracy in these approaches. For example the solid modeler has an advantage in accuracy because it provides an accurate geometric representation for the workpiece. Therefore in the solid modeler based approach the most accurate representations of the *CWEs* are obtained. But on the other hand this modeler uses numerical techniques that are limited primarily by efficiency and robustness.

The Cutter Workpiece Engagements in Solid Models are presented in section (6.1). This section contains two methodologies: Engagement Extraction Methodology in 3-Axis Milling (section 6.1.1) and Engagement Extraction Methodology in 5-Axis Milling (section 6.1.3) respectively. In the 3-axis milling methodology the cutter surfaces are decomposed with respect to the feed direction as explained in chapter (5), and then these decomposed surfaces are intersected with their removal volumes for obtaining the closed *CWE* area. In the 5-axis methodology the similar approach is utilized with one difference. In this case the in-process workpiece is used instead of cutter removal volumes. The developed solid modeler based methodologies are implemented using ACIS solid modeling kernel. The both methodologies are supported by examples.

The Cutter Workpiece Engagements in Polyhedral Models are presented in section (6.2). Also this section contains two methodologies. In the 3-axis *CWE* methodology (section 6.2.1) the chordal error problem described in chapter (1) is addressed. For finding the *CWEs* a polyhedral representation of the removal volume is mapped from Euclidean space into a parametric space. Thus *CWE* calculations are reduced to line-plane intersections. In this methodology the formulas are developed for the linear, circular and helical toolpaths. For the 5-axis milling a direct triangle/surface intersection approach (section 6.2.2) is developed. In this approach for generating *CWE* area, without doing mapping the cutter surface is intersected with the triangular facets obtained from the in-process workpiece. The Cutter Workpiece Engagements in Vector Based Models are presented in section (6.3). In this methodology the workpiece geometry is broken into a set of evenly distributed discrete vectors and also the cutter is discretized into slices perpendicular to the tool axis. For generating *CWEs* the intersections are performed between discrete vectors and cutter slices. Finally the chapter ends with the discussion in section (6.4).

### **6.1 Cutter Workpiece Engagements in Solid Models**

This section presents Solid modeling methodologies for finding Cutter Workpiece Engagements (*CWEs*) generated during 3 and 5-axis machining of free – form surfaces using a range of different types of cutting tools and tool paths. Figure (6.3) summarizes the steps involved in *CWE* extraction using B-rep based solid modeler. Inputs from CAD/CAM include the tool paths in the form of a CL Data (cutter location data) file, geometric description of the cutting tool and a geometric representation (B-rep) of the initial workpiece. Key steps include swept and removal volume generation for each tool path. Although computational complexity and robustness, for limited applications, remain issues that need to be addressed, solid modelers have been recognized as one approach to finding *CWE* geometry. Solid modelers have an advantage in accuracy because they generate the exact mathematical representation for the intersections. The methodologies in this section have been implemented using a commercial geometric modeler (ACIS) which is selected to be the kernel around which the geometric simulator is built. In these approaches, in-process workpiece updating and cutter/workpiece engagement extraction are performed using geometric and topologic algorithms within the solid modeler kernel. In these situations the

solid modeling approach applies numerical surface intersection algorithms which are based on subdivision, and curve tracing (marching) methods.

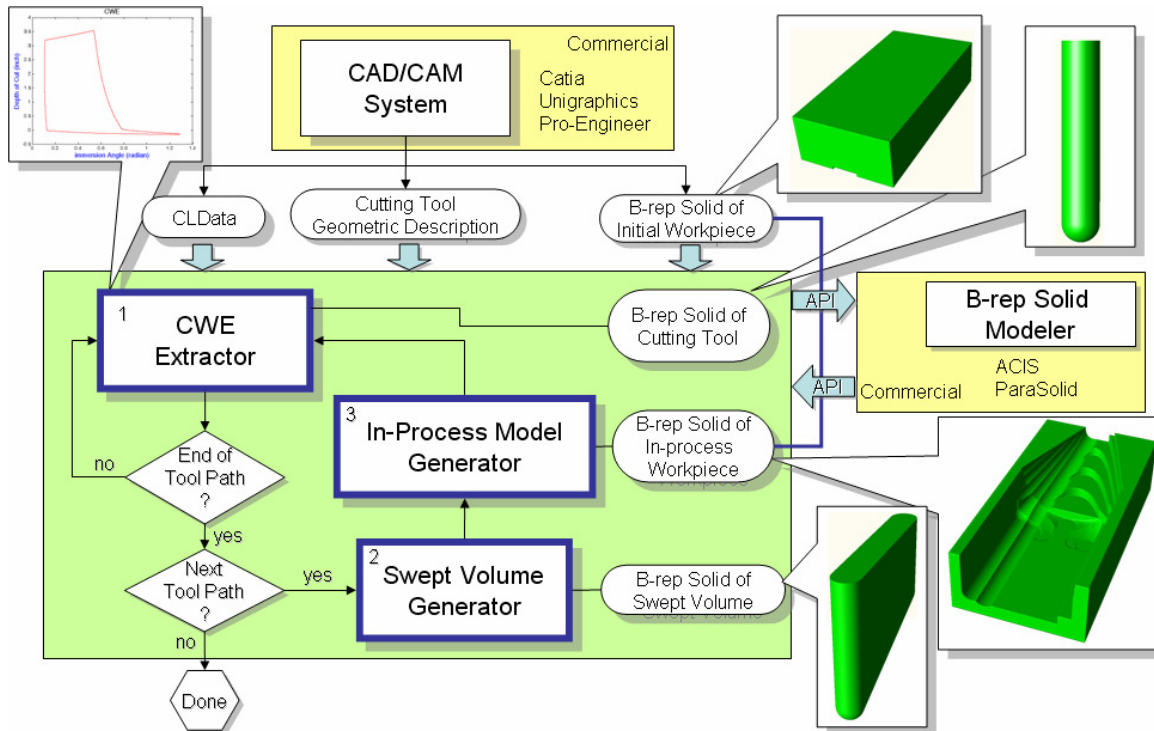


Figure 6.3: A B-rep Solid Modeler based *CWE* extraction

### 6.1.1 Engagement Extraction Methodology in 3-Axis Milling

This section presents a B-rep Solid modeler based methodology for finding *CWEs* generated during 3-axis machining. For this purpose cutter surfaces are decomposed with respect to the tool feed direction and then they intersected with their removal volumes for obtaining the boundary curves of the closed *CWE* area in 3D Euclidian space. Later these boundary curves are mapped from Euclidean space to a parametric space defined by the *engagement angle* and the *depth-of-cut* for a given tool geometry.

As explained in chapter (5), a typical NC cutter has different surfaces with varying geometries and during the machining the engagement characteristics of each surface become different. Under this consideration in this section the kinematically feasible engagement points  $CWE_K$  are divided into constituent sub sets. The primary task in finding the *CWE* geometry is finding the boundary of the engagement region. The boundary set of *CWE* is

represented by  $bCWE$ . This defines the geometry required for input to process modeling (i.e. force prediction). Thus

$$bCWE(t) \subset CWE(t) \subset CWE_K(t) \quad (6.1)$$

These three sets are illustrated in (Figure 6.4) for the Flat-End mill performing a helical tool motion. In this figure the sets  $bCWE$ ,  $CWE$  and  $CWE_K$  are shown separately for the side (cylindrical) face and the bottom (flat) face of the Flat-End mill.

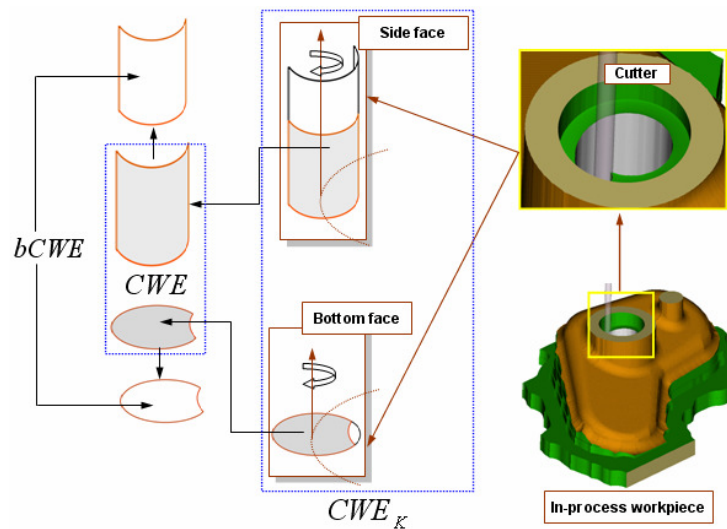


Figure 6.4: Point sets used in defining Engagements

For the force model described in [5] in-cut segments of the cutting edges are needed. In this section for obtaining in-cut segments both  $bCWE$  and the cutting edges are mapped into 2D space defined by the *engagement angle* ( $u$ ) and the *depth of cut* ( $v$ ). Then the curve/curve intersection is performed between  $bCWE$  and the cutting edges. The common milling cutters have different surface geometries i.e. a Ball-End mill is defined by two natural quadric surfaces – spherical and cylindrical. As a result of this the parameterization of the engagement area differs for each cutter surface. In the Flat-End mill, for example, the depth of cut  $v$  for an arbitrary point  $\mathbf{P} \in CWE$  is the distance between the location of  $\mathbf{P}$  and the cutter tool tip along the tool rotation axis, and the engagement angle  $u$  is measured from the  $y_L$  axis of  $TCS$  (Figure 6.5).

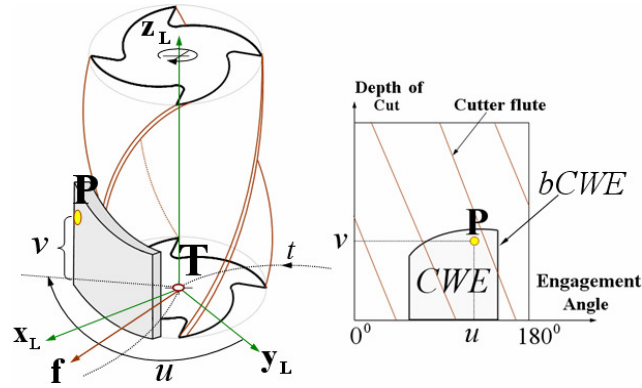


Figure 6.5: CWE parameters of an arbitrary point  $\mathbf{P}$ .

The engagement parameters for different cutter surfaces are illustrated in Figure (6.6). Because the Flat-End, the Taper-End and the Fillet-End cutters have a flat surface at their bottom, also in this figure the engagement parameters of the cutter bottom surface are shown. As explained in chapter (5), when the feed angle is in the range of (B1 to B4) the cutter bottom surface can have contact with the workpiece during the machining.

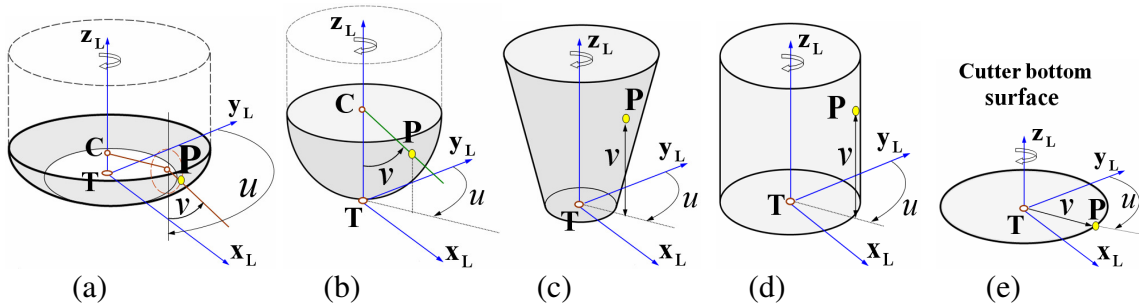


Figure 6.6: Defining  $CWE$  parameters  $u$  and  $v$  on (a) torus, (b) sphere, (c) frustum of a cone, (d) cylinder, and (e) flat bottom surfaces of common milling cutters.

It has been shown in chapter (5) for the 3-axis machining that according to the feed angle ranges the cutter can have three types of motion: Ascending type (F1 to F4), Horizontal type (F5) and Descending type (B1 to B4). These motion types effect the construction of the kinematically feasible engagement point set  $CWE_K$  and consequently this changes the angular ranges of the engagement parameter  $u$  as follows

- If the feed angle is in the range of (F1 to F5) only the front face of the cutter can have contact with the workpiece and the engagement angle  $u$  covers  $[0, \pi]$  range i.e.  $0 \leq u(\mathbf{P} | \mathbf{P} \in CWE) \leq \pi$ .

- If the feed angle is in the range of (B1 to B4), both the front and the back faces of the cutter can have contact with the workpiece. This time the range of the engagement angle  $u$  becomes:  $0 \leq u(\mathbf{P} | \mathbf{P} \in CWE) \leq 2\pi$

The two cases above show that based on the kinematics of the 3-axis machining the cutter surfaces differently contribute to the  $CWE$  extraction. For this reason cutter surfaces are broken down into their constituent sub surfaces. It has been shown in chapter (5) that, the front and the back surfaces are separated by an unbounded plane which passes through  $\mathbf{y}_L$  and  $\mathbf{z}_L$  axes of  $TCS$ . Also if the cutter has a flat bottom surface then this surface lies on another unbounded plane which passes through  $\mathbf{x}_L$  and  $\mathbf{y}_L$  axes of  $TCS$ . This decomposition is shown for the Taper-End and Flat-End mills in Figure (6.7), where  $G_{Back}$ ,  $G_{Bottom}$  and  $G_{Front}$  represent the constituent sub surfaces of the cutter geometry  $G$ . Table (6.1) shows the decomposition of the surface geometries for the common milling tools.

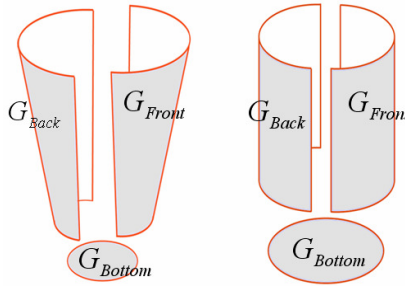


Figure 6.7: Geometric decomposition of the cutter surfaces

Surface geometry	Constituent surfaces
<b>Torus</b>	$G_{Back}$ , $G_{Bottom}$ , $G_{Front}$
<b>Sphere</b>	$G_{Back}$ , $G_{Front}$
<b>Frustum of a cone</b>	$G_{Back}$ , $G_{Bottom}$ , $G_{Front}$
<b>Cylinder</b>	$G_{Back}$ , $G_{Bottom}$ , $G_{Front}$

Table 6.1: Constituent surfaces of cutter geometries after geometric decomposition in 3-axis milling.

Each constituent surface of a cutter geometry given in the Table (6.1) generates its kinematically feasible engagement point set with respect to the cutter feed vector. For example when a Fillet-End mill has a descending motion described by (B1 to B4) all three

constituent surfaces of the toroidal part:  $G_{Back}$ ,  $G_{Bottom}$  and  $G_{Front}$  generate the sets  $CWE_{K,Back}$ ,  $CWE_{K,Bottom}$  and  $CWE_{K,Front}$  respectively (see Figure 6.8). Thus the following equation can be written for a toroidal part performing this motion

$$CWE_K = CWE_{K,Back} \cup^* CWE_{K,Bottom} \cup^* CWE_{K,Front} \quad (6.2)$$

where  $\cup^*$  and later  $\cap^*$  represent regularized Boolean union and intersection set operations respectively.

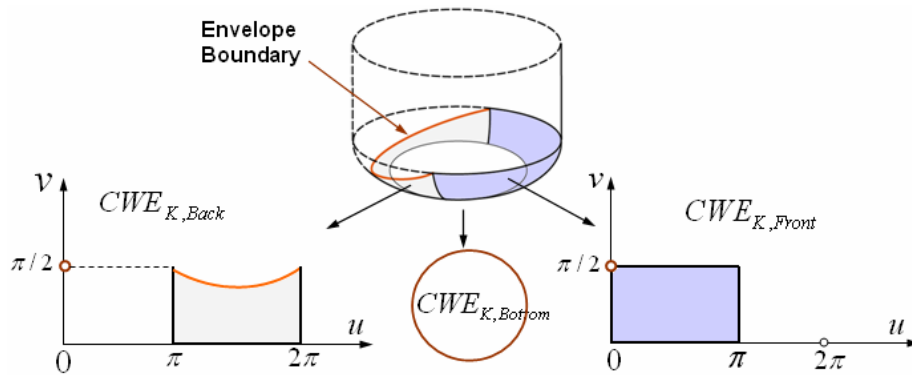


Figure 6.8: Decomposing the point set  $CWE_K$  of the torus into three parts.

Note that depending on the motion type some of these subsets can be empty. For example in the ascending motion (F1 to F5) only the front part of the cutter engages with the workpiece and therefore only the set  $CWE_{K,Front}$  is considered as a full set. Table (6.2) shows these three sets for different cutter geometries with respect to the feed angle ranges. The symbol  $\emptyset$  represents an empty set for a given feed angle range.

Surface Geometry	(F1 to F5)			(B1 to B4)		
	$CWE_{K,Back}$	$CWE_{K,Bottom}$	$CWE_{K,Front}$	$CWE_{K,Back}$	$CWE_{K,Bottom}$	$CWE_{K,Front}$
<b>Torus</b>	$\emptyset$	$\emptyset$	Full	Full	Full	Full
<b>Sphere</b>	$\emptyset$	$\emptyset$	Full	Full	$\emptyset$	Full
<b>Frustum</b>	$\emptyset$	$\emptyset$	Full	Full	Full	Full
<b>Cylinder</b>	$\emptyset$	$\emptyset$	Full	$\emptyset$	Full	Full

Table 6.2: Feasible engagement points for cutter surfaces with respect to the tool motions

The following properties (6.1) and (6.2) motivate finding the Cutter Workpiece Engagements in 3-axis milling.

**Property 6.1:** Given a tool path  $T_i$  for the  $i^{\text{th}}$  tool motion and the cutter surface geometry:

**a)** Sweeping the point sets  $CWE_{K,Back}$ ,  $CWE_{K,Bottom}$  and  $CWE_{K,Front}$  along  $T_i$  generates the swept volumes of the corresponding cutter surfaces i.e.  $SV_i$  (Back),  $SV_i$  (Bottom) and  $SV_i$  (Front) respectively. For a given tool motion and the cutter surface geometry the constituent parts of the set  $CWE_K$  are chosen from the Table (6.2) for sweeping. For example Figure (6.9) illustrates this for the Fillet-End mill which follows a linear toolpath in descending motion (B1 to B4).

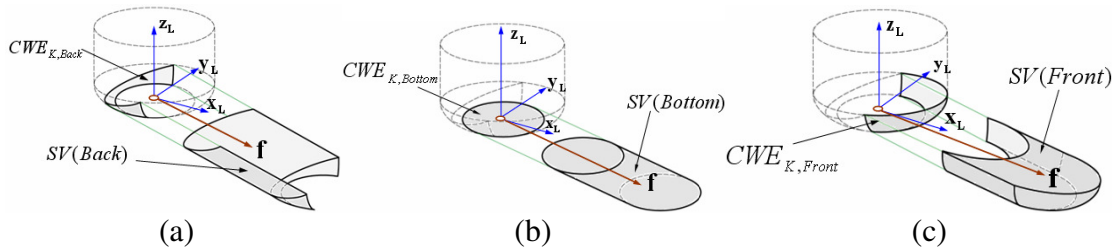


Figure 6.9: Swept volumes generated by the kinematically feasible engagement point sets.

**b)** Intersecting the swept volumes from the property 1(a) with the in-process workpiece  $W_{i-1}$  generates the removal volumes as follows

$$\begin{aligned}
 W_{i-1} \cap^* SV_i(Back) &\rightarrow RV_i(Back) \\
 W_{i-1} \cap^* SV_i(Bottom) &\rightarrow RV_i(Bottom) \\
 W_{i-1} \cap^* SV_i(Front) &\rightarrow RV_i(Front)
 \end{aligned} \tag{6.3}$$

where  $RV_i(\cdot)$  represents the corresponding removal volume of each swept volume. Note that for the  $i^{\text{th}}$  tool motion the total removed material from the in-process workpiece can be denoted as follows

$$RV_i = RV_i(Back) \cup^* RV_i(Bottom) \cup^* RV_i(Front) \tag{6.4}$$

**Property 6.2:** The intersection of constituent surfaces  $G_{Back}$ ,  $G_{Bottom}$  and  $G_{Front}$  with their corresponding removal volumes  $RV_i(.)$  generates the cutter workpiece engagement boundary  $bCWE_i$  for the given cutter location as follows

$$\begin{aligned}
 bCWE_i = & \{G_{Back} \cap^* RV_i(Back)\} \cup^* \\
 & \{G_{Bottom} \cap^* RV_i(Bottom)\} \cup^* \\
 & \{G_{Front} \cap^* RV_i(Front)\}
 \end{aligned} \tag{6.5}$$

The 3-axis  $CWE$  extraction methodology is summarized in Figure 6.10. The inputs are  $i^{\text{th}}$  toolpath segment  $T_i$ , in-process workpiece  $W_{i-1}$  and the constituent surfaces of the cutter geometry  $G$ .

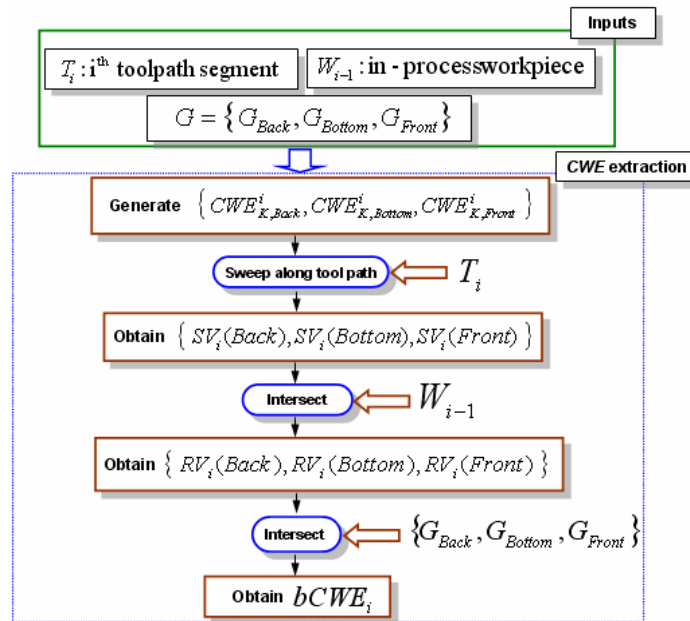


Figure 6.10: Procedure for obtaining the  $CWEs$

The reported method has been implemented using a commercial geometric modeler (ACIS) which is selected to be the kernel around which the geometric simulator is built. In the described methodology for generating the  $bCWEs$ , the face-face intersections between cutter surfaces and the removal volume surfaces are performed. For this purpose a given removal volume is decomposed into its faces by using ACIS function  $api\_get\_faces$ . The faces obtained from this function are intersected with the cutter surface which is also

represented as a FACE Entity. These intersections are performed by using the function *api\_fafa\_int*. For obtaining the cutter surface i.e.  $G_{Front}$ , first the circular wires which are perpendicular to the tool axis are generated along the tool axis and then they are skinned by using the function *api\_skin\_wires*. It has been shown in chapter (1) that ACIS representational hierarchy contains BODY, LUMP and SHELL etc. Therefore a body can be represented by LUMPs, a LUMP can be represented by SHELLs and so on. The function *api\_fafa\_int* generates intersection curves as a BODY Entity. For obtaining the properties of these curves i.e the start and end coordinates, these BODYs are decomposed into LUMPs, SHELLs, WIRES and EDGES respectively. The Algorithm (6.1) for this process is shown below in the C++ format. The inputs are  $RV_i(\text{Front})$ ,  $G_{Front}$  and a cutter location point  $P_{CL}$ . It generates the closed boundary set of the *CWE* area for the given cutter location point.

```

Input:  $RV_i(\text{front})$ ,  $G_{Front}$ ,  $P_{CL} (x_{CL}, y_{CL}, z_{CL})$ 
Output:  $bcWE_i$  at  $P_{CL}$ 

```

---

```

ENTITY_LIST face_list; // Container of removal volume faces
FACE *ff = api_get_faces( $RV_i(\text{front})$ , face_list); //points the first face of the face_list
FACE *cutter_face =  $G_{Front}$ ;
BODY *int_curve = NULL; //a member from  $bcWE$ 
LUMP *rem_vol_lump = NULL;
SHELL *rem_vol_shell = NULL;
WIRE *rem_vol_wire = NULL;
EDGE *rem_vol_edge = NULL;

while( (ff = (FACE*)face_list.next()) != NULL) { //iterates until all faces of the
//removal volume is processes

    api_fafa_int(cutter_face, ff, int_curve);
    rem_vol_lump = int_curve->lump();
    while(rem_vol_lump != NULL){
        rem_vol_shell = rem_vol_lump->shell();
        while(rem_vol_shell != NULL){
            rem_vol_wire = rem_vol_shell->>wire();
            while(rem_vol_wire != NULL){
                rem_vol_edge = rem_vol_wire->coedge()->edge();

                // process the edge here for obtaining  $bcWEs$ 

                rem_vol_wire = rem_vol_wire->next();
            }
            rem_vol_shell = rem_vol_shell->next();
        }
        rem_vol_lump = rem_vol_lump->next();
    }
    ff = ff->next();
}
}

```

Algorithm 6.1: Obtaining the closed boundaries of the *CWEs*

### 6.1.2 Implementation

Figures (6.11) and (6.12) show Flat-End and Taper-End mills removing material along a linear ramping tool path i.e. the tool moves in all three axes simultaneously. The removal volumes associated with the different cutter surfaces are separated. In the case of the Flat-End mill this gives the material removed by the cylindrical at the side and the flat at the bottom surfaces. Plots of *CWEs* at different Cutter Locations (CLs) are illustrated. These are obtained by intersecting the constituent surfaces of the cutter with their corresponding removal volumes. Two formats are used for plotting the *CWEs*. The first is an XY plot of depth-of-cut  $v$  (as measured from the tool tip point) versus engagement angle  $u$ . The second plot shows the engagement area of the cutter bottom surface in a polar format: cutter bottom radius  $r$  versus engagement angle  $u$ . In Figure (6.11) the Flat-End mill is performing a descending motion in which the feed angle is in the range of (B1 to B4). Thus both the cylindrical and the bottom surface remove material. For this motion type of the Flat End mill only the  $CWE_{K,Front}$  and the  $CWE_{K,Bottom}$  point sets are active. The XY plots show the engagement between zero and  $\pi$  for the front face, and polar plots show the engagement between zero and  $2\pi$  for the bottom flat face.

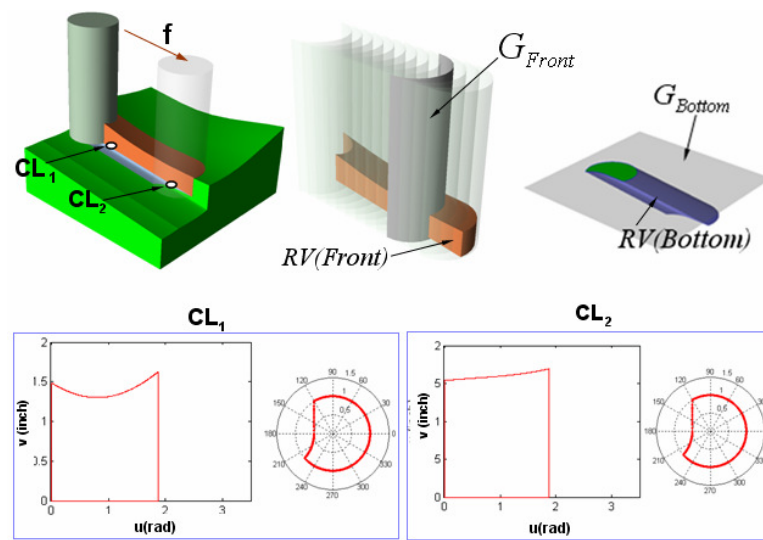


Figure 6.11: *CWEs* for the Flat End mill performing a linear 3-axis descending motion.

In Figure (6.12) because the Taper-End mill is ramping up in which the feed angle is in the range of (F1 to F5), only the point set  $CWE_{K,Front}$  is active during the material removal. Thus

for this motion type, only the front face of the cutter contributes to the  $CWE$  extraction procedure with the engagement angle  $u$  changes between zero and  $\pi$  radian.

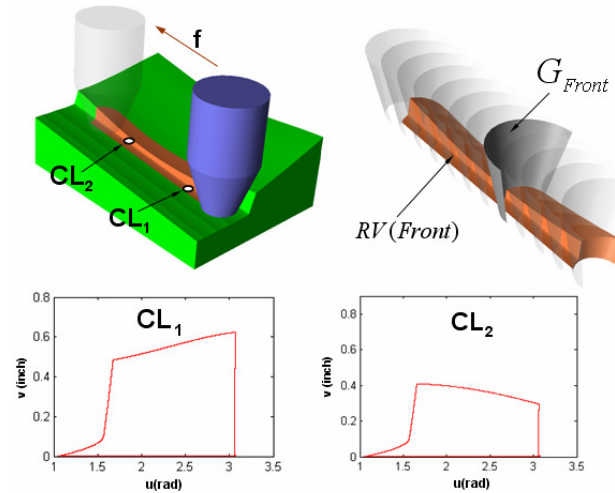


Figure 6.12:  $CWEs$  for the Taper-End mill performing a linear 3-axis ascending motion.

In the last example (Figure 6.13) a Flat-End mill is following a helical toolpath (plunging cutting) for enlarging a hole. In this example both the side and the bottom faces of the Flat-End mill are removing material. The cutter performs three half turns each corresponding to a  $0^\circ - 180^\circ$  range i.e. third turn has the starting angle  $360^\circ$  and ending angle  $540^\circ$ . In this motion of the Flat-End mill the point sets  $CWE_{K,Front}$  and  $CWE_{K,Bottom}$  are active. The total removed material  $RV(Front)$  and  $RV(Bottom)$  are shown for each half turn with different colors. For the cutter location  $CL_1$  both types of plots are shown because the bottom of the cutter is removing material at this location also. For  $CL_2$  only the side (cylindrical) face of the cutter has engagement with the workpiece.

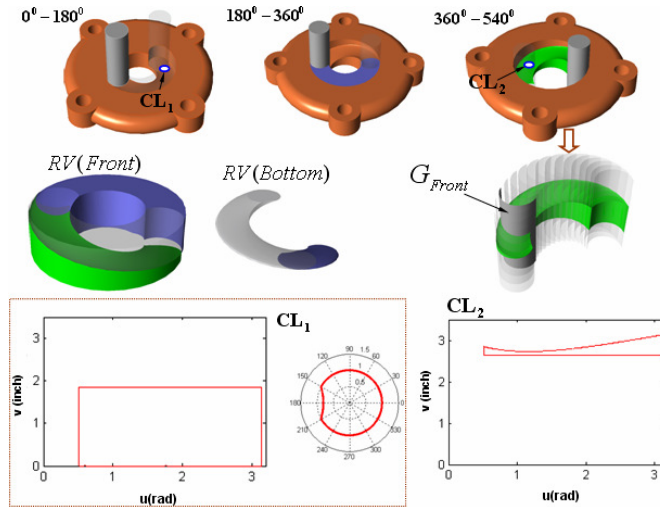


Figure 6.13: Helical Tool Motions with a Flat-End Mill and *CWEs*

### 6.1.3 Engagement Extraction Methodology in 5-Axis Milling

This section presents a B-rep Solid modeler based methodology for calculating *CWEs* in 5-axis milling operation. Many of the steps defined in the previous section for the 3-axis *CWE* methodology are applicable for the 5-axis *CWE* methodology in this section. There is only one main difference between these two methodologies. In 5-axis *CWE* methodology for obtaining *bcWEs* the feasible contact surface of a cutter will be intersected with the in-process workpiece instead of the removal volume which is used in the 3-axis *CWE* methodology. At any given instance of the 5-axis tool motion the bottom center and top center of the rigid cutter may move in directions that do not lie in the same plane. For example in Figure (6.14-a), the top velocity vector  $V_{Top}$  and the bottom velocity vector  $V_{Bottom}$  point to the different directions. An arbitrary velocity  $V$  on the tool axis can be calculated by linearly interpolating  $V_{Top}$  and  $V_{Bottom}$  as follows

$$\mathbf{V} = u \mathbf{V}_{Top} + (1 - u) \mathbf{V}_{Bottom} \quad (6.6)$$

where  $u \in [0,1]$ . On the other hand in 3-axis milling the top and bottom centers of the cutter move in the same direction (Figure 6.14-b).

As explained in chapter (5), a cutter contacts in-process workpiece through the set of  $CWE_K$ . Most of the points in this set lie towards the front of the cutter and are machined away as the tool leaves its current position. Only those points for which the motion direction

is perpendicular to the cutter surface normal are left behind on the machined surface as a curve. As explained in chapter (5), these points define the envelope boundary of the cutter which describes the geometric limits of the set  $CWE_K$ .

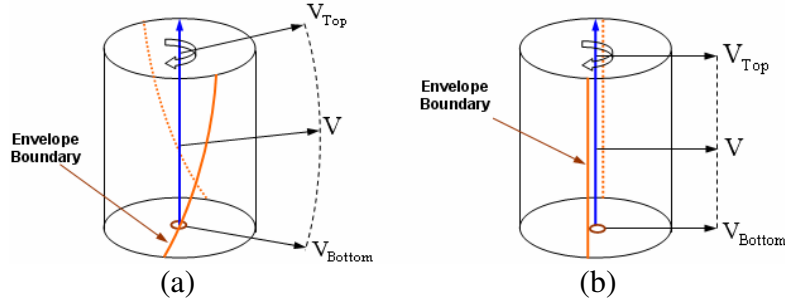


Figure 6.14: (a) Envelope boundary in 5-axis milling, and in (b) 3-axis milling respectively.

As explained in chapter (5), for defining the boundaries of the feasible contact surfaces (*FCS*) envelope boundary set is used. As illustrated in Figure (6.14-b) for the Flat-End mill performing 3-axis machining, because the top and the bottom velocity vectors of the cutter point to the same direction the envelope boundary has a linear characteristic. But on the other hand in the 5-axis tool motions the velocity vector on the cutter axis continuously changes and as a result the envelope boundary loses its linearity (see Figure 6.14-a). In this case the envelope boundary curves are approximated by splines. For example in the case of a Flat-End mill, these boundaries are represented by the helix like curves [12]. Because of the approximation in the envelope boundary curves the *CWE* methodology described for the 3-axis milling does not properly work for the 5-axis milling. The intersections obtained numerically by the B-rep solid modeler become non robust. For solving this problem a methodology based on the intersections between the *FCS* and the in-process workpiece is presented in this section. This methodology is explained for an impeller machining using a Taper-Ball-End mill and it can also be applied to other milling cutters performing 5-axis tool moves.

In Figure (6.15-a) a Taper-Ball-End mill is shown for a given Cutter Location (CL) point. At this CL point the feasible contact surface defined by the envelope and cutter surface boundaries is constructed (Figure 6.15-b). In the next stage (Figure 6.15-c) we offset this surface in the (+/-) directions of the velocity vector  $V$  with an infinitesimal amount ( $\epsilon/2$ ). This process makes this surface a volume which is called as *BODY*. To minimize the error

introduced by this offsetting the location of the vector  $V$  is taken in the middle of the tool axis. This causes a geometric error at both  $V_{Top}$  and  $V_{Bottom}$  in equal magnitude and zero error halfway between these two points.

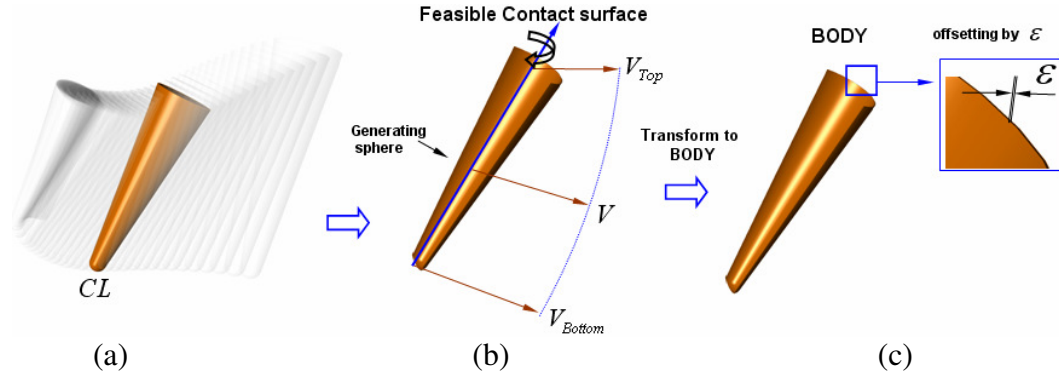


Figure 6.15: Offsetting the feasible contact surface

As illustrated in Figure (6.16) there are three main steps for generating the  $CWEs$ . In the first step the  $BODY$  obtained by offsetting the feasible contact surface is intersected with the in-process workpiece at a given cutter location point. This intersection generates a removal volume. In the second step the removal volume is decomposed into its constituent faces and between these faces and the feasible contact surface face/face intersections are performed. Each one of these intersections generates a curve. The full boundary of the  $CWE$  area,  $bCWE$  is the combination of each individual curve obtained from face/face intersections. Finally in the last step,  $bCWE$  represented in 3D Euclidian space is mapped into 2D space defined by the immersion (engagement) angle and the depth of cut. Note that these 3 steps are performed for each cutter location point on a toolpath segment.

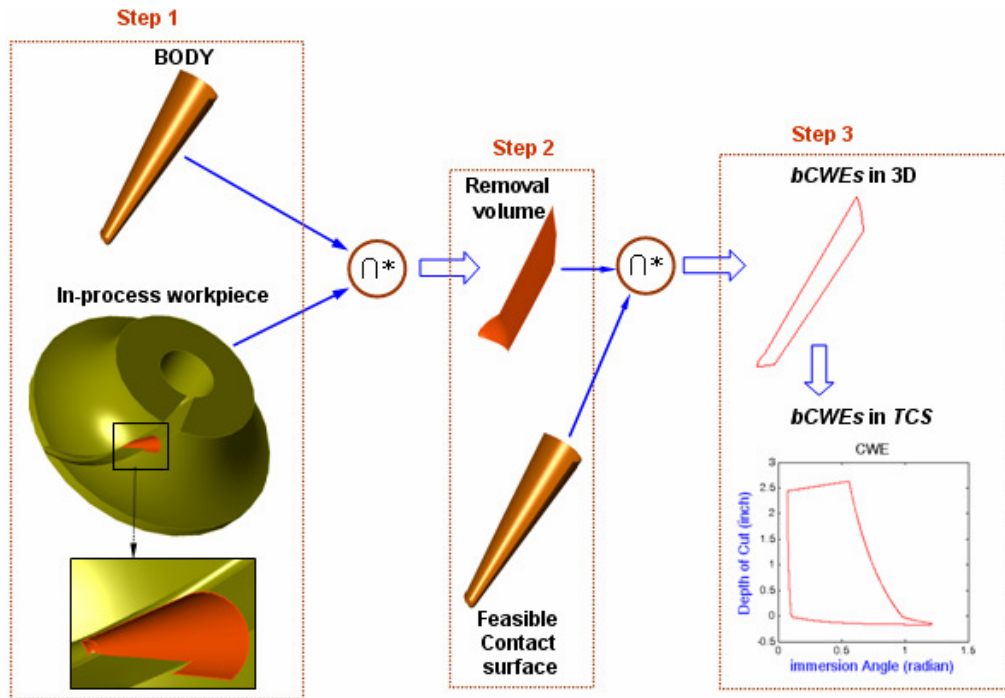


Figure 6.16: *CWE* steps in 5-axis milling methodology

The implementation of the 5-axis *CWE* methodology is illustrated in Figures (6.17) to (6.19) respectively. For this implementation the solid modeler kernel (ACIS) and C++ is used. The ACIS function *api\_get\_faces* decomposes the faces of the in-process workpiece. Then each one of these faces is intersected with the feasible contact surface utilizing the function *api\_fafa\_int*. For obtaining the closed boundaries of the *CWEs* the same procedure described in Algorithm (6.1) is followed. In Figures (6.17) and (6.18) for the given three cutter location points XY plots of depth-of-cut versus immersion angle are plotted. These examples are illustrated for the first and second passes of the cutter. Also in these figures the removal volumes for each passes are shown. From these two figures it can be seen that the amount of the removed material in the first pass is more than that of the second pass. In Figure (6.19) the in-process workpiece is shown after the third and fourth passes respectively.

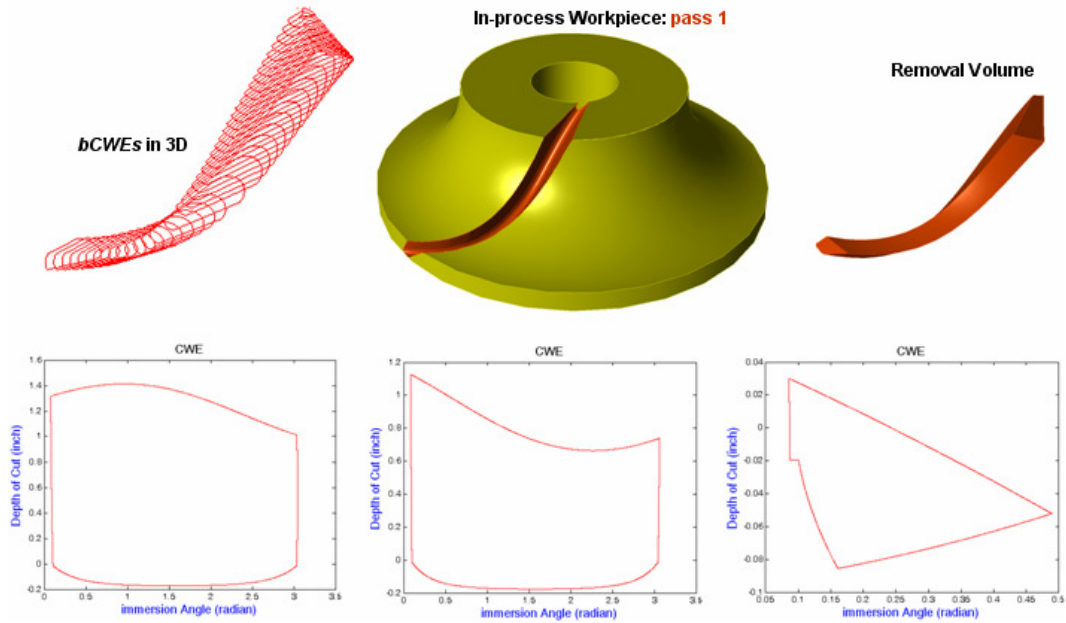


Figure 6.17: 5-axis *CWEs* during the first pass of the impeller machining

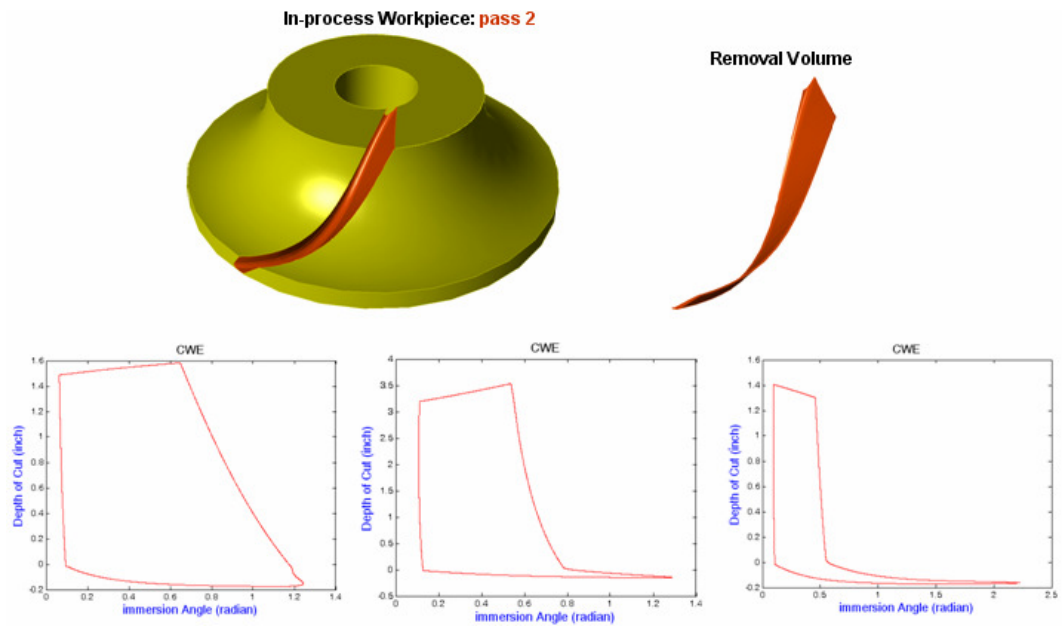


Figure 6.18: 5-axis *CWEs* during the second pass of the impeller machining

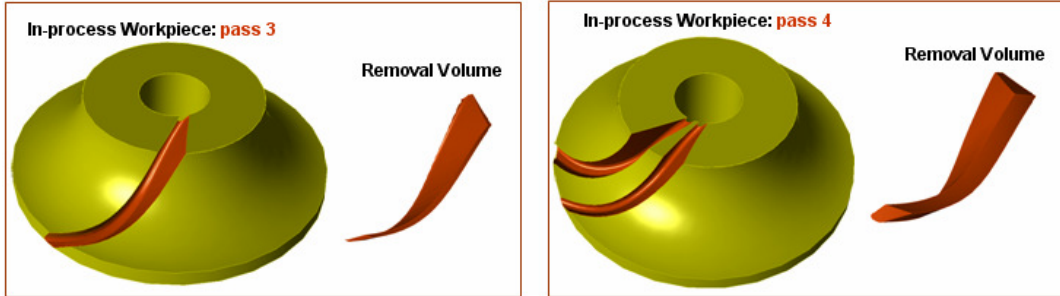


Figure 6.19: In-process workpieces after the third and fourth passes respectively.

## 6.2 Cutter Workpiece Engagements in Polyhedral Models

Polyhedral models provide the advantage of simplifying the workpiece surface geometry to planes which consist of linear boundaries. Thus the intersection calculations reduce to line / surface intersections. These can be performed analytically for the geometry found on cutting tools. For obtaining *CWE* area, facets which contain linear boundaries are intersected with the surface of the cutter and then the intersection points are connected to each other. If the cutter surface has the second order equation, e.g. cylinder, cone or sphere natural quadric surfaces, each line – surface intersection gives two roots. If the cutter surface has the fourth order equation e.g. torus, each line surface intersection gives four roots. In most cases only one of these roots are needed for obtaining the *CWEs* and the rest is redundant. *CWE* extraction algorithms must be robust enough to handle the complete set of intersection cases between the cutting tool and a triangular facet (see Figure 6.20).

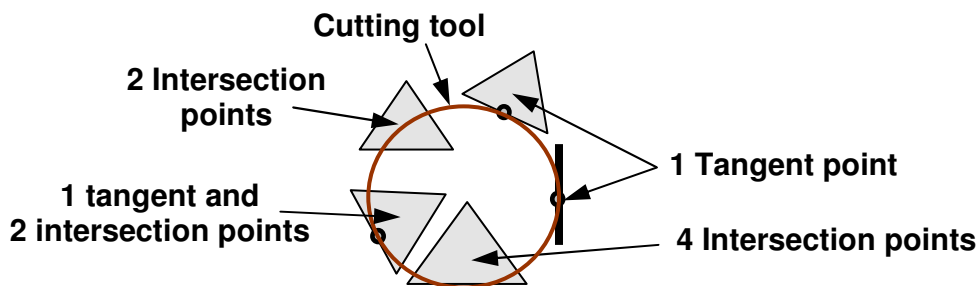


Figure 6.20: Typical intersections between a facet and a cutting tool

A major consideration in *CWE* extraction is the form of the in-process geometry. Beyond there being differences based on the type of model being used there is also a choice of using the in-process workpiece or the removal volume. Either can be generated by applying

Boolean operations between the swept volume for a tool path and the initial workpiece or in-process workpiece generated by the previous tool path (subtraction or intersection). The use of the removal volume instead of the in-process workpiece has a number of advantages:

- The size of the geometry model that must be manipulated by the *CWE* extraction algorithms is significantly smaller for the removal volume.
- The use of the removal volume model better supports parallel computation strategies for *CWE* extraction. The *CWEs* for each removal volume can be extracted independently. An agent based methodology that does just this is described in [85].

For these reasons the removal volume is used in the research described in this chapter to capture the in-process geometry.

Since a polyhedral model is an approximate representation of the exact analytical surface from which it was generated it would seem that similar accuracy issues to those found in the discrete modeling approaches exist. One example is illustrated in (Figure 6.21). Shown is the polyhedral model of a removal volume machined from the workpiece by a cylindrical end mill. The faceting algorithm that generates this model approximates surfaces to a specified chordal error. As can be seen from the 2D view this results in facets that lie outside the tool envelop at a given location even though the cutting tool is in contact with the actual removal volume surface. This facet should be considered in finding the *CWE* boundary but would be difficult to detect since it does not intersect with the tool geometry.

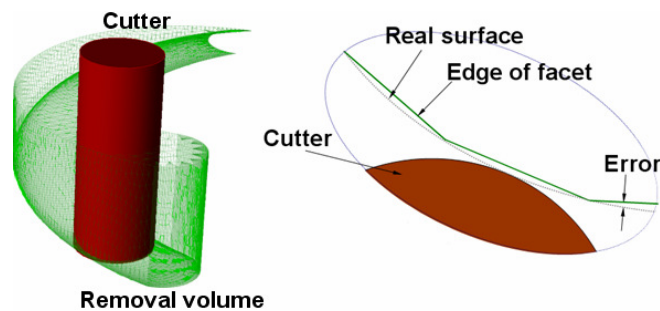
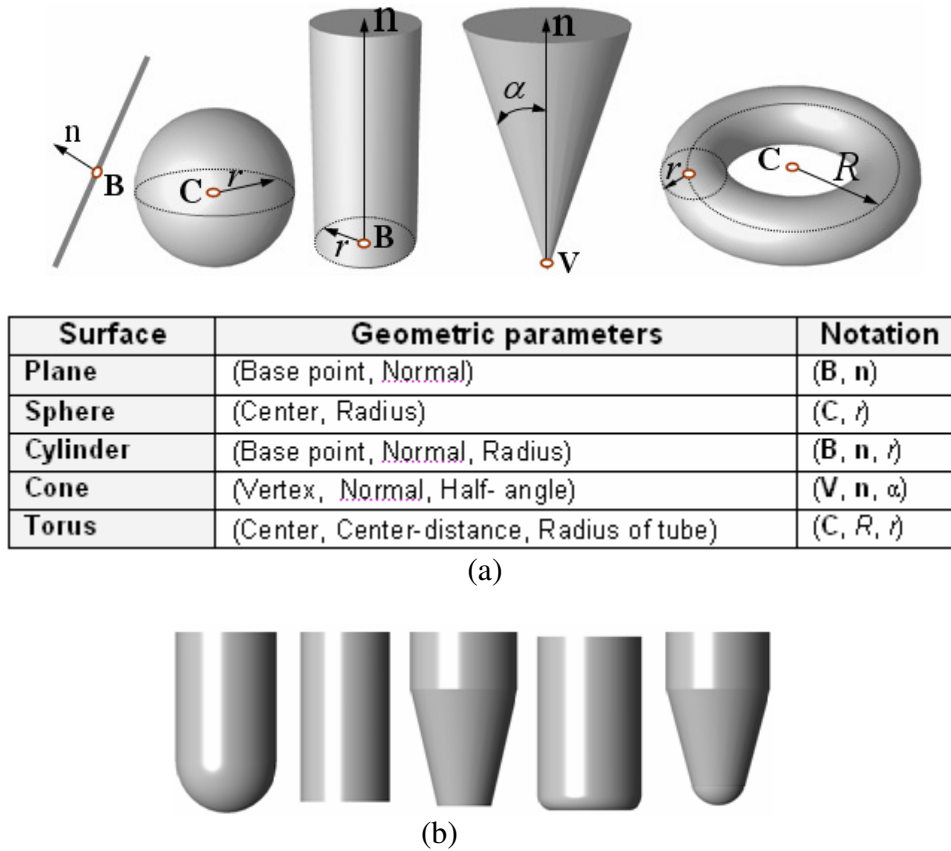


Figure 6.21: The edges of facets deviate from the real surface

In this section *CWEs* are calculated for the common milling cutters performing 3-axis and 5-axis tool movements. In calculations the cutting tool geometries are represented implicitly

by natural quadrics and toroidal surfaces. Natural quadrics (Figure 6.22-a) consist of the sphere, circular cylinder and the cone. Together with the plane (a degenerate quadric) and torus these constitute the surface geometries found on the majority of cutters used in milling. For example a ball nose end mill (BNEM) is defined by two natural quadric surfaces – spherical and cylindrical. Other examples are shown in Figure (6.22-b).



Surface	Geometric parameters	Notation
Plane	(Base point, Normal)	( $B, n$ )
Sphere	(Center, Radius)	( $C, r$ )
Cylinder	(Base point, Normal, Radius)	( $B, n, r$ )
Cone	(Vertex, Normal, Half- angle)	( $V, n, \alpha$ )
Torus	(Center, Center-distance, Radius of tube)	( $C, R, r$ )

Figure 6.22: (a) Constituent surfaces of milling cutters and (b) some typical milling cutter surfaces.

In developing the *CWE* methodologies for the polyhedral models the implicit equations of the cutter geometries will be used. These are

$$\text{Sphere: } (\mathbf{P} - \mathbf{C}) \bullet (\mathbf{P} - \mathbf{C}) - r^2 = 0 \quad (6.7-a)$$

$$\text{Cylinder: } (\mathbf{P} - \mathbf{B}) \bullet (\mathbf{P} - \mathbf{B}) - [(\mathbf{P} - \mathbf{B}) \bullet \mathbf{n}]^2 - r^2 = 0 \quad (6.7-b)$$

$$\text{Cone: } [(\mathbf{P} - \mathbf{V}) \bullet \mathbf{n}]^2 - \cos^2(\alpha) (\mathbf{P} - \mathbf{V}) \bullet (\mathbf{P} - \mathbf{V}) = 0 \quad (6.7-c)$$

$$\text{Torus: } [(\mathbf{P} - \mathbf{C}) \bullet (\mathbf{P} - \mathbf{C}) - r^2 - R^2]^2 + 4R^2[(z - z_c)^2 - r^2] = 0 \quad (6.7-d)$$

$$\text{Plane: } (\mathbf{P} - \mathbf{B}) \bullet \mathbf{n} = 0 \quad (6.7-e)$$

where  $\mathbf{P}$  represents the position of an arbitrary point on the cutter's surface and the coordinates of  $\mathbf{C}$  are  $(x_C, y_C, z_C)$ .

### 6.2.1 Engagement Extraction Methodology in 3-Axis Milling

This section presents a methodology for calculating *CWEs* from polyhedral models that addresses the chordal error problem described in section (6.2) and which reduces the problem to line-plane intersections for the common milling cutter geometries and move types. In this methodology for finding the *CWEs* in 3-Axis milling, a polyhedral representation of the removal volume is mapped from Euclidean space into a parametric space. The nature of the swept geometry and the goal of engagement extraction points towards a preferred parameterization. As shown in Figure(6.23), the *engagement(immersion) angle* ( $\varphi$ ), *depth of cut* ( $d$ ) for points on the cutter surface and *the tool tip distance* ( $L(t)$ ) make up this parameterization,  $P(\varphi, d, L(t))$  where  $(0 \leq t \leq 1)$ .

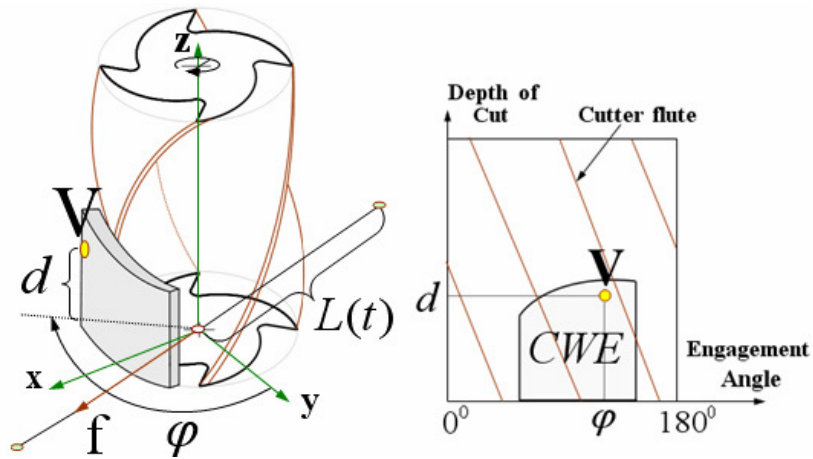


Figure 6.23: *CWE* parameters

This mapping as will be seen has the effect of reducing the cutting tool geometry to an unbounded plane. Thus the boundary of the *CWE* is found by performing first order intersections between the planar representation of the cutting tool and the planar facets in the polyhedral representation of the removal volume.

### General Terminology

$T_i$  : Tool path for the  $i^{\text{th}}$  tool motion

$RV_i$  : Removal volume generated for  $i^{\text{th}}$  tool motion in  $E^3$ .

$M$  : A transformation that maps  $RV_i$  from  $E^3$  to  $P(\varphi, d, L)$  i.e.  $M: E^3 \rightarrow P(\varphi, d, L)$

$RV_i^P$  : The map of  $RV_i$  in  $P(\varphi, d, L)$ .

$\mathbf{N}$  : Surface normal of a point on cutter.

$CWE_K(t)$ : The set of all points on the surface of a cutter at location  $t$  along a tool path where  $\mathbf{f} \cdot \mathbf{N} \geq 0$ . These are kinematically feasible engagement points for a given instantaneous feed vector  $\mathbf{f}$ .

$CWE(t)$ : The set of all points on the surface of a cutter at location  $t$  along a tool path that are engaged with the workpiece.

$bCWE(t)$ : Points on the boundary of  $CWE(t)$ .

In finding engagement geometry the following property of the representations for removal volumes in the parametric space  $P(\varphi, d, L)$  motivate finding the mapping  $M: E^3 \rightarrow P(\varphi, d, L)$ .

**Property 6.3:** Given  $RV_i^P$  a representation of the removal volume  $RV_i$  for tool path  $T_i$  in  $P(\varphi, d, L)$ , its intersection with an unbounded plane  $Q$  generates a closed set of points  $CWE(t)$  that constitutes all points in engagement with the workpiece at location  $t$  along the tool path.

Of interest is the boundary set of  $CWE(t)$ ,  $bCWE(t)$ . This defines the geometry required for input to process modeling (i.e. force prediction). Thus

$$bCWE(t) \subset CWE(t) \subset CWE_K(t) \quad (6.8)$$

These three sets are illustrated in Figure (6.24).

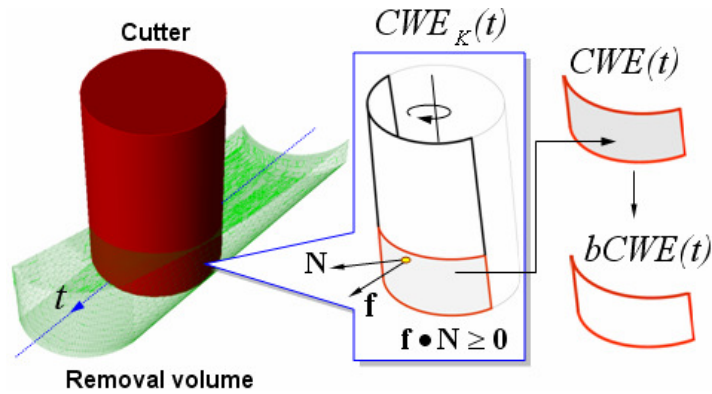


Figure 6.24: Point sets  $CWE_K(t)$ ,  $CWE(t)$  and  $bCWE(t)$  used in defining engagements

The property given above point to a novel approach for finding the engagement geometry assuming that the mapping  $M$  can be constructed: Given  $RV_i^P$  generated by applying  $M$  to  $RV_i$ ,  $CWE(t)$  and  $bCWE(t)$  can be found by intersecting  $RV_i^P$  with an unbounded plane for each cutter location defined by  $t$  (Figure 6.25). The use of an unbounded plane in finding engagements eliminates the problem highlighted in Figure (6.21) where the chordal error in the polyhedral representation of a removal volume introduces uncertainty in the intersection calculation. Further the reduction of the cutter surface geometry to a first order form simplifies intersection calculations particularly when the removal volume is polyhedral.

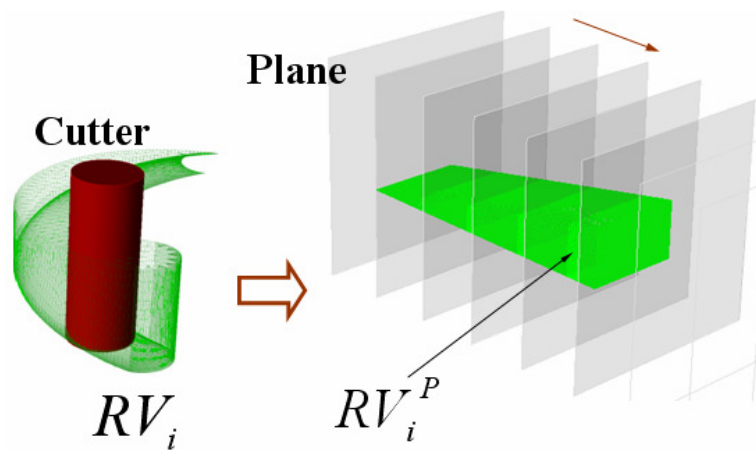


Figure 6.25:  $CWE$  calculations in the parametric domain  $P(\varphi, d, L)$ .

### 6.2.1.1 Mapping $M$ for Linear Toolpath

In this section derivations for the linear tool path will be shown for the Ball Nose End Mill (BNEM) and formulas for the other cutter types can be found in Appendix A-2. A BNEM is made up of a hemi-spherical and a cylindrical surface. Based on the kinematics of 3-axis machining subsets of these surfaces denoted  $CWE_{K,S}(t)$  and  $CWE_{K,C}(t)$  respectively will contribute to the set  $CWE_K(t)$  as defined in chapter (5) i.e.

$$CWE_K(t) = CWE_{K,S}(t) \cup CWE_{K,C}(t)$$

Transformation formulas will be derived for the mapping of the hemi-spherical surface,  $M_{sphere}$ . The methodology and many of formulae developed apply equally to the mapping for the cylindrical surface of the cutter,  $M_{cyl}$ . This will be further explained later in this section.

#### Derivation of $M_{sphere}$ for the BNEM

In addition to the geometric definition of the surface the location of a point on the cutter geometry as it moves along a tool path is also required. To do this the following terms are introduced (see Figure 6.26).

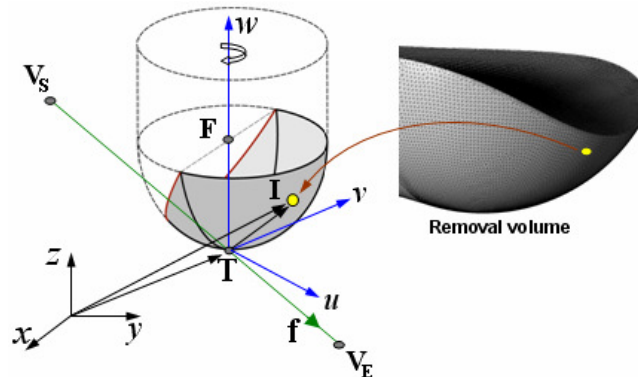


Figure 6.26: Description of a point on a cutter moving along a Tool Path

**WCS:** *Workpiece Coordinate System* ( $\mathbf{i}, \mathbf{j}, \mathbf{k}$ ). This is where the geometry of the removal volume and tool paths are defined.

**TCS:** *Tool Coordinate System* ( $\mathbf{u}, \mathbf{v}, \mathbf{w}$ ) positioned at the tool tip with  $\mathbf{w}$  along the cutter axis. It is assumed that the  $\mathbf{x}$  axis of the local tool coordinate system is aligned with the feed vector direction.

- T(t):** The position of the tool tip point  $(x_T, y_T, z_T, t)$  at  $t$  along tool path  $T_i$  in the WCS.
- I:** The position of a point  $(x_I, y_I, z_I)$  on the cutter surface that belongs to the set  $CWE_K(t)$  at  $t$  along tool path  $T_i$  in the WCS.
- F(t):** The position of a reference point  $(x_R, y_R, z_R, t)$  on the cutting tool axis at  $t$  along tool path  $T_i$ .

Note that in this section the components of the (TCS) are defined by  $\mathbf{u}, \mathbf{v}$  and  $\mathbf{w}$  which are different than those defined in chapter (5). The reason for this is to maintain the clarity in the variable symbolization i.e. to use less subscripts. The possible 3-axis linear tool motions are shown in Figure (6.27): horizontal, ascending and descending (from left to right) respectively.

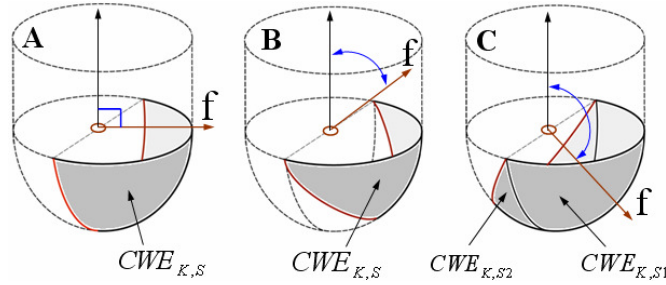


Figure 6.27: 3-axis Linear Tool Motions with a BNEM

For motions **A** and **B** the engagement angle of a point at  $\mathbf{I} \in CWE_{K,S}(t)$  must lie within  $[0, \pi]$  i.e.  $0 \leq \varphi(\mathbf{I} | \mathbf{I} \in CWE_{K,S}(t)) \leq \pi$ . At **C** both the front and the back sides of the hemi-spherical surface of the cutter have engagements and the total engagement area covers the full  $[0, 2\pi]$  range i.e.  $0 \leq \varphi(\mathbf{I} | \mathbf{I} \in CWE_{K,S}(t)) \leq 2\pi$ . The mapping will be developed for the most general case **C** where the hemi-spherical surface engages the workpiece in two regions – the front contact face  $CWE_{K,S1}(t)$  and the back contact face  $CWE_{K,S2}(t)$  where

$$CWE_{K,S}(t) = CWE_{K,S1} \cup CWE_{K,S2}$$

Figure (6.28) shows the engagement regions and parameters  $(\varphi, d, L)$  for a point at  $\mathbf{I}$  on the hemi-spherical surface.

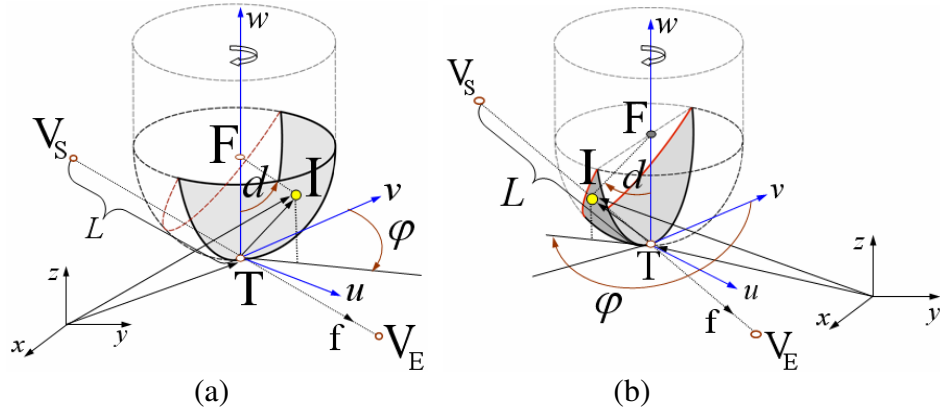


Figure 6.28: Engagement regions of the (a) front and (b) back contact faces

The mapping methodology is summarized in Figure (6.29) and consists of 4 steps. The inputs are a point on the removal volume  $\mathbf{I}(x_i, y_i, z_i) \in E^3$ , the implicit representation of the cutter surface geometry  $G$  and the parametric form of the tool path  $T_i$ .

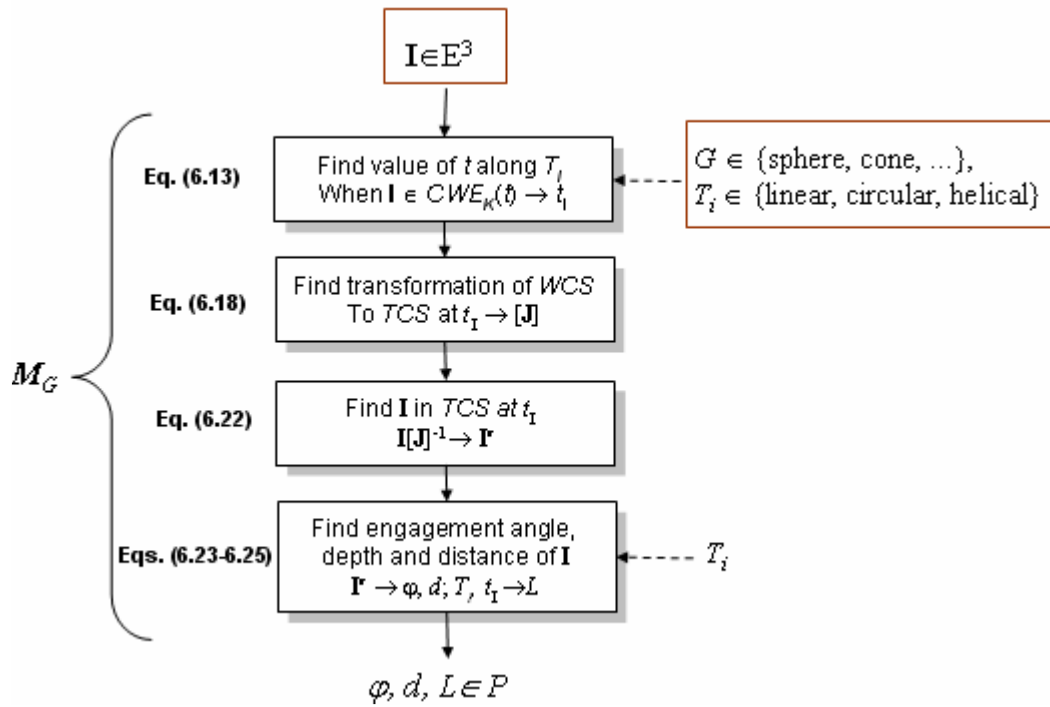


Figure 6.29: Procedure for performing Mapping  $M_G: E^3 \rightarrow P(\varphi, d, L)$ .

**Step 1:** In this step the parameter value  $t$  along  $T_i$  is found. For a linear tool path, the tool tip coordinates with respect to tool path start  $V_S(x_S, y_S, z_S)$  and end  $V_E(x_E, y_E, z_E)$  points are given by,

$$\mathbf{T}(t) = \mathbf{V}_S + (\mathbf{V}_E - \mathbf{V}_S)t, \quad 0 \leq t \leq 1 \quad (6.9)$$

For a BNEM the reference point at  $\mathbf{F}$  is chosen to be the center of the sphere. Its location can be expressed using the cutting tool tip coordinates as,

$$\mathbf{F}(t) = \mathbf{T}(t) + r \mathbf{n} \quad (6.10)$$

where  $r$  and  $\mathbf{n}$  are the radius of the hemi-sphere and unit normal vector of the tool axis respectively. When the hemi-spherical surface moves along a tool path, a family  $G_S(t)$  of surfaces is generated. An expression for this family of surfaces is obtained by substituting in the coordinates of the reference point at  $\mathbf{F}$  from Eq.(6.10) into the implicit form of a sphere given by Eq.( 6.7-a).

$$G_S(t) : (\mathbf{P} - \mathbf{F}) \bullet (\mathbf{P} - \mathbf{F}) - r^2 = 0 \quad (6.11)$$

When the point at  $\mathbf{P}$  belongs to the set  $CWE_{K,S}(t)$ , Eq.(6.11) can be rewritten as,

$$CWE_{K,S}(t) : (\mathbf{I} - \mathbf{F}) \bullet (\mathbf{I} - \mathbf{F}) - r^2 = 0 \quad (6.12)$$

Given a point at  $\mathbf{I}$  that is known to be an engagement point, Eq.(6.12) can be expanded to take on the following quadratic form,

$$A_2 t^2 + A_1 t + A_0 = 0 \quad (6.13)$$

where the coefficients  $A_2$ ,  $A_1$  and  $A_0$  are given by,

$$\begin{aligned} A_2 &= |\mathbf{V}_E - \mathbf{V}_S|^2 \\ A_1 &= -2 [(\mathbf{I} - \mathbf{V}_S - r \mathbf{n}) \bullet (\mathbf{V}_E - \mathbf{V}_S)] \\ A_0 &= |\mathbf{I} - \mathbf{V}_S - r \mathbf{n}|^2 - r^2 \end{aligned} \quad (6.14)$$

Solving for  $t$  in Eq.(6.13) gives the position of the cutter tool tip when the point at  $\mathbf{I}$  is an engagement point between the cutter and the workpiece. In finding the correct tool position for an intersection point  $\mathbf{I}$  the following property is used.

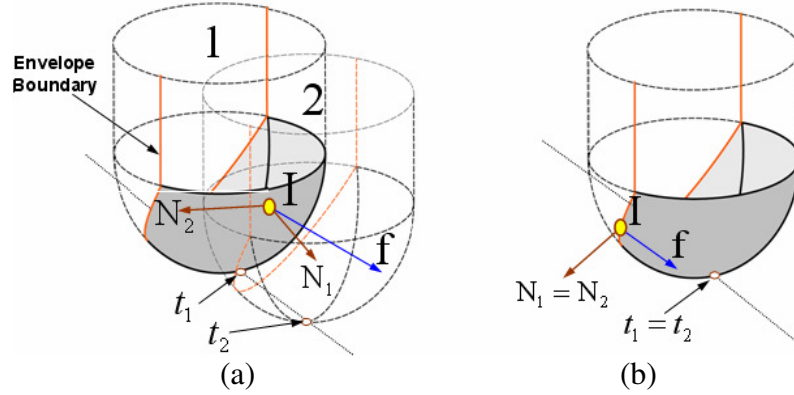
**Property 6.4:** Given a linear tool path  $T_i$  and the cutter surface geometry  $G$ , for 3-axis machining,

- a) The maximum number of tool positions where the cutter touches a point in space is equal to the degree of the cutter surface geometry  $G$ , i.e. sphere is a degree of two surface.
- b) If a point belongs to the removal volume then there is at least one cutter location where the cutter surface touches this point.
- c) If the point is on the boundary of the swept volume  $SV_i$  of the cutter there is a single tool position where the cutter surface touches this point.

The solution for Eq.(6.13) gives two real roots (Property 6.4-a,b)  $t_1$  and  $t_2$  where  $t_1 \leq t_2$ . These roots represent two possible cutter locations where the intersection point  $\mathbf{I}$  lies on the spherical surface as shown in Figure (6.30-a). To differentiate between the two choices and make the correct selection for  $t$ , the sign of the dot products  $\mathbf{f} \cdot \mathbf{N}_1$  and  $\mathbf{f} \cdot \mathbf{N}_2$  between the feed vector  $\mathbf{f}$  and the surface normals  $\mathbf{N}_1$  and  $\mathbf{N}_2$  for the two positions of the cutter is used. A negative value indicates that  $\mathbf{I}$  is in the shadow of the cutter and so cannot be a member of  $CWE_K(t)$ . For example, as shown in the figure at location  $t_2$  the dot product is negative while at  $t_1$ , it is positive. It is easy to see that for linear tool motions the smaller root of Eq.(6.13) should always be used.

For the special case where  $\mathbf{I}$  lies on the boundary of the swept volume of the cutter such that the scalar product  $\mathbf{f} \cdot \mathbf{N}_1, \mathbf{N}_2 = 0$ , the cutting tool has only one cutter location (Property 6.4-c) as shown in Figure (6.30-b). The solution to Eq. (6.13) yields a repeated root and also  $\mathbf{I}$  satisfies the following system of equations as shown at [82]

$$G_s(x_1, y_1, z_1, t) = 0 \quad , \quad \frac{\partial G_s(x_1, y_1, z_1, t)}{\partial t} = 0 \quad (6.15)$$


 Figure 6.30: Different cutter locations for  $\mathbf{I} \in CWE_K(t)$ .

**Step 2:** Given the value of the tool path parameter  $t = t_I$  when the cutter surface passes through  $\mathbf{I}$ , a transformation is created to map the global coordinate system ( $WCS$ ) to a local tool coordinate system ( $TCS$ ) at this location on the tool path. With the  $\mathbf{w}$  axis of cutter being one of the axes of the  $TCS$  the  $\mathbf{v}$  axis (see Figure 6.28) is obtained from the cross product of  $\mathbf{w}$  and the instantaneous feed direction vector  $\mathbf{f}(t=t_I)$ . The third axis  $\mathbf{u}$  is perpendicular to the first two.

$$\mathbf{v} = (\mathbf{w} \times \mathbf{f}) / |\mathbf{w} \times \mathbf{f}| \quad (6.16)$$

$$\mathbf{u} = (\mathbf{v} \times \mathbf{w}) / |\mathbf{v} \times \mathbf{w}|$$

where

$$\mathbf{f} = (x_E - x_S) \mathbf{i} + (y_E - y_S) \mathbf{j} + (z_E - z_S) \mathbf{k} \quad (6.17)$$

Using Eqs.(6.16) the transformation of a point in the  $TCS$  to one in the  $WCS$  is given by,

$$\mathbf{I} = \mathbf{I}' [\mathbf{J}]_{t=t_I} \quad (6.18)$$

where

$$[\mathbf{J}]_{t=t_I} = \begin{bmatrix} \mathbf{u} & 0 \\ \mathbf{v} & 0 \\ \mathbf{w} & 0 \\ \mathbf{T}(t) & 1 \end{bmatrix}_{t=t_I} \equiv \begin{bmatrix} x_u & y_u & z_u & 0 \\ x_v & y_v & z_v & 0 \\ x_w & y_w & z_w & 0 \\ x(t)_T & y(t)_T & z(t)_T & 1 \end{bmatrix}_{t=t_I} \quad (6.19)$$

and  $\mathbf{I}'$  are the coordinates of  $\mathbf{I}$  in the TCS.

**Step 3:** To find  $\varphi(t)$  and  $d(t)$  the coordinates of an engagement point in the TCS is required. This is obtained from Eq.(6.18) as,

$$\mathbf{I}' = \mathbf{I}[\mathbf{J}]_{t=t_1}^{-1} \quad (6.20)$$

Given that  $[\mathbf{J}]_{t=t_1}$  is orthogonal, its inverse is defined by,

$$[\mathbf{J}]_{t=t_1}^{-1} = \begin{bmatrix} x_u & x_v & x_w & 0 \\ y_u & y_v & y_w & 0 \\ z_u & z_v & z_w & 0 \\ -\mathbf{u} \bullet \mathbf{T}(t) & -\mathbf{v} \bullet \mathbf{T}(t) & -\mathbf{w} \bullet \mathbf{T}(t) & 1 \end{bmatrix}_{t=t_1} \quad (6.21)$$

Expanding equation (6.20) using (6.21) gives the coordinates of  $\mathbf{I}'(x'_1, y'_1, z'_1)$ . These are,

$$\begin{aligned} x'_1 &= \mathbf{I} \bullet \mathbf{u} - \mathbf{u} \bullet \mathbf{T}(t = t_1) \\ y'_1 &= \mathbf{I} \bullet \mathbf{v} - \mathbf{v} \bullet \mathbf{T}(t = t_1) \\ z'_1 &= \mathbf{I} \bullet \mathbf{w} - \mathbf{w} \bullet \mathbf{T}(t = t_1) \end{aligned} \quad (6.22)$$

**Step 4:** Given the coordinates of  $\mathbf{I}'$  on the hemi-spherical surface of the BNEM, its tool engagement angle  $\varphi(t)$  is obtained using spherical coordinates. The Engagement angle for the front contact face  $CWE_{K,s1}(t)$  is given by

$$\varphi(t = t_1) = \cos^{-1} \left( \frac{y'_1}{\sqrt{x'^2_1 + y'^2_1}} \right) \quad (6.23-a)$$

and for the back contact face  $CWE_{K,s2}(t)$  is given by

$$\varphi(t = t_1) = 2\pi - \cos^{-1} \left( \frac{y'_1}{\sqrt{x_1'^2 + y_1'^2}} \right) \quad (6.23-b)$$

The depth of the engagement point for the spherical part is the angle from  $\mathbf{T}(t)$  to  $\mathbf{I}'$  such that:

$$d(t = t_1) = \cos^{-1} \left( 1 - \frac{z'_1}{r} \right) \quad (6.24)$$

and finally the parameter  $L(t)$  of  $\mathbf{I}$  is obtained using,

$$L(t = t_1) = t \left| \mathbf{V}_E - \mathbf{V}_S \right| \quad (6.25)$$

### **Derivation of $M_{cyl}$ for the BNEM**

The mapping for the cylindrical surface of the Ball end cutter is obtained following the same steps just developed for the hemispherical cutter surface. It can be seen that except for the first, all steps and equations to accomplish the mapping remain the same. For the first step, the geometry of the cylinder changes Eqs.(6.11) and (6.12) to,

$$G_c(t) : (\mathbf{P} - \mathbf{F}) \bullet (\mathbf{P} - \mathbf{F}) - [(\mathbf{P} - \mathbf{F}) \bullet \mathbf{n}]^2 - r^2 = 0 \quad (6.26)$$

and,

$$CWE_{K,C}(t) : (\mathbf{I} - \mathbf{F}) \bullet (\mathbf{I} - \mathbf{F}) - [(\mathbf{I} - \mathbf{F}) \bullet \mathbf{n}]^2 - r^2 = 0 \quad (6.27)$$

respectively (see Figure 6.31). Where  $r$  and  $\mathbf{n}$  are the radius of the cylindrical surface and the unit normal vector of the tool rotation axis respectively. As with Eq.(6.13), Eq.(6.27) results in a quadratic equation in  $t$  when  $\mathbf{I}$  and  $\mathbf{F}$  are substituted. The solution to this and the remaining steps in the mapping procedure lead to the representation of a point  $\mathbf{I}$  on the cylindrical surface of the BNEM in  $(\varphi, d, L)$  coordinates. Detailed transformation formulas for the cylindrical end mill can be found in the Appendix A.2.



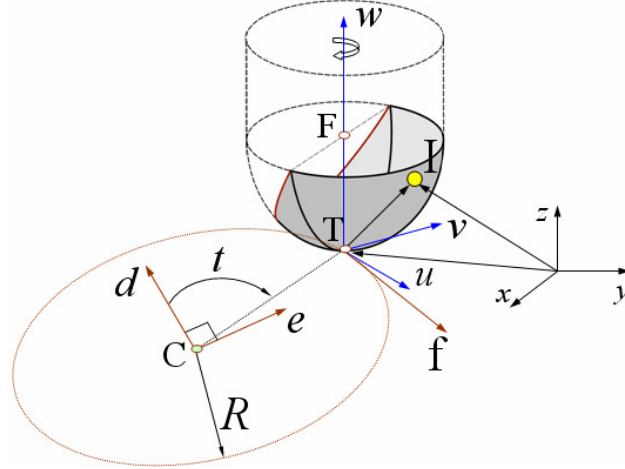


Figure 6.32: Moving coordinate frame for circular tool path

As with linear tool paths the local tool coordinate system *TCS* defined with  $\mathbf{u}$ ,  $\mathbf{v}$  and  $\mathbf{w}$  has its origin at the tool tip point. The reference point  $\mathbf{F}$  is expressed in terms of the cutting tool tip coordinates using Eq.(6.10). Following the same steps outlined in section (6.2.1.1) Eq.(6.28) is substituted into Eq.(6.10) then into the implicit equation of the hemispherical surface of the cutter (6.7-a) with the coordinates of a point  $\mathbf{I}$  belonging to the  $CWE_K(t)$  obtained from the removal volume. The resulting equation can be expressed in terms of the parameter  $t$  in the following form

$$A_2 \cos(t) + A_1 \sin(t) + A_0 = 0 \quad (6.29)$$

where  $A_2$ ,  $A_1$  and  $A_0$  are constants for the current intersection point  $\mathbf{I}$  given by the following expressions

$$\mathbf{a} = [(x_I - x_C - rn_x) \quad (y_I - y_C - rn_y) \quad (z_I - z_C - rn_z)], \quad (6.30)$$

$$A_2 = -2R (\mathbf{a} \bullet \mathbf{d}), \quad A_1 = -2R (\mathbf{a} \bullet \mathbf{e}), \quad A_0 = |\mathbf{a}|^2 + R^2 - r^2$$

Eq.(6.29) in  $t$  can be written in the following form

$$\sqrt{A_1^2 + A_2^2} \sin(t + \theta) + A_0 = 0 \quad (6.31)$$

where  $\theta = \tan^{-1}(A_2, A_1)$ . This leads to the following general equation for  $t$

$$t = -\theta + (-1)^n \alpha + n \pi ,$$

$$\alpha = \sin^{-1} \left( \frac{-A_0}{\sqrt{A_1^2 + A_2^2}} \right) \quad (6.32)$$

where  $n$  is integer. Define  $n_1$  to be the smallest  $n$  such that  $t > t_0$ . Then  $n_1$  can be calculated as

$$n_1 = \min \left( 2 \left\lceil \frac{\theta - \alpha + t_0}{2\pi} \right\rceil, 2 \left\lceil \frac{\theta + \alpha + t_0}{2\pi} - \frac{1}{2} \right\rceil \right) \quad (6.33)$$

After  $n_1$  is found it can be incremented by unit steps to calculate the next tool tip point  $\mathbf{T}$  for the given  $\mathbf{I}$ . There can be up to two cutter location points in the interval for a given engagement point  $\mathbf{I}$  (Figure 6.33). As explained in section (6.2.1.1) the minimum root is selected. If  $\mathbf{I}$  is on the envelope surface of the cutter (Property 6.4-c), Eq.(6.29) gives two repeated roots. Having solved for the parameter  $t$  value when  $\mathbf{I}$  is an engagement point, it is substituted into equation (6.28) to find the tool tip coordinates. The direction of the feed vector at this location is given by

$$\mathbf{f}(t = t_1) = \frac{d\mathbf{T}}{dt} = R(-\sin(t) x_d + \cos(t)x_e) \mathbf{i} + R(-\sin(t) y_d + \cos(t)y_e) \mathbf{j} + R(-\sin(t) z_d + \cos(t)z_e) \mathbf{k} \quad (6.34)$$

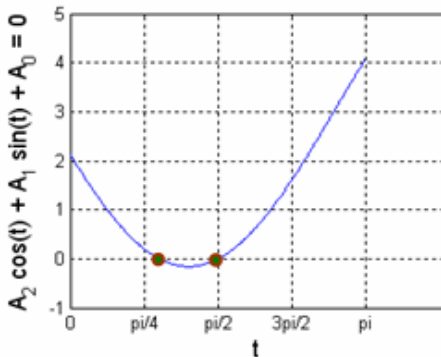


Figure 6.33: Parameter values of the cutter tool tip

Given  $\mathbf{f}$  and  $t$ , Eqs.(6.23-a,b) and (6.24) are used to find  $(\varphi, d)$  parameters for  $\mathbf{I}$  and  $L(t)$  of  $\mathbf{I}$  is obtained using

$$L(t = t_I) = R t \quad (6.35)$$

the mapping for the cylindrical portion of the cutter follows the same steps using the implicit surface for a cylinder.

### 6.2.1.3 Mapping $M$ for Helical Toolpath

A special case of 3-axis machining is helical milling shown in Figure (6.34). In this operation a cutting tool is feed along its tool axis (Z-axis) as a circle is interpolated by the other two (X and Y axes). The cutter follows a helical trajectory. This operation is useful for (1) contour milling of cylindrical protrusions or for enlarging of pre-machined or pre-formed holes, (2) for hole machining into solid stock.

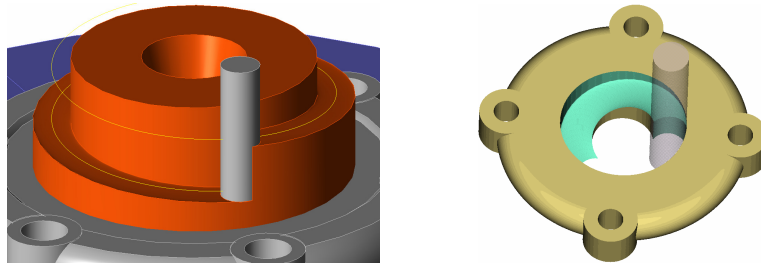


Figure 6.34: Sweeps for Helical Milling

In this section derivations of the mapping  $M$  for the helical toolpath will be shown for the Flat-End mill. The methodology and many of formulae developed apply equally to the mapping for the other types of the cutter geometries. A Flat end mill is made up of a cylindrical surface for its side and a flat surface for its bottom. Based on the kinematics of 3-axis machining these surfaces denoted  $CWE_{K,c1}(t)$  and  $CWE_{K,c2}(t)$  respectively will contribute to the set  $CWE_K(t)$  as defined before i.e.

$$CWE_K(t) = CWE_{K,c1}(t) \cup CWE_{K,c2}(t)$$

As explained in section (5), during machining each cutter surface contributes to *CWEs* differently. Because of this the removal volumes generated by the side and flat surfaces of the Flat-End mill are separated in this research. The Side face (Figure 6.35-a) has an engagement in the range of zero to  $\pi$ , and the bottom face (Figure 6.35-b) in the range of zero to  $2\pi$ .

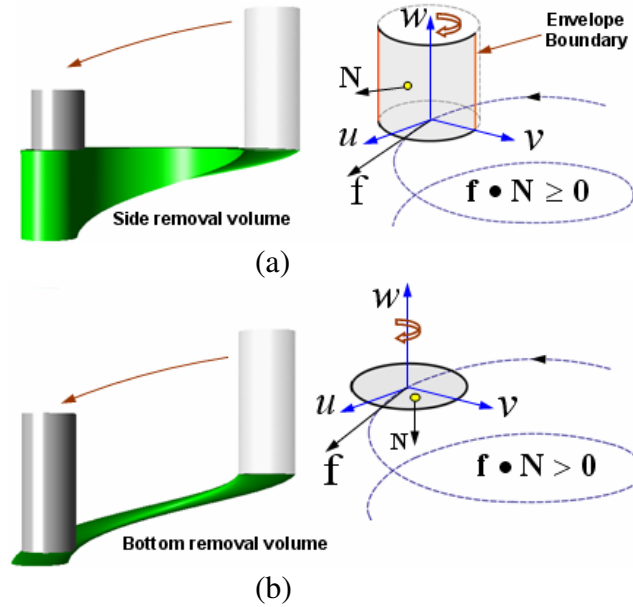


Figure 6.35: Removal volumes of (a) side face and (b) bottom face.

In this section the mapping methodology to be described is applied to the removal volume generated by the cutter side face only. This is because directly intersecting a plane which is perpendicular to the tool rotation axis with the removal volume of the bottom face gives the *CWEs* of the bottom face. For the cylindrical surface tool reference point  $\mathbf{F}$  equals to the tool tip point  $\mathbf{T}$  (see Figure 6.36) and the parametric representation for the tool tip point for a helical tool path of radius  $R$  centered at  $\mathbf{C}(x_c, y_c, z_c)$  is

$$\mathbf{F}(t) = \mathbf{T}(x_T, y_T, z_T, t) = \begin{pmatrix} x_c + R \cos(t) \\ y_c + R \sin(t) \\ z_c + c t \end{pmatrix} \quad (6.36)$$

where  $t \in [0, 2\pi]$  and  $2\pi c$  is a constant giving the vertical separations of the helix's loops where  $c < 0$ .

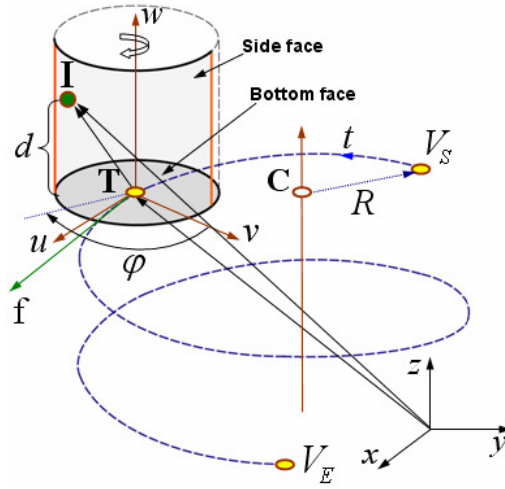


Figure 6.36: Parameters describing a helical tool motion for the Flat-End mill

Following the same steps outlined in section (6.2.1.1), Eq.(6.36) is substituted into the implicit equation of the cylindrical surface of the cutter (6.7-b) with the coordinates of a point **I** belonging to the  $CWE_K(t)$  obtained from the removal volume. The resulting equation can be expressed in terms of the parameter  $t$  in the following form

$$A_2 \cos(t) + A_1 \sin(t) + A_0 = 0 \quad (6.37)$$

where

$$A_2 = -2(x_I - x_C)R$$

$$A_1 = -2(y_I - y_C)R$$

$$A_0 = (x_I - x_C)^2 + (y_I - y_C)^2 + R^2 - r^2$$

Eq.(6.37) in  $t$  can be solved by applying the Eqs.(6.32) and (6.33). There can be up to two cutter location points in the interval for a given engagement point **I** (Figure 6.37). As explained in Property (6.4) the minimum root is selected.

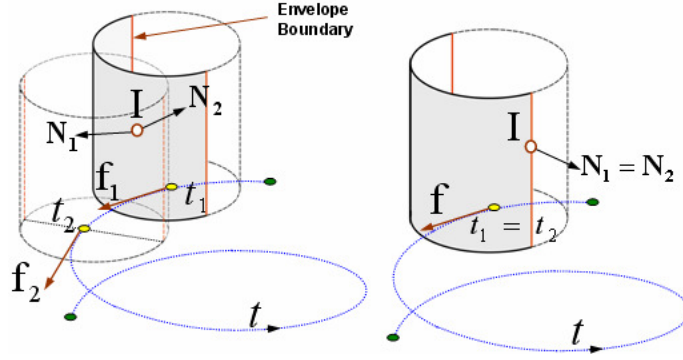


Figure 6.37: Different cutter locations for an engagement point  $\mathbf{I} \in CWE_K(t)$ .

As with linear tool paths the local tool coordinate system  $TCS$  defined with  $\mathbf{u}$ ,  $\mathbf{v}$  and  $\mathbf{w}$  has its origin at the tool tip point. The direction of the feed vector for the parameter  $t$  value from Eq.(6.36) is given by

$$\mathbf{f}(t = t_1) = \frac{d\mathbf{T}}{dt} = -R \sin(t) \mathbf{i} + R \cos(t) \mathbf{j} + c \mathbf{k} \quad (6.38)$$

Using  $t$ , the parameter  $L(t)$  of  $\mathbf{I}$  is obtained by

$$L(t = t_1) = t_1 \sqrt{R^2 + c^2} \quad (6.39)$$

Given  $\mathbf{f}$  and  $t$ , the Eq.(6.23-a) is used to find  $\varphi$  parameter for  $\mathbf{I}$  and finally, the depth of the engagement point as defined by the distance from  $\mathbf{T}(t)$  to  $\mathbf{I}'$  measured along the tool axis vector is simply the z-coordinate of  $\mathbf{I}'$ .

$$d(t = t_1) = z'_I = \mathbf{I} \cdot \mathbf{w} - \mathbf{w} \cdot \mathbf{T}(t = t_1) \quad (6.40)$$

### 6.2.1.4 Implementation

In this research the mappings developed in the previous sections are applied directly to a polyhedral representation of the removal volume. The specific representation utilized is the STL (“Stereo Lithography”) format though other representations (VRML, .jt, .hsf etc.) can as easily be adopted. As explained in chapter (1), in the STL representation the geometry of surfaces is represented by small triangles called facets. These facets are described by three

vertices and the normal direction of the triangle. To test the methodology for *CWE* extraction, a prototype system has been assembled using existing commercial software applications and C++ implementations of the mapping procedure described above. This system is shown in (Figure 6.38). Simulation of the CLData is performed using VERICUT a commercial NC verification application. This application uses a voxel-based model to capture changes to the in-process workpiece. STL representations of in-process workpiece states can be generated from the voxel representation prior to any tool path motion in the CLData file. Not currently available through the programmable APIs provided for customization is a function for outputting STL representations of removal volumes. However, this is probably an easy extension to implement. Thus, to obtain removal volumes for a given tool motion, (ACIS) is utilized to model a B-rep solid of the associated swept volume.

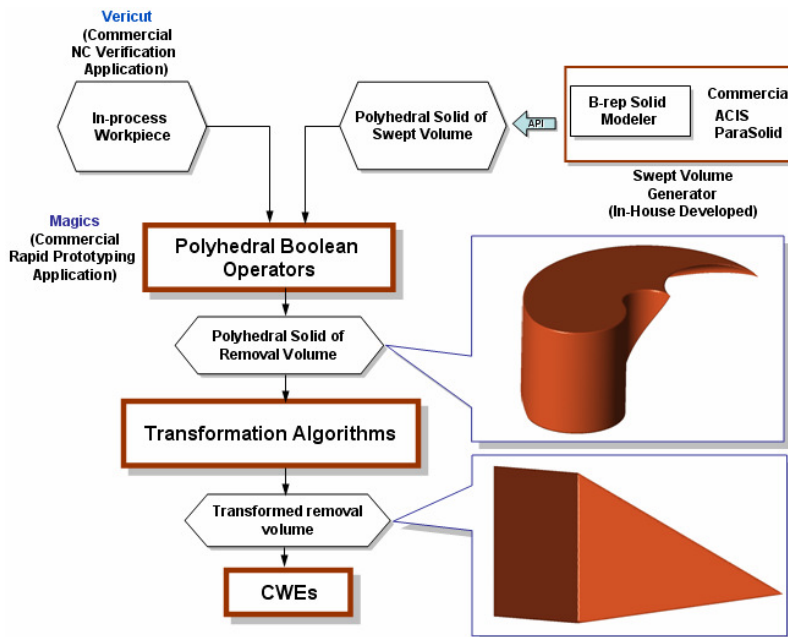


Figure 6.38: Implementation of *CWE* extraction methodology

These swept volumes are exported to STL format. A Boolean intersection between this swept volume and the current in-process workpiece output from Vericut is performed using the polyhedral modeling Boolean operators implemented in a third commercial application, Magics X [51]. Though currently a manual process this prototype system creates STL models

of removal volumes generated during the machining of complex components. It utilizes the same CAD/CAM data generated for machining the part.

In this section examples of the application of the mapping  $M$  to removal volumes generated by different types of cutting tools and tool motions are presented. The first set of examples is designed to demonstrate the generality of the approach with respect to tool geometry and linear, circular and helical tool motions. The second set comes directly from applying the prototype system described in the previous section to CAD/CAM data created in machining a gearbox cover. This demonstrates the practicality of the methodology.

### **Example Set 1**

In this example set different cutting tools and linear, circular and helical tool motions are presented to demonstrate the generality of the approach. Figures (6.39) to (6.41) show Ball, Flat and Tapered-Flat End mills removing material along a linear ramping tool path i.e. the tool moves in all three axes simultaneously. In each case the original and transformed removal volumes are given. The removal volumes associated with the different cutter surfaces are separated. In the case of the flat end mill this gives the material removed by the cylindrical (Side Face) and flat (Bottom Face) cutter surfaces. Plots of  $CWEs$  at different Cutter Locations (CL) along the tool path are illustrated. These are obtained by intersecting the transformed removal volume with a plane representing the cutting tool. Two formats for plotting the  $CWEs$  are used. The first is an XY plot of depth-of-cut (as measured from the tool tip point) versus engagement angle. The second plot shows the engagement area of the cutter bottom surface (Figure 6.40) in a polar format.

In the linear ramping example of the Ball-End mill the plots show that engagement of the cutter occurs over the full range i.e.  $[0, 2\pi]$ . Between zero and  $\pi$  the engagement is due to the front contact face (the  $CWE$  in this zone is divided to illustrate this) and between  $\pi$  and  $2\pi$  due to the back contact face. For the Flat-End mill XY plots show the engagement between zero and  $\pi$  for the side face and polar plots show the engagement between zero and  $2\pi$  for the bottom face. Because the Tapered-Flat-End mill is ramping up only its front face has engagement with the workpiece and it changes between zero and  $\pi$ .

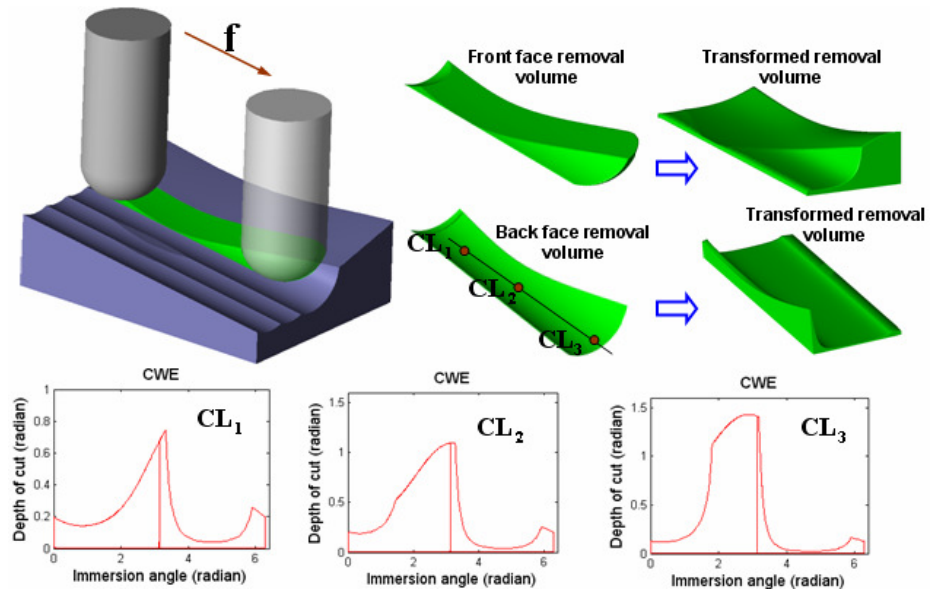


Figure 6.39: *CWEs* for Ball-End mill performing a linear 3-axis move

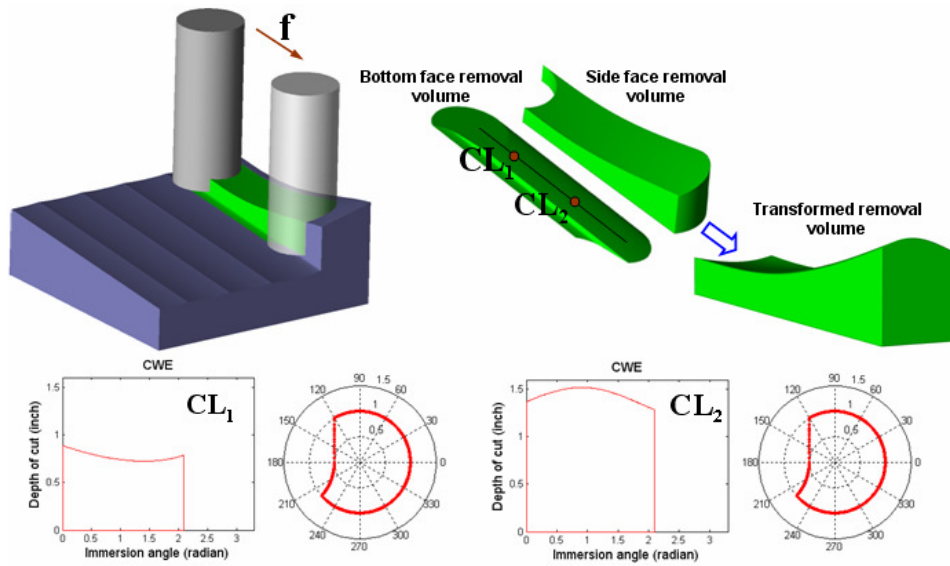


Figure 6.40: *CWEs* for Flat End mill performing a linear 3-axis move

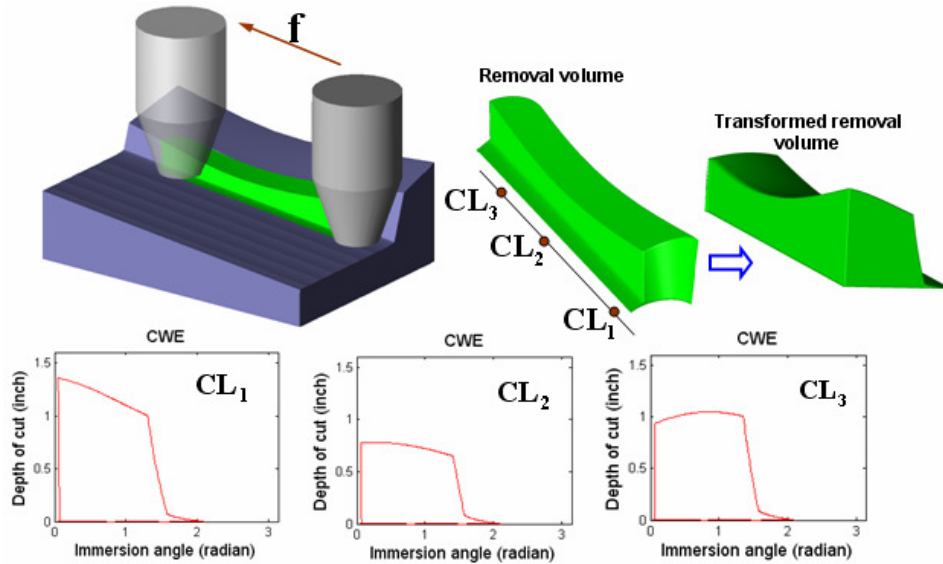


Figure 6.41: *CWEs* for Tapered-Flat-End mill performing a linear 3-axis move

The next example shows a Flat-End mill removing material along a helical tool path (Figures 6.42 – a,b,c). In each case the original and transformed removal volumes are shown. In Figure (6.42-d) the transformed removal volumes for the side face are shown and for the given CLs (cutter location points) *CWEs* are obtained by intersecting a plane representing the cutting tool with the transformed removal volume. Two formats for plotting the *CWEs* are used. The first is an XY plot of the depth of cut (DOC) and immersion angle which is generated by the side face of the flat end mill. The engagement of this surface of the cutter occurs over the  $[0, \pi]$  range as can be seen. The second is a polar plot of the cutter radius versus the immersion angle which is generated by the bottom surface of the flat end mill. The engagement for the bottom face of the cutter occurs over the  $[0, 2\pi]$  range. For  $CL_1$  and  $CL_2$  both types of plots are shown because the bottom of the cutter is removing material at these locations. For the other cutter locations only the side face of the end mill is engaging the workpiece.

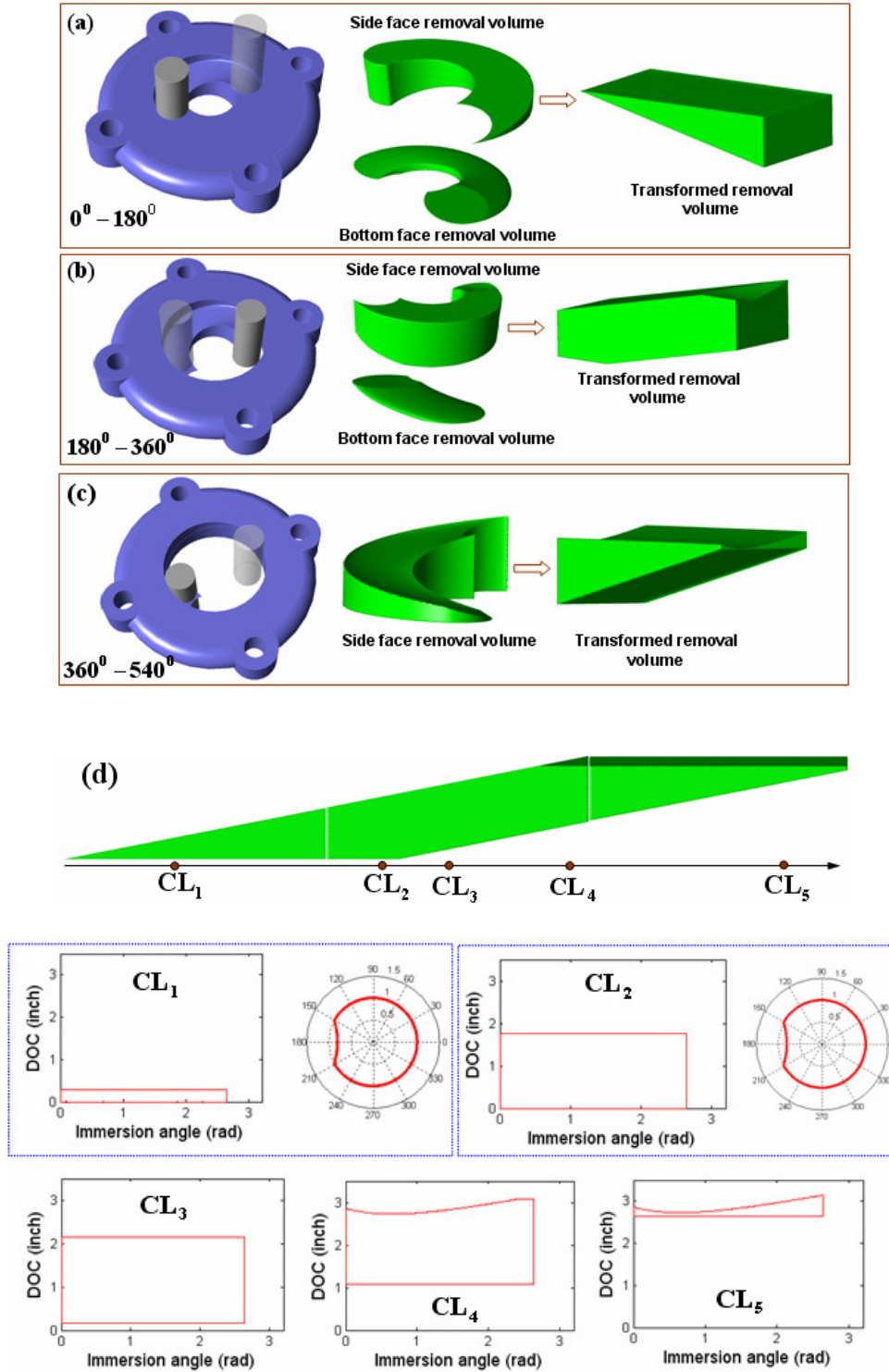


Figure 6.42: Helical Tool Motions with a Flat-End mill and *CWEs*

The final example (Figure 6.43) demonstrates the transformation as applied to a circular 2½D tool path. These results together show that the mapping methodology reduces various

combinations of cutter and tool path geometry to a generic form to which a single intersection operator can be applied.

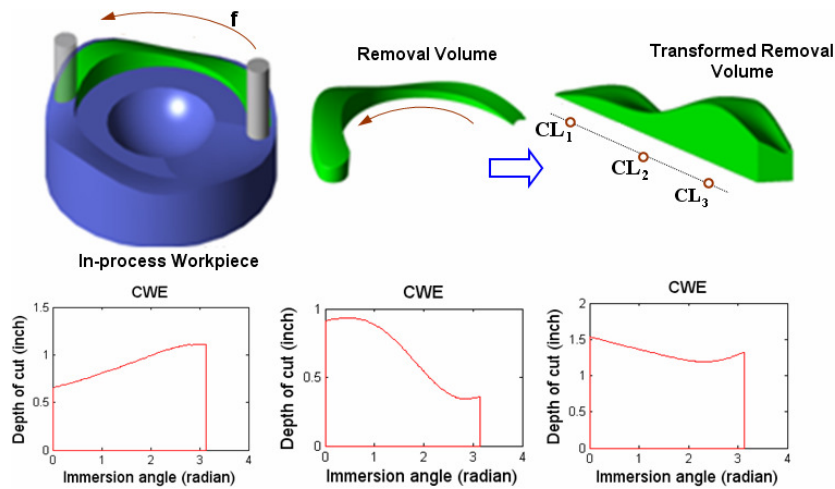


Figure 6.43: *CWEs* for Flat-End mill performing a circular move

### Example Set 2

The examples in this section are created using the steps outlined in Figure (6.38). The Figure (6.44) shows model of a gearbox cover to be machined from rectangular stock. The CAD model and tool paths for machining were both created using Unigraphics NX3. In this figure, it is shown in-process workpiece and the removal volume for the next tool path generated by Vericut, ACIS and Magics. The removal volume generated by the ball nose end mill clearly shows the complicated removal volume shapes and resulting *CWEs* that can be generated when machining complex parts.

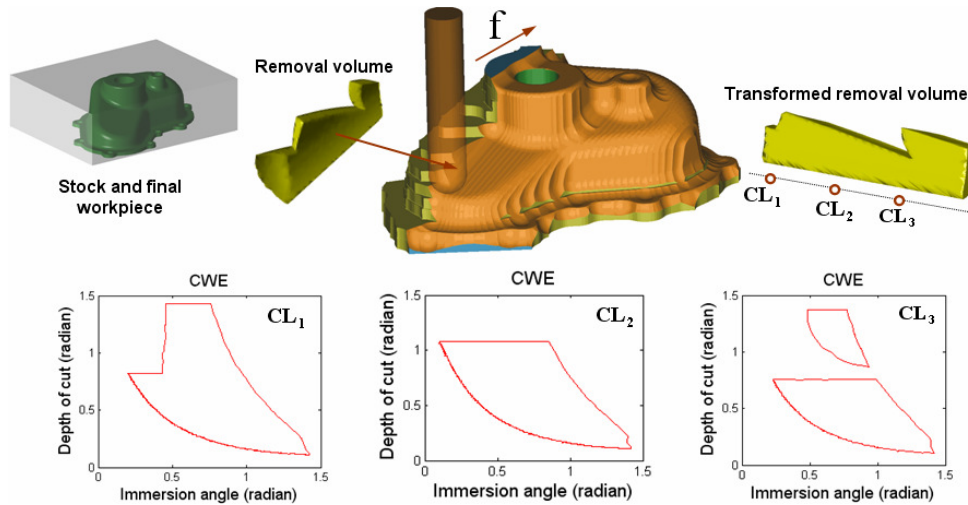


Figure 6.44: *CWEs* for Ball-End mill performing a linear 3-axis move

Figure (6.45) shows a helical milling operation for enlarging a hole. In this example both the side and the bottom faces of the Flat-End mill are removing material. In this figure side face removal volumes are shown. The cutter performs four half turns each corresponding to a  $0^\circ - 180^\circ$  range i.e. third turn has the starting angle  $360^\circ$  and ending angle  $540^\circ$  along the tool path.

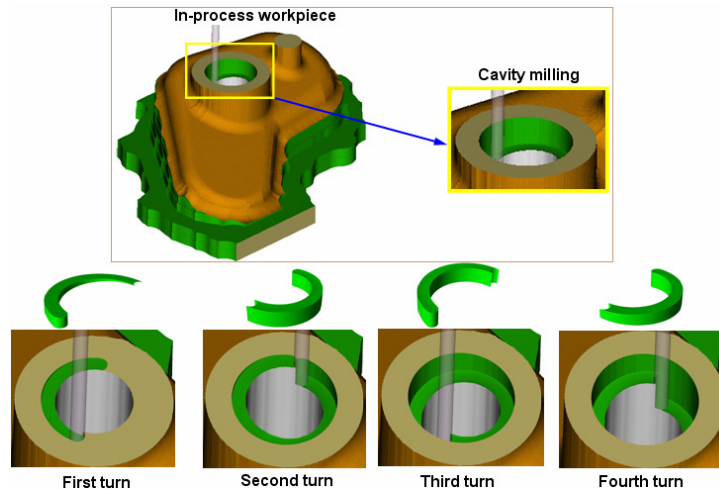


Figure 6.45: Helical tool path application with removal volumes for each half turn.

It can be seen from Figure (6.46) that starting from the first turn the material removal rate is constantly increasing. Then this rate becomes constant for the third and the fourth turns.

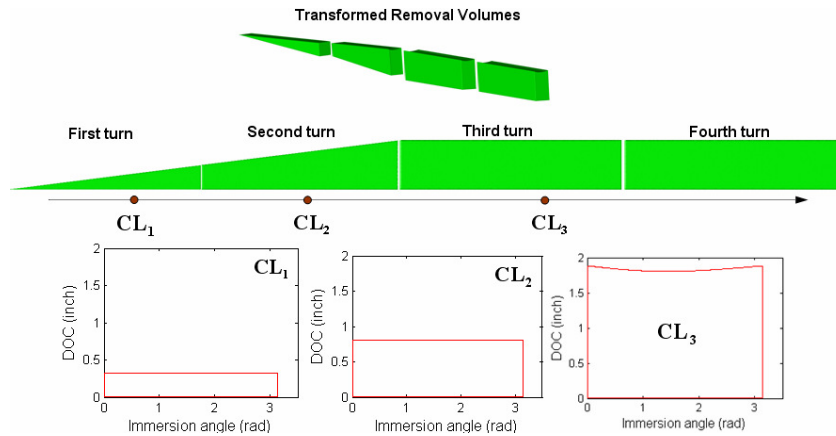


Figure 6.46: *CWEs* of the Helical Tool Motions

### 6.2.2 Engagement Extraction Methodology in 5-Axis Milling

In 3-axis milling cutter translates along a tool path with a fixed tool axis vector. For the 3-axis *CWE* methodology described in the previous section the mapping is performed with respect to the Tool Coordinate System (*TCS*) in which the  $z$  -axis was fixed. In this methodology it is assumed that the size of the facets of the removal volume must be small enough. Thus during the mapping of the removal volume the triangle deformation stays small enough. Later this will be discussed in the discussion section. On the other hand in 5-axis tool motions the direction of the tool axis vector continuously changes. When the mapping described in the previous section is applied to the removal volume obtained from the 5-axis tool motions, the deformation on the triangles becomes big. One of the solutions for reducing the deformation is to use much smaller triangular facets but this brings a heavy computational load to *CWE* extractions. Therefore, in this research, the mapping methodology is not applied for obtaining *CWEs* in the 5-axis milling. We developed a new methodology for the 5-axis *CWE* extractions. This methodology is explained in Figure (6.47) for the impeller machining by using a Taper-Flat-End mill and it has 3 main steps:

**Step 1:** In this stage there are two components: the in-process workpiece and the BODY. Both of them are represented by triangular facets having vertices and normal vectors. For a given Cutter Location (CL) point the BODY is generated as a solid using the methodology described in section (6.1.3) and then it is exported to STL format for obtaining the tessellated representation. A Boolean intersection between this tessellated BODY and the current in-

process workpiece is performed using the polyhedral modeling Boolean operator. This intersection process creates an STL model of the removal volume for a given CL point.

**Step 2:** In this stage there are two components also: The removal volume in the STL format and the feasible contact surface in the solid format. The analytical surface/line intersections are performed between the feasible contact surface and the triangles of the removal volume. For example in Figure (6.47)-steps 2, triangles of the removal volume are intersected with the cone and sphere parts of the feasible contact surface.

**Step 3:** In this last step the connection of the intersection points obtained in the previous step generates the boundary of the *CWE*, *bCWE*. Then this boundary described in 3D Euclidian space is mapped into 2D space defined by the engagement angle and the depth of cut.

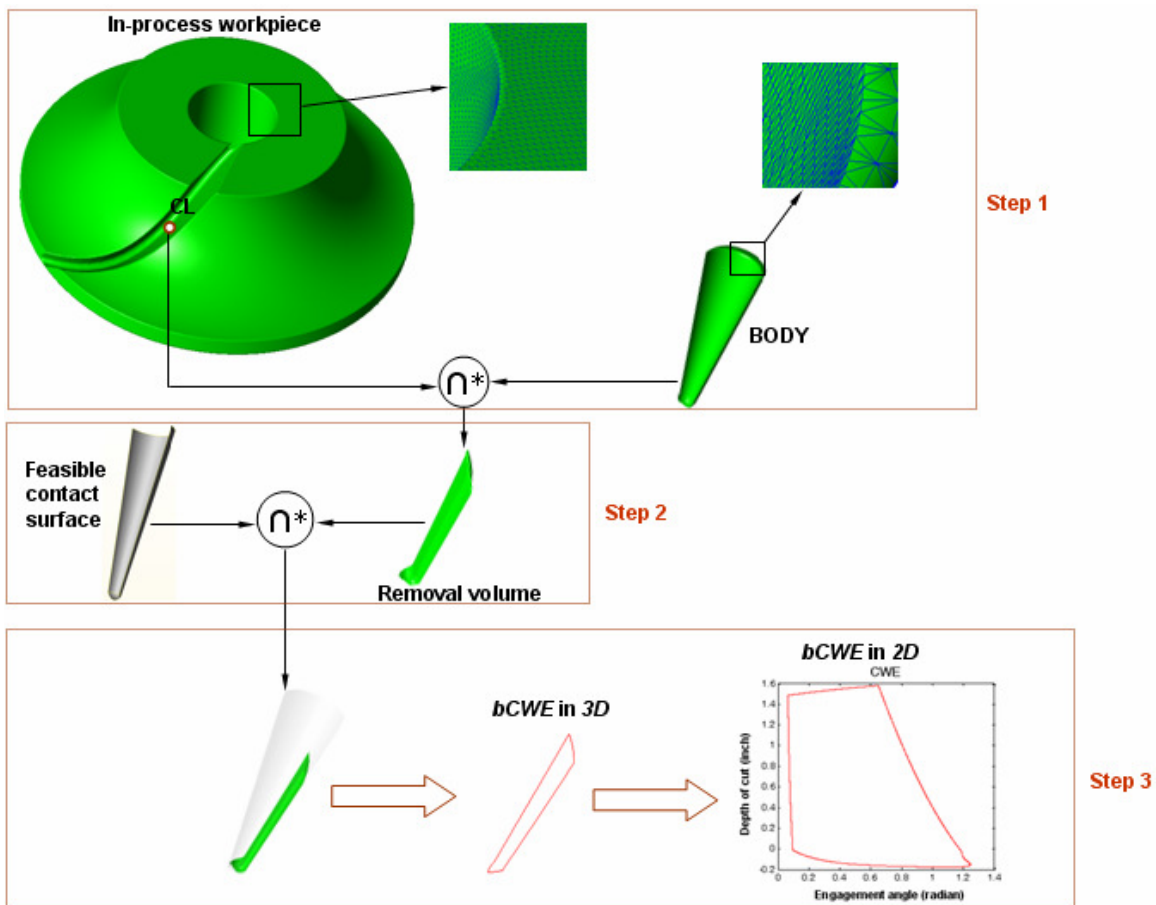


Figure 6.47: *CWE* extraction steps for 5-axis milling.

Although this 5-axis *CWE* methodology in polyhedral models is explained by using the Taper-Flat-End mill, the methodology applies equally for the other cutter surfaces also. If the

cutter surface has the second order equation, e.g. cylinder, cone or sphere natural quadric surfaces, each line – surface intersection gives two roots. If the cutter surface has the fourth order equation e.g. torus, each line surface intersection gives four roots. In most cases only one of these roots are needed for obtaining the *bCWEs* and the rest is redundant. During the implementation the ACIS geometric kernel with C++ is used for creating and tessellating the BODY and the Magics is used for the polyhedral Boolean intersections and updating the in-process workpiece. These three steps are performed for each tool path segment. After processing a toolpath segment for *CWE* extractions, the material is removed from the in-process workpiece in the vicinity of the toolpath segment.

### 6.3 The Cutter Workpiece Engagements in Vector Based Model

In this section for the *CWE* calculations the cutting tool geometries are represented implicitly by natural quadrics and the plane (a degenerate quadric). Natural quadrics consist of the sphere, circular cylinder and the cone.

#### 6.3.1 Intersecting Segment Against Plane

Given a point  $P$  with normal  $\mathbf{n}$  on a plane  $\pi$ , the following equation can be written for all points  $X$  on this plane

$$\mathbf{n} \cdot (X - P) = 0 \quad (6.41)$$

In the above equation the vector  $(X-P)$  is perpendicular to the vector  $\mathbf{n}$ . When the dot product in Eq.(6.41) is distributed across the subtraction the implicit representation of the plane takes the form of  $\mathbf{n} \cdot X = d$  where  $d = \mathbf{n} \cdot P$ . Let a segment is given by  $I(v) = I_a + (I_b - I_a)v$  for  $0 \leq v \leq 1$ . For finding the intersection point  $I$  (see Figure 6.48) between the segment and the plane the equivalent of  $I(v)$  is substituted for  $X$  in the plane equation and then this equation is solved for  $v$

$$\mathbf{n} \cdot (I_a + (I_b - I_a)v) = d \quad (6.42)$$

Isolating  $v$  in the above equation yields  $v = (d - \mathbf{n} \cdot I_a) / (\mathbf{n} \cdot (I_b - I_a))$ . The expression for  $v$  can now be inserted the parametric equation of the segment  $I(v)$  for finding the intersection points  $I$

$$I = I_a + [(d - \mathbf{n} \cdot I_a) / (\mathbf{n} \cdot (I_b - I_a))] (I_b - I_a) \quad (6.43)$$

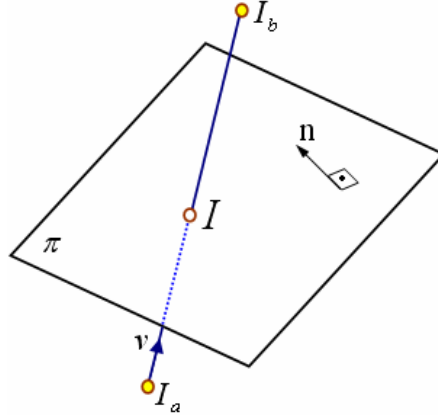


Figure 6.48: Intersecting a segment against a plane

### 6.3.2 Intersecting Segment Against Sphere

Let a segment is given by  $I(v) = I_a + (I_b - I_a)v$  for  $0 \leq v \leq 1$ . Let the sphere surface defined by  $(X - C) \cdot (X - C) = r^2$ , where  $C$  is the center of the sphere, and  $r$  is radius. To find the  $v$  value at which the segment intersect the sphere surface  $I(v)$  is substituted for  $X$ , giving

$$(I_a + (I_b - I_a)v - C) \cdot (I_a + (I_b - I_a)v - C) = r^2 \quad (6.44)$$

Let  $\mathbf{k} = I_a - C$  and  $\mathbf{d} = (I_b - I_a) / \|I_b - I_a\|$  then the Eq.(6.44) takes the form of  $(\mathbf{k} + v\mathbf{d}) \cdot (\mathbf{k} + v\mathbf{d}) = r^2$ . Expanding the dot product yields the following quadratic equation in  $v$

$$v^2 + 2(\mathbf{k} \cdot \mathbf{d})v + (\mathbf{k} \cdot \mathbf{k}) - r^2 = 0 \quad (6.45)$$

The solutions of this quadratic equation is given by

$$v_{1,2} = -(\mathbf{k} \cdot \mathbf{d}) \mp \sqrt{(\mathbf{k} \cdot \mathbf{d})^2 - [(\mathbf{k} \cdot \mathbf{k}) - r^2]} \quad (6.46)$$

Solution of the above equation gives three outcomes with respect to the discriminant  $\Delta = (\mathbf{k} \cdot \mathbf{d})^2 - [(\mathbf{k} \cdot \mathbf{k}) - r^2]$ . If  $\Delta > 0$  there are two real roots for which segment intersects the sphere twice (Figure 6.49-a), If  $\Delta = 0$  there are two equal real roots for which the segment hits the sphere tangentially (Figure 6.49-b), and if  $\Delta < 0$  there are no real roots which corresponds to segment missing the sphere completely (Figure 6.49-c). Although for the case given by  $\Delta > 0$  there are two real roots, one of them can be false intersection (Figure 6.49-d,e). In this case the segment can start inside or outside sphere. One of the  $v$  values from Eq.(6.45), its value is in the range of  $v \in [0,1]$ , gives the intersection point.

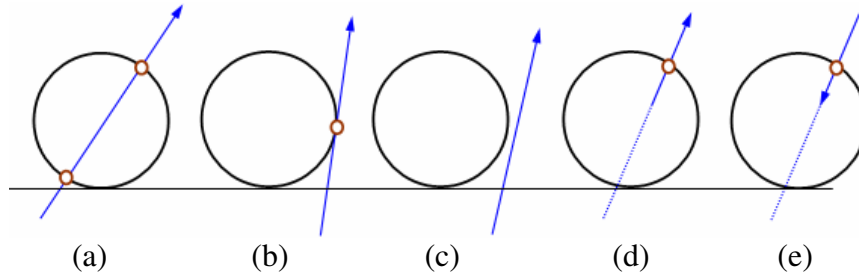


Figure 6.49: Different cases in segment/sphere intersections: (a) Two intersection points, (b) intersecting tangentially, (c) no intersection, (d) segment starts inside sphere, and (e) segment starts outside sphere.

### 6.3.3 Intersecting Segment Against Cylinder

A cylinder with an arbitrary orientation can be described by an axis which passes through points  $B$  and  $Q$ , and by a radius  $r$  (see Figure 6.50). Let  $X$  denotes a point on the cylinder surface. The projection of the vector  $(X-B)$  onto the cylinder axis defined the vector  $(Q-B)$  yields

$$\|P - B\| = (X - B) \cdot \mathbf{n} \quad (6.47)$$

where the unit vector  $\mathbf{n} = (Q - B) / \|Q - B\|$ . Applying Pythagorean Theorem to triangle defined by the points  $B$ ,  $X$  and  $P$  yields

$$\|X - B\|^2 = (X - B) \cdot (X - B) = \|P - B\|^2 + r^2 \quad (6.48)$$

Plugging Eq.(6.47) into Eq.(6.48) yields the following implicit representation for a cylinder surface

$$(X - B) \cdot (X - B) - \{(X - B) \cdot \mathbf{n}\}^2 - r^2 = 0 \quad (6.49)$$

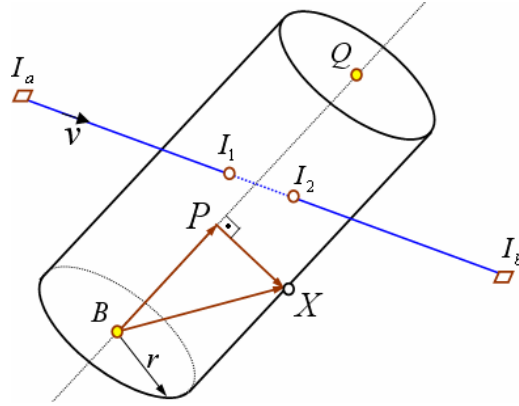


Figure 6.50: A segment is intersected against the cylinder given by points  $B$  and  $Q$  and the radius  $r$ .

The intersection of a segment  $I(v) = I_a + (I_b - I_a)v$  with the cylinder can be found by substituting  $I(v)$  for  $X$  into Eq.(6.49) and solving for  $v$ .

$$(I_a + (I_b - I_a)v - B) \cdot (I_a + (I_b - I_a)v - B) - \{(I_a + (I_b - I_a)v - B) \cdot \mathbf{n}\}^2 - r^2 = 0 \quad (6.50)$$

Setting  $\mathbf{d} = I_a - B$  and  $\mathbf{k} = I_b - I_a$  in the above equation the above equation can be written in the following form

$$A_2 v^2 + 2A_1 v + A_0 = 0 \quad (6.51)$$

where

$$A_2 = \mathbf{k} \cdot \mathbf{k} - (\mathbf{k} \cdot \mathbf{n})^2$$

$$A_1 = \mathbf{k} \cdot \mathbf{d} - (\mathbf{k} \cdot \mathbf{n})(\mathbf{d} \cdot \mathbf{n})$$

$$A_0 = \mathbf{d} \cdot \mathbf{d} - (\mathbf{d} \cdot \mathbf{n})^2 - r^2$$

Solving Eq.(X) for  $v$  gives

$$v_{1,2} = \frac{-A_1 \mp \sqrt{A_1^2 - A_2 A_0}}{A_2} \quad (6.52)$$

The sign of  $(A_1^2 - A_2 A_0)$  determines the number of real roots in the above equation. If the sign is positive, there are two real roots, which correspond to the line intersecting the cylinder in two points. If the sign is negative, there are no real roots, which corresponds to the line not intersecting the cylinder. When  $(A_1^2 - A_2 A_0)$  equals to zero there are two equal real roots signifying that the line tangentially touching the cylinder.

### 6.3.4 Intersecting Segment Against a Cone

The cone (see Figure 6.51) is defined by a vertex  $\mathbf{V}$ , unit axis direction vector  $\mathbf{n}$  and half-angle  $\alpha$ , where  $\alpha \in (0, \pi/2)$ . Let  $\mathbf{P}$  define the points on the cone surface. The half-angle  $\alpha$  is between  $\mathbf{P}-\mathbf{V}$  and  $\mathbf{n}$ , therefore the following expression can be written

$$\mathbf{n} \cdot \left( \frac{\mathbf{P} - \mathbf{V}}{\|\mathbf{P} - \mathbf{V}\|} \right) = \cos \alpha \quad (6.53)$$

The above equation is squared for eliminating the square root calculations and this yields the following quadratic equation

$$(\mathbf{n} \cdot (\mathbf{P} - \mathbf{V}))^2 = (\cos \alpha \|\mathbf{P} - \mathbf{V}\|)^2 \quad (6.54)$$

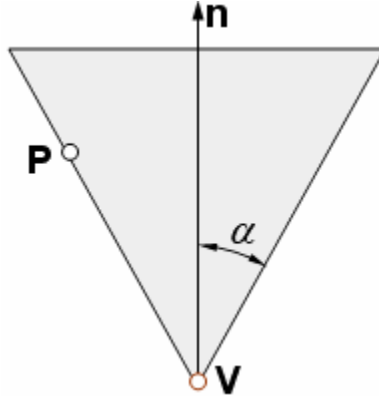


Figure 6.51: A cone with defining parameters

The Eq.(6.54) represents a double cone which has the original cone and its reflection in the opposite direction of  $\mathbf{n}$ . For the intersection calculations the original cone is needed. For eliminating the reflected cone the constraint  $\mathbf{n} \cdot (\mathbf{P} - \mathbf{V}) > 0$  is taken into account also. The quadratic cone equation given in Eq.(6.54) can be written in a quadratic form as  $(\mathbf{P} - \mathbf{V})^T M (\mathbf{P} - \mathbf{V}) = 0$ , where  $M = \mathbf{n} \mathbf{n}^T - \cos^2 \alpha I$ . Therefore the original cone which has the unit axis vector  $\mathbf{n}$  can be defined by

$$(\mathbf{P} - \mathbf{V})^T M (\mathbf{P} - \mathbf{V}) = 0, \text{ and } \mathbf{n} \cdot (\mathbf{P} - \mathbf{V}) > 0 \quad (6.55)$$

Let the line segment is defined by  $I(v) = I_a + (I_b - I_a)v$ , where  $v \in \mathbb{R}$ . For obtaining the intersection points between the line segment and the cone  $I(v)$  is substituted into Eq.(6.55) and this yields the following quadratic equation in one variable

$$A_2 v^2 + 2A_1 v + A_0 = 0 \quad (6.56)$$

where

$$A_2 = (I_b - I_a)^T M (I_b - I_a)^T$$

$$A_1 = (I_b - I_a)^T M (\mathbf{P} - \mathbf{V})$$

$$A_0 = (\mathbf{P} - \mathbf{V})^T M (\mathbf{P} - \mathbf{V})$$

As explained in section (6.3.3) the sign of  $(A_1^2 - A_2A_0)$  determines the number of real roots in the above equation.

### 6.3.5 Obtaining the Cutter Workpiece Engagements

In the discrete vector approach calculating the *CWEs* are straight forward. By intersecting the line segments with the cutter geometries the intersection points are obtained. For mapping the intersection points into 2D domain represented by the engagement angle vs. depth of cut, cutter surfaces are decomposed into the grids (Figure 6.52). During simulation if any one of these grids contains an intersection point, then it is mapped into 2D space. The resolution of the grids on the cutter surfaces is adjusted with respect to the resolution of the discrete vectors of the workpiece.

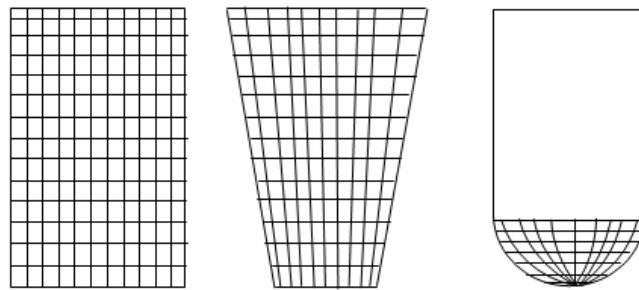


Figure 6.52: Decomposing cutter surfaces into grids.

### 6.4 Discussion

The methodologies presented in this chapter target the important problem of finding Cutter Workpiece Engagements (*CWEs*) in the milling operations. The *CWEs* have been calculated for supporting the force prediction model which requires the *CWE* area in the format described by the engagement angle versus the depth of cut respectively. The developed methodologies can be classified into three categories based on the mathematical representation of the workpiece geometry: Solid modeler based, polyhedral modeler based and vector based methodologies. There is always a tradeoff between computational efficiency and accuracy in these approaches. For example the polyhedral and vector based approaches generate approximated *CWE* results and because of this they require a shorter

computational time than does the solid modeler based approach. But on the other hand in the solid modeler based approach the most accurate *CWEs* are obtained.

In section (6.1) the B-rep solid modeler based *CWE* methodologies for the 3 and 5-axis milling have been developed using a range of different types of cutters and tool paths. In the 3-axis methodology the decomposed cutter surfaces have been intersected with their removal volumes for obtaining the boundary curves of the closed *CWE* area. For this purpose a removal volume has been decomposed into its constituent faces and then the face/face intersection have been performed between the feasible contact surface and these constituent faces at a given cutter location point. Examples have been presented to show that the approach generates proper engagements. Also it can be seen from the examples that in this methodology the computational load in terms of the required Boolean operations is higher for the descending motions described in chapter (5). For example in the ascending motion of a Flat-End mill only the cylindrical part removes the material from in-process workpiece and because of this one Boolean intersection is needed for obtaining the required removal volume in this methodology. But on the other hand the descending motion of the same cutter requires two Boolean intersections one for the cylindrical part and another for the bottom flat part. For the 5-axis milling we had to develop another methodology. As explained in section (6.1.3), because the envelope boundary for 5-axis tool motions are approximated by spline curves applying the same methodology described for the 3-axis milling generates non robust results. Because of this in 5-axis methodology a BODY obtained from the feasible contact surface has been intersected with the in-process workpiece at a given cutter location point. Then the face/face intersections have been performed for obtaining the boundaries of the *CWEs*. In this methodology for minimizing the error introduced by offsetting the feasible contact surface infinitesimally, the offset direction vector has been chosen at the middle of the tool rotation axis.

In section (6.2) the polyhedral modeler based *CWE* methodologies for the 3 and 5-axis milling have been developed. For the 3-axis milling a mapping methodology has been developed that transforms a polyhedral model of the removal volume from Euclidean space to a parametric space which is defined by the *cutter engagement angle*, *depth of cut* and *cutter location*. To reduce the size of the data structure that needs to be manipulated the removal volume has been used instead of the in-process workpiece. This approach also has

the potential of being implemented using a parallel processing strategy [85]. This mapping methodology brings some important advantages over other approaches [88,90]. First, the complexity in the *CWE* calculations is reduced to first order analytical plane-plane intersections. When compared to other polyhedral modeling approaches it has greater robustness because it addresses the chordal error problem found in intersecting polyhedral models. In this methodology it has been assumed that the size of the facets in the removal volume is sufficiently small so as not to introduce significant errors in the *CWE* boundaries. To study this, a comparison has been made between engagements obtained from intersecting the removal volume using a B-rep solid modeler (the most accurate approach) and those from the 3-axis polyhedral approach described in this chapter using different faceting resolutions. Examples of the original and transformed removal volumes are shown in Figure 6.53(a) and (b) respectively. *CWEs* are obtained for cutter locations  $CL_1$  to  $CL_{29}$ . For  $CL_5$  the *CWEs* from the solid modeler (Figure 6.53(c)) and polyhedral modeler at facet resolutions of 2 mm (Figure 6.53(d)), and 6mm (Figure 6.53(e)) are shown. To compare the effect of the size of the facets the *CWE* area is decomposed using a QuadTree [22] spatial data structure (Figure 6.53(f)).

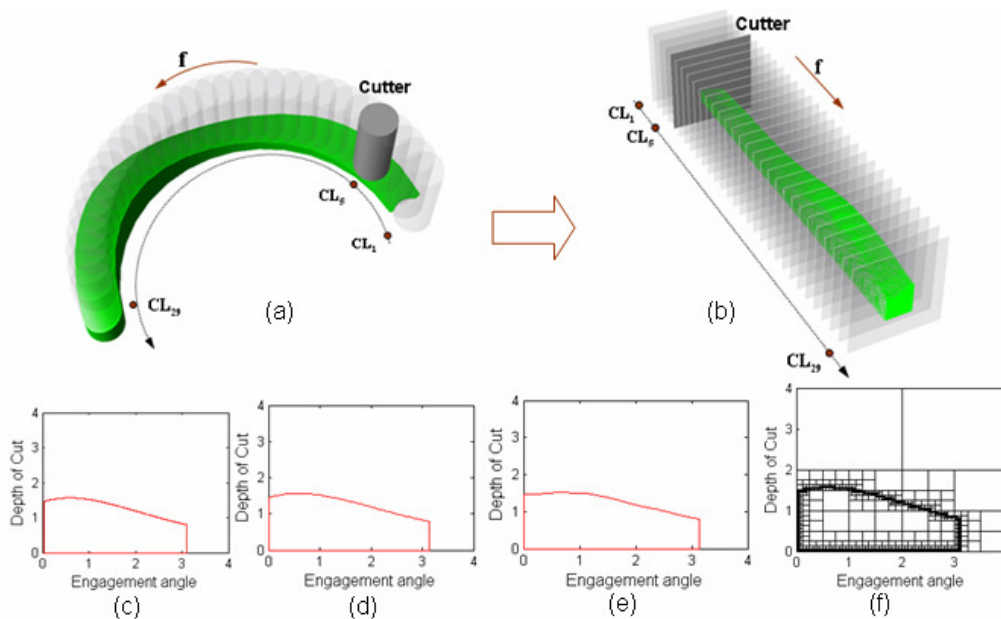


Figure 6.53: Removal Volumes and *CWEs* for different resolutions

The area of the *CWE* is obtained by accumulating the square areas that lie within the QuadTree representation of the *CWE* boundary. For each CL point the areas obtained from the different resolutions are compared with that of the B-rep solid modeler (Figure 6.54(a)). The graph shows a 4% error at 6mm and less than 1% at 2mm. Figure 6.54(b) shows the facet size vs. intersection time i.e. the time for obtaining the *CWE* area for a given cutter location point. While the absolute value would vary depending on the implementation, the trend should remain the same. This shows that there is a small increase in the intersection time as the resolution is decreased from 6mm to 2mm after which it increases significantly. Both the error and intersection time results point to 2mm being a practical limit for the facet size in this example. We point out that this limit will vary depending on the cutter size. An expression needs to be developed to calculate the resolution that considers this parameter.

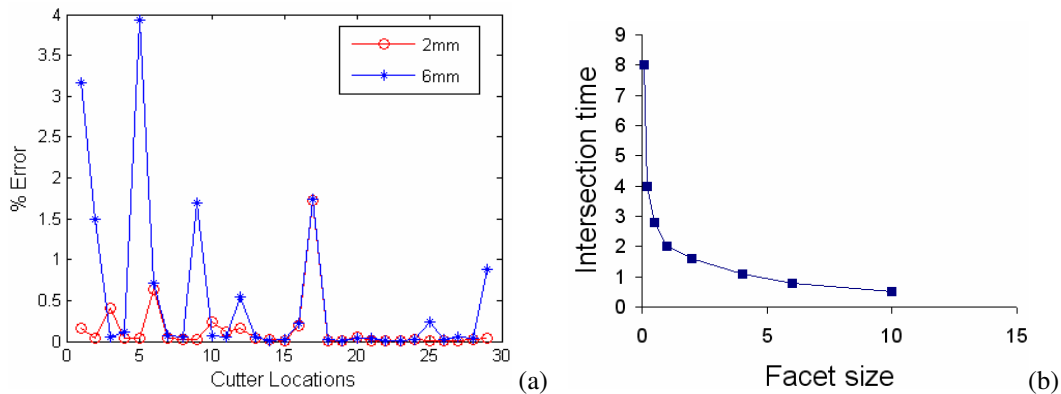


Figure 6.54: The effect of the facet resolutions

Because in 5-axis tool motions the direction of the tool axis vector continuously changes applying the mapping described for the 3-axis milling has increased the distortions of the facets. Therefore an approach similar to that of the 5-axis solid modeler has been developed. In this approach the only difference was the application of the face-face intersections. These intersections have been performed between triangular facets of a BODY and a solid representation of the feasible contact surface.

And finally in section (6.3) a vector based *CWE* methodology has been developed. In this methodology the cutter has been discretized into slices perpendicular to the tool axis. For obtaining the *CWEs* the intersections have been performed between discrete vectors and cutter slices. The intersection calculations are straight forward.

## Chapter 7

### Conclusions

#### 7.1 Contributions and Limitations

In this thesis new methodologies have been proposed to facilitate Cutter Workpiece Engagement (*CWE*) extractions in milling process modeling. This includes an analytical methodology for determining the shapes of the cutter swept envelopes in multi-axes milling, methodologies for updating the in-process workpiece surfaces, analysis of the feasible cutting faces and finally algorithms for extracting *CWEs*. More specifically the contributions are summarized as follows:

- An analytical approach for determining the envelope of a swept volume generated by a general surface of revolution performing multi-axes machining has been developed.

In this approach the cutter geometries are represented using canal surfaces and for describing the cutter envelope surfaces the *two-parameter-family of spheres* has been introduced. Analytically it has been proven that for cutter surfaces performing 5-axis tool motions any point on the envelope surface is also a member of the point set generated from the two-parameter-family of spheres formulation. Later the methodology is generalized for cutters with general surfaces of revolution which performs 5-axis tool motions. In this methodology, by describing the radius function and the trajectory of the moving sphere, different cutter surfaces can be obtained. In this sense the methodology is independent of any particular cutter geometry. The implementation of the methodology is simple. Especially when the cutter geometries are pipe surfaces, fewer calculations are needed for describing the cutter envelope surfaces. Although examples from the application of this methodology have been shown for common milling cutter geometries described by the 7-parameter APT model, this methodology can be also applied to rare cutter geometries. In some cases of 5-Axis milling the cutter swept volume maybe self-intersecting, which requires special processing to handle the topological and geometric problems due to the complex tool motions. Self intersections in this research have not been considered. Modifications to the methodology will need to be developed for this special case.

- A discrete vector model based in-process workpiece update methodology has been developed.

During machining simulation, for each tool movement modification of the in-process workpiece geometry is required to keep track of the material removal process. In this thesis in-process workpiece modeling (or updating) methodologies have been developed using a discrete vector representation. These vectors having orientations in the directions of the  $x,y,z$ -axes of  $R^3$  are intersected with tool envelopes. With this representation more vectors in different directions are used when compared to other discrete vector approaches. Therefore especially when the workpiece has features like vertical walls and sharp edges, the quality in the visualization of the final product has been increased. Also the localization advantage of the *Discrete Vertical Vector* approach has been preserved. For simplifying the intersection calculations the properties of the canal surfaces have been utilized. For cutter geometries defined by a circular cylinder, frustum of a cone, sphere and plane the vector intersection calculations for updating have been made analytically. Because of the complexity of the torus geometry the calculations in this case have been made by using a numerical root finding method. For this purpose a root finding analysis has been developed for guaranteeing the root(s) in the given interval. A typical milling tool path contains thousands of tool movements and during the machining simulation for calculating the intersections only a small percentage of all the discrete vectors is needed. For this purpose a localization methodology, based on the Axis Aligned Bounding Box (AABB) of each tool movement, has been developed. The best feature of the AABB is its fast overlap check, which simply involves direct comparison of individual coordinate values. As explained in chapter (4), for some workpiece geometries 3-axis machining is not suitable for updating the surfaces. Also exact 5-axis milling tool motions are not preferable in workpiece update simulations because the calculations require using the nonlinear root finding algorithms and therefore the computational time becomes high. Therefore in the developed methodologies tool motions using (3+2)-axis milling are considered instead. Using (3+2)-axis tool motions in which a cutter can have an arbitrary fixed orientation in space, 5-axis tool motions can be approximated. An example has been given for illustrating this situation. The Discrete Normal Vector (*DNV*) approach has not been considered in this research. The *DNV* approach can represent the workpiece surface features well with respect to a given tolerance. But because

in this approach the directions of discrete vectors are not identical, localizing the cutter envelope surface during machining simulation becomes difficult. If the workpiece surfaces are represented by *DNVs* then an efficient localization methodology will need to be developed.

- The engagement behaviors of NC cutter surfaces under varying tool motions have been analyzed.

A typical NC cutter has different surfaces with varying geometries and during the material removal process restricted regions of these surfaces are eligible to contact the in-process workpiece with respect to the tool motions. In this thesis for representing these regions the terminology *feasible contact surfaces (FCS)* has been introduced. The word *feasible* has been used because although these surfaces are eligible to contact the in-process workpiece, they may or may not remove material depending on the cutter position relative to the workpiece. When the *FCS* contact the in-process workpiece the Cutter Workpiece Engagements (*CWEs*) are generated. Since *CWEs* are subsets of the *FCS*, formalizing the *FCS* helps us to better understand the *CWE* generation process. The *FCS* have been formalized by using the cutter surface and the cutter envelope boundaries. The cutter surface boundaries are fixed, but on the other hand the cutter envelope boundaries may change depending on the tool motion. For modeling the cutter envelope boundaries a tangency function defined by using the surface normal and the tool velocity has been utilized. Later by changing the tool velocity direction the distributions of the *FCS* on the cutter have been analyzed. The results from these analyses are later used in the development of the *CWE* extraction methodologies.

- Methodologies for obtaining Cutter Workpiece Engagements (*CWEs*) in milling have been developed.

A major step in simulating machining operations is the accurate extraction of the *CWE* geometries at changing tool locations. These geometries define the instantaneous intersection boundaries between the cutting tool and the in-process workpiece at each location along a tool path. The methodologies presented in this thesis target the important problem of finding *CWEs* in milling operations. The *CWEs* are calculated for supporting the force prediction

model requires the *CWE* area in the format described by the engagement angle versus the depth of cut. In these methodologies a wide range of cutter geometries, toolpaths including 5-axis tool motions and workpiece surfaces have been used. The workpiece surfaces cover different surface geometries including sculptured surfaces. The developed *CWE* extraction methodologies can be classified into three categories based on the mathematical representation of the workpiece geometry: Solid modeler based, polyhedral modeler based and vector based methodologies. There is always a tradeoff between computational efficiency and accuracy in these approaches.

In 3-axis solid and polyhedral model based approaches developed in this thesis to reduce the size of the data structure that needs to be manipulated the removal volume has been used instead of the in-process workpiece. In the 3-axis solid modeler methodology the cutter surfaces have been decomposed into different regions with respect to the feed vector direction. Then these surface regions have been intersected with their removal volumes for obtaining the boundary curves of the closed *CWE* area. Decomposing the cutter surfaces in this way allows *CWEs* to be obtained for different parts of a given cutter geometry, e.g. bottom flat or back side of a cutter. Using a solid modeler based representation the envelope boundaries generated by 5-axis tool motions are approximated by spline curve. Applying the solid model based methodology described for 3-axis tool motions to the removal volume obtained from 5-axis tool motions can generate un-expected results because of the non-robust surface/surface intersections. Therefore in this thesis for 5-axis tool motions in-process workpiece has been used instead of the removal volume. In this approach the feasible contact surface generated at a given cutter location point has been offsetted linearly with an infinitesimal amount. As a result of this linear offsetting a surface volume has been generated. Then this volume has been intersected with the in-process workpiece. Later face/face intersections have been performed for obtaining the boundaries of the *CWEs*. In this 5-axis solid model based methodology by linearly offsetting the feasible contact surfaces, the *CWE* extractions have become more robust.

For addressing the chordal error problem in polyhedral models a 3-axis mapping technique has been developed that transforms a polyhedral model of the removal volume from Euclidean space to a parametric space defined by location along the tool path, engagement angle and depth-of-cut. As a result, intersection operations have been reduced to

first order plane-plane intersections. This approach reduces the complexity of the cutter/workpiece intersections and also eliminates robustness problems found in standard polyhedral modeling. Because in 5-axis tool motions the direction of the tool axis vector continuously changes applying the mapping described for the 3-axis milling increases the distortions of the facets. Therefore a *CWE* extraction approach similar to the 5-axis solid modeler based approach has been developed. In the polyhedral model based *CWE* extractions 2mm was the practical limit for the facet size. Still needed is an expression for finding the optimal facet size.

## 7.2 Future Work

The future research work based on this thesis is summarized in the following:

- In this thesis for the polyhedral model based *CWE* extraction methodologies a prototype system has been assembled using existing commercial software applications and C++ implementations. For future work a standalone polyhedral based *CWE* extraction approach that replaces the various commercial components will be developed.
- The *CWE* areas must be decomposed for integrating with the force prediction model. More efficient decomposition techniques (e.g. Quadtrees) will be investigated as a way for representing the engagement geometry. A study of such techniques can lead to a new formulation for the force prediction model that may be more efficient and provide greater capability to manipulate and interpret the results.
- An efficient localization methodology will be developed for localizing the cutter swept envelopes during the material removal process, in which the workpiece surfaces are represented by Discrete Normal Vectors (*DNV*).
- The *CWE* extraction algorithms developed in this thesis will be integrated with the Virtual Machining.

## Bibliography

- [1] Abdel-Malek K., Yeh H.-J., Geometric representation of the swept volume using Jacobian rank-deficiency conditions, *Computer Aided Design* 29 (6) (1997) 457– 468.
- [2] Abdel-Malek K., Seaman, W., Yeh H.-J., “NC-verification of up to 5 axis machining processes using manifold stratification”, *ASME Journal of Manufacturing Science and Engineering* 122 (2000) 1–11.
- [3] Abdel-Malek K., Blackmore D., Joy K., “Swept volumes: foundations, perspectives and applications”, *International Journal of Shape Modeling*, 2004.
- [4] ACIS, Spatial Technology, Inc., Boulder, CO.
- [5] Altintas, Y., ”Manufacturing Automation: Metal Cutting mechanics, Machine Tool Vibrations, and CNC Design”, Cambridge University Press, 2000.
- [6] Atherton P., Earl C., Fred C., "A Graphical Simulation System for Dynamic Five- Axis NC Verification," *Proc. Autofact, SME, Dearborn, Mich.*, 1987, pp. 2-1 to 2- 12.
- [7] Baek N., Maeng S.R., Shin S.Y., Choi B.K., “ A Z-map update method for linearly moving tools”, *Computer Aided design* 35 (2003) 995-1009
- [8] Baek N., Maeng S.R., Shin S.Y., Choi B.K., “A fast NC simulation method for circularly moving tools in the Z-map environment”, *Proceeding of the Geometric Modeling and Processing 2004(GMP’04)*
- [9] Bailey T.E., Jenkins D.M., Spence A.D., Elbestawi, M.A., Integrated Modeling for Metal Removal Operations, *Proc. IMECE, DSC-58 (Nov. 1996), ASME*, 191-198.
- [10] Bajaj C.L., Hoffman C.M., Lynch R.E., Hopcroft J.E.H., “Tracing Surface Intersections”, *Computer Aided Geometric Design*, v 5, n 4, p 285-307, 1988.
- [11] Barnhill R.E., Kersey S.N., “A marching method for parametric surface/surface intersection”, *Computer Aided geometric Design*, Vol. 7, Issue 1-4, p 257-280, 1990.
- [12] Bedi S., Mann S., “Flank Milling with Flat End Milling Cutters”, Preprint submitted to Elsevier Preprint, 29 June 2001.
- [13] Blackmore, D., Leu, M.C., Wang, K. K., “Applications of Flows and Envelopes to NC Machining”, 1992, *Annals of CIRP*, 41/1:493-496.
- [14] Blackmore, D., Leu, M.C., Wang, L.,”The Sweep-Envelope Differential Equation Algorithm and its Application to NC Machining Verification”, *Comp. Aided Des.* 1996.
- [15] Blackmore D., Leu M.C., Wang L.P., “The sweep-envelope differential equation algorithm and its application to NC-machining verification”, *Computer Aided Design* 29 (9) (1997) 629–637.
- [16] Blackmore D., Samulyak R., Leu M.C., “Trimming swept volumes”, *Computer Aided Design*, Vol. 31 No.3, 1999, pp.215-224.
- [17] Brent Richard. P., “Algorithms for Minimization without Derivatives”, Prentice- Hall, Englewood Cliffs, New Jersey, 1973.
- [18] Choi B.K., Jerard R.B., “Sculptured Surface Machining: Theory and Applications”, Kluwer Academic Publishers, 1998.
- [19] Chappel I.T., "The Use of Vectors to Simulate Material Removed by Numerically Controlled Milling," *Computer-Aided Design*, Vol. 15, No. 3, May 1983, pp. 156-158.
- [20] Chiou C-J, Lee Y-S. “Swept surface determination for five-axis numerical control machining”, *Int J Mach Tools Manufact* 2002;42: 1497–507.

- [21] Chung Y.C., Park J.W., Shin H., Choi B.K., "Modeling the surface swept by a generalized cutter for NC verification", *Computer-Aided Design* 1998; 30(8):587-594
- [22] Clifford A. S., Hanan S., "Set operations for Unaligned Linear Quadrees", *Computer Vision, Graphics and Image Processing* 50, 29-49 (1990)
- [23] Drysdale R.L., Jerard R.B., "Discrete Simulation of NC Machining," Proc. ACM Symposium Computational Geometry, ACM, New York, 1987, pp. 126-135.
- [24] Drysdale, R.L., Jerard, R.B., Schaudt, B., Hauck, K., "Discrete simulation of NC machining", *Algorithmica*, Vol. 4, pp. 33-60, 1989.
- [25] Elber G., Kim M.-S., Offsets, sweeps, and Minkowski sums, *Computer Aided Design* 31 (3) (1999) 163–173.
- [26] El-Mounayri H., Elbestawi M. A., Spence A. D., Bedi S., "General Geometric Modelling Approach for Machining Process Simulation", *Int J. Adv. Manuf. Technol.* (1997), 13:237-247.
- [27] Ericson. C., "Real-Time Collision Detection", The Morgan Kaufmann Series in Interactive 3-D Technology, 2005.
- [28] Farouki R.T., Sverrisor R., "Approximation of rolling-ball blends for free-form parametric surfaces", *Comput.-Aided Design* 28 (1996) 871–878.
- [29] Forsythe G.E., Malcolm M.A., Moler C.B., "Computer Methods for Mathematical Computations", Prentice Hall, 1976.
- [30] Fussell, B. K., Hemmett, J. G., Jerard, R. M., 1994, "Geometric and Mechanistic Modeling Integration for Five-Axis Milling Force Prediction," *Proceedings of the Japan-USA Symposium on Flexible Automation, Kobe, Japan, 2*, pp. 747–750.
- [31] Fussell B.K., Hemmett J.G., Jerard R.B., "Modeling of five-axis end mill cutting using axially discretized tool moves", *Proceedings of the 1999 NAMRC Conference, Berkeley, CA, May 25-28, MR99-160*
- [32] Fussell B.K., Jerard R.B., Hemmett J.G., "Modeling of cutting geometry and forces for 5-axis sculptured surface machining", *Computer aided design* 35 (2003) 333-346
- [33] Goldman R.N., Miller J.R., "Combining Algebraic Rigor with Geometric Robustness for Detection and Calculation of Conic Sections in the Intersection of two Natural Quadric Surfaces", 1991, ACM 089791-427- 9/91/0006/0221.
- [34] Gupta S.K., Saini S.K., Spranklin B.W., Yao Z., "Geometric algorithms for computing cutter engagement functions in 2.5D milling operations", *Computer- Aided Design* 37 (2005) 1469–1480.
- [35] [http://en.wikipedia.org/wiki/Wikipedia:Featured\\_picture\\_candidates/Csg\\_tree](http://en.wikipedia.org/wiki/Wikipedia:Featured_picture_candidates/Csg_tree)
- [36] <http://www.sescoi.com/us/>
- [37] Imani B. M., Sadeghi M. H., Elbestawi M. A., "An improved process simulation system for ball-end milling of sculptured surfaces", *International Journal of Machine Tools and Manufacture*, Vol. 38, Issue 9, 1998, 1089-1107.
- [38] Imani B.M., Elbestawi M.A., "Geometric Simulation of Ball-End Milling Operations", *Journal of Manu. Sci. Eng. ASME*, Vol. 123, 177- 184, 2001.
- [39] Jerard R.B., Hauck K., Drysdale R.L., "Simulation of Numerical Control Machining of Sculptured Surfaces," 15th Int'l Symposium on Automotive Technology and Automation, Paper No. 86057, ISATA, Automotive Automation, Ltd., Croydon, UK, 1986.

- [40] Jerard R.B., Drysdale R.L., Hauck K., "Geometric Simulation of Numerical Control Machining," Proc. ASME Int'l Computers in Engineering Conf., ASME, New York, 1988, pp. 129-136.
- [41] Jerard R.B., Drysdale R.L., Hauck K.E., Schaudt B., Magewick J., "Methods for detecting errors in numerically controlled machining of sculptured surfaces", Computer Graphics and Applications, *IEEE*, Vol. 9, Issue 1, p 26-39, 1989.
- [42] Jerard R.B., Fussel B.K.I, Ercan M.T., "On-Line Optimization of Cutting Conditions for NC Machining", NSF Design, Manufacturing & Industrial Innovation Research Conference, Jan 7-10, 2001
- [43] Jung W. Park, Yang H. Shin, Yun C. Chung, "Hybrid cutting simulation via discrete vector model", *Computer-Aided Design* 37 (2005) 419-430.
- [44] Kern, W. F., Bland, J. R. "Solid Mensuration with Proofs, 2nd ed." New York: Wiley, 1948. (page 87).
- [45] Kim KU-Jin, Lee In-Kwon, "The Perspective Silhouette of a Canal Surface, Computer graphics Forum, Vol. 22 (2003),no:1, pp.15-22
- [46] Kral I.H., "Numerical Control Programming in APT", Prentice-Hall, New Jersey, 1986.
- [47] Larue A., Altintas Y., 2004, "Simulation of Flank Milling Processes", *Int. J. Machine Tools and Manuf.*, vol. 45, pp.549-559.
- [48] Levin J.Z., "Mathematical Models for Determining the Intersections of Quadric Surfaces", *Comput. Graph, Image process.* Vol. 11 No 1 1979
- [49] Liu S.Q. , Ong S.K., Chen Y.P., Nee A.Y.C., "Real-time, dynamic level-of-detail management for three-axis NC milling simulation", *Computer-Aided Design*, 38 (2006), 378-391.
- [50] Maekawa T., Patrikalakis N.M., Sakkalis T., Yu G., "Analysis and applications of pipe surfaces. *Computer Aided Geometric Design*, 15:437-458, 1998.
- [51] Magics X, developed by Dimensionalize.
- [52] Mann S., Bedi S. "Generalization of the imprint method to general surfaces of revolution for NC machining", *Computer-Aided Design* (March 2002).
- [53] Martin R., Stephenson P., "Sweeping of three-dimensional objects", *Computer Aided Design* 22 (4) (1990) 223-234.
- [54] Matlab®, The MathWorks, Inc.
- [55] Miller J.R., Goldman R.N., "Geometric Algorithms for Detecting and Calculating All Conic Sections in the Intersection of Any Two Natural Quadric Surfaces", *GRAPHICAL MODELS AND IMAGE PROCESSING*, Vol. 57, No. 1, January, pp. 55-66, 1995
- [56] Miller J.R., 1987, "Geometric approaches to Nonplanar Quadric Surface Intersection Curves", *ACM transactions on Graphics*, Vol.6, No.4, pages 274-307.
- [57] Nishita T., Johan H., "A scan line algorithm for rendering curved tubular objects. In *Proc. of Pacific Graphics '99*, pp. 92-101. 1999.
- [58] Oliver J.H., Goodman E.D., "Color Graphic Verification of N/C Milling Programs for Sculptured Surface Parts," First Symposium on Integrated Intelligent Manufacturing, ASME, New York, 1986.
- [59] Patrikalakis N.M., Maekawa T., "Shape Interrogation for Computer Aided Design and Manufacturing", *Springer Verlag*, ISBN 3-540-42454-7, February 2002.

- [60] Peternell M., Pottmann H. "Computing rational parametrizations of canal surfaces." *Journal of Symbolic Computation*, 23:255–266, 1997.
- [61] Pottmann H., Peternell M., "Envelopes—computational theory and applications", Proceedings, Spring Conference on Computer Graphics and its Applications, Budmerice, Slovakia, 2000, pp. 3–23.
- [62] Quinn J., "Accurate verification of five-axis numerically controlled machining", PhD Thesis, Department of Computer Science, Dartmouth College, Tech Reports PCS-TR93-191, 1993.
- [63] Sarraga R.F. "Algebraic methods for intersections of quadric surfaces in GMSOLID" *Comput. Vision Graph. & Image Proc.* Vol. 22 No. 2 (1983)
- [64] Saturley P.V., Spence, A.D., "Integration of Milling Process Simulation with On-Line Monitoring and Control". *Int. J. Adv. Manuf. Technol.* 16 (2000), 92-99.
- [65] Sederberg T.W., "Algorithm for algebraic curve intersection", *Computer Aided Design*, Vol. 21, Issue 9, p 547-554, 1989.
- [66] Shani U., Ballard D.H., "Splines as embeddings for generalized cylinders", *Comput. Vision Graphics Image Process.* 27(1984) 129–156.
- [67] Sheltami K., Bedi S., Ismail F., "Swept volumes of toroidal cutters using generating curves", *International Journal of Machine Tools and Manufacture* 1998; 38:855-70
- [68] Shpitalni M., Fischer A., 1991, "CSG Representation as a Basis for Extraction of Machining Features," *CIRP Ann.*, 40, pp. 157–160.
- [69] Spence A., Altintas Y., Kirkpatrick D., 1990, "Direct Calculation of Machining Parameters From a Solid Model," *Comput Ind.*, 14, pp. 271–280.
- [70] Spence A.D., Altintas Y., "A Solid modeler based milling process simulation and planning system", *Journal of Engineering for Industry, Transactions of the ASME.* Vol. 116 (1) pp.61-69, 1994.
- [71] Spence A. D., Abrari F., Elbestawi M. A., 2000, "Integrated Solid Modeller Based Solutions for Machining," *Comput.-Aided Des.*, 32\_8\_, pp. 553–568.
- [72] Spence A. D., Li Z., 2001, "Parallel Processing for 2-1/2 D Machining Simulation," *Proceedings of the 6th ACM Symposium on Solid Modeling and Applications*, Ann Arbor, MI, pp. 140–148.
- [73] Sungurtekin, U. A., Voelcker, H. B., 1986, "Graphical Simulation and Automatic Verification of NC Machining Programs," *Proceedings of the IEEE International Conference on Robotics and Automation*, San Francisco, CA. 2, pp. 156–165.
- [74] Oliver J.H., "Graphical Verification of Numerically Controlled Milling Programs for Sculptured Surface Parts", doctoral dissertation, Michigan State Univ., E. Lansing, Mich., 1986.
- [75] Roth D., Bedi S., Ismail F., Mann S., "Surface swept by a toroidal cutter during 5-axis machining", *Computer Aided Design* 33 (1) (2001) 57–63.
- [76] Takata S., 1989, "A Cutting Simulation System for Machinability Evaluation Using a Workpiece Model" *CIRP Ann.*, 38/1, pp. 417–420.
- [77] UGS NX, CAD/CAM/CAE, Siemens.
- [78] Van Hook T., "Real-Time Shaded NC Milling Display," *Computer Graphics (Proc. SIGGRAPH)*, Vol. 20, No. 4, Aug. 1986, pp. 15-20.
- [79] VERICUT, CGITech Inc.

- [80] Voelcker H. B., Hunt W. A., 1981, "Role of Solid Modelling in Machining-Process Modelling and NC Verification," SAE Preprints, Vol. 810195.
- [81] Wang W.P., Wang K.K., "Real-Time Verification of Multiaxis NC Programs with Raster Graphics," IEEE Proc. Int'l Conf. Robotics and Automation, CS Press, Los Alamitos, Calif., 1986, pp. 166-171.
- [82] Wang W.P., Wang K.K., "Geometric modeling for swept volume of moving solids", IEEE Computer Graphics and Applications 6 (12) (1986) 8–17.
- [83] Wang L., Leu M.C., Blackmore D., "Generating sweep solids for NC verification using the SEDE method, in: Proceedings of the Fourth Symposium on Solid Modeling and Applications, Atlanta, Georgia, 14–16 May 1997, pp. 364–375.
- [84] Wang H., Jang P., Stori J.A., "A Metric-Based Approach to Two-Dimensional (2D) Tool-Path Optimization for High-Speed Machining", Journal of Manufacturing Science and Engineering, Vol. 127 33-48 , 2005.
- [85] Wang, J., Peng, X., Yip-Hoi, D., "A multi-agent system for distributed, Internet enabled cutter/workpiece engagement extraction", *Proceedings of the ASME Design Engineering Technical Conference*, v 2006, 11 p.
- [86] Weinert K., Du S.-J., Damm P., Stautner M., "Swept volume generation for the simulation of machining processes", International Journal of Machine Tools & Manufacture 44 (6) (2004) 617–628.
- [87] Wijk J.J. van. "Ray tracing of objects defined by sweeping a sphere. In *Computer Graphics Forum (Eurographics'84)*, pp. 73–82. 1984.
- [88] Yao, Z., "Finding Cutter Engagement For Ball End Milling of Tesellated Free- Form Surfaces", "*Proceedings of IDETC/CIE 2005, ASME International Design Engineering Technical conferences*", DETC2005-84798.
- [89] Yip-Hoi D., Huang X., "Cutter/Workpiece Engagement Feature Extraction from Solid Models for End Milling", *Journal of Manufacturing Science and Engineering, Transactions of the ASME*, Vol. 128, Issue 1, pp. 249-260, 2006.
- [90] Yip-Hoi D., Peng X., "R\*-Tree Localization for Polyhedral Model Based Cutter/Workpiece Engagements Calculations in Milling", ASME CIE, sept 4-7, 2007
- [91] Yun Won-Soo, Ko Jeong Hoon, Lee Han UI, Cho Dong-Woo, Ehmann Kornel F., "Development of a virtual machining system, Part 3: Cutting process simulation in transient cuts", *International Journal of Machine Tools and Manufacture*, v 42, n15, p 1617-1626, 2002.

## Appendix A

### Obtaining the grazing points for cutter geometries represented by pipe surfaces.

As mentioned in chapter (3), the cylinder and torus surfaces are called as *pipe surfaces*. By definition a pipe surface is an envelope of the family of spheres with a constant radius. In this surface type the centers of the characteristic circle and the moving sphere equal to each other. In this section because of its complexity the property (3.2) is proven for the torus surface and for the cylindrical surface similar steps can be used. When the components of the Frenet frame given in Eq.(3.53) are plugged into Eq. (3.52), the torus surface is obtained as a set of the characteristic circles in the following form

$$K(t, u, \theta) = \mathbf{C}(t, u) + R(t, u)(\cos \theta \mathbf{M}(t, u) + \sin \theta \mathbf{B}(t, u)) \quad (\text{A.1})$$

where  $\theta \in [0, 2\pi]$ . The radius of the moving sphere for the pipe surfaces is constant. Therefore the partial derivative of the radius with respect to the toolpath parameter  $t$  equals to zero, i.e.  $r_t(t) = 0$ . Thus under this condition the radius and the center of the characteristic circle from Eqs. (3.50) and (3.51) become as

$$R(t, u) = r, \quad \mathbf{C}(t, u) = \mathbf{m}(t, u) \quad (\text{A.2})$$

Plugging the equations given in (A.2) into (A.1) yields

$$K(t, u, \theta) = \mathbf{m}(t, u) + r (\cos \theta \mathbf{M}(t, u) + \sin \theta \mathbf{B}(t, u)) \quad (\text{A.3})$$

For obtaining a point (so called grazing point) on the cutter envelope surface Eq.(A.3) is plugged into Eq. (3.55) and then the resultant equation representing the surface normal is plugged into Eq. (3.56). These yields

$$\cos \theta (\mathbf{m}_u \cdot \mathbf{M}) + \sin \theta (\mathbf{m}_u \cdot \mathbf{B}) = 0 \quad (\text{A.4})$$

The trigonometric terms from Eq.(A.4) are extracted as follows

$$\cos \theta = \frac{\mathbf{m}_u \cdot \mathbf{B}}{\sqrt{(\mathbf{m}_u \cdot \mathbf{M})^2 + (\mathbf{m}_u \cdot \mathbf{B})^2}}, \quad \sin \theta = \frac{-\mathbf{m}_u \cdot \mathbf{M}}{\sqrt{(\mathbf{m}_u \cdot \mathbf{M})^2 + (\mathbf{m}_u \cdot \mathbf{B})^2}}$$

or

$$\cos \theta = \frac{-\mathbf{m}_u \cdot \mathbf{B}}{\sqrt{(\mathbf{m}_u \cdot \mathbf{M})^2 + (\mathbf{m}_u \cdot \mathbf{B})^2}}, \quad \sin \theta = \frac{\mathbf{m}_u \cdot \mathbf{M}}{\sqrt{(\mathbf{m}_u \cdot \mathbf{M})^2 + (\mathbf{m}_u \cdot \mathbf{B})^2}} \quad (\text{A.5})$$

Plugging  $\cos \theta$  and  $\sin \theta$  from Eq.(A.5) into Eq.(A.3) yields

$$K(t, u, \theta) = \mathbf{m}(t, u) \mp r \left( \frac{(\mathbf{m}_u \cdot \mathbf{B})\mathbf{M} - (\mathbf{m}_u \cdot \mathbf{M})\mathbf{B}}{\sqrt{(\mathbf{m}_u \cdot \mathbf{M})^2 + (\mathbf{m}_u \cdot \mathbf{B})^2}} \right) \quad (\text{A.6})$$

For simplifying the Eq.(A.6) the following cross product representation is used

$$\mathbf{a} \times (\mathbf{b} \times \mathbf{c}) = (\mathbf{a} \cdot \mathbf{c})\mathbf{b} - (\mathbf{a} \cdot \mathbf{b})\mathbf{c} \quad (\text{A.7})$$

Under the rule given in Eq.(A.7) the nominator and inside the parenthesis of Eq.(A.6) can be written as follows

$$(\mathbf{m}_u \cdot \mathbf{B})\mathbf{M} - (\mathbf{m}_u \cdot \mathbf{M})\mathbf{B} = \mathbf{m}_u \times (\mathbf{M} \times \mathbf{B}) \quad (\text{A.8})$$

Also from Eq.(A.7) the length of the nominator inside the parenthesis can be written as follows

$$\| (\mathbf{m}_u \cdot \mathbf{B})\mathbf{M} - (\mathbf{m}_u \cdot \mathbf{M})\mathbf{B} \| = \mathbf{m}_u \times (\mathbf{M} \times \mathbf{B}) = \sqrt{(\mathbf{m}_u \cdot \mathbf{M})^2 + (\mathbf{m}_u \cdot \mathbf{B})^2} \quad (\text{A.9})$$

It can be seen that Eq.(A.9) equals to the denominator given inside the parenthesis of Eq.(A.6). Plugging equivalents of nominator and denominator given inside the parenthesis of Eq.(A.6). from Eqs.(A.8) and (A.9) yields

Appendix A. Obtaining the grazing points for cutter geometries represented by pipe surfaces.

$$K(t, u, \theta) = \mathbf{m}(t, u) \mp r \left( \frac{\mathbf{m}_u \times (\mathbf{M} \times \mathbf{B})}{\|\mathbf{m}_u \times (\mathbf{M} \times \mathbf{B})\|} \right) \quad (\text{A.10})$$

In the above equation the cross product of the normal and bi-normal unit vectors are equal to the tangent vector of the spine curve i.e.  $\mathbf{T} = \mathbf{M} \times \mathbf{B}$ . Thus Plugging the equivalent of  $\mathbf{T}$  from Eq.(3.53) into Eq.(A.10) yields two grazing points  $P_{1,2}$

$$K(t, u, \theta) = P_{1,2} = \mathbf{m}(t, u) \mp r \left( \frac{\mathbf{m}_u \times \mathbf{m}_t}{\|\mathbf{m}_u \times \mathbf{m}_t\|} \right) \quad (\text{A.11})$$

Thus the property (3.2) is proven for the torus which is also a pipe surface.

## Appendix B

### Mapping parameters for milling cutter geometries

#### B.1 Derivation of $M_{cyl}$

A Flat end mill is made up of a cylindrical surface  $CWE_{K,c1}(t)$  at the side and a flat surface  $CWE_{K,c2}(t)$  at the bottom (Figure B.1-a,b). Based on the kinematics of the 3-axis machining these surfaces will contribute to the set  $CWE_K(t)$  as defined in section (6.2.1) i.e.  $CWE_K(t) = CWE_{K,c1} \cup CWE_{K,c2}$ . For the cylinder surface the engagement angle of a point at  $\mathbf{I} \in CWE_{K,c1}(t)$  must lie within  $[0, \pi]$  i.e.  $(0 \leq \varphi(\mathbf{I} | \mathbf{I} \in CWE_{K,c1}(t)) \leq \pi)$  and for the flat surface it must lie within  $[0, 2\pi]$  i.e.  $(0 \leq \varphi(\mathbf{I} | \mathbf{I} \in CWE_{K,c2}(t)) \leq 2\pi)$ .

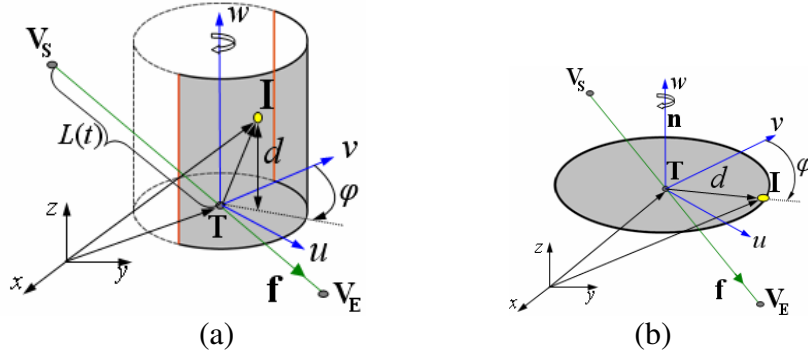


Figure B.1: (a) Cylindrical  $CWE_{K,c1}(t)$ , and (b) bottom  $CWE_{K,c2}(t)$ , faces of the Flat End Mill

#### B.1.1 Obtaining $CWE$ Parameters for the Cylindrical Surface

For the cylindrical surface tool reference point  $\mathbf{F}$  equals to the tool tip point  $\mathbf{T}$ .

$$\mathbf{F}(t) = \mathbf{T}(t) = \mathbf{V}_s + (\mathbf{V}_E - \mathbf{V}_s)t \quad (\text{B.1})$$

For the first step, the geometry of the cylinder changes Eq.(6.11) and (6.12) to,

$$G_c(t) : (\mathbf{P} - \mathbf{F}) \bullet (\mathbf{P} - \mathbf{F}) - \{(\mathbf{P} - \mathbf{F}) \bullet \mathbf{n}\}^2 - r^2 = 0 \quad (\text{B.2})$$

and,

$$CWE_{K,C}(t) : (\mathbf{I} - \mathbf{F}) \bullet (\mathbf{I} - \mathbf{F}) - \{(\mathbf{I} - \mathbf{F}) \bullet \mathbf{n}\}^2 - r^2 = 0 \quad (\text{B.3})$$

respectively. As with Eq.(6.13), Eq.(B.3) results in a quadratic equation in  $t$  when  $\mathbf{I}$  and  $\mathbf{F}$  are substituted. In this case the coefficients  $A_2, A_1$  and  $A_0$  are given by,

$$\begin{aligned} \mathbf{a} &= [(x_I - x_S) \quad (y_I - y_S) \quad (z_I - z_S)] \\ A_2 &= |\mathbf{V}_E - \mathbf{V}_S|^2 - [\mathbf{n} \bullet (\mathbf{V}_E - \mathbf{V}_S)]^2 \\ A_1 &= 2(\mathbf{a} \bullet \mathbf{n}) [\mathbf{n} \bullet (\mathbf{V}_E - \mathbf{V}_S)] - (2\mathbf{a}) \bullet (\mathbf{V}_E - \mathbf{V}_S) \\ A_0 &= |\mathbf{a}|^2 - (\mathbf{n} \bullet \mathbf{a})^2 - r^2 \end{aligned} \quad (\text{B.4})$$

Two real roots of the Eq.(B.3) represent two cutter locations according to Property (6.4) the minimum of them is taken to be the correct tool position as explained in section (6.2.1.1). Using Eq.(6.23-a) and (6.25) the parameters  $\varphi$  and  $L$  are obtained. Finally, the depth of the engagement point as defined by the distance from  $\mathbf{T}(t)$  to  $\mathbf{I}'$  measured along the tool axis vector is simply the z-coordinate of  $\mathbf{I}'$ .

$$d(t) = z'_I = \mathbf{I} \bullet \mathbf{w} - \mathbf{w} \bullet \mathbf{T}(t) \quad (\text{B.5})$$

### B.1.2 Obtaining *CWE* Parameters for the Flat Surface

*CWE* parameters for the Flat surface are obtained without doing mapping. An unbounded plane which is perpendicular to the tool rotation axis is intersected with the original removal volume of the bottom surface for a given cutter location point. Engagement angle  $\varphi$  is found by Eqs.(6.23-a) and (6.23-b). The depth of the cut for the bottom surface is the distance between the intersection point  $\mathbf{I}$  and the center of the bottom surface such that

$$d = \sqrt{x_I'^2 + y_I'^2} \quad (\text{B.6})$$

## B.2 Derivation of $M_{cone}$

Conical part of a Tapered Flat End Mill is made up of a front  $CWE_{K,co1}(t)$  and back  $CWE_{K,co2}(t)$  conical contact faces at the side and a flat surface  $CWE_{K,co3}(t)$  at the bottom respectively (see FigureB.2). Based on the kinematics of the 3-axis machining these surfaces will contribute to the set  $CWE_{K,Co}(t)$  as defined in section (6.2.1) i.e.

$$CWE_{K,Co}(t) = CWE_{K,co1} \cup CWE_{K,co2}(t) \cup CWE_{K,co3}(t) \quad (B.7)$$

For the given tool motion type C in Figure (6.27), the cutter has engagements with all its surfaces and the total engagement area covers the full  $[0,2\pi]$  range i.e.  $0 \leq \varphi(\mathbf{I} | \mathbf{I} \in CWE_{K,Co}(t)) \leq 2\pi$ .

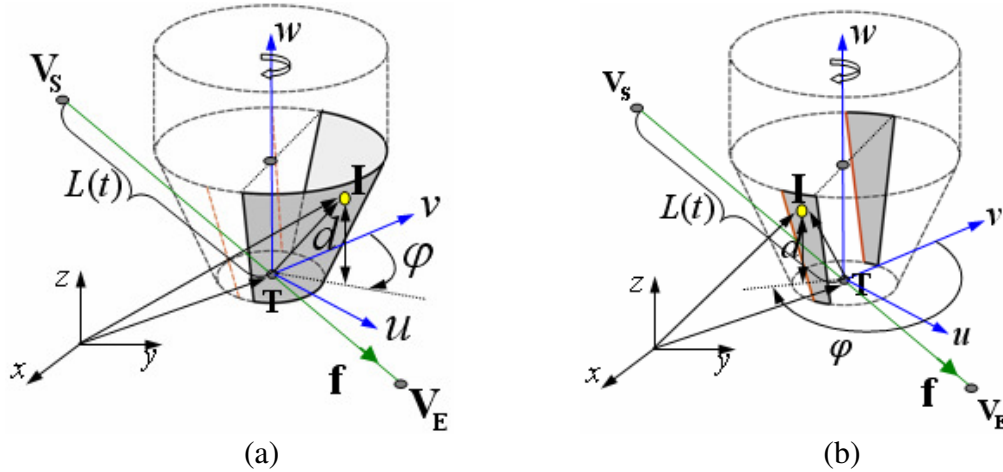


Figure B.2: (a) Front  $CWE_{K,co1}(t)$ , and (b) back  $CWE_{K,co2}(t)$  conical faces of Tapered Flat End Mill

$CWE$  parameters for the flat surface are used from **B.1.2**. For the Tapered Flat End Mill tool reference point  $\mathbf{F}$  equals to the tool tip point  $\mathbf{T}$ , Eq.(B.1). For the first step, the geometry of the cone changes Eqs.(6.11) and (6.12) to,

$$G_{Co}(t) : (\mathbf{P} - \mathbf{V}) \cdot (\mathbf{P} - \mathbf{V}) - (1 + \tan^2 \alpha) \{(\mathbf{P} - \mathbf{V}) \cdot \mathbf{n}\}^2 = 0 \quad (B.8)$$

and

$$CWE_{K,Co} : (\mathbf{I} - \mathbf{V}) \bullet (\mathbf{I} - \mathbf{V}) - (1 + \tan^2 \alpha) \{(\mathbf{I} - \mathbf{V}) \bullet \mathbf{n}\}^2 = 0 \quad (\text{B.9})$$

where  $\alpha$ ,  $\mathbf{n}$  and  $\mathbf{V}$  are the cone half angle, unit normal vector of the tool rotation axis and cone vertex coordinates (see Figure 6.22-a) respectively. The relationship between  $\mathbf{V}$  and  $\mathbf{F}$  is given by

$$\mathbf{V} = \mathbf{F} - \frac{r}{\tan \alpha} \mathbf{n} \quad (\text{B.10})$$

where  $r$  is the radius of the cone bottom surface. As with Eq.(6.13), Eq.(B.9) results in a quadratic equation in  $t$  when  $\mathbf{I}$  and  $\mathbf{F}$  are substituted. In this case the coefficients  $A_2, A_1$  and  $A_0$  are given by,

$$\begin{aligned} \mathbf{a} &= \left[ \left( x_I - x_S + \frac{r}{\tan \alpha} n_x \right) \left( y_I - y_S + \frac{r}{\tan \alpha} n_y \right) \left( z_I - z_S + \frac{r}{\tan \alpha} n_z \right) \right] \\ A_2 &= |\mathbf{V}_E - \mathbf{V}_S|^2 - (1 + \tan^2 \alpha) [\mathbf{n} \bullet (\mathbf{V}_E - \mathbf{V}_S)]^2 \\ A_1 &= (-2\mathbf{a}) \bullet (\mathbf{V}_E - \mathbf{V}_S) + 2(1 + \tan^2 \alpha) (\mathbf{a} \bullet \mathbf{n}) [\mathbf{n} \bullet (\mathbf{V}_E - \mathbf{V}_S)] \\ A_0 &= |\mathbf{a}|^2 - (1 + \tan^2 \alpha) (\mathbf{n} \bullet \mathbf{a})^2 \end{aligned} \quad (\text{B.11})$$

Two real roots of the Eq.(B.9) represent two cutter locations according to property (6.4) and the minimum of them is taken to be the correct tool position as explained in the section (6.2.1.1). Using Eqs.(6.23-a,b),(6.25) and (B.5) the parameters ( $\varphi$ ,  $d$ ,  $L$ ) are obtained.

### B.3 Derivation of $M_{torus}$

A Toroidal portion of the end mill is made up of front  $CWE_{K,t1}(t)$  and back  $CWE_{K,t2}(t)$  contact faces at the side and a flat surface  $CWE_{K,t3}(t)$  at the bottom respectively (see Figure (B.3)). Based on the kinematics of the 3-axis machining these surfaces will contribute to the set  $CWE_{K,T}(t)$  as defined in section (6.2.1) i.e.

$$CWE_{K,T}(t) = CWE_{K,t1} \cup CWE_{K,t2}(t) \cup CWE_{K,t3}(t). \quad (\text{B.12})$$

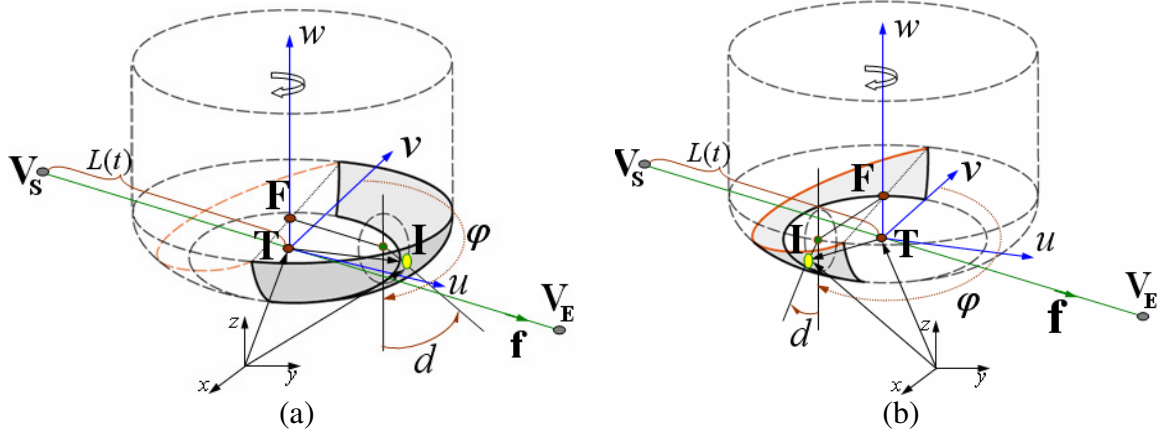


Figure B.3: (a) Front  $CWE_{K,t1}(t)$ , and (b) back  $CWE_{K,t2}(t)$  contact faces of Toroidal End Mill

$CWE$  parameters for the flat surface are used from **B.1.2**. The reference point at  $\mathbf{F}$  is chosen to be the center of the torus. Its location can be expressed by the cutting tool tip coordinates as,

$$\mathbf{F}(t) = \mathbf{T}(t) + r\mathbf{n} \quad (\text{B.13})$$

where  $r$  and  $\mathbf{n}$  are the radius of tube (Figure (B.3-a)) and unit normal vector of the tool axis respectively. For the first step, the geometry of the torus changes Eqs.(6.11) and (6.12) to,

$$G_T(t) : \{(\mathbf{P} - \mathbf{F}) \bullet (\mathbf{P} - \mathbf{F}) - r^2 - R^2\}^2 + 4R^2\{(z - z_C)^2 - r^2\} = 0 \quad (\text{B.14})$$

and

$$CWE_{K,T} : \{(\mathbf{I} - \mathbf{F}) \bullet (\mathbf{I} - \mathbf{F}) - r^2 - R^2\}^2 + 4R^2\{(z - z_C)^2 - r^2\} = 0 \quad (\text{B.15})$$

respectively. Eq.(B.15) results in a quartic 4<sup>th</sup> order polynomial equation in  $t$  when  $\mathbf{I}$  and  $\mathbf{F}$  are substituted.

$$A_4 t^4 + A_3 t^3 + A_2 t^2 + A_1 t + A_0 = 0 \quad (\text{B.16})$$

In this case the coefficients  $A_4, A_3, A_2, A_1 A_0$  are given by,

$$\begin{aligned}
 \mathbf{a} &= (\mathbf{V}_E - \mathbf{V}_S), \quad \mathbf{b} = (\mathbf{I} - \mathbf{V}_S) \\
 A_4 &= |\mathbf{a}|^4, \quad A_3 = -4|\mathbf{a}|^2 (\mathbf{a} \cdot \mathbf{b}) \\
 A_2 &= 4 (\mathbf{a} \cdot \mathbf{b})^2 + 2|\mathbf{a}|^2 (|\mathbf{b}|^2 - r^2 - R^2) + 4R^2(z_E - z_S)^2 \\
 A_1 &= -4 (\mathbf{a} \cdot \mathbf{b}) (|\mathbf{b}|^2 - r^2 - R^2) - 8R^2(z_I - z_S)(z_E - z_S) \\
 A_0 &= (|\mathbf{b}|^2 - r^2 - R^2)^2 + 4R^2[(z_I - z_S)^2 - r^2]
 \end{aligned} \tag{B.17}$$

The Eq.(B.16) gives four roots and according to the property (6.4) toroidal surface has maximum four locations for  $\mathbf{I}$ . For example, two *CWE* points  $\mathbf{I}_1$  and  $\mathbf{I}_2$  are shown in Figure(B.4). Along the tool path, toroidal surface touches the point  $\mathbf{I}_1$  at four interference locations i.e.  $\mathbf{T}_1, \mathbf{T}_2, \mathbf{T}_3, \mathbf{T}_4$  thus for  $\mathbf{I}_1$  the Eq.(B.16) gives four distinct real roots such that  $t_1 < t_2 < t_3 < t_4$  and as explained in section (6.2.1.1) minimum of them is taken to be the tool location when cutter touches this point.

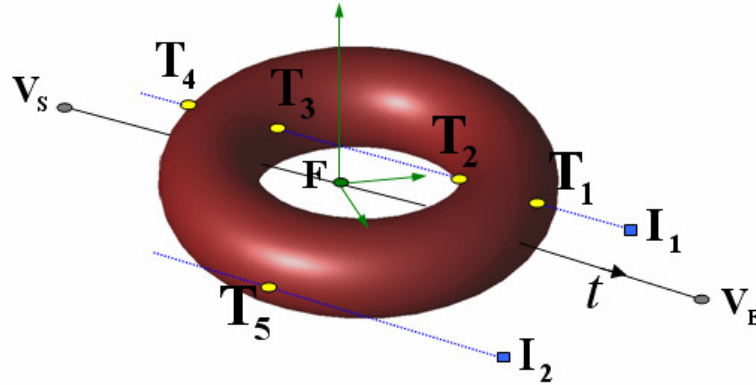


Figure B.4: Cutter interferences with a point in space

Toroidal surface touches  $\mathbf{I}_2$  at the interference location  $\mathbf{T}_5$  and because  $\mathbf{I}_2$  is on the envelope surface of the cutter, Eq.(B.16) gives repeated real roots for this point. Using Eqs.(6.23-a,b) and (6.25),  $(\varphi, L)$  parameters are obtained. The depth of the engagement point is obtained by

*Appendix B. Mapping parameters for milling cutter geometries.*

$$d(t) = \cos^{-1}\left(1 - \frac{z'_I}{r}\right) \tag{B.18}$$